

Microtissue models for studying the dynamics of host-pathogen interactions in the urinary bladder

Présentée le 16 avril 2021

Faculté des sciences de la vie
Unité du Prof. McKinney
Programme doctoral en biotechnologie et génie biologique

pour l'obtention du grade de Docteur ès Sciences

par

Kunal SHARMA

Acceptée sur proposition du jury

Prof. A. C. Oates, président du jury
Prof. J. McKinney, Dr N. Dhar, directeurs de thèse
Prof. C. Dehio, rapporteur
Prof. M. Ingersoll, rapporteuse
Prof. M. Lütolf, rapporteur

Contents

| | |
|---|-----------|
| Acknowledgements..... | 10 |
| Abstract..... | 13 |
| Résumé | 15 |
| Chapter 1. Literature review | 18 |
| 1.1 Bacterial infections..... | 18 |
| 1.2 Bacterial persistence..... | 18 |
| 1.3 Host-Pathogen Interactions | 20 |
| 1.4 Urinary Tract Infections | 22 |
| 1.5 Physiology of uroepithelium | 24 |
| 1.6 Disease model for UPEC pathogenesis..... | 25 |
| 1.6.1 Uropathogenic <i>Escherichia coli</i> (UPEC)..... | 25 |
| 1.6.2 Intracellular bacterial communities | 30 |
| 1.6.3 IBC response to antibiotic and neutrophil mediated stresses | 31 |
| 1.6.4 Quiescent intracellular reservoirs as niche for bacterial persistence and recurrence of UTIs..... | 31 |
| 1.7 Immune responses during UTIs | 32 |
| 1.7.1 Bladder immune system | 32 |
| 1.7.2 Uroepithelial regeneration in response to exfoliated uroepithelial cells | 34 |
| 1.8 Neutrophils..... | 34 |
| 1.8.1 Mechanics of leukocyte motion while undergoing transendothelial migration | 35 |
| 1.8.2 Neutrophil swarming | 36 |
| 1.8.3 Neutrophil extracellular traps | 38 |
| 1.9 <i>In vitro</i> model systems to mimic tissue physiology and study diseases | 41 |
| 1.10 Various architectures used in organ-chip systems | 45 |
| 1.10.1 Organ-on-chip based upon microfluidic membrane | 46 |
| 1.10.2 Organ-on-chip based upon microfluidic scaffolds..... | 46 |
| 1.10.3 Organ-on-chip based upon microfluidic hydrogels..... | 47 |
| 1.10.4 Organs-on-plate..... | 47 |
| 1.11 Different organ-chip systems developed for various organs..... | 47 |
| 1.11.1 Lung-chip systems | 47 |
| 1.11.2 Gut-chip systems..... | 49 |
| 1.11.3 Liver-chip systems | 50 |
| 1.11.4 Kidney-chip systems | 50 |
| 1.12 Organoid systems..... | 51 |

| | | |
|---|---|-----------|
| 1.12.1 | Organoid model systems for disease modelling..... | 51 |
| 1.12.2 | Current technologies to address limitations of the organoid systems..... | 53 |
| 1.12.3 | Synergistic studies by combining organ-chip and organoid systems..... | 54 |
| 1.13 | <i>In vitro</i> model systems of UTIs..... | 56 |
| 1.13.1 | Flow chamber model for uroepithelial cell culture..... | 56 |
| 1.13.2 | Microfluidic model for studying the dynamics of IBCs | 57 |
| 1.13.3 | Organoid model for UPEC infection studies with differentiated urothelial cells | 58 |
| 1.13.4 | Urine-dependent human urothelial organoid model for infection..... | 59 |
| 1.14 | Need for advanced bladder microtissue models..... | 61 |
| 1.15 | Aims of doctoral thesis..... | 62 |
| 1.16 | References | 63 |
| Chapter 2. Bladder organoids as a model system for studying UPEC pathogenesis..... | | 80 |
| 2.1 | Abstract | 81 |
| 2.2 | Introduction | 81 |
| 2.3 | Results | 83 |
| 2.3.1 | Establishment of differentiated mouse bladder organoids..... | 83 |
| 2.3.2 | Invasion of UPEC into the bladder wall provides protection against antibiotics | 84 |
| 2.3.3 | Neutrophils swarm towards intra-organoid UPEC with three distinct migratory | 85 |
| 2.3.4 | Bacteria within the wall of the bladder organoid are refractory to clearance by | 86 |
| 2.3.5 | Volumetric electron microscopy reveals five distinct bacterial niches within | 88 |
| 2.4 | Discussion | 90 |
| 2.5 | Figures..... | 94 |
| 2.6 | Supplementary Figures..... | 101 |
| 2.7 | Supplementary Movie Legends..... | 105 |
| 2.8 | Acknowledgements | 108 |
| 2.9 | Author Contributions | 108 |
| 2.10 | Materials and Methods..... | 109 |
| 2.10.1 | Generation of mouse bladder organoids from mouse bladder uroepithelial cells | 111 |
| 2.10.2 | UPEC culture and injection of mouse bladder organoids | 112 |
| 2.10.3 | Isolation of neutrophils and labelling with CellTracker™ dye..... | 113 |
| 2.10.4 | Co-culture of mouse neutrophils and infected organoids in collagen gels | 114 |

| | | |
|-------------------|---|------------|
| 2.10.5 | Immunofluorescence of uninfected and infected mouse bladder organoids | 114 |
| 2.10.6 | Time-lapse confocal imaging of infected organoids | 115 |
| 2.10.7 | Experimental setup and image analysis for ampicillin treatment experiments | 115 |
| 2.10.8 | Image analysis for confocal live-cell imaging | 116 |
| 2.10.9 | Serial block face-scanning electron microscopy (SBEM) of co-culture of infected organoids with migrating neutrophils | 117 |
| 2.10.10 | Labelling of bacteria, epithelial cells, neutrophils, and organoid lumen in SBEM images | 118 |
| 2.10.11 | 3D analysis and modelling of the infected organoid | 118 |
| 2.10.12 | Scanning electron microscopy of infected organoids | 119 |
| 2.11 | References: | 120 |
| Chapter 3. | Bladder-chip as a model system for studying UPEC pathogenesis | 125 |
| 3.1 | Abstract | 126 |
| 3.2 | Introduction | 127 |
| 3.3 | Results | 129 |
| 3.3.1 | Reconstitution of bladder uroepithelium and bladder vasculature | 129 |
| 3.3.2 | Modelling bladder filling and bladder voiding in the bladder-chip | 129 |
| 3.3.3 | UPEC infection of the epithelial layer under flow in the bladder-chip model | 130 |
| 3.3.4 | Diapedesis of neutrophils across the epithelial-endothelial barrier in response to UPEC infection in the bladder-chip | 131 |
| 3.3.5 | Neutrophil extracellular traps (NETs) formation in response to UPEC infection | 133 |
| 3.3.6 | Heterogenous dynamics of intracellular bacterial communities within urothelial cells | 134 |
| 3.3.7 | Dynamic persistence of intracellular bacterial communities within uroepithelial cells | 136 |
| 3.4 | Discussion | 138 |
| 3.5 | Figures | 141 |
| 3.6 | Supplementary Figures | 147 |
| 3.7 | Supplementary Movie Legends | 159 |
| 3.8 | Acknowledgements | 162 |
| 3.9 | Author Contributions | 163 |
| 3.10 | Materials and Methods | 164 |
| 3.10.1 | Cell culture of human bladder epithelial and bladder endothelial cells | 167 |
| 3.10.2 | UPEC culture for infection of bladder epithelial cells in the bladder-chip | 168 |
| 3.10.3 | Recapitulation of human bladder physiology in human bladder-on-a-chip device | 168 |

| | | |
|-------------------|--|------------|
| 3.10.4 | Characterization and immunostaining of human bladder epithelial and human bladder epithelial cells in ibidi wells and human bladder-chip | 169 |
| 3.10.5 | Characterization of strain-pressure curve in the bladder-chip model ... | 169 |
| 3.10.6 | Mimicking bladder filling and voiding cycle in human bladder-chip... | 170 |
| 3.10.7 | Experimental setup and imaging parameters for time lapse imaging for UPEC infection in the human bladder-chip devices | 170 |
| 3.10.8 | Time lapse imaging for UPEC infections in the human bladder-chip devices | 171 |
| 3.10.9 | Image analysis of confocal live-cell images | 173 |
| 3.10.10 | Isolation and Labelling of human neutrophils from fresh human blood | 173 |
| 3.10.11 | Scanning electron microscopy of human bladder-chip | 174 |
| 3.10.12 | Preparation for transmission electron microscopy (TEM) | 174 |
| 3.11 | References | 176 |
| Chapter 4. | Experimental <i>in vitro</i> approaches to generate stratified uroepithelium | 183 |
| 4.1 | Need for stratified uroepithelium | 183 |
| 4.2 | <i>In vitro</i> systems with stratified uroepithelium | 183 |
| 4.3 | Stratification and differentiation of human uroepithelial cells | 184 |
| 4.4 | Stratification of bladder epithelial cells inside bladder-chip devices with plastic and PDMS membranes | 192 |
| 4.4.1 | Stratification of bladder epithelial cells inside bladder-chip devices with small pores | 194 |
| 4.4.2 | Direct exposure of bladder epithelial cells to flow of diluted pooled urine | 195 |
| 4.4.3 | Air-liquid interface in the bladder-chip followed by urine exposure | 195 |
| 4.5 | Infection of stratified uroepithelium in bladder-chip | 197 |
| 4.6 | Stratified uroepithelium from dissociated bladder organoids splayed on transwell inserts | 198 |
| 4.7 | Splaying up isolated mouse bladder for <i>ex vivo</i> UPEC infection | 200 |
| 4.8 | Transwell insert as a model system for studying UPEC infection in epithelial monolayer | 205 |
| 4.9 | Conclusions | 207 |
| 4.10 | Materials and Methods | 208 |
| 4.10.1 | Protocol for stratification of bladder epithelial cells on the transwell inserts | 208 |
| 4.10.2 | Protocol for seeding of dissociated bladder organoids on transwell inserts | 213 |
| 4.11 | References | 217 |
| Chapter 5. | Conclusions and outlook | 220 |
| | Publications during this PhD and with collaborations | 228 |
| | Resume | 229 |

TABLE OF FIGURES

| | |
|---|-----|
| Figure 1.1: Persistence and Resistance in bacteria..... | 18 |
| Figure 1.2: Persistent infections and antibiotic persistence..... | 19 |
| Figure 1.3: Spectrum of distinct host-pathogen interactions and their ramifications..... | 21 |
| Figure 1.4: Different infection outcomes between intracellular bacteria-immune cell interaction..... | 22 |
| Figure 1.5: Schematic of different layers of uroepithelium: basal cells, intermediate cells, umbrella cells..... | 24 |
| Figure 1.6: Proposed model for UPEC pathogenesis in acute and chronic cystitis..... | 26 |
| Figure 1.7: Pathogenesis of urinary tract infections..... | 28 |
| Figure 1.8: Intracellular bacterial communities (IBCs) develop pod-like structures in the superficial layer of uroepithelium..... | 29 |
| Figure 1.9: IBC fluxing and filamentation in mouse bladder explants..... | 29 |
| Figure 1.10: Immune responses in the bladder..... | 33 |
| Figure 1.11: Stages in transendothelial migration of leukocytes..... | 36 |
| Figure 1.12: Schematic of extravascular neutrophil swarming..... | 37 |
| Figure 1.13: Neutrophil extracellular traps associated with bacteria..... | 39 |
| Figure 1.14: NET formation pathways: NETosis and Non-lytic NETosis..... | 39 |
| Figure 1.15 : Cells in 2D and 3D cell culture systems experience different adhesive, topographical, mechanical and soluble cues from with their surroundings..... | 42 |
| Figure 1.16: Reconstituting tissue level physiology and tissue barrier function on-chip..... | 45 |
| Figure 1.17: Comparison of human organoid systems with other model systems for disease modelling and studying developmental biology..... | 52 |
| Figure 1.18: Combining organoid and organ-chip technologies to build better tissue models..... | 55 |
| Figure 1.19: Flow-chamber based monoculture model for studying dynamics of intracellular bacterial communities..... | 56 |
| Figure 1.20: Microfluidic monoculture model for studying dynamics of intracellular bacterial communities..... | 57 |
| Figure 1.21: Organoid model for UPEC infection studies with terminally differentiated human urothelial cells..... | 59 |
| Figure 1.22: Generation of urothelial organoids on transwell inserts..... | 60 |
| Figure 2.1: Mouse bladder organoids recapitulate the stratification of bladder uroepithelium..... | 94 |
| Figure 2.2: Bacteria within the bladder organoid wall are refractory to antibiotic clearance..... | 95 |
| Figure 2.3: Neutrophil swarming dynamics in response to bacterial infection..... | 97 |
| Figure 2.4: Bacteria within the bladder organoid wall are protected from clearance by neutrophil swarms..... | 98 |
| Figure 2.5: Volumetric electron microscopy reveals five distinct bacterial niches within an infected organoid..... | 99 |
| Figure 2.6: Solitary bacteria within the bladder organoid wall are rod-shaped and flagellated, whereas coccoid forms are non-flagellated..... | 100 |
| Figure 2.7: Mouse bladder organoids recapitulate the stratification of bladder uroepithelium..... | 101 |
| Figure 2.8: Bacteria within the bladder organoid wall are refractory to antibiotic clearance..... | 101 |
| Figure 2.9: Infected organoids have abnormal CK8 expression..... | 102 |
| Figure 2.10: Distinct volume profiles of different neutrophil swarms formed inside infected organoids..... | 102 |
| Figure 2.11: Additional examples of snapshots from time-lapse imaging showing the formation of distinct neutrophil swarms..... | 103 |
| Figure 2.12: Characterization of neutrophil swarm behaviour in infected organoids..... | 104 |
| Figure 2.13: Correlative confocal and serial block electron microscopy image of an infected organoid..... | 104 |
| Figure 2.14 : Flagellin expression was attenuated in UPEC found inside the infected organoids..... | 104 |
| Figure 3.1: Human Bladder-chip model of UTI recapitulates the physiology of bladder filling and voiding..... | 141 |
| Figure 3.2: Neutrophil diapedesis and NET formation on-chip..... | 142 |
| Figure 3.3: Bladder-chip reveals dynamics of IBC growth, shedding and exfoliation..... | 144 |
| Figure 3.4: IBCs offer a semi-protective niche that delays clearance of bacteria by antibiotics..... | 145 |
| Figure 3.5: Characterization of co-cultures of bladder epithelial cells and bladder endothelial cells in bladder-chip..... | 147 |
| Figure 3.6: Characterization of monocultures of HTB9 bladder epithelial cells and HMVEC-Bd bladder microvascular endothelial cells..... | 148 |
| Figure 3.7: Quantification of the linear strain in the PDMS membrane as a function of applied negative pressure in the vacuum channels of the bladder-chip..... | 149 |
| Figure 3.8: Quantification of UPEC attachment to bladder epithelial cells on-chip under flow..... | 149 |
| Figure 3.9: Timeseries highlighting neutrophil diapedesis and swarm formation..... | 150 |
| Figure 3.10: Neutrophils isolated from human blood are CD15+..... | 150 |
| Figure 3.11: Neutrophil attachment to endothelial cells is enhanced upon bacterial infection..... | 151 |

| | |
|--|-----|
| Figure 3.12: Neutrophil diapedesis is stimulated by a pro-inflammatory cytokine gradient across the epithelial-endothelial barrier. | 152 |
| Figure 3.13: NETs formation on the epithelial and endothelial layers of an infected bladder-chip. | 153 |
| Figure 3.14: SEM characterization of uninfected and infected bladder-chips. | 154 |
| Figure 3.15: Neutrophils do not form NETs in response to shear stress in the bladder-chip. | 155 |
| Figure 3.16: Non growing UPEC in response to ampicillin administration in the bladder-chip. | 156 |
| Figure 3.17: Immunofluorescence characterization of IBC formation..... | 157 |
| Figure 3.18: IBC formation from filamentous UPEC. | 157 |
| Figure 3.19: UPEC growth in IBCs during ampicillin treatment. | 158 |
| Figure 3.20: UPEC infection leads to a higher bacterial burden in bladder-chips perturbed with duty cycle. | 158 |
| Figure 4.1: Schematic for generation of islands of stratified uroepithelium under air-liquid interface on transwell inserts..... | 187 |
| Figure 4.2: HTB9 cells undergo non-uniform stratification in air-liquid interface on transwell inserts. | 188 |
| Figure 4.3: Schematic for generation of uniform stratification in bladder epithelial cells on 0.4 μm pore transwell inserts..... | 189 |
| Figure 4.4: Uniform stratification of epithelial cells under urine-liquid interface maintained across epithelium-endothelium on transwell inserts..... | 189 |
| Figure 4.5: Long sheets of uniformly stratified uroepithelium on transwell inserts..... | 190 |
| Figure 4.6: Uroepithelial cells in the upper layer of the uniformly stratified epithelium had bigger nuclei..... | 191 |
| Figure 4.7: Schematic diagram of the bladder-chip device..... | 192 |
| Figure 4.8: PDMS-plastic bonding at room temperature by the formation of amine-epoxy bond at the PDMS-plastic interface. | 194 |
| Figure 4.9: Flow of urine on epithelial side and medium supplemented with 2 mM Ca^{2+} on the endothelial side did not induce stratification in epithelial cells. | 195 |
| Figure 4.10: Island of stratified uroepithelium in bladder-chip. | 197 |
| Figure 4.11: UPEC infection of an island of stratified uroepithelium in bladder-chip. | 198 |
| Figure 4.12: Bladder organoids back to 2D culture in liquid-liquid interface on transwell inserts..... | 199 |
| Figure 4.13: Cells in upper layers of the splayed bladder organoids were bigger in size compared to the cells in the lower and middle layers of the splayed bladder organoid. | 199 |
| Figure 4.14: Modified incubation chamber for studying infected bladder..... | 200 |
| Figure 4.15: Animal retraction system with magnets used for immobilizing stretched bladder..... | 201 |
| Figure 4.16: Isolation and mounting of mouse bladder in a block of low melting agarose..... | 201 |
| Figure 4.17: Imaging <i>ex vivo</i> infected mouse bladder with upright confocal microscope. | 203 |
| Figure 4.18: Infected bladder tissue stained for actin and cell membrane | 204 |
| Figure 4.19: Biofilm like communities in infected bladder tissue housed inside cell culture incubator. Scale bar is 10 μm | 204 |
| Figure 4.20: Transwell insert model for studying the dynamics of UPEC infection in epithelial monolayers. | 205 |
| Figure 4.21: Time lapse imaging of infected epithelial cells on the transwell inserts..... | 206 |

Do not go gentle into that good night

By Dylan Thomas

Do not go gentle into that good night,
Old age should burn and rave at close of day;
Rage, rage against the dying of the light.

Though wise men at their end know dark is right,
Because their words had forked no lightning they
Do not go gentle into that good night.

Good men, the last wave by, crying how bright
Their frail deeds might have danced in a green bay,
Rage, rage against the dying of the light.

Wild men who caught and sang the sun in flight,
And learn, too late, they grieved it on its way,
Do not go gentle into that good night.

Grave men, near death, who see with blinding sight
Blind eyes could blaze like meteors and be gay,
Rage, rage against the dying of the light.

And you, my father, there on the sad height,
Curse, bless, me now with your fierce tears, I pray.
Do not go gentle into that good night.
Rage, rage against the dying of the light.

Acknowledgements

The struggle ends when the gratitude begins.

by Anonymous

First of all, I would like to thank my thesis director Prof. John McKinney for being an incredible teacher, scientific thinker and playing the role of “Reviewer 4” in my research work. I appreciate all the opportunities and freedom you have given me to pursue the project from bottom-up, present our work at conferences and start collaborations within and outside EPFL. One of the things that I admire deeply and tried to learn from John is the art of giving simple and elegant scientific presentations. I remember and respect the time and energy you put into making me learn how to give scientific presentations.

Thanks a lot, to my thesis co-director, Dr. Neeraj Dhar, who I take the liberty to call my scientific father and microbiology encyclopedia. I respect and admire your sheer level of patience in sharing both your theoretical and experimental knowledge of the subject with me. You have nurtured a mechanical engineer to learn microbiology and cell culture techniques. Your advice and scientific explanations even to complex results always lit the light in a dark tunnel. As my scientific father, you were always there for me, and I will never forget that in my lifetime.

The manuscripts from this PhD thesis will not have been possible without the physicist Dr. Vivek Thacker. In the darkness, light from the physicist was needed to convert my research into bladder organoid-bladder chip dual systems. When things were getting chaotic, you pushed me in the right direction under your charismatic magnetic field. I enjoyed going to conferences and spending quality time discussing various topics - microbiology, tissue engineering and most importantly physics. You are amongst the most intelligent, hard-working, quick-learning, multi-talented and well-read persons I have ever met, period. “What one man can do, another can learn”: this axiom will keep me motivated and ambitious during my next ventures. You have inspired me a lot during these last five years, and I would look up to take inspiration from you, always.

I thank the jury members of my thesis committee: Prof. Matthias Lutolf, Prof. Christoph Dehio, Prof. Molly Ingersoll and Prof. Andy Oates for taking your precious time to review my research work. I got inspired in the field of tissue engineering after taking courses on biomaterials and stem cells by Matthias. Your advice during my candidacy helped me to steer this project towards success. I thank Prof. Dehio for useful discussions and future collaboration with McKinney Lab to further pursue my research work. I benefitted significantly from Prof. Molly Ingersoll’s expertise and feedback on my projects. Prof. Andy Oates has a motivating and friendly personality which enabled bioengineers like me to enjoy the research. Prof. Philippe Renaud for useful advice during my master’s degree and transferring the passion for bioengineering. Prof. Gisou van der Goot for allowing me to perform critical and pending time-lapse experiments during the partial lockdown.

I thank Thomas Simonet (“PEC PEC”) for being an amazing colleague and another encyclopedia on UPEC. Your help and enthusiasm were indispensable to partially domesticate this extracellular pathogen to intracellular buddy. I want to thank Dr. Chiara Toniolo on giving useful advice and hope during challenging times in this journey. Other PhD students in McKinney Lab (Gaëlle, Ophélie and Fred), your scientific discussions and relaxation during lab lunches was very pleasing and much needed at times. I will thank François for teaching me cell culture and for neutrophil isolations. The suicide bombers will not have revealed its amazing behaviours in my projects without you. Alumni of the McKinney lab: Dr. Matthieu Délince, Dr. Katrin Schneider, Dr. Joelle Ven and Dr. Amanda

Verpoorte. I would like to thank all of you for providing inspiration and useful tips in the field of microfabrication and single-cell imaging. Dr. Paul Murima for giving two useful idioms for surviving in PhD: “Science is not hard. Doing science with people is hard” and “A PhD will make you cry sometimes, other-times it will make you happy” Thanks to you for passing your enthusiasm for science, and for training this baby microbiologist.

Different core facilities at EPFL played an important role in this research work: Bioimaging & Optics Core Facility (BIOP). In BIOP, I would like to express my big thanks to Dr. Arne Seitz who accepted my request to purchase and install a water objective on the confocal microscope, which turned out to be the tipping point for getting results in my PhD. I want to thank the microscope specialists’ team at BIOP: Thierry Laroche, Dr. Nicolas Chiaruttini, José Artacho and Luigi Bozzo. All of you guys have shown tremendous patience and put your mind & energy to fix a problem whenever the SP8 made my cry. All the complex 3D data would have made me insane without the help of highly talented imaging specialists: Olivier Burri and Dr. Romain Guet. You guys trained and helped me immensely with Imaris. Without you guys, the amazing videos would not have been possible. The batch processing pipelines that you both created saved me weeks of ‘donkey’ work. Last but not the least, I would like to give hugs and kisses to my virtual friends at BIOP, Leica SP8 confocal microscope and Peacock Spider computer. Here I must confess shamelessly that with the SP8 microscope and Peacock Spider computer, we managed to deliver my first baby: PhD thesis. You got me excited, you made me cry, but you were always there with me while alone in that dark BIOP room: AI 0132. I know this is one-sided love, but deep in my heart, I will always cherish the long nights that I have spent with both of you.

When confocal imaging did not satisfy my appetite for high enough image resolution, I went down the alley to Bio-electron microscopy (BioEM) facility’s captain: Dr. Graham Knott. I benefited immensely from your expertise and thorough scientific rigor on electron microscopy. You single-handedly made us achieve and realize the true potential of high-resolution EM imaging. I still remember the time and effort you put into making me learn the first baby steps to get nice high-resolution images of bacteria with a scanning electron microscope. That 20-20 cricket match (master’s thesis) became a long test match (PhD thesis) where you always kept EM side of the game under your control with patience and elegance as a “Wall”. I also express my gratitude to the highly coordinated team at BioEM: Stéphanie Rosset, Marie Croisier and Anaëlle Dubois for different electron microscopy techniques. Your help in optimizing the protocols and getting the electron microscopy image from the difficult samples brought by “yours kindly” makes you the Powerpuff girls at BioEM facility.

I will thank EPFL Histology Core Facility team, especially Dr. Jessica Sordet-Desimoz and Gian-Filippo Mancini for assistance with immunostaining and sectioning with vibrating microtome. All the beautiful immunostaining images had the digital fingerprint of your time and effort into my projects. I also thank EPFL centre of micronanotechnology (CMI) for help during the first year of my PhD. I kicked myself out of CMI soon enough to realize that biology was much harder than microfabrication.

I express my gratitude to different students whom I have supervised during the student projects: Alexandre Marcos (the guy with a moustache), Isabelle Heimgartner, Maria Clapés Cabrer, Simon Bérard and Lydia Kozma. All of you have contributed significantly to my projects. I shall always be indebted for that. I would like to especially give big thanks to Alexandre Marcos, Isabelle Heimgartner and Maria Clapés Cabrer for their hard work and persistence. I have learnt a lot from all of you. Sometimes I was unreasonable in my demands from more effort and time from you, but I wish that you cherished it and learnt something important about how experimental lab work can be both frustrating and exciting.

My gratitude to Dr. Ludovic Serex for being a good collaborator, different members of Lutolf lab (Mike, Nikolche, Andrea and Devanjali) for sharing useful tips and tricks to organoid culture, Hans Mattias Larsson and Elfi Vardar for sharing information about uroepithelial cells, all members of Persat lab for sharing your enthusiasm about microbiology and microfluidics, Patrick Wenger for IT support, Bitplane Imaris and Teamviewer for being the life saviors for image processing and remote working, SV animal facility (Dr. Gisèle Ferrand, Dr. Eleonora Simeoni) and safety (Dr. Camille Freyssenet) for their help and solving the problems related to animal license and training.

I thank Dr. Wareed Ahmad and Dr. Sunil Kumar for inspiring me to remain motivated and ambitious while doing Science. The suicide bombers, “Neutrophils” isolation would not have been possible without protocols from Dr. Germann Markus. Only then I found my hidden love for these mysterious cells. I will thank Prof. Hans Clevers and Dr. Jasper Mullenders for giving me the opportunity to learn bladder organoid culture in their lab. Dr. Selene Gluck and Dr. Kathleen Shah for being wonderful friends and inspiring scientists. I thank Dr. Fatih Gülen and Dr. David Adams for useful discussions. The Indian gang at EPFL (Mohit, Nithin, Sangram, Shravan, Chethana, Harshit, Harshal, Sanket, Ashish, Rishabh) and Uzair who have cheered me through all the tough and exciting times at EPFL.

I have learnt working hard from my father and mother, who still keep me on my toes. My father’s passion in mechanics research influenced me from a young age. My mother has provided me with the love, emotional support and kept my curiosity alive. Thanks to my younger brother who has always been my staunch supporter. This whole PhD would not have been possible without my “better half”: Dr. Maneesha Rupakula. She always supported me during my excited times and more importantly handled my frustration around experimental failures. You were the sink to my negative energy and source of positive energy. Luck was on my side and I made the best decision of my life to find you as my “better half”. I will thank my mother-in-law and father-in-law for their continuous love and support, Dr. Aamani Rupakula and Dr. Sarandeep Boyanapalli, Ved for being a lovely family and sharing my enthusiasm in science and mentoring me.

I would also like to thank uropathogenic *Escherichia coli* for developing such an elusive lifestyle. I did develop a Stockholm syndrome for you. You taught me persistence. This journey was all about chasing you....

Kunal Sharma

Abstract

Urinary tract infections (UTIs) are amongst the most common bacterial infections and are the second-most frequent reason for antibiotic prescriptions. Moreover, in about 25% of all treated cases, recurrence of infection occurs. Uropathogenic *Escherichia coli* (UPEC) is the most common causative agent of UTIs. Much of our current understanding about UTIs has come from mouse models of UTI which have highlighted the intracellular lifestyle of this pathogen in the forms of intracellular bacterial communities (IBCs) as the prominent cause for bacterial persistence. Recurrent infections are thought to be caused by bacterial fluxing from persistent IBCs in the umbrella cell layer of the epithelia in the bladder. Although, *in vitro* model systems of UTIs have been developed to study acute phases of infection including the formation of IBC and their dispersal, they suffer from certain shortcomings. For example, these models lack vasculature and the possibility to impose mechanical stresses, such as those experienced by the cells during bladder filling and voiding. Moreover, the design of these *in vitro* systems makes it difficult to study long-term UPEC persistence when exposed to antibiotic or neutrophil mediated stresses.

In the last two decades, two bioengineering approaches have emerged to generate functional and physiological tissues: organoid and organ-chip systems. Differentiating cells self-organize in a hydrogel and enable the formation of organoids, which mimic various aspects of organ physiology and function in a three-dimensional structure. Organ-chip systems rely upon co-culturing pre-differentiated cells across a synthetic membrane in a defined geometry. The organ-chip systems allow dynamic control over environmental (nutritive) state and over the mechanical stresses experienced by the emulated tissue. In this thesis, I showcase the development of model systems to study UPEC pathogenesis using both these approaches.

In the first part of this thesis, we developed a bladder organoid model of UPEC infection that recapitulates the stratified bladder architecture within a volume suitable for high-resolution live-cell imaging. Bacteria injected into the organoid lumen rapidly enter umbrella cells and proliferate to form IBCs. Unexpectedly, we identified populations of individual “solitary” bacteria that form independently of IBCs and which penetrate deeper layers of the organoid wall and evade killing by antibiotics and neutrophils. Volumetric electron microscopy revealed that these solitary bacteria may be intracellular or pericellular (sandwiched between uroepithelial cells) and are rod-shaped and flagellated, unlike coccoid-shaped and unflagellated bacteria within IBCs. Bacterial fluxing from IBCs is

therefore not an essential requirement for the establishment of persistent bacterial populations in the bladder wall.

The dynamic responses of IBCs to host stresses and antibiotic therapy are difficult to assess *in situ*. In another study, we focussed on examining the lifecycle and persistence of IBCs during early stages of UTIs. We developed a human bladder-chip model wherein superficial umbrella cells and bladder microvascular endothelial cells are co-cultured under flow in urine and nutritive media respectively. Bladder filling and voiding was mimicked mechanically by application and release of linear strain. Using time-lapse microscopy, we show that rapid recruitment of neutrophils from the vascular channel to sites of infection leads to swarm and neutrophil extracellular trap formation but does not prevent IBC formation. Subsequently, we tracked bacterial growth in individual IBCs through two cycles of antibiotic administration interspersed with recovery periods. Analysis of the bacterial growth dynamics revealed that the killing of bacteria within IBCs by the antibiotic was delayed, and in some instances, did not occur at all. During the recovery period, rapid proliferation in a significant fraction of IBCs reseeded new foci of infection through bacterial shedding and host cell exfoliation. These insights reinforce a dynamic role for IBCs as harbours of bacterial persistence, with significant consequences for non-compliance with antibiotic regimens.

Taken together, this thesis presents two novel microtissue models for studying the dynamics of host-pathogen interactions in UTIs. The findings from bladder microtissue models of UTIs will have important ramifications for treatment of not only UTIs but also other bacterial infections that exhibit high levels of recurrence. The model systems can serve as a useful tool for bioengineers and researchers studying immunology, microbiology, cancer, and bacterial persistence in the urinary bladder.

Keywords: bladder organoids, bladder-chip, uropathogenic *Escherichia coli* (UPEC), intracellular bacterial communities (IBCs), bacterial persistence, antibiotic treatment, neutrophil swarms, neutrophil extracellular traps, shear stress, stretching, confocal live-cell imaging

Résumé

Les infections des voies urinaires (IVU) font partie des infections bactériennes les plus courantes et constituent le deuxième motif le plus fréquent de prescription d'antibiotiques. En outre, dans environ 25 % des cas traités, l'infection récidive. Les *Escherichia coli* uropathogènes (UPEC) sont la cause la plus courante d'infection urinaire. Une grande partie des connaissances actuelles sur les infections urinaires provient de modèles murins qui ont mis en évidence le mode de vie intracellulaire de cet agent pathogène sous forme de communautés bactériennes intracellulaires (CBI) comme étant la cause principale de la persistance bactérienne. On pense en effet que les infections récurrentes sont dues à la présence de communautés bactériennes intracellulaires persistantes dans la couche superficielle de l'épithélium de la vessie, constituée de cellules parapluie. Bien que des systèmes modèles *in vitro* d'infections urinaires aient été développés pour étudier les phases aiguës de l'infection, y compris la formation des CBI et leur dispersion, ils présentent certaines lacunes. En particulier, ces modèles sont généralement dépourvus de vascularisation et ne permettent pas l'imposition de contraintes mécaniques, telles que celles subies par les cellules pendant le remplissage et la vidange de la vessie. En outre, la conception de ces systèmes *in vitro* rend difficile l'étude de la persistance à long terme des UPEC lorsqu'elles sont exposées à des antibiotiques ou au stress induits par les neutrophiles.

Au cours des deux dernières décennies, deux approches de bio-ingénierie ont émergé pour générer des modèles de tissus fonctionnels et physiologiques : les systèmes d'organoïdes et d'organes-sur-puce. Les cellules en voie de différenciation s'auto-organisent dans un hydrogel et permettent la formation d'organoïdes, qui imitent divers aspects de la physiologie et de la fonction des organes dans une structure tridimensionnelle. Les systèmes d'organes-sur-puce reposent sur la co-culture de cellules pré-différenciées à travers une membrane synthétique dans une géométrie définie. Les systèmes d'organes-sur-puce permettent un contrôle dynamique de l'état de l'environnement (nutritif) et des contraintes mécaniques subies par le tissu ainsi reproduit. Dans cette thèse, je présente le développement de systèmes modèles pour étudier la pathogenèse des UPEC en utilisant ces deux approches.

Dans la première partie de cette thèse, nous avons mis au point un modèle d'organoïde vésical d'infection par les UPEC qui recrée l'architecture stratifiée de la vessie dans un volume adapté à l'imagerie à haute résolution des cellules vivantes. Les bactéries injectées dans la lumière de l'organoïde pénètrent rapidement dans les cellules de la vessie et y prolifèrent pour former des CBI.

De manière inattendue, nous avons identifié des populations de bactéries individuelles "solitaires" qui se forment indépendamment des CBI, pénètrent dans les couches plus profondes de la paroi de l'organoïde et échappent à l'éradication par les antibiotiques ou les neutrophiles. La microscopie électronique volumétrique a également révélé que ces bactéries solitaires pouvaient être intracellulaires ou péricellulaires (prises en sandwich entre les cellules uroépithéliales), qu'elles étaient en forme de bâtonnets et pourvues de flagelles, contrairement aux bactéries cocoïdes et non-flagellées présentes dans les CBI. La présence de CBI n'est donc pas une condition essentielle pour l'établissement de populations bactériennes persistantes dans la paroi de la vessie.

Les réponses dynamiques des CBI au stress de l'hôte ainsi qu'à l'antibiothérapie sont difficiles à évaluer *in situ*. Dans une autre étude, nous nous sommes donc concentrés sur l'examen du cycle de vie et de la persistance des CBI au cours des premiers stades des infections urinaires. Nous avons développé un modèle de puce vésicale humaine dans lequel les cellules épithéliales superficielles dites cellules parapluie et les cellules endothéliales microvasculaires de la vessie sont co-cultivées dans des conditions d'écoulement, en présence respectivement d'urine et de milieu nutritif. Le remplissage et la vidange de la vessie sont simulés mécaniquement par l'application et le relâchement d'une contrainte linéaire. En utilisant la technique de vidéomicroscopie, nous avons pu montrer que le recrutement rapide des neutrophiles du canal vasculaire vers les sites d'infection conduisait à la formation d'un essaim de neutrophiles ainsi que de pièges extracellulaires de neutrophiles mais n'empêchait pas la formation des CBI. Par la suite, nous avons suivi la croissance bactérienne dans les CBI individuels au cours de deux cycles d'administration d'antibiotiques entrecoupés de périodes de récupération. L'analyse de la dynamique de la croissance bactérienne a révélé que l'éradication des bactéries par antibiotique dans les CBI était retardée, voire n'avait pas lieu dans certains cas. Durant la période de récupération, la prolifération rapide d'une fraction significative des CBI permet également la création de nouveaux foyers d'infection à travers l'excrétion des bactéries et l'exfoliation des cellules hôtes. Ces observations renforcent le rôle dynamique des CBI en tant que médiateurs de la persistance bactérienne, avec des conséquences importantes en cas de non-observance des régimes antibiotiques.

Dans l'ensemble, cette thèse présente deux nouveaux modèles de micro-tissus pour étudier la dynamique des interactions hôte-pathogène dans le cadre des infections urinaires. Les résultats obtenus à partir des modèles de micro-tissus vésicaux d'infections urinaires auront des conséquences importantes pour le traitement non seulement des infections urinaires mais aussi d'autres infections bactériennes qui présentent des niveaux élevés de récurrence. Les systèmes modèles peuvent servir

d'outils utiles aux bioingénieurs et aux chercheurs qui étudient l'immunologie, la microbiologie, le cancer et la persistance bactérienne dans la vessie.

Mots clés : organoïdes vésicaux, puces vésicales, *Escherichia coli* uropathogène (UPEC), communautés bactériennes intracellulaires (CBI), persistance bactérienne, traitement antibiotique, essaims de neutrophiles, pièges extracellulaires de neutrophiles, contrainte de cisaillement, contrainte linéaire, imagerie confocale de cellules vivantes

Chapter 1. Literature review

1.1 Bacterial infections

Bacterial infections are a major cause of human morbidity and mortality. For example, tuberculosis, caused by the bacterium *Mycobacterium tuberculosis*, is the biggest killer among bacterial infections accounting for 1.4 million deaths per year (WHO, 2020). Apart from this, several other pathogenic bacterial strains from genus such as *Staphylococcus*, *Streptococcus*, *Pseudomonas* and *Escherichia coli* are responsible for severe disease burden worldwide. While the discovery and implementation of antibiotics has helped our fight against these infections, the evolution and spread of drug-resistant strains have severely compromised our ability to control these infections. Therefore, while there is an urgent need for the discovery of novel compounds with antimicrobial activities, the fight against bacterial infections also needs a better understanding of the mechanisms by which these bacterial strains are able to survive and persist in the host in the presence of host-derived antimicrobial effectors as well as antibiotics.

1.2 Bacterial persistence

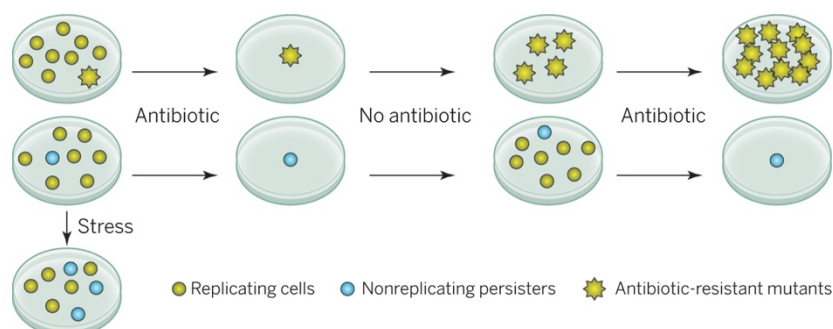


Figure 1.1: Persistence and Resistance in bacteria.

Bacterial populations can include persisters and drug resistant mutants. Bacterial cells that are not killed inherit resistance and eventually produce resistant clones. Image taken from: (Holden, 2015).

Within a short period of time after the discovery of penicillin by Alexander Fleming in 1928, it was observed that few cells survive the antibiotic treatment. Joseph Bigger demonstrated that the fraction of surviving cells was indistinguishable from the first generation upon regrowth (Bigger, 1944; Holden, 2015) (Figure 1.1). This implied that the daughter cells were similarly sensitive to antibiotics as their parents. Thus, the survivors were recognized as persisters rather than drug-resistant mutants whose phenotype was maintained across generations in absence or presence of drugs (Dhar and McKinney, 2007; Holden, 2015). Antibiotic-mediated inhibition of bacterial growth or killing is quantified via the establishment of the minimum inhibitory concentrations (MIC), which is defined as the lowest concentration of antibiotic that will inhibit the bacterial growth after overnight incubation (Andrews, 2001). Antibiotic resistance is a progressive phenomenon: low level resistance arises

at higher MIC, whereas higher level resistance can occur at any antibiotic concentration (Balaban et al., 2019; Wistrand-Yuen et al., 2018). Antibiotic persistence is described by the biphasic killing of bacteria. In contrast, slower killing of bacteria by antibiotics is defined as antibiotic tolerance. Both tolerance and persistence do not result in an increase in MIC compared to resistance (Balaban et al., 2019).

Persistent infections are infections in the host which are not completely cleared out by the host immune system (Balaban et al., 2019) (Figure 1.2). Persistent infection can have multiple causes: bacteria could lie dormant or latent and reactivate only later, or they may be resistant to clearance by the immune system by occupying niches that are hard to access or by modulating and inactivating immune cell function (Dhar and McKinney, 2007; Dhar et al., 2016; Manina et al., 2015). As a consequence of this, infections are often treated by antibiotics, which adds another level of complexity.

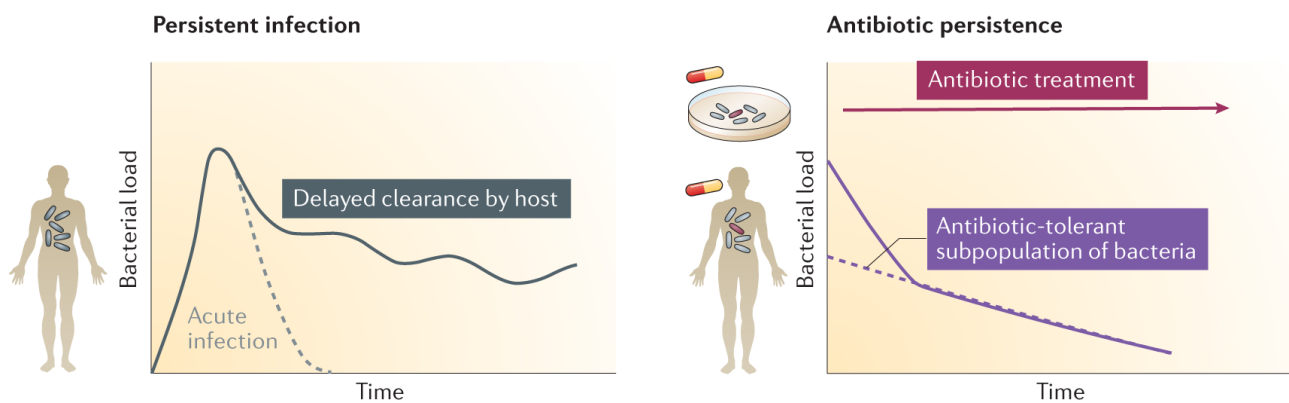


Figure 1.2: Persistent infections and antibiotic persistence.

Persistent infections are slowly cleared by the host. However, the host invokes acute response to clear majority of the pathogen burden. Antibiotic persistence defines the delayed bacterial clearance by antibiotics due to diverse outcomes of bacterial populations in response to antibiotics, *in vitro* or *in vivo*. Image taken from (Balaban et al., 2019).

Antibiotic persistence is defined upon antibiotic therapy to cure bacterial infections (Figure 1.2). Antibiotic persistence highlights the bacterial population that survives the antibiotic treatment and is recalcitrant to antibiotic killing. Antibiotic persistence manifests in the ability of some bacteria to survive high doses of antibiotic treatment due to fluctuations in their cellular function (Balaban et al., 2004, 2019; Dhar et al., 2016; Wakamoto et al., 2013). These non-inheritable fluctuations can over time lead to the accumulation of inheritable mutations that may lead to antibiotic resistance (Balaban et al., 2019; Cohen et al., 2013).

Thus, in contrast to persistent infections which are defined in the context of infections within the host, antibiotic persistence is defined in the context of both *in vivo* and *in vitro* settings. The diverse response of bacterial populations to antibiotic clearance inside the host is due to a spectrum of encounters between the host and the pathogen.

1.3 Host-Pathogen Interactions

The interaction between a bacterium and a host is very complex and can result in diverse outcomes ranging from killing of the bacteria and clearance of the infection to bacterial survival and proliferation leading to eventual killing of the host. These outcomes are influenced by various factors such as “virulence of the pathogen, dose of infectious material, host innate and adaptive immune responses, as well as antimicrobial effectors” (Bumann, 2015; Casadevall and Pirofski, 2000; Dhar et al., 2016; Justice et al., 2004; Lacerda Mariano and Ingersoll, 2020). Moreover, the diverse and heterogeneous host environments provide distinct and often contrasting microenvironmental niches for the pathogen. The host successfully eradicates pathogen subsets within some microenvironmental niches, whereas in others, the pathogen can survive and grow back inside other microenvironmental niches (Bumann, 2015). These diverse host-microbial interactions could be due to heterogeneity in host cell types, nutritive status, antimicrobial effectors such as reactive oxygen species (ROS), reactive nitrogen species (RNS) and acidic pH, or the preferential ability of the pathogen to colonize certain tissues (Figure 1.3). All these heterogeneous environments and varying degrees of stresses result in increased phenotypic heterogeneity both on the bacterial and host side. Often this phenotypic heterogeneity can be crucial for survival and persistence of bacteria under fluctuating environmental conditions (Dhar and McKinney, 2007; Wakamoto et al., 2013). For example, bacteria can enter into a non-growing latent state, from which they can relapse to cause active disease (Manina et al., 2015). Treatment with antibiotics also has been shown to enrich subpopulations of non-growing bacteria that persist and then resume growth and cause relapse after discontinuation of chemotherapy (Levin and Rozen, 2006).

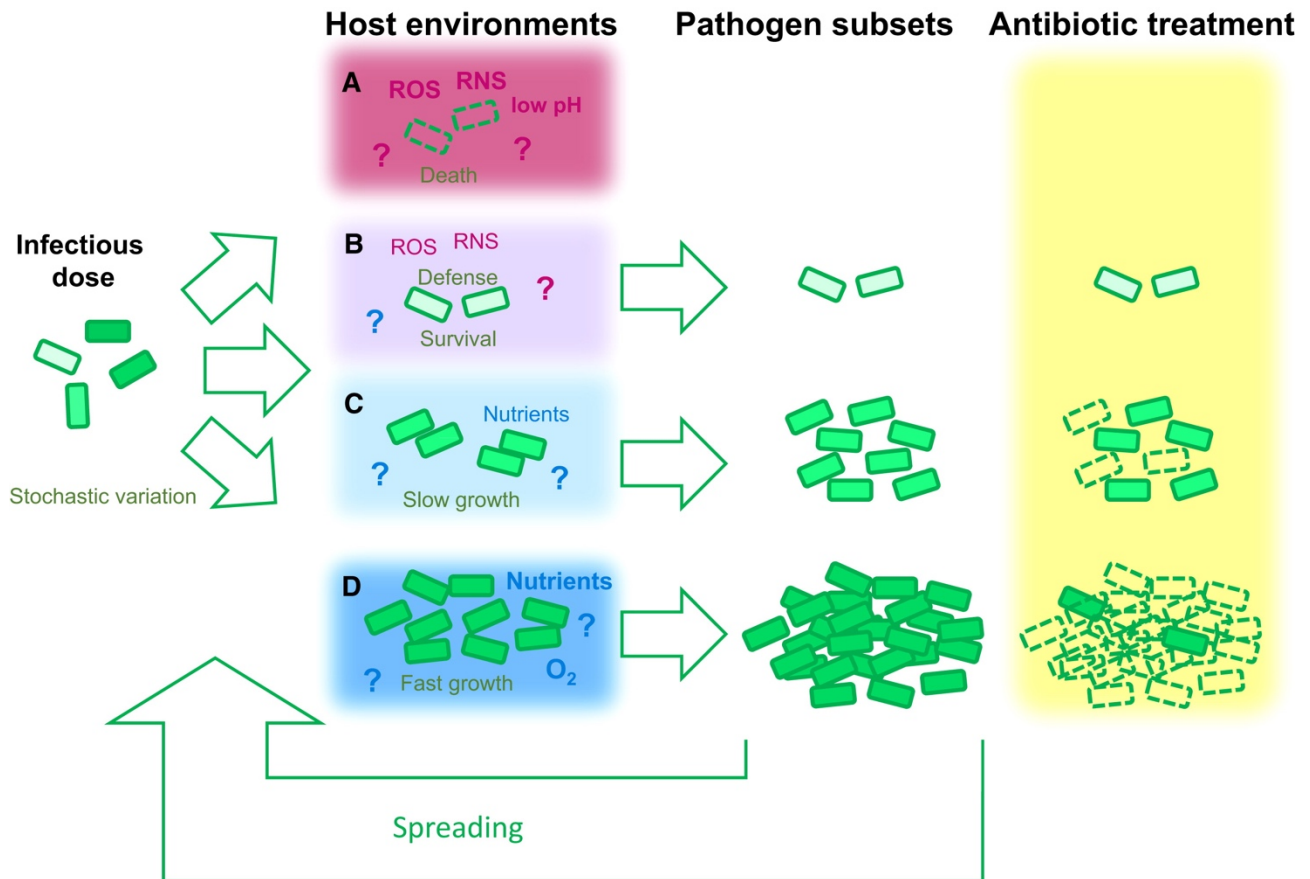


Figure 1.3: Spectrum of distinct host-pathogen interactions and their ramifications.

(A-D) Bacterial populations with stochastically different phenotypes experience disparate microenvironments inside the infected host. Host invokes different known antimicrobial responses (reactive oxygen species (ROS), reactive nitrogen species (RNS), low pH) to kill bacterial populations. These antimicrobial responses could help in emergence of pathogen subsets prior to antibiotic treatment. Bacterial subpopulations arising after different microenvironmental conditions inside the host (A-D) spread across other niches. Upon antibiotic treatment, fast-growing bacterial subpopulations are killed whereas nongrowing bacterial subpopulations survive. Image taken from (Bumann, 2015).

These complex host-microbial interactions are dynamic and have substantial cell-to-cell heterogeneity which exists both in the pathogen (Manina et al., 2015; Wakamoto et al., 2013) as well as the host (Avraham and Hung, 2016; Delincé et al., 2016). The heterogeneity in host-pathogen interactions at the population level could be dissected by using single-cell approaches (Claudi et al., 2014; Helaine et al., 2010). Single-cell approaches reveal diverse outcomes in the interactions between the immune cells such as macrophages and bacteria (Helaine et al., 2010, 2014; Jain and Vogel, 2018; Möller et al., 2012; Pisu et al., 2020; Toniolo et al., 2021). For example, within the same macrophage and bacterial population, some macrophages kill the bacteria, and some macrophages get killed by the bacteria (Avraham and Hung, 2016) (Figure 1.4). Some bacteria persist within the host cells and other bacteria divide unrestrictedly within the host. Still some macrophages exist which do not interact with the bacteria and remain uninfected (Figure 1.4).

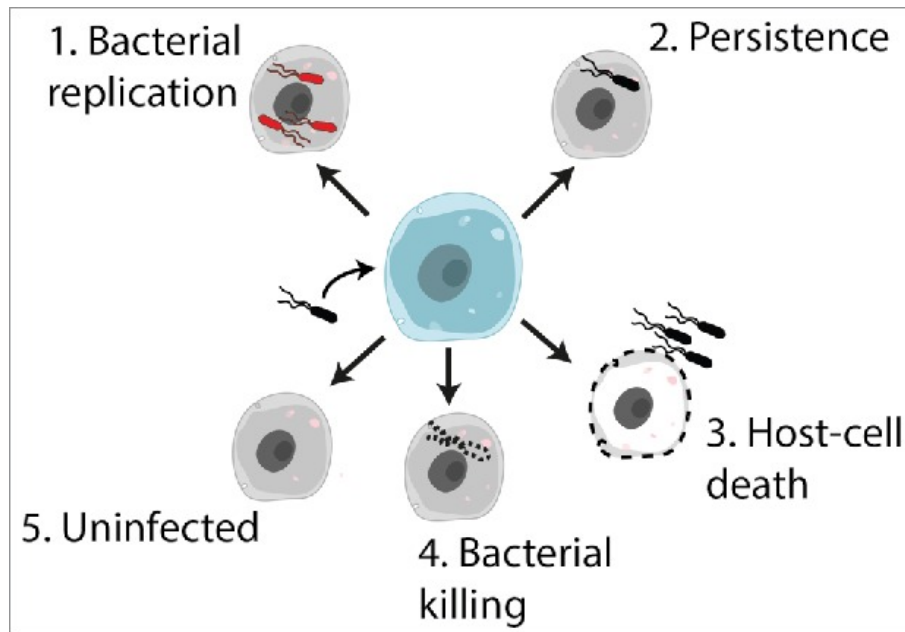


Figure 1.4: Different infection outcomes between intracellular bacteria-immune cell interaction.

Interactions of immune cells such as macrophages with intracellular bacteria can lead to disparate outcomes: 1. Bacterial proliferation, 2. Bacterial persistence, 3. Host cell death and bacterial spreading, 4. Bacterial restriction within the host, or 5. Uninfected host cells. Image taken from: (Avraham and Hung, 2016)

1.4 Urinary Tract Infections

Escherichia coli is a Gram-negative bacterium that inhabits the digestive tracts of humans. Many strains of *E. coli* are beneficial commensals while others (pathogenic strains) can cause several gastrointestinal and urinary tract infections (UTIs). The majority of UTIs are caused by uropathogenic *E. coli* (UPEC), which affect 150 million people worldwide (Lacerda Mariano and Ingersoll, 2020; Öztürk and Murt, 2020). UTIs are an especially important cause of morbidity and mortality among infants, older people, and women (Flores-Mireles et al., 2015). It is estimated that more than 60% of all women report a UTI at least once in their lifetime (Foxman, 2002; Foxman et al., 2000; Klein and Hultgren, 2020). Moreover 20-30% of women with an acute infection could experience infection relapse three or more times in a one-year period. Secondary UTIs post-catheter mediated intervention is also one of the main causes of hospital acquired infections (Foxman, 2010).

The urinary bladder has a resident microbial community in urine known as urinary microbiota (Brubaker and Wolfe, 2016). However, presence of pathogenic bacteria in urine results in diseases known as UTIs. UTIs are classified into disease categories depending upon the site of infection: bacteriuria (urine), cystitis (bladder), and pyelonephritis (kidney) (Flores-Mireles et al., 2015). Infection of the bladder and kidney in immunocompetent people is considered as an uncomplicated UTI, whereas infections in patients with “underlying anatomical or functional abnormalities” is considered as a

complicated UTI (Lacerda Mariano and Ingersoll, 2020). Catheter associated UTI is the most common cause of hospital acquired infections (Geerlings, 2019; Jacobsen et al., 2008). Prominent symptoms of UTIs include recurring urination, burning sensations, and pain during micturition. These symptoms are effects of the “mucosal inflammatory reaction to bacterial colonization of the bladder” (Hannan et al., 2012). Chronic bladder infections can occur as asymptomatic bacteriuria (ABU) (Hannan et al., 2012). The early heterogeneity of innate immune responses to UPEC play an important role in the evolution of UTIs and the likelihood that recurring cystitis will ensue (Hannan et al., 2010). Problems with urine voiding and incontinence increase the chance of recurrent cystitis.

The reason behind higher susceptibility of women to UTIs is attributed to their anatomical predisposition (shorter urethra), shorter distance between anal and urethral opening, and hormonal changes in post-menopausal women (Foxman, 2010). Although UTIs are more common in women, 20% of UTIs occur in men (Ronald et al., 2001). There is a lower prevalence (<1%) of UTIs in younger men which increases significantly to 6% in older men (over 65) (Foxman, 2010; Griebeling, 2005). Thus, with old age, incidence of UTIs in men becomes comparable to the women of the same age group (Ruben et al., 1995). However, the urethral length does not change with age in men. In a recent study, male mice were transurethrally infected with UPEC (Scharff et al., 2019). In this study, both the male mice and testosterone treated female mice were found to be chronically infected with UPEC for up to a month. So, the reasoning about lower number of UTIs in young men (<65 years) due to longer urethra compared to women does not hold true.

Unresolved lower UTIs in male can result in infection of the prostate (Tandan et al., 2016), a condition known as prostatitis (Lupo and Ingersoll, 2019). The principal causative agent for prostatitis is also UPEC. Approximately 50% of men will get prostatitis with prevalence up to 10% (Khan et al., 2017). One clinical study found that antibiotic treatment for UTIs for more than one week in patients with prostatitis or pyelonephritis was correlated to increased chances of recurrent UTIs (Germanos et al., 2019). Thus, prostatitis is also now suggested as a type of complicated UTI (Lupo and Ingersoll, 2019; Meares and Stamey, 1972). The disproportionate number of lower cases for UTIs in men is also attributed to the sex influenced levels of hormones for example, testosterone or estrogen (Robinson et al., 2013). Some reports have hinted at protective role of estrogen based upon higher risk to infections. For example, estrogen application strengthened urothelial tight junctions and increased expression of antimicrobial gene human β -defensin 3 (Lüthje et al., 2013). Estrogen supplementation reduced the chance of recurrent UTI in postmenopausal women (Raz and Stamm, 1993). These

studies highlight that gender influences the host immune response (Ingersoll, 2017; Klein and Flanagan, 2016; Markle and Fish, 2014).

1.5 Physiology of uroepithelium

The uroepithelium is an epithelial layer that covers the inner surface of the urinary tract. As illustrated in [Figure 1.5](#), it is a stratified epithelial tissue that comprises of three distinct layers: basal cells, intermediate cells, and umbrella cells. The basal cell layer includes a single-cell stratum that forms close contact with underlying capillaries. Basal cells are columnar with a diameter of 5-10 μm . Basal cells contain tissue-specific stem cells, which can multiply and differentiate into intermediate cells and umbrella cells (Apodaca, 2004; Yu, 2007). Intermediate cells (about 20 μm diameter) are usually pear shaped with a single unlobed nucleus. Intermediate cells harbour cytoplasmic vesicles. They can be arranged in a unicellular or multicellular layered architecture depending upon the extent of bladder stretching. Umbrella cells are generally of hexagonal shape, but their size and geometry vary depending on the degree of mechanical stretch experienced by the bladder.

The superficial layer of umbrella cells serves as a tissue mechanosensor that senses bladder filling and communicates signals to the nervous system to stimulate micturition. Electrophysiological properties of umbrella cells are sensitive to the direction, magnitude, and rate of applied force. Umbrella cells respond to mechanical stimuli by increased ion transport and membrane traffic (Truschel et al., 2002; Yu, 2007).

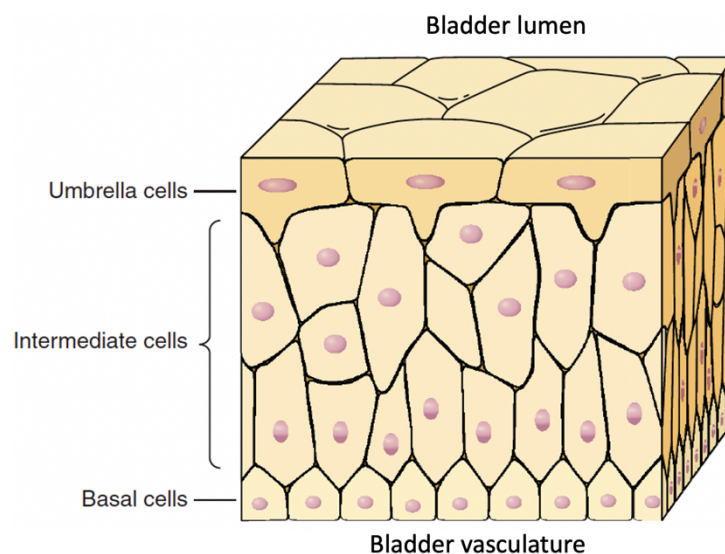


Figure 1.5: Schematic of different layers of uroepithelium: basal cells, intermediate cells, umbrella cells.

The uroepithelium is exposed to the urine in the bladder lumen whereas it receives nutrition from the bladder vasculature. Image modified from: (Yu, 2007).

The early stages of bladder filling are characterized by a rapid increase in the bladder's surface area. In the later stages, the tissue approaches a mechanical equilibrium, and the surface area increases only slowly with time. The mean time and mean rate for natural bladder filling in humans has been observed to be 24.2 min and 1.4 ml/min during cystometry (Lee and Kim, 2008). Cytoplasmic fusiform vesicles increase in number and fuse with the apical surface of umbrella cells in response to bladder filling. Upon voiding, the added membrane is endocytosed to recycle the population of dynamic vesicles. The uroepithelium becomes thinner as intermediate and basal cells are pushed laterally in response to the increasing volume of urine. Umbrella cells change from a flat shape in the empty bladder to a thinner squamous shape in the filled bladder (Apodaca, 2004).

The basolateral membrane of uroepithelium undergoes mechanical extension and contraction during alternate cycles of bladder filling and voiding. It has been shown that stretch *per se*, rather than the hydrostatic pressure within the bladder, activates ion transport and membrane turnover in umbrella cells (Truschel et al., 2002; Yu, 2007).

1.6 Disease model for UPEC pathogenesis

1.6.1 Uropathogenic *Escherichia coli* (UPEC)

UPEC has acquired “pathogenicity islands, plasmids and DNA segments by horizontal gene transfer (Moblely, 2016). The major pathogenic *E. coli* strains are CFT073, UTI89 (Lloyd et al., 2007). Virulent pathogenic strains generally have more distinct fimbriae, toxins and iron receptors than non-pathogenic strains (Lloyd et al., 2007; Mobley, 2016). These acquired characteristics promote bacterial survival and persistence within adverse environments (such as the urinary tract) and during antibiotic therapy. Expression of toxins like haemolysin and cytotoxic necrotizing factor 1 allows UPEC to inflict tissue damage, colonize host tissues, and dampen the host immune response (Dhakal and Mulvey, 2012; Mills et al., 2000; Wiles et al., 2008). These toxins can also manipulate host inflammatory responses and host cell survival. Some studies have elucidated the role of ion transporters as key players in UPEC pathogenesis. These transporters include UPEC genes involved in copper efflux, nickel import, and potassium import (Subashchandrabose et al., 2014).

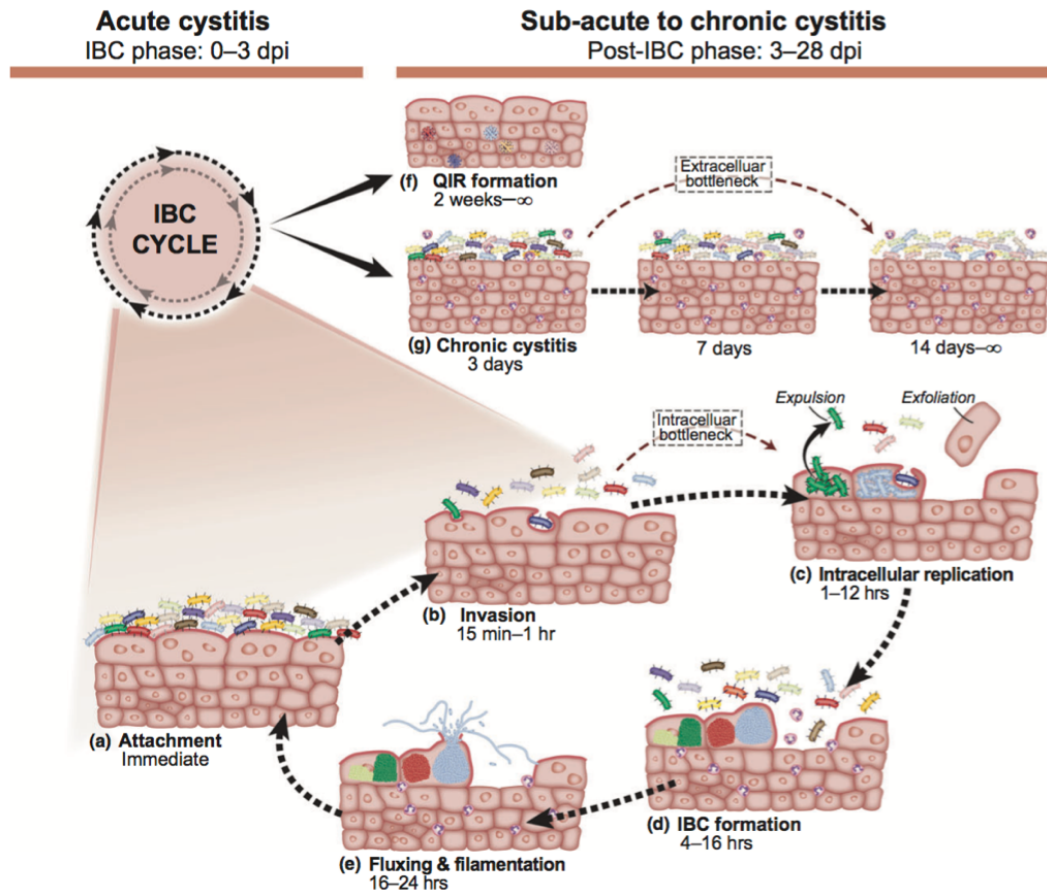


Figure 1.6: Proposed model for UPEC pathogenesis in acute and chronic cystitis.

(a) Bacteria attach to the superficial layer of the uroepithelium. (b–d) Post-bacterial attachment, few bacteria manage to invade the uroepithelium and subsequently proliferate intracellularly to form intracellular bacterial communities (IBCs). (e) IBCs filaments and fluxes to release bacteria which could reseed other uroepithelial cells and repeat the whole cycle of IBC formation in acute UTI. (f) During acute infection, solitary bacteria can remain in dormant state as quiescent intracellular reservoirs (QIRs) and persist in the uroepithelium for several weeks. (g) In chronic cystitis, the uroepithelium does not support IBC formation. Subsequently UPEC either remains adherent to the uroepithelium and grows extracellularly within the bladder lumen. Image taken from (Hannan et al., 2012).

The currently accepted model for acute and chronic cystitis is shown in Figure 1.6. UTIs start when uropathogenic bacteria invade and populate the urethra. Some of the ways by which UPEC invasion of the urethra can occur are, for example, either from the gut (Hooton, 2001; Lacerda Mariano and Ingersoll, 2020), sexual intercourse (Moore et al., 2008a), catheter mediated infections (Jacobsen et al., 2008) or due to problems with bladder voiding during urinary incontinence (Moore et al., 2008b).

Once uropathogens attach to the periurethral area, they can ascend to the bladder and invade the umbrella cells lining the bladder wall with the help of adhesive appendages (pili and adhesins), as shown in Figure 1.7. UPEC and other uropathogens can bind to uroplakin, a high-mannose glycoprotein abundantly expressed on the surface of umbrella cells in mice and humans, through type 1 adhesive pili (Mulvey et al., 1998). Attachment of UPEC to host cells is mediated by unusual “catch-

bonds” such that the strength of adhesion increases from weak to strong with a corresponding increase in shear stress (up to a limit, beyond which rupture occurs) (Sauer et al., 2016; Thomas et al., 2002). This attachment between type 1 pili and uroplakins on the urothelial surface is strong enough to resist clearance by the shear forces of micturition. In addition, UPEC lacking type 1 pili can invade into bladder epithelial cells using other adhesive structures, such as P pili, S/FIC pili, and the Afa/Dr family of adhesins (Mulvey, 2002; Servin, 2014).

UPEC infection of the urinary bladder is countered by innate defences of the host, including influx of anti-bacterial neutrophils (Haraoka et al., 1999) and epithelial exfoliation at the infected site (Rosen et al., 2007). The host bladder epithelial cells (BECs) rejuvenate the damaged/exfoliated superficial epithelial cells by initiating a genetic program to differentiate and proliferate the underlying transitional epithelial cells and cause them to proliferate (Shin et al., 2011). Neutrophils generate cytotoxic environments (including the oxidative burst that is triggered by contact with bacteria) and BECs experience oxidative stress within infected bladder tissue. Uropathogens evade destruction by the host immune system by invading into host cells and forming recalcitrant biofilms (Figure 1.7, Figure 1.8). After damaging the host bladder tissue, some uropathogens (including UPEC) may ascend via the ureters to the kidney, causing pyelonephritis. Finally, advanced UTIs may culminate in bacteraemia when uropathogens cross the tubular epithelial cells of the kidney to enter the blood circulatory system (Figure 1.7).

Bacterial expulsion is a potent immune defence mechanism to reduce bacterial burden within the epithelium. Uroepithelium expels UPEC trapped within Rab27b (Bishop et al., 2007) and Rab11a vesicles (Miao et al., 2017) and this expulsion could be mediated by cross talk between Rab27b and Rab11a vesicles (Miao et al., 2017). However, a small subpopulation is able to replicate inside bladder cells upon escape from vesicles. These bacteria grow to form biofilm-like communities within bulging globular structures called “pods” (Anderson et al., 2003) (Figure 1.8). These pods of tightly packed intracellular bacteria have been shown to reside within the host cell cytoplasm rather than being enclosed within membrane-bound compartments. The bacteria inside the pod are themselves altered; the bacteria within IBCs frequently transition from rod-shaped bacterium to shorter coccoid morphology (Anderson et al., 2003).

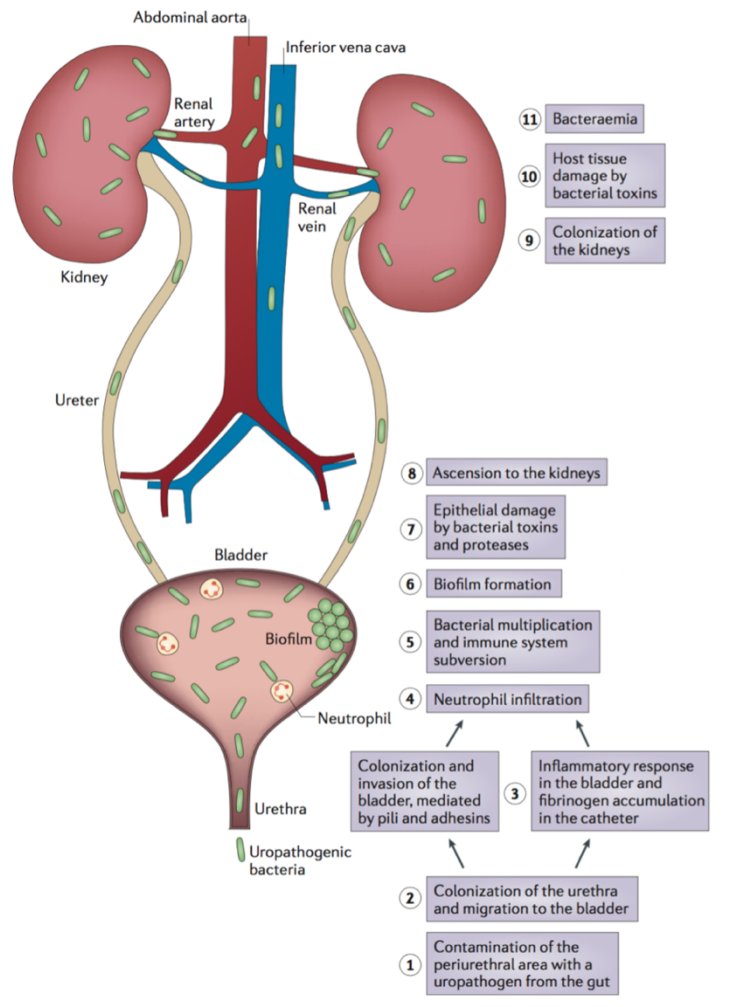


Figure 1.7: Pathogenesis of urinary tract infections.

(1) Uropathogens start UTIs with contamination of the bladder from the gut via colonization through the urethra. (2) Bacteria migrate to the bladder and use its pili to cause invasion inside umbrella cells. (3,4) Host evokes inflammatory response via neutrophil migration to the bladder lumen clearing extracellular bacteria. (5) Bacteria evade the immune system by morphological changes in cell shape. (6) Invaded bacteria proliferate to form intracellular biofilm-like communities. (7) Bacteria produces toxins and proteases that lead to uroepithelium damage. (8) Some nutrients are released from damaged host cells which help bacteria in ascending to the kidneys. (9,10) Bacteria invade the kidney and release toxins to cause kidney damage. (11) Uncontrolled bacteria can break the tubular epithelial barrier to reach the blood stream, a condition known as bacteraemia. Image taken from (Flores-Mireles et al., 2015).

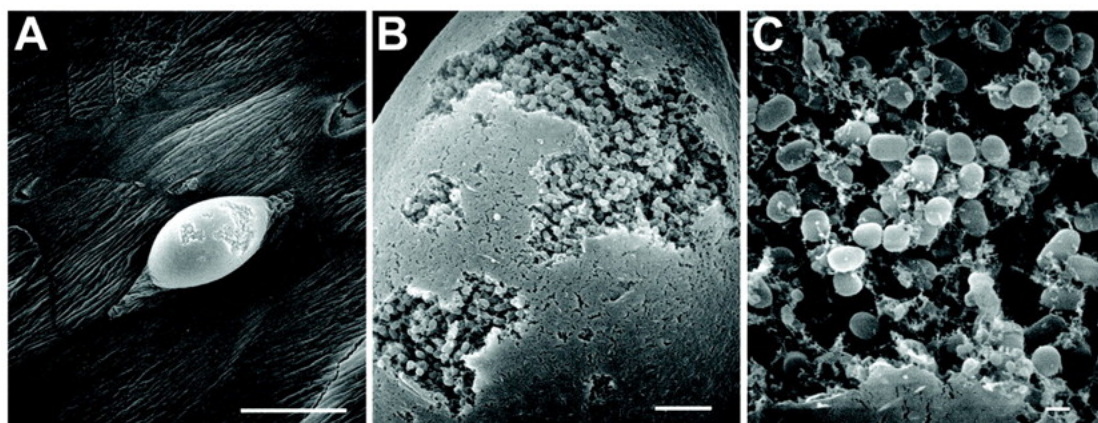


Figure 1.8: Intracellular bacterial communities (IBCs) develop pod-like structures in the superficial layer of uroepithelium.

Bladders of UPEC-infected C3H/HeJ mice were dissected at 24 hours post-infection, fixed, and visualized by scanning electron microscopy. Scale bars: 50 μm (a), 5 μm (b), 0.5 μm (c). Image taken from (Anderson et al., 2003).

Progression of IBCs in the bladder of infected mice has been proposed to go through different stages of bacterial proliferation, biofilm formation and finally bacterial dissemination (Justice et al., 2004; Scott et al., 2015) (Figure 1.9). In the initial stages of infection, the bacteria are non-motile and rod-shaped, and they undergo rapid multiplication within umbrella cells. At later stages, IBCs contain mainly coccoid-shaped and slowly replicating bacteria. In order to colonize other tissues, the bacteria become motile and detach from the IBC. The formation of intracellular bacterial pods has been shown to protect UPEC from killing mediated by host neutrophils (Justice et al., 2004). UPEC filamentation, which occurs as part of the bacterial SOS stress response, may enhance UPEC resistance to uptake and killing by phagocytic cells of the host (Justice et al., 2006).

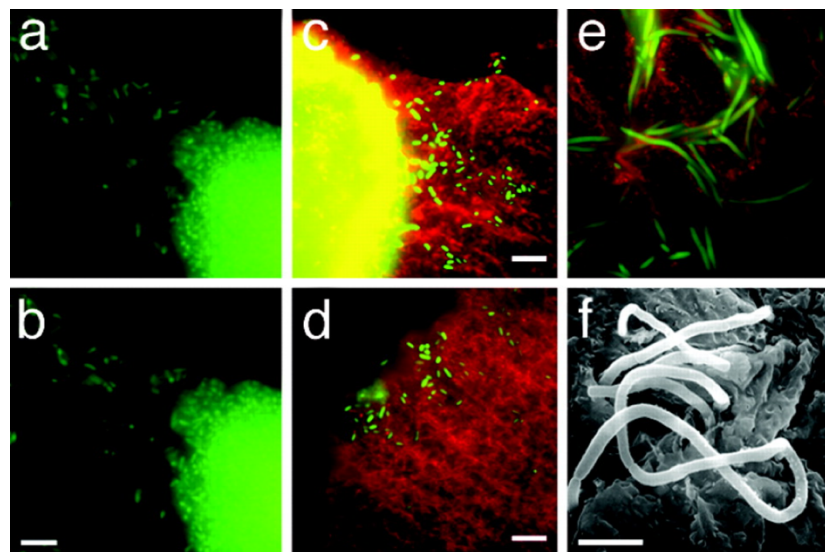


Figure 1.9: IBC fluxing and filamentation in mouse bladder explants.

(a, b). Detachment and fluxing are shown with images taken at 3-second intervals. The individual bacteria are detached via bacterial shedding from IBCs. (c, d) Fluorescence images showing escaped bacteria (green) on the surface of superficial epithelial cells (red). The bright yellow patch (c) is IBC epifluorescence within the umbrella cell. (e, f) Filamentous bacteria on the bladder surface are shown by fluorescence microscopy (e) and scanning electron microscopy (f). Scale bars: 10 μm (b, c, d, h) and 5 μm (f). Image taken from (Justice et al., 2004).

1.6.2 Intracellular bacterial communities

The mouse models of UTIs recapitulates IBCs *in situ* in the mouse bladder. However, IBCs are difficult to detect in mouse bladder and in urine (Scott et al., 2015). Only 2% of the invaded bacteria (or .002% of the bacterial inoculum) manage to successfully form IBCs (Schwartz et al., 2011). This low frequency of IBCs formation in the mouse tissue makes it difficult to perform genetic and molecular studies of IBCs (Duraismamy et al., 2018). Despite these challenges, IBCs have been harvested in urine from UTI patients (Robino et al., 2013). *E.coli* strains harvested from female UTI patients were shown to form IBCs in 15/18 cases in mice from 5 different genetic backgrounds. The remaining 2/3 strains were able to generate an IBC after co-inoculation with IBC generating strain (Garofalo et al., 2007). However clinically relevant finding of IBCs from urine harvested from cystitis patients found IBCs and filamentous bacteria in 18% and 41% of total 80 samples respectively (Rosen et al., 2007). Transcriptional profiling of bacteria within IBCs revealed upregulation of genes involved in iron acquisition and oxidative stress resistance (Conover et al., 2016; Duraismamy et al., 2018; Subashchandrabose et al., 2014). Some recent studies have developed simple protocols to isolate IBCs from infected mouse bladder for downstream single-cell genomics (Duraismamy et al., 2018; Yang et al., 2019). Some studies with other uropathogens *Enterococcus faecalis* and *Klebsiella pneumoniae* have also recapitulated IBC formation in the infected tissue (Barber et al., 2013; Rosen et al., 2008).

In the context of UPEC associated UTIs, IBCs development has been characterized into early, middle and late stages. In the following paragraphs, the spatiotemporal characterization of this process is described in the context of infection of the mouse model.

Early stage of IBC formation: In the early phase of infection (less than 6 hours after infection in the mouse model), bacteria are identified as loose and sporadic inhabitants within superficial epithelial cells. UPEC undergo rapid proliferation (till 8 hours) with doubling time of around 30-45 minutes (Justice et al., 2004; Scott et al., 2015) and form a loose collection within the cytoplasm. *In vitro* studies show that UPEC maintains its classical rod shape (2-3 μm) within early phase of IBC development.

Middle stage with IBC maturation: By 6-8 hours post infection, UPEC doubling time is increased to 60 minutes and rod-shaped UPEC transitions to coccoid form (0.5-1 μm) and reside within tightly packed communities. Bacterial growth is restricted to the intracellular volume which results in

densely packed biofilm communities. These biofilm-like communities are recalcitrant to antibiotic and neutrophil mediated killing (Justice et al., 2004; Scott et al., 2015).

Late stage IBC undergoing fluxing and release: Around 12 hours later, post IBC maturation, UPEC reverts its shape back to rod-shaped form ($\sim 2 \mu\text{m}$). UPEC starts shedding from IBCs and regains its motility (with higher flagellar expression) to infect other bladder epithelial cells. This IBC shedding starts another round of UPEC invasion and IBC formation. Late-stage IBCs are also associated with long filamentous bacteria ($50\text{-}70 \mu\text{m}$) (Justice et al., 2004; Scott et al., 2015). These filamentous bacteria grow with diminished septation. However, previous studies have been unable to demonstrate the origin of filamentous bacteria either within the cytoplasm or on the surface of uroepithelial cells (Scott et al., 2015).

1.6.3 IBC response to antibiotic and neutrophil mediated stresses

Bacteria inside IBCs are protected from the neutrophil swarms formed inside infected a mouse bladder (Justice et al., 2004). *In vitro* studies of bladder epithelial cells revealed susceptibility of intracellular bacterial populations to antibiotics such as nitrofurantoin and fluoroquinolones such as ciprofloxacin and sparfloxacin (Blango and Mulvey, 2010). Antibiotic studies on IBCs in *ex vivo* infected bladders have also shown the susceptibility of IBCs to long-term treatment of antibiotics (Blango and Mulvey, 2010). Also, the combination of antibiotics and chitosan has been shown to reduce the bacterial burden inside the mouse bladder (Blango et al., 2014). These studies have suggested the role of IBCs as transient biofilms inside the infected bladder which assist in infecting deeper layers of the uroepithelium to form intracellular bacterial reservoirs.

1.6.4 Quiescent intracellular reservoirs as niche for bacterial persistence and recurrence of UTIs

In the current model of UPEC pathogenesis, exfoliation of infected superficial epithelial cells is thought to steer the host-pathogen balance towards dormant population inside uroepithelium known as quiescent intracellular reservoirs (QIR) [Figure 1.6f](#)). These dormant populations can stay trapped within Lamp1⁺ endosomes within cells from the transitional uroepithelium (Mysorekar and Hultgren, 2006). In a study by Mysorekar et.al (Mysorekar and Hultgren, 2006), treatment with protamine sulfate resulted in epithelial sloughing and complete removal of superficial epithelial cells harbouring QIRs. However, QIRs residing inside transitional uroepithelium led to resurgence of secondary infection from persistent population (Mulvey et al., 2001). The bacteria in the form of QIRs were

reported to persist for months and resist antibiotic mediated killing before emerging out of a dormant state to cause recurrent UTIs (Schilling et al., 2002). Mouse model of UTIs also found superficial epithelial cells with smaller UPEC and subsequent follow up of infection at later time points (4-12 days) detected UPEC in the form of QIRs and no reported bacteriuria in these studies (Justice et al., 2004).

1.7 Immune responses during UTIs

The immune response to microbial infection and corresponding inflammatory response is controlled within a tight balance to prevent damage to the uroepithelium integrity and yet avoid incomplete killing of the microbial challenge. The upper superficial layer of uroepithelium is covered by mucus layer consisting of proteoglycans and glycosaminoglycans (GAGs), comprising hyaluronic acid and chondroitin sulfate, also known as GAG layer (Hurst, 1994; Lacerda Mariano and Ingersoll, 2020). The GAG layer is known to provide tissue impermeability and protection to bladder uroepithelium from aggregated toxins in the urine (Hurst, 1994). The GAG layer also provides a physical barrier against pathogens (Cornish et al., 1988; Parsons, 2007). Therefore, GAG layer provides the first layer of “constitutive” defense against pathogens (Lacerda Mariano and Ingersoll, 2020) (Figure 1.10). The urinary tract also secretes antimicrobial peptides such as uromodulin (also known as Tamm-Horsfall urinary glycoprotein), which is one of the most abundant proteins in urine (Serafini-Cessi et al., 2003). Uromodulin competes with uroplakins for type1 pili binding and thus induces UPEC aggregation which prevents UPEC binding to the epithelial cells (Pak et al., 2001). Uromodulin can trigger TLR4 pathway and stimulate maturation of dendritic cells. Thus, uromodulin could influence innate and adaptive immune response in UTIs (Säemann et al., 2005).

UPEC infection also induces secretion of proinflammatory cytokines such as granulocyte colony-stimulating factor (G-CSF). Neutralization of G-CSF during UPEC infection resulted in reduced neutrophil migration into the bladder and was associated with increased secretion of macrophage stimulating cytokines and IL-1 β (Ingersoll et al., 2008). Infected uroepithelial cells secrete IL-1, IL-6 and IL-8 as proinflammatory cytokines, which have been shown to recruit immune cells to infected tissue (Agace et al., 1993; Hedges et al., 1992; Nagamatsu et al., 2015; Song et al., 2007).

1.7.1 Bladder immune system

Mouse bladder has a complex resident immune system (Figure 1.10). Recent studies have identified different populations of resident macrophages in muscle and in the lamina propria via transcriptomics

(Lacerda Mariano et al., 2020). The macrophages in the muscles were observed to be more phagocytic and anti-inflammatory, whereas macrophages in the lamina propria died quickly during the infection (Lacerda Mariano et al., 2020). Other studies with tissue resident macrophages have shown that Ly6C⁻ macrophages can stimulate migration of Ly6C⁺ macrophages and circulating neutrophils from the bloodstream. Recruited Ly6C⁺ macrophages secreted tumour necrosis factor (TNF) which triggered C-X-C Motif Chemokine Ligand 2 (CXCL2) release from Ly6C⁻ macrophages (Schiwon et al., 2014).

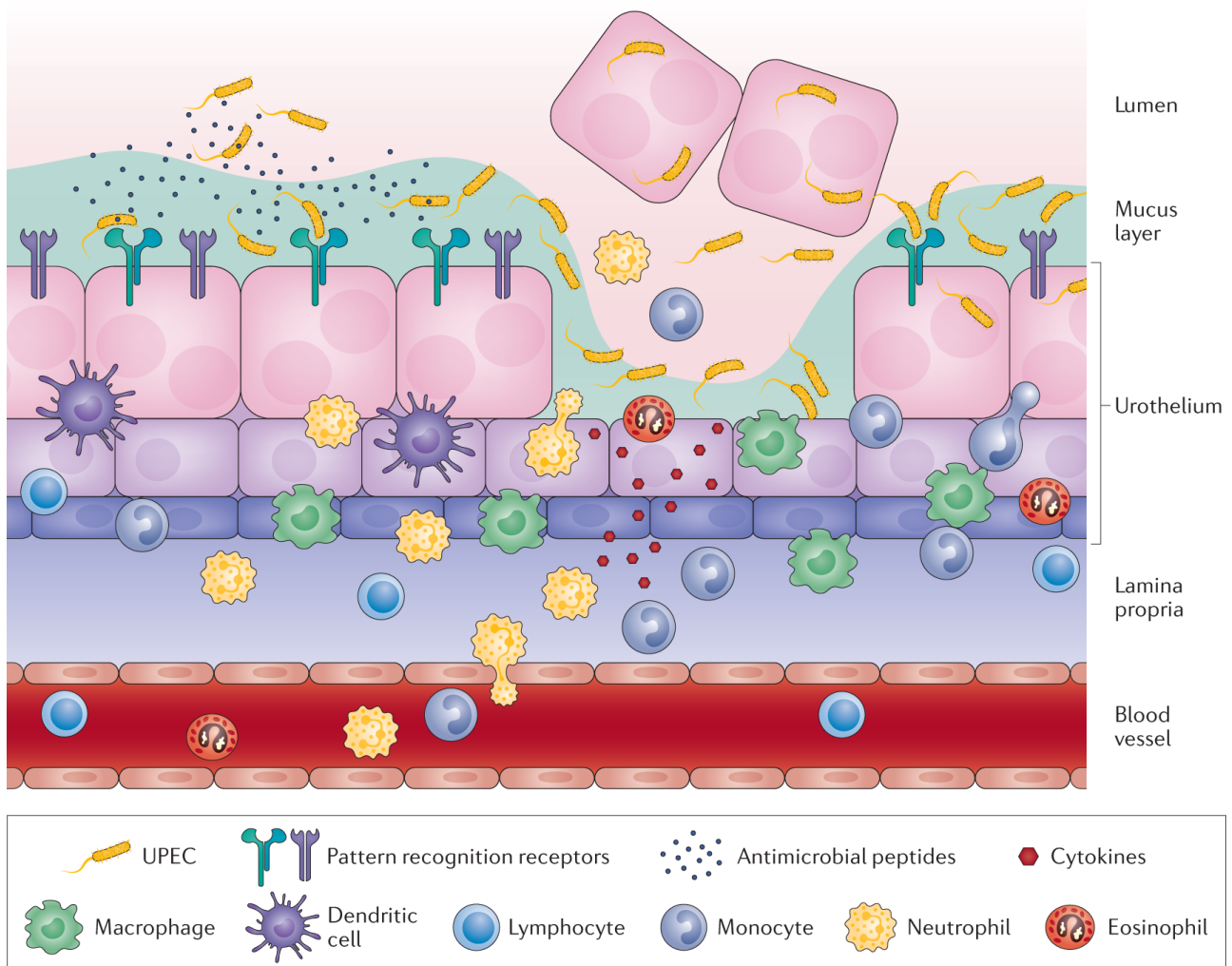


Figure 1.10: Immune responses in the bladder

UPEC infection of the uroepithelium invokes “constitutive and induced immune response” in the bladder. The constitutive immune response of the bladder includes the resident immune cell population such as macrophages, dendritic cells, lymphocytes. The superficial epithelial cells exfoliate to reduce the intracellular bacterial burden. However, the underlying layers are exposed for UPEC infection. The inflamed uroepithelium and resident immune cells release antimicrobial molecules and cytokines which not only kill bacteria but invoke “induced immune response” in the bladder. This induced immune cell response consists of inflammatory cells such as neutrophils, and lymphocytes which are recruited from the blood stream. Image taken from (Lacerda Mariano and Ingersoll, 2020).

The factors required for neutrophil migration have been elucidated. For example, it has been shown that neutrophils storm the infected uroepithelium due to chemokine stimulated matrix metalloproteinases-9 activation. Furthermore, migration to infected epithelium requires TNF signalling as TNF deficient mice failed to recruit neutrophils (Schiwon et al., 2014). Chemokines such as CCL2, CCL3, and CCL4 have been reported in the urine of patients suffering from UTIs, which likely stimulate neutrophil migration (Sundac et al., 2016).

1.7.2 Uroepithelial regeneration in response to exfoliated uroepithelial cells

Differentiated uroepithelial cells can exfoliate and shed during acute phase of cystitis. This uroepithelial shedding acts as a double-edged sword for the host. Exfoliation of the infected uroepithelial cells reduces bacterial burden, but bacteria released from exfoliated epithelial cells allows the pathogen to infect other areas of uroepithelium. Loss of the exfoliated cell also leads to bladder inflammation and injury.

In contrast to the intestinal epithelium, which has a high regenerative capacity, uroepithelium regeneration occurs slowly over months. Normal healthy uroepithelium has been proposed to take months for replacement of differentiated cell layer (Apodaca, 2004; Hicks, 1975). However, uroepithelial cell injury via UPEC infection in mouse models have shown to dramatically reduce this time to days for urothelial regeneration (Mulvey et al., 1998; Mysorekar et al., 2002, 2009; Shin et al., 2011). UPEC infected uroepithelium goes through quick sloughing of differentiated cells and increase in basal cell proliferation. Bone morphogenetic protein 4 (from TGF- β receptor family) and sonic hedgehog signalling (Shh) has been shown to be important for urothelial regeneration (Mysorekar et al., 2009; Shin et al., 2011). Knockout mice deficient for bone morphogenetic protein 4 (from TGF- β receptor family) had abnormalities in urothelial regeneration (Mysorekar et al., 2009). Injured uroepithelium has increased Shh expression in basal cells and Wnt expression in stromal cells, which can subsequently induce uroepithelium proliferation (Shin et al., 2011). Moreover, UPEC infection induces structural or morphological changes in the bladder leaving uroepithelium susceptible to reinfections (O'Brien et al., 2016; Yu et al., 2019).

1.8 Neutrophils

Neutrophils are an important part of innate arm defense against the microbial pathogens (Nauseef and Borregaard, 2014). Due to their amorphous shape, neutrophils are also known as polymorphonuclear leukocytes. Neutrophils engulf pathogens through phagocytosis and release antimicrobial enzymes to clear bacterial and fungal infections (Kolaczowska and Kubes, 2013). Neutrophil responses to

microbial infection and corresponding inflammatory response are controlled within a tight balance. This balance which ensures less damage to the epithelium integrity and incomplete killing of the invaded pathogens.

Neutrophils differentiate in the bone marrow and upon stimulation mature neutrophils are released into the circulatory system to monitor the activation status of endothelial cells (Borregaard, 2010). Lower number of neutrophils released into the bloodstream (condition known as neutropenia) can make the host more susceptible to microbial infections. On the contrary, superfluous neutrophil migration is deleterious for the host. Thus, neutrophil development and trafficking from the bone marrow into the circulatory system is a tightly regulated process.

1.8.1 Mechanics of leukocyte motion while undergoing transendothelial migration

Upon leukocyte entry into the bloodstream, the migration of leukocytes inside blood vessels and tissue interstitium is a complex process, which involves different locomotion strategies: “rolling over, adhesion, crawling and transendothelial migration via paracellular and transcellular modes” (Figure 1.11). Freely flowing leukocytes inside the blood stream adhere to the stimulated endothelium, resulting in leukocyte rolling along the endothelium. The leukocyte adherence to the endothelium involves a cascade of “selectin-controlled rolling, chemokine stimulated activation and integrin-controlled movement and eventual arrest on the endothelium” (Ley et al., 2007). The leukocyte rolling, attachment and scanning of the endothelium is controlled by a barricade of different selectins, namely E-selectin (in endothelial cells), L-selectin (in leukocytes) and P-selectin (in platelets and endothelial cells) (Kansas, 1996). Leukocyte adhesion via selectins (L-selectin and P-selectin) is dependent on shear stress as rolling leukocytes detach when flow is stopped. This behaviour of P-selectins is attributed to the catch bond mechanisms, which become stronger as tensile force is applied to them (Alon et al., 1995). Leukocytes also use their mucin to bind to the E or P-selectin expressed on the surface of endothelial cells. After undergoing trans-endothelial migration, Lymphocyte function-associated antigen 1 (LFA-1) integrins on rolling neutrophils bind to intercellular adhesion molecules (ICAMs) present on the surface of endothelial cells. This binding establishes a tight adhesion that stops neutrophil migration.

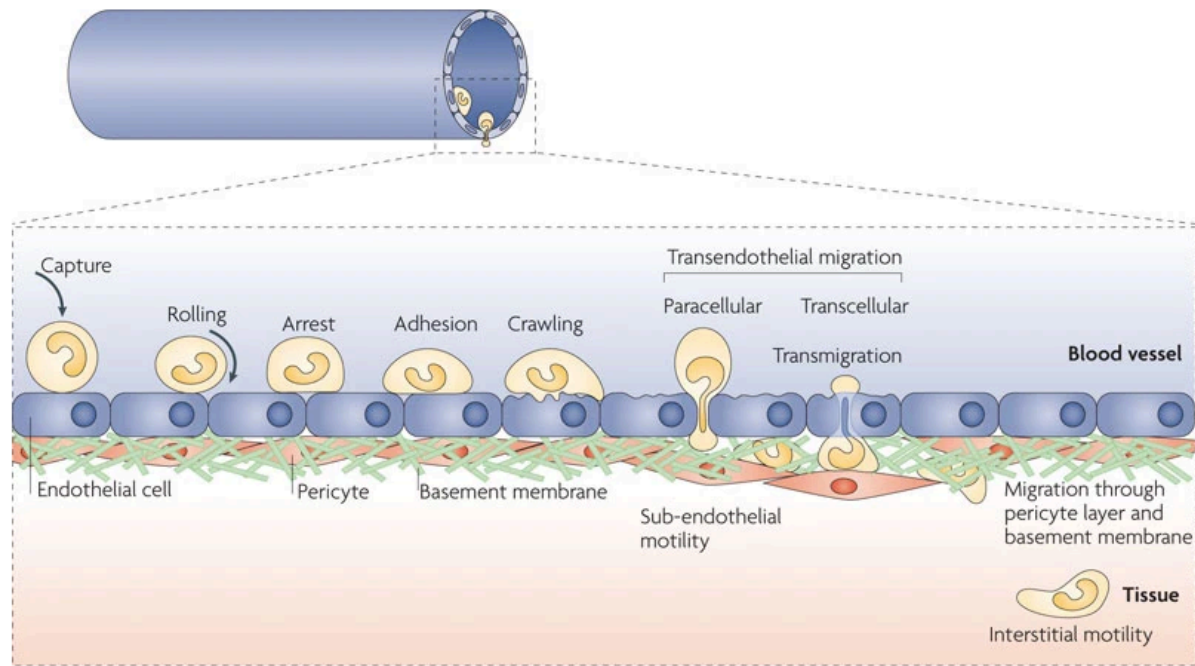


Figure 1.11: Stages in transendothelial migration of leukocytes.

The three stage of leukocyte transendothelial migration involves slow rolling, firm adhesion, intraluminal crawling and paracellular/transcellular migration through the endothelial cells. Image taken from (Nourshargh et al., 2010)

1.8.2 Neutrophil swarming

The dynamics of neutrophil migration into the wounded or infected tissue has been studied through intravital imaging (Lämmermann et al., 2013; Poplimont et al., 2020; Uderhardt et al., 2019). Neutrophils demonstrate a directed and coordinated migration towards the site of infection or tissue injury. Coordinated chemotaxis is ensued by the clustering and accumulation of neutrophils at the epithelial site of inflammation. This coordinated behaviour by neutrophils is known as “neutrophil swarming” (Kienle and Lämmermann, 2016; Lämmermann et al., 2013) (Figure 1.12). Neutrophil swarms have been reported in infections with fungi (Bruns et al., 2010; Hopke et al., 2020; Reátegui et al., 2017), parasites (Coombes et al., 2013; Peters et al., 2008) and bacteria (Kreisel et al., 2010; Liese et al., 2012; Waite et al., 2011).

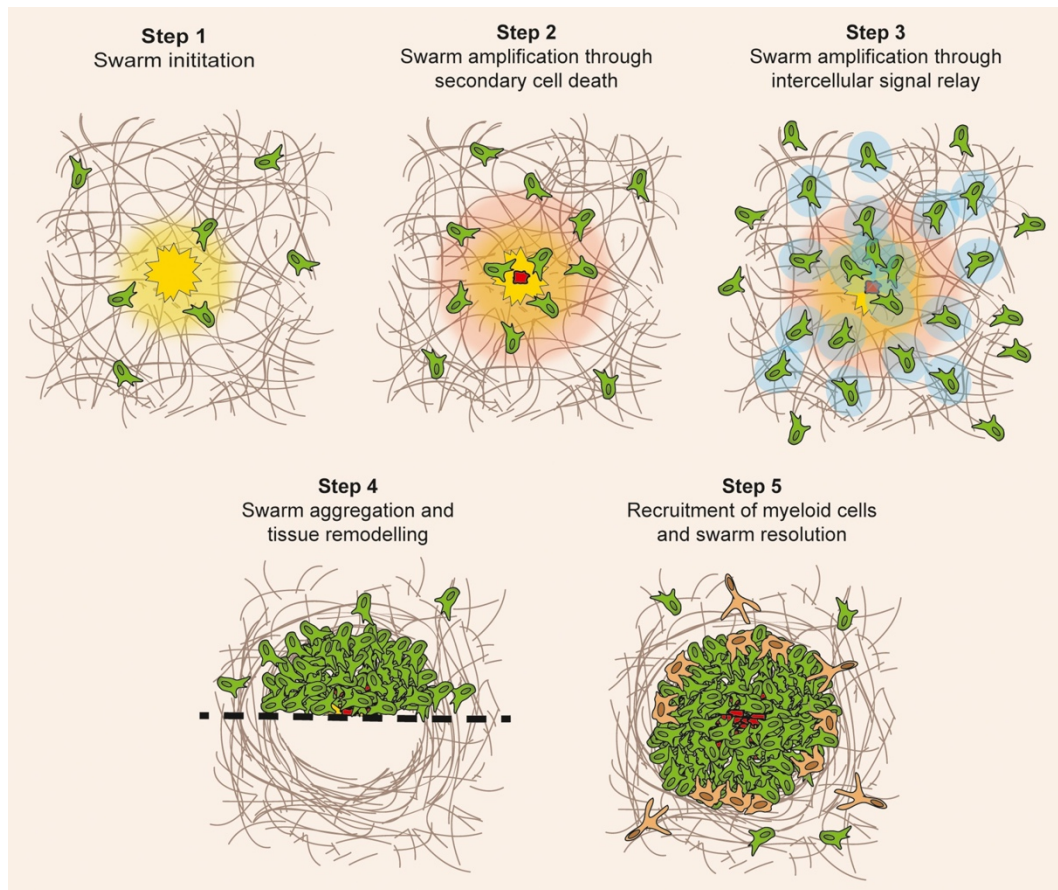


Figure 1.12: Schematic of extravascular neutrophil swarming.

The schematic shows the five-step cascade of neutrophil swarm formation. (Step 1) The tissue wound will release some chemokines (yellow) and neutrophils close to the injury site sense these chemotactic signals. (Step 2) Chemokines (red) released by death of few early recruited neutrophils amplifies the process of neutrophil recruitment. (Step 3) Leukotriene B4 (blue) released by neutrophils amplifies the signal between migrating neutrophils. (Step 4) Aggregated neutrophils remodel the extracellular matrix at the epithelial site of inflammation. (Step 5) End of neutrophil recruitment and resolution of the neutrophil swarm via delayed migration of CXCR1-positive myeloid cells (brown). Image taken from (Kienle and Lämmermann, 2016).

A screen for the chemokines released within the neutrophil swarm identified lipid attractant leukotriene B4 as the important relay signal molecule responsible for communication among neutrophils (Lämmermann et al., 2013). After the first stages of highly coordinated motion towards the site of inflammation, neutrophils slow down as primitive neutrophil clusters and initiate formation of larger and dense neutrophil aggregates (Figure 1.12). The aggregated neutrophils modify and rearrange the surrounding extracellular matrix in the tissue interstitium. The last phase of swarm resolution is not well understood whether this step is influenced either by migrated neutrophils or secreted factors from the tissue interstitium (Kienle and Lämmermann, 2016). In the studies of sterile tissue injury model, neutrophil swarm formation stops soon after formation (ca. 1 hour). This time period also synchronized with the appearance of CX3CR1 positive myeloid cells (Lämmermann et al., 2013). Tissue-resident macrophages sense the death of neutrophils and form membrane process around the neutrophil swarm. This “cloaking” mechanism by resident macrophages controls excessive

neutrophil mediated damage and maintain tissue homeostasis around the local site of tissue injury (Uderhardt et al., 2019).

Neutrophil swarms have also been categorized into two categories i.e transient and persistent swarms depending upon the size of the neutrophil swarm and the time taken for the dissolution of the neutrophil swarm (Kienle and Lämmermann, 2016). Smaller sized neutrophil swarm consisting of between 10 and 100 neutrophils that aggregate and are dispersed within 10-40 minutes after formation of the neutrophil aggregate are known as transient swarms. On the other hand, persistent neutrophil swarms consist of more than 300 neutrophils, are larger in size and have an extended recruitment phase with a slow dispersal of aggregated neutrophils. In a more recent study, Hopke et al. (Hopke et al., 2020) also labelled another category of neutrophil swarms as dynamic swarms. The size of the dynamic swarms fluctuated, and the swarms did not resolve at the end of the experiment.

1.8.3 Neutrophil extracellular traps

Neutrophils have complex responses to infections (Oliveira et al., 2016), including the formation of neutrophil extracellular traps (NETs). NETs are extracellular web like structures made up of uncondensed chromatin with attached azurophilic granules. These cytosolic azurophilic granules surround a scaffold of decondensed chromatin and potentially serves to trap and kill extracellular bacteria (Brinkmann et al., 2004; Pilsczek et al., 2010; Yipp et al., 2012) (Figure 1.13). NETs have been shown to consist of antimicrobial granules such as myeloperoxidase (Metzler et al., 2011) and neutrophil elastase (Papayannopoulos et al., 2010). The content of NETs has been shown to contain both nuclear and mitochondrial DNA (McIlroy et al., 2014; Yousefi et al., 2009). NETs have been also been reported to trap and kill viruses (Saitoh et al., 2012; Veras et al., 2020), and suggested to stop fungal dissemination (Branzk et al., 2014; Hopke et al., 2020; Urban et al., 2006). NET release process has been demonstrated to be pathogen size dependent (Branzk et al., 2014). Neutrophils have been shown to release NETs upon incubation with large sized pathogens and not in response to single bacteria or yeast (Branzk et al., 2014).

The process associated with NET release leading to neutrophil death, is a mechanism known as NETosis (Fuchs et al., 2007a) (Figure 1.14). Upon pathogen or chemical perturbation (Fuchs et al., 2007b), the stimulated neutrophils release reactive oxygen species (Zhang et al., 2003). In these cells, the nucleus becomes delobulated and nuclear membrane is ruptured into vesicles. Subsequently, the nuclear content (karyoplasm) is mixed with the cytoplasmic granules (cytoplasm) (Brinkmann and Zychlinsky, 2007). Neutrophils round up, arrest their actin dynamics, undergo depolarization and

chromatin decondensation. Eventually, the cell membrane is disintegrated to release its milieu of uncondensed chromatin. Release of NETs into the extracellular environments continues 3-8 hours after the first stimulation of neutrophils (Fuchs et al., 2007a; Hopke et al., 2020; Pilszczek et al., 2010; Yipp et al., 2012). NETs can persist for a long duration of time post infection and are known to be cleared by host secreted plasma nuclear DNaseI (Hakkim et al., 2010; Jiménez-Alcázar et al., 2017; Lim, 2018).

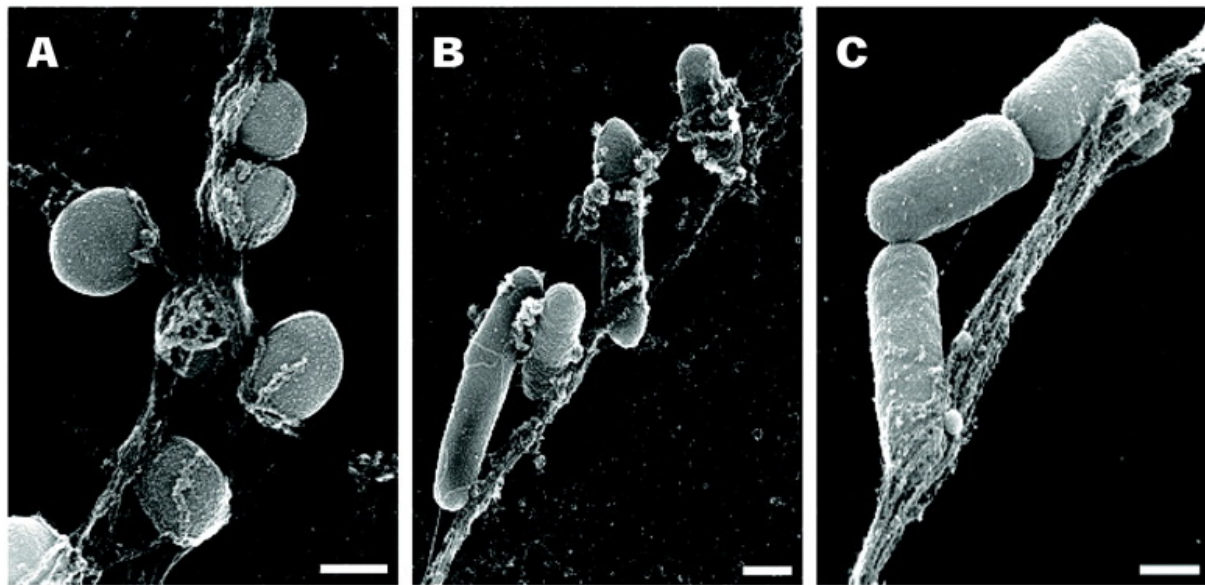


Figure 1.13: Neutrophil extracellular traps associated with bacteria.

Scanning electron micrographs of NETs around *S. aureus* (A), *S. typhimurium* (B), and *S. flexneri* (C). Scale bars equal to 500nm. Image taken from: (Brinkmann et al., 2004).

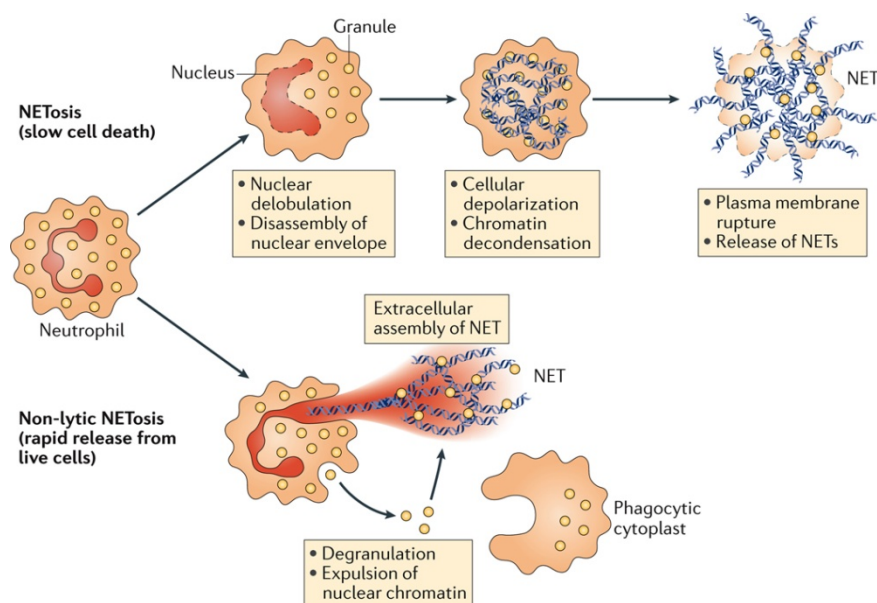


Figure 1.14: NET formation pathways: NETosis and Non-lytic NETosis.

Neutrophil extracellular traps formation can occur through two pathways. The first pathway involves cell death known as NETosis that starts with disassembly of nuclear membrane followed by chromatin decondensation. The plasma membrane finally ruptures to release NETs. The second pathway involves non-lytic form of NETosis that can occur independently of cell death. The secreted nuclear chromatin components assemble extracellularly and leave behind active and alive anucleated cytoplasts that continue to ingest microorganisms by phagocytosis. Image taken from: (Papayannopoulos, 2017).

Compared to the lytic pathway involving disintegration of the neutrophil plasma membrane (Figure 1.4), there are other mechanisms, which involve non-lytic release of NETs on exposure to pathogens mediated through secretion of chromatin and granule contents (Pilszczek et al., 2010; Yipp et al., 2012). Neutrophils can still crawl while undergoing NETosis. These neutrophils develop decondensed nuclei and ultimately get rid of their DNA. Post NETs release, anucleated cytoplasts can crawl and phagocytosize the pathogen *Staphylococcus aureus* (Yipp et al., 2012).

1.9 *In vitro* model systems to mimic tissue physiology and study diseases

Typically, the interaction of the host and pathogen in diseases is modelled *in vivo* using animal models (complex) or *in vitro* using tissue culture models (simple). Scientists have used animal models to study human diseases. Animal models have improved significantly in the last decades in developing more accurate models for disease research. Moreover, transgenic animals allow scientists to decipher the role played by different molecular pathways in a disease. However, animal models have their own limitations as described in [Table 1](#). The use of animals for research has led to some ethical concerns that have been increasing in the society. In this direction, Russel and Burch outlined 3R principles for use of animals in research (Russell and Birch, 1960). These 3R stand for replacement, reduction and refinement for animal use in research. Animal models are expensive and moreover animal protocols can be time-consuming.

Imaging experiments with animal models can be technically challenging, it is often difficult if not impossible to study these interactions at the single-cell level, particularly with a good spatiotemporal resolution. Apart from being extremely difficult to carry out, animal experiments are unable to capture the contribution of bacterial phenotypic heterogeneity to disease outcomes (Bumann, 2015).

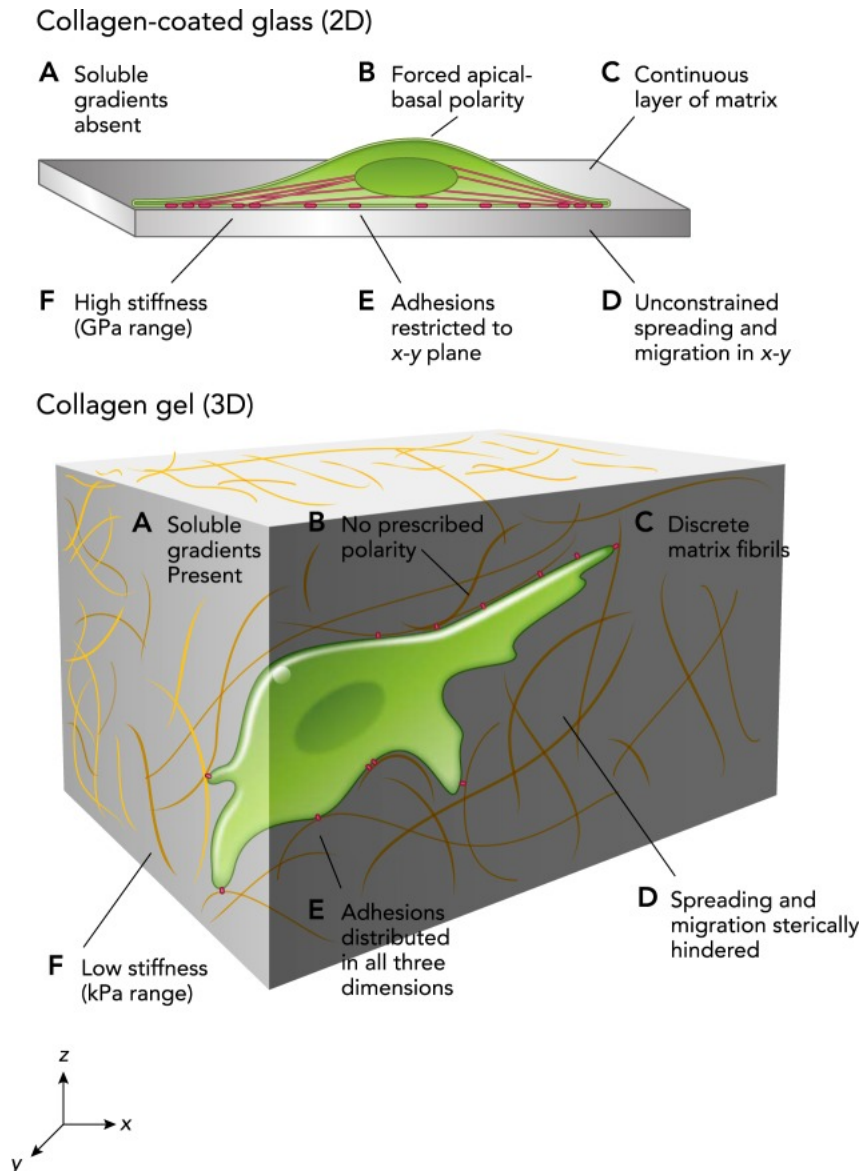


Figure 1.15 : Cells in 2D and 3D cell culture systems experience different adhesive, topographical, mechanical and soluble cues from with their surroundings.

Cells encounter different microenvironmental conditions such as (A) molecular gradients, (B) apical-basal polarity, (C). extracellular matrix, (D) substrate stiffness, (E) adhesion to substrate, and (F) spatial hindrance to spreading and migration. Image taken from: (Duval et al., 2017) and adapted from: (Baker and Chen, 2012)

Cell culture model systems have emerged as an alternative approach to complement or replace animal models. Using cell culture systems, cells harvested from animal or human tissues can be grown in Cell culture systems are supplemented with growth factors and are grown in controlled microenvironmental conditions, which include conditions such as temperature, humidity, pH, and gaseous exchange (Bédard et al., 2020). Different cell culture techniques with growing cells either in 2D on planar substrates or 3D in extracellular matrix (ECM) have been developed.

Generally, two-dimensional (2D) cell cultures are generated by growing cells as monolayers on plastic surfaces (Figure 1.15). Extensive studies using these 2D monolayers have provided many important insights into the cellular and molecular mechanisms of host-pathogen interactions. However, various studies have also demonstrated that 2D cultures sometimes fail to recapitulate the important phenotypic and functional responses that are observed in whole-animal infection models. 2D platforms fail to mimic the 3D organization of cells around ECM, which varies the cells' microenvironment from that experienced *in vivo*. These and other limitations as shown in Figure 1.15, do not allow recapitulation of cell-to-cell and cell-to-ECM interactions as experienced *in vivo*. In contrast, 3D cell culture overcomes these limitations and provide better environment for cell proliferation, differentiation and migration (Figure 1.15).

In vitro tissue-culture models are often too simplistic; typically, they do not capture the diversity of host-pathogen interactions and are unable to recreate the heterogeneous physical niches that pathogens typically encounter. Lesions within the same host are often different and the bacteria within different regions of the same individual lesion can be in various metabolic states (Dhar et al., 2016; Manina et al., 2015). Tissue culture models often fail to recapitulate all these diverse interactions. Taken together, there is a need for “intermediate” model systems that provide the convenience and experimental power of 2D culture systems while still capturing some of the important complexity of animal models, as discussed in Table 1. Two bioengineering approaches have emerged to generate functional and physiological stem-cell derived tissues: organ-chip systems developed by bioengineers and organoid systems developed by stem cell biologists (Zhang et al., 2018).

| Characteristics | Animal Models | 2D Cell Culture | 3D Cell Culture |
|---------------------------|---------------|-----------------|-----------------|
| Cost | +++ | + | ++ |
| Ethical concerns | +++ | + | + |
| Gene expression | +++ | + | ++ |
| Morphology | +++ | + | +++ |
| Mimicking <i>in vivo</i> | N/A | + | ++ |
| Transferability to humans | ++ | + | ++ |
| Complexity of environment | +++ | + | ++ |
| Reproducibility | ++ | +++ | ++ |
| High throughput | + | +++ | ++ |
| Modularity | + | + | +++ |
| Vascularization | +++ | N/A | ++ |
| Immune cell interactions | +++ | + | ++ |
| | | | |

| Techniques/interventions | | | |
|--------------------------|----|-----|-----|
| Optical imaging | + | +++ | +++ |
| feature tracking | + | +++ | ++ |
| antibiotic treatment | + | +++ | +++ |
| electron microscopy | ++ | +++ | +++ |

Table 1: Comparison of animal models with 2D and 3D cell culture systems

Table adapted from: (Roy et al., 2020)

1.10 Various architectures used in organ-chip systems

Human tissues and organs are made up of heterogeneous cell populations. The complexity and physiology of organs are achieved through intracellular and intercellular communications across physical barriers within the tissue microenvironmental niche. These intracellular and intercellular interactions are possible through organ-chip systems, which are microfluidic cell culture systems (Zhang et al., 2018). Tissue and organ level physiology could be achieved by reverse engineering the tissue architecture, recreation of the physiochemical microenvironment niche and with addition of the vasculature (Bhatia and Ingber, 2014).

Tissue interface based on synthetic materials

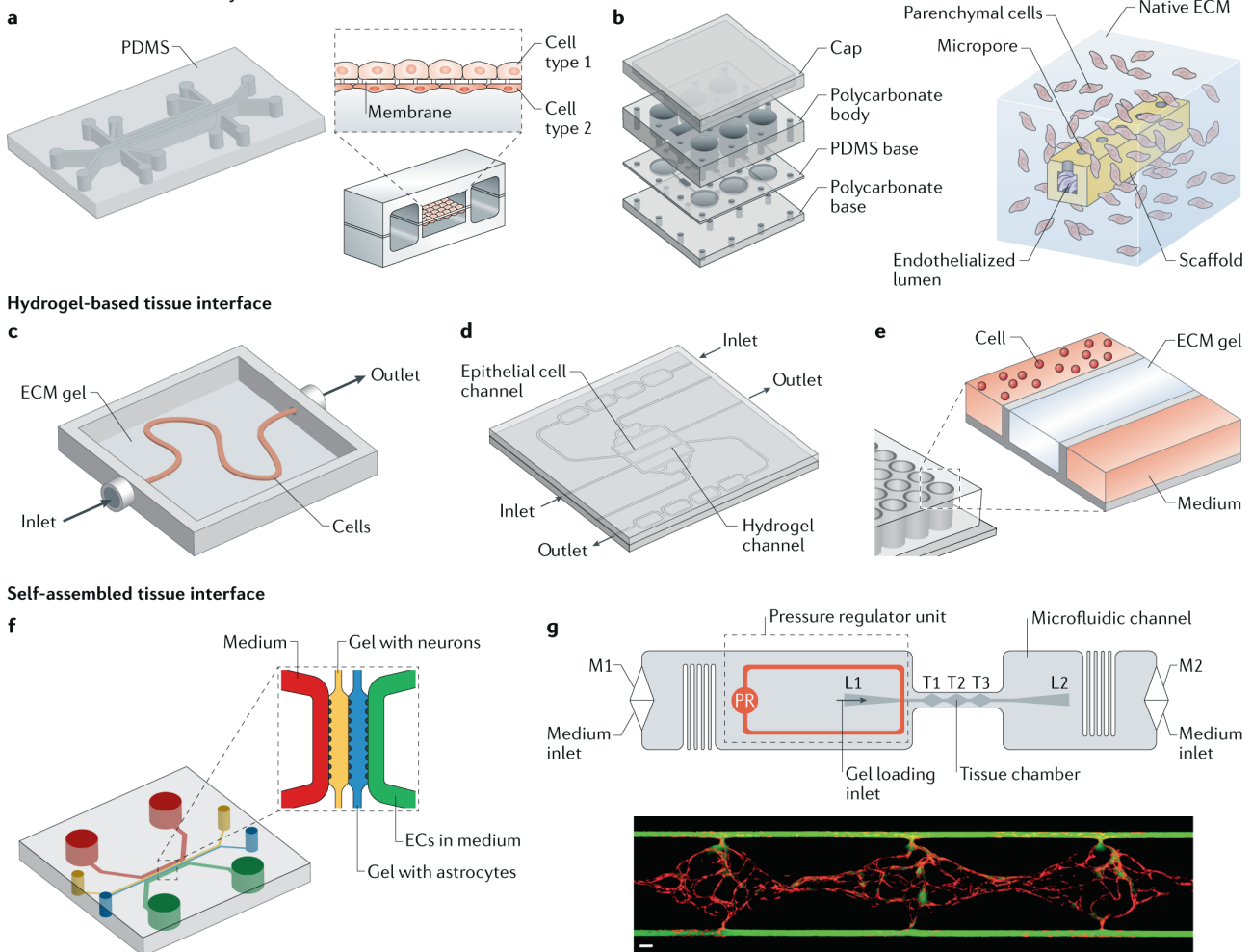


Figure 1.16: Reconstituting tissue level physiology and tissue barrier function on-chip.

Organ-chip devices can recapitulate tissue barrier by culturing different cell types either on porous and flexible PDMS membranes (a) or with flow compatible bioreactors made from microfabricated scaffolds (b), tissue recapitulation within bioprinted hydrogel (c), molded hydrogels (d), phase-guided hydrogels (e). Image taken from: (Zhang et al., 2018). The images in the subpanels (a-g) are taken or modified by Zhang et.al (Zhang et al., 2018) from following studies: a (Huh et al., 2010a), b (Zhang et al., 2016), c (Homan et al., 2016), d (Weber et al., 2016), e (Trietsch et al., 2017).

The organ-chip system offers one or many of the following functionalities:

- (a) Geometrically defined co-culture of different cell types
- (b) Medium perfusion with physiologically relevant fluid volume and shear stress
- (c) Controllable microenvironment with application of tissue specific mechanical or electrical stimuli, addition or removal of drugs and growth factors, gaseous exchange
- (d) Sensor integration to monitor tissue physiological readouts with built-in electrodes, optical imaging and biomarker detection.

Using the functionalities described by Zhang et.al (Zhang et al., 2018) in [Figure 1.16](#), organ-chip systems have been developed using several approaches as described in the subsequent sections:

1.10.1 Organ-on-chip based upon microfluidic membrane

The first biomimetic organ-chip system was established to recapitulate the functional alveolar-capillary interface within the human lung (Huh et al., 2010a) ([Figure 1.16a](#)). The compartmentalized lung-on-a-chip microfluidic device was fabricated from the transparent elastomer polydimethylsiloxane (PDMS), which allowed separate microfluidic control over fluid flow, seeding of cells, and nutrient delivery to the epithelial and endothelial cell layers. Since the first demonstration of the organ-chip system (Huh et al., 2010a), PDMS or plastic membranes have been used to recapitulate organ-level functionality in other organ-chip systems (Benam et al., 2016a; Jalili-Firoozinezhad et al., 2019; Jang et al., 2013, 2019; Kim and Ingber, 2013; Kim et al., 2016).

1.10.2 Organ-on-chip based upon microfluidic scaffolds

Synthetic scaffolds with inbuilt microfluidic channels can be fabricated to allow generation of vascularized tissue (Zhang et al., 2016) ([Figure 1.16b](#)). These scaffolds allow mechanical stability for vascularization and growth of the surrounding epithelial tissue. Microfluidic scaffold system could be disassembled to recover the mature-functional tissue for surgical implantation inside animals. Another organ-on-chip system with inbuilt plastic nanoporous membrane allowed crosstalk between human gut epithelial cells and microorganisms (Shah et al., 2016). This device provided dynamic measurements of transepithelial electrical resistance and oxygen concentration (Shah et al., 2016).

1.10.3 Organ-on-chip based upon microfluidic hydrogels

The natural extracellular matrix around the tissue creates a soft microenvironment for the tissue growth (Lutolf and Hubbell, 2005). Conventionally the cell culture is done on either plastic or PDMS substrates that do not reconstitute the biodegradable microenvironmental niche around the growing tissue (Lutolf et al., 2009). Organ-chip systems with microfluidic hydrogel allow tissue growth and modelling around more physiologically relevant extracellular niche such as collagen, Matrigel (Zhang et al., 2016). Microfluidic hydrogels have been used to generate complex vascular networks (Zheng et al., 2012). Bioprinting of sacrificial hydrogel inside a hydrogel mixture of gelatin-fibrinogen allowed the *in vitro* recreation of kidney proximal tubule (Homan et al., 2016) (Figure 1.16c). Medium perfusion of proximal tubular epithelial cells induced formation of a 3D tubular structure inside collagen extracellular matrix (Weber et al., 2016) (Figure 1.16d). Assembly of endothelial cells in channels surrounded by collagen matrix led to the generation of vasculature (Zheng et al., 2015). Using complex geometries, it was found that assembly of von Willebrand factor bundles on endothelial cells depended upon the microfluidic geometry and applied shear stress. Another system recapitulated homeostatic mini-guts inside a mixture of collagen gel and matrigel (Nikolaev et al., 2020).

1.10.4 Organs-on-plate

Organ-chip devices, membrane-based and hydrogel-based systems are limited in throughput due to challenges in liquid handling either manually by pipettes or with syringe pumps. Moreover, the technical expertise required to handle these devices thwarts their clinical translation. Microfluidic hydrogel devices have been perfused with gravity-driven flow by periodic tilting of the platform (Duinen et al., 2017; Trietsch et al., 2017) (Figure 1.16e). This system developed by MIMETAS (Netherlands) has been used to generate 3D culture of intestinal epithelium and endothelium. Another system in a 96 well-platform allowed high-throughput culture of airway epithelium (Mejías et al., 2020). Another system developed by SUN bioscience allows scalable generation and analysis of thousands of gastrointestinal organoids (Brandenberg et al., 2020).

1.11 Different organ-chip systems developed for various organs

Organ-chip systems have been made using different platforms mentioned in 1.10.1-1.10.4. Here I mention some of the well-established organ-chip systems.

1.11.1 Lung-chip systems

The first demonstration of organ-chip system was achieved for alveolar-capillary interface for human lung-on-chip system (Huh et al., 2010b). In lung-on-chip, alveolar epithelial cells upregulated ROS production when stimulated with both mechanical strain and silica nanoparticles. Mechanical strain

also upregulated the nanoparticle translocation across the alveolar-capillary interface, compared to static lung-on-a-chip and similar culture conditions in a transwell insert. The system also demonstrated the ability to recreate immune responses to infections. Infection of the alveolar epithelial cells with *E.coli* resulted in neutrophil migration from vascular to alveolar side (Huh et al., 2010a).

In a follow-up study on lung-chip system, the disease pathology for human pulmonary edema was simulated with IL-2 treatment. The disease progression was revealed to be independent from flowing immune cells on the vascular channel. However, cyclic breathing motion resulted in the increased endothelium-to-epithelium leakage (Huh et al., 2012). Furthermore, endothelium stimulation with conjunction of IL-2, prothrombin and fibrinogen accentuated formation of fibrin clots on the alveolar epithelial side (Huh et al., 2012).

Similarly, a model of the upper airway was reconstituted with differentiated bronchiolar epithelium and supporting lung microvascular endothelium (Benam et al., 2016a). The differentiated mucociliary epithelium recapitulated synchronous cilia beating with functional mucociliary transport. Cytokine stimulation with IL-13 treatment resulted in reduced ciliary movement, abnormal epithelium with hyperplasia and fibrosis, increased secretion of other cytokines such as G-CSF and GM-CSF (Benam et al., 2016a). In a subsequent study on a small airway-chip (Benam et al., 2016b), the effect of whole smoke was tested on airway cells derived from healthy normal and chronic obstructive pulmonary disease (COPD) patients. The smoking lung airway-chip system also revealed irregular ciliary movements, higher oxidative stress and COPD-specific molecular biomarkers” (Benam et al., 2016b).

Lung-chip system can model cancer growth and tumor dormancy for human non-small-cell-lung cancer (NSCLC) (Hassell et al., 2017). NSCLC cancer cells co-cultured with lung airway epithelial cells were found to have reduced growth under conditions of cyclic stretching. Treatment of NSCLC cancer cells with tyrosine kinase inhibitor resulted in decreased IL-8 secretion. The human cancer cells were non-growing and entered into dormant phase, which hinted at the presence of cancer persister cell population. (Hassell et al., 2017).

Compared to one-dimensional cyclic stretching in lung-chip systems (Huh et al., 2010b, 2012), three-dimensional cyclic stretching has been incorporated in another lung-system developed by Stucki et.al (Stucki et al., 2014). This lung-chip system recreated diaphragm mediated breathing motion using electro-pneumatically actuated micro-diaphragm. This model has reiterated the role for mechanical strain in influencing the metabolic activity and cytokine secretion by primary pulmonary epithelial cells. Similarly, another lung-chip model has incorporated lung fibroblasts grown on plastic

membranes (Sellgren et al., 2014). In this tripartite microfluidic model, the fibroblast layer was sandwiched between airway epithelial cells and microvascular endothelial cells.

1.11.2 Gut-chip systems

In the gut-chip system (Kim and Ingber, 2013), human Caco-2 cells subjected to peristaltic and shear flow conditions stimulated formation of 3D structures mimicking intestinal villi. In this system, mechanical stretching induced polarization and differentiation of Caco-2 cells into structures mimicking intestinal columnar epithelium. The gut-chip was then co-cultured with several commensal microbes (Kim et al., 2016). Discontinuation of peristaltic motion stimulated “epithelial deformation and bacterial overgrowth” despite the presence of shear flow conditions (Kim et al., 2016). The gut-chip system was further developed to establish long-term co-culture of intestinal epithelium with aerobic and anaerobic microbiome species (Jalili-Firoozinezhad et al., 2019). In contrast to aerobic gut-chip, application of hypoxia gradient in the anaerobic gut-chip enhanced tissue barrier formation and sustenance of higher microbial diversity (Jalili-Firoozinezhad et al., 2019). Another gut-chip system allowed crosstalk between human gut epithelial cells and microorganisms using a nanoporous membrane (Shah et al., 2016). This device provided dynamic measurements of transepithelial electrical resistance and oxygen concentration.

Intestinal-organoids-on-chip was achieved by co-culture of dissociated human intestinal organoids and human intestinal microvascular endothelial cells on the two sides of the PDMS membrane (Kasendra et al., 2018). The intestinal organoid-chip recapitulated several intestinal cell types such as goblet cells, absorptive enterocytes, enteroendocrine cells, and paneth cells as reported in gut-chip system previously (Kim and Ingber, 2013). Regular isolation of cell fluid exudes allowed quantification of nutrient digestion and mucus secretion by intestinal epithelial cells. Co-culture with endothelial cells reduced the confluency time for organoid fragments from 6 days to 2 days, demonstrating the role played by endothelial-epithelial communication in the intestinal-organoids-on-chip.

Micropatterned collagen hydrogel surrounded by extracellular niche have been shown to recapitulate self-renewing intestinal epithelium (Wang et al., 2017). Application of chemical gradients enhanced stem cell proliferation and “allowed cellular migration and rearrangement along the crypt-villus axis” (Wang et al., 2017). By combining hydrogel patterning and a microfluidics approach, intestinal stem cells generated tubular shaped intestinal epithelia with an accessible lumen (Nikolaev et al., 2020). The intestinal tissue consisting of crypts and villi was built by using self-organization properties of epithelial cells. The continuous perfusion of the mini-gut tubes with medium increased tissue lifespan

by continuous removal of dead cells. The regenerative potential of the epithelial cells in the mini-gut tubes was shown via damage induced with (a) ultraviolet laser beam (b) dextran sodium sulfate and (c) lower doses of gamma-radiation. The mini-gut tubes were also colonized with *C. parvum* to model host-pathogen interactions and recapitulate full life cycle of the pathogen within the mini-gut lumen. The infected mini guts revealed higher interferon- α response and metabolic changes compared to uninfected mini-guts (Nikolaev et al., 2020).

1.11.3 Liver-chip systems

Liver-chip system created with an interface of primary hepatocytes and liver sinusoidal endothelial cells was used for testing hepatotoxicities in different species: rat, dog and human (Jang et al., 2019). Liver-chip was developed to study drug induced liver injury, which is an acute form of liver injury and leading cause for liver failure. Cells remained in metabolically active state with sustained albumin production in two-week cultures inside the liver-chip system. Liver-chip also recapitulated “hepatocyte necrosis, inflammation and fibrosis” on treatment with some drugs known to have caused similar effects in animal studies (Jang et al., 2019). Another liver-chip system was developed by culturing rat primary hepatocytes and endothelial cells (Kang et al., 2015). This liver-chip was further used to model hepatitis B virus proliferation inside the hepatocytes.

1.11.4 Kidney-chip systems

In the kidney-chip system, primary human kidney epithelial cells were cultured on a polyester membrane coated with collagen IV, thus reconstituting an apical “luminal” and basal “interstitial” interface. In this system, physiologically relevant fluid shear stress (0.2 dyne/cm²) led to increased epithelial polarization and cilia formation. The tubular epithelial cells increased albumin transport and glucose reabsorption (Jang et al., 2013).

Another kidney-chip system was developed by Zhou et. al (Zhou et al., 2013) to model epithelial-to-mesenchymal transition in proximal tubular epithelial cells, a known pathology for “proteinuric nephropathy and renal interstitial fibrosis”. Urine flow on the proximal tubular epithelial cells was stimulated with heat-inactivated serum and complement C3a. Proximal tubular epithelial cells developed mesenchymal phenotype on exposure to C3a and not with heat inactivated serum (Zhou et al., 2013).

In another effort, glomerulus-on-chip system developed for studying human glomerular hypertension was shown to mimic hypertensive nephropathy (Zhou et al., 2016). Glomerulus-on-a-chip system

consisted of two apposed layers of podocytes and glomerular endothelial cells cultured under physiologically relevant shear stress conditions. The mechanical forces experienced by glomerulus cells resulted in increased glomerular leakage and cytoskeleton abnormalities. The increased perfusion was also found to damage the glomerular endothelium (Zhou et al., 2016).

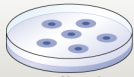
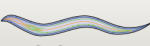





1.12 Organoid systems

Organoid systems are based upon the premise of isolating stem cells from primary tissue to regenerate “multicellular self-assembled systems that can recapitulate basic tissue-level functional physiology” (Rossi et al., 2018). Organoids are complex 3D multicellular structures that are generated either from stem cells or organ-specific progenitor cells (Clevers, 2020). In the last decade, organoids have emerged as miniaturized physiological and functionalized versions of organs (Clevers, 2016).

A major advance in the organoid research came from lineage tracing studies done by Barker et.al (Barker et al., 2007), which demonstrated $Lgr5^{+ve}$ intestinal stem cells are required for the long-term renewal of intestinal epithelium. This pioneering study along with the evidence of continuous intestinal turn-over encouraged Toshi Sato to culture intestinal stem cells in an extracellular matrix. In the first demonstration, the extracellular 3D microenvironment in high Wnt medium provided support for even a single $Lgr5^{+ve}$ intestinal stem cell to form intestinal crypt-villus unit without surrounding mesenchymal (non-epithelial) niche (Sato et al., 2009). The extracellular niche was supplemented with growth factors that stimulated pathways for Wnt signalling, Notch signaling and BMP inhibition. This research about identification of $Lgr5^{+ve}$ stem cells and optimization of niche factors that control epithelial stemness has allowed development of other organoid culture systems such as lung (Sachs et al., 2019), stomach (Barker et al., 2010), liver (Takebe et al., 2013), gut (Sato et al., 2009), pancreas (Huch et al., 2013), breast (Lee et al., 2007; Sachs et al., 2018) and bladder (Lee et al., 2018b; Mullenders et al., 2019).

1.12.1 Organoid model systems for disease modelling

Biologists have conventionally used different model systems for understanding organ development and modelling disease pathologies (Figure 1.17). Organoid systems offer convenience of 2D cell culture systems and tissue complexity achieved in different model organisms (Kim et al., 2020) (Figure 1.17). Specifically, patient derived organoids from cancer and neurodegenerative diseases have opened up avenues for personalized medicine. The inherent potential of organoids for regenerative medicine has been supplemented with recent advances with CRISPR gene editing approaches (Driehuis and Clevers, 2017). As an example, CRISPR was used to repair the disease-causing mutation in human intestinal organoids derived from cystic fibrosis patients (Schwank et al., 2013).

| |  2D cell culture |  <i>C. elegans</i> |  <i>D. melanogaster</i> |  <i>D. rerio</i> |  <i>M. musculus</i> |  PDX |  Human organoids |
|---|---|---|--|---|--|---|---|
| Ease of establishing system | ✓/✗ | ✓ | ✓ | ✓ | ✓ | ✓ | ✓ |
| Ease of maintenance | ✓ | ✓ | ✓ | ✓ | ✓ | ✓ | ✓ |
| Recapitulation of developmental biology | ✗ | ✓ | ✓ | ✓ | ✓ | ✗ | ✓ |
| Duration of experiments | ✓ | ✓ | ✓ | ✓ | ✓ | ✓ | ✓ |
| Genetic manipulation | ✓ | ✓ | ✓ | ✓ | ✓ | ✗ | ✓ |
| Genome-wide screening | ✓ | ✓ | ✓ | ✓ | ✗ | ✗ | ✓ |
| Physiological complexity | ✗ | ✓ | ✓ | ✓ | ✓ | ✓ | ✓ |
| Relative cost | ✓ | ✓ | ✓ | ✓ | ✓ | ✓ | ✓ |
| Recapitulation of human physiology | ✓ | ✓ | ✓ | ✓ | ✓ | ✓ | ✓ |

✓ Best ✓ Good ✓ Partly suitable ✗ Not suitable

Figure 1.17: Comparison of human organoid systems with other model systems for disease modelling and studying developmental biology.

The most widely used model systems are either organisms such as *Caenorhabditis elegans*, *Drosophila melanogaster*, *Danio rerio*, or patient-derived xenografts (PDX). Organoids provide convenience and experimental power of 2D culture systems while still capturing some of the important tissue complexities of other model systems. Image taken from: (Kim et al., 2020).

Organoid model systems are now increasingly used to model infectious diseases. The first demonstration of the organoid as a model system for studying infectious diseases was done with *Helicobacter pylori* infection of gastric organoids (Bartfeld, 2016; Bartfeld and Clevers, 2015). In the subsequent studies, Clevers and collaborators have also studied *Cryptosporidium* infection of lung and small intestinal organoids (Heo et al., 2018). The organoids were able to support the complex life cycle of the parasite. The parasite *C. parvum* was able to proliferate and propagate more easily in differentiated small intestinal organoids compared to highly proliferating lung organoids (Heo et al., 2018). Recently developed perfusable mini-gut tubes have also been used to recapitulate infection cycle of the parasite *C. parvum* (Nikolaev et al., 2020). Another infection model system with *Salmonella* Typhimurium infection of the intestinal organoids revealed bacterial invasion into the epithelium and found bacteria residing inside vacuoles (Forbester et al., 2015).

The first example of viral infection of human organoids was done with human norovirus infection of human enteroids (Ettayebi et al., 2016). Further studies with respiratory syncytial virus (RSV) infection of human airway organoids derived from cystic fibrosis patients recapitulated key features of the disease and neutrophil migration to viral infected organoids (Sachs et al., 2019). Epithelial cells inside these RSV infected organoids were remodelled and found with “structural abnormalities such as disrupted cytoskeleton, extruded and multinucleated cells”. RSV infected organoids rotated and moved

within the surrounding hydrogel. This organoid motility at the macroscale was found to be mediated through coordinated cell motilities (Sachs et al., 2019). The human airway organoid model system was also used for influenza infection studies with avian influenza H7N9 virus and pandemic 2009 H1N1 virus strain (Zhou et al., 2018), enterovirus 71 infection (Sanden et al., 2018). Hui et al. (Hui et al., 2018) studied host responses in human influenza, a viral infection of human airway organoids. In another study, human brain organoids were used to study zika virus induced microcephaly in a developing human fetal brain (Qian et al., 2017).

The recent viral epidemic caused by severe acute respiratory syndrome-coronavirus 2 (SARS-CoV-2) in December 2019 (Zhu et al., 2020) resulted in organoids as a potential experimental model system for studying SARS-CoV-2 infection (Clevers, 2020). Using kidney epithelial organoids established from human induced pluripotent stem cells (iPSCs), a recent study has shown that intervention of human Angiotensin converting enzyme 2 (ACE2) led to SARS-CoV-2 recovery of kidney organoids (Monteil et al., 2020). Three independent studies (Lamers et al., 2020; Zang et al., 2020; Zhou et al., 2020) from different research groups have shown gut enterocyte infection with SARS-CoV-2 in human small intestinal organoids. These recent studies demonstrate intestinal epithelium as a permissive niche for SARS-CoV-2 proliferation (Clevers, 2020; Lamers et al., 2020). Moreover, expression of two mucosa-specific serine proteases increased SARS-CoV-2 entry into intestinal cells (Zang et al., 2020). Recently human distal lung organoids were generated from alveolar epithelial type II cells which expressed basal cell markers such as CK5 (Salahudeen et al., 2020). The SARS-CoV-2 infection of these distal lung organoids resulted in infection of alveolar epithelial type II cells.

1.12.2 Current technologies to address limitations of the organoid systems

Organoids rely on passive diffusion of the nutrients and oxygen to allow for sustainable growth. With the increase in the size of the organoids, the trapped dead cells generate toxic metabolites for surrounding live cells. The waste products are removed passively and dying cells are trapped within the lumen of the organoids. Also, the surrounding extracellular matrix is remodelled and degraded with growing organoids and larger organoids start collapsing to start 2D growth. The organoids also need to be passaged continuously and sheared mechanically to scale down its size.

The current approaches rely on cell suspensions inside hydrogels to generate organoids do not allow for strict control over size and its local microenvironment. The surrounding extracellular matrix also restricts addition of modular elements to increase complexity and dynamic microenvironment for organogenesis. Robotic automation and other technological innovations could reduce the size variability and time spent in organoid culture. In this direction of scaling up the organoid approaches, soft

hydrogel microwell arrays have been fabricated and functionalized with combination of extracellular matrix proteins or synthetic designer matrices (Gjorevski et al., 2016) in an automated system (Gobaa et al., 2011). Such synthetic biomaterials are now further developed and used as *in vitro* extracellular microenvironmental niche to mimic *in vivo* stem cell niches (Kobel and Lutolf, 2011). Tissues can be generated in microfluidic PEG hydrogel networks generated with laser ablation (Brandenberg and Lutolf, 2016). In the direction of standardizing the organoid size, microstructured thin hydrogel films inside 24 well plate system has been shown to reduce the variability in organoid size due to tight control on surrounding space. Brandenberg et. al (Brandenberg et al., 2020) used microcavity array approach for medium throughput real-time analysis of mouse and human gastrointestinal organoids. A recent study by Serex et al (Serex et al., 2020) has also shown generation of bladder organoids with a custom-made 3D bioprinter for printing epithelial cells at predefined concentration inside hydrogels.

However, despite these tissue patterning approaches, the metabolic and physical requirements for larger organoids to sustain its growth and differentiation state of underlying epithelial cells is difficult to maintain for weeks. Inside the body, developing organs requires development of vasculature to sustain growth through active supply of nutrients, removal of toxic products and maintenance of tissue homeostasis with circulating immune cells. Similarly, the organoids need perfusion-based systems to remove dead cells inside the lumen. Organoid systems are also limited by vasculature and possibility to co-culture with resident immune cells or add immune cells under flow. These limitations make it difficult to achieve immune cell chemotaxis in response to inflammatory insults with cytokines or pathogens. Organoid systems could therefore benefit from the modularity achieved with the organ-chip systems.

1.12.3 Synergistic studies by combining organ-chip and organoid systems

The organoid and organ-chip systems are being combined to generate organoid-on-chip systems (Park et al., 2019; Takebe et al., 2017) (Figure 1.18). Some studies have demonstrated enhanced vascularization and maturation of organoids with embedded endothelial cells under flow (Homan et al., 2019). Whereas others have generated perfusable homeostatic mini-gut tubes capable of tissue regeneration under different environmental insults (Nikolaev et al., 2020). Luminal flow inside the human gastric organoids was achieved by cannulating the organoids with micropipettes and connecting it to a peristaltic pump (Lee et al., 2018a). The hanging drop method to culture 3D spheroids has also been integrated with fluidics to control nutrient supply and allow multi-tissue metabolic communication (Frey et al., 2014).

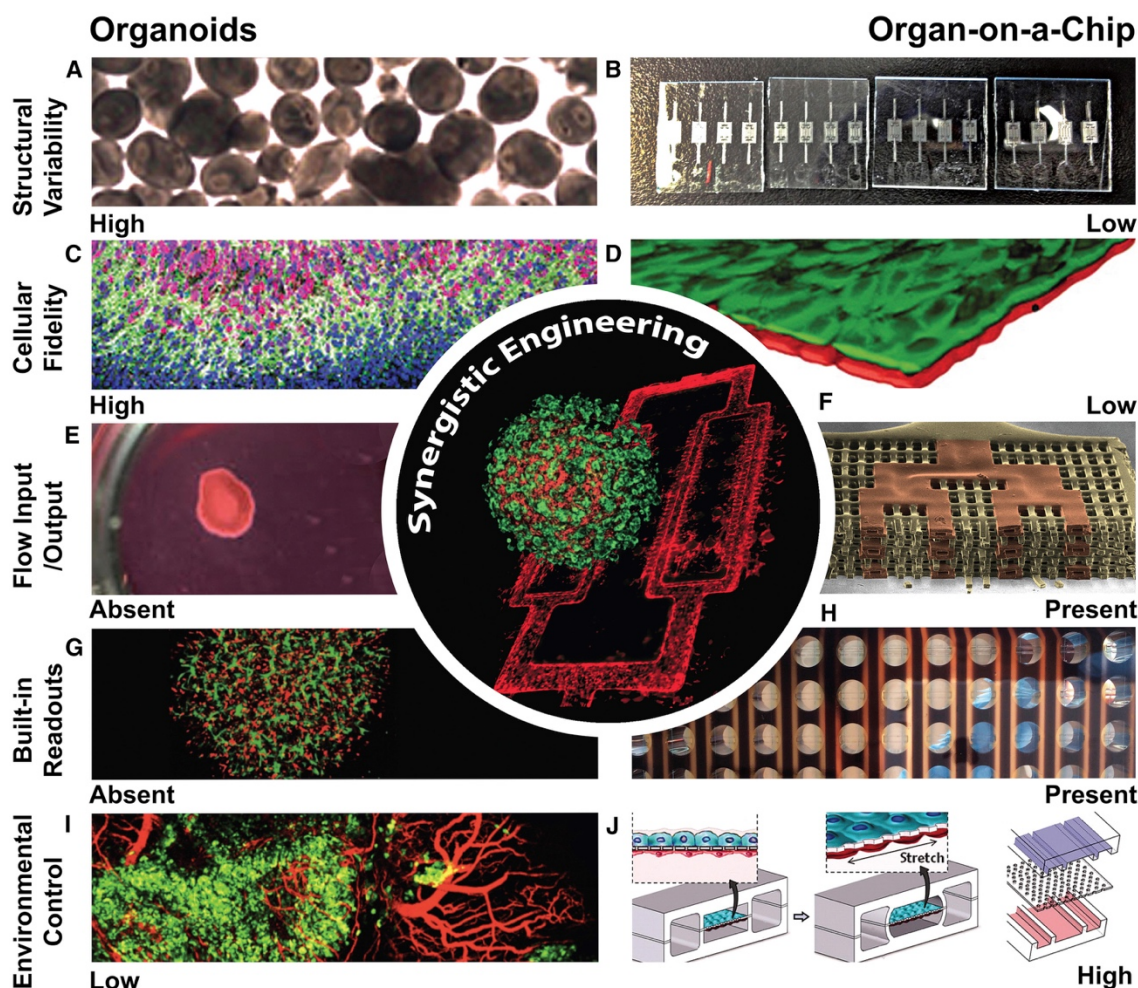


Figure 1.18: Combining organoid and organ-on-chip technologies to build better tissue models.

Organoid technology has higher cellular fidelity and better extracellular niche for culturing tissue. In contrast, organ-chips have lower structural variability, possibility to add medium flow and tissue relevant mechanical stresses. Organ-chips also provide easier microenvironmental control and possibility to add vasculature. Both organoid and organ-chips could be merged to complement their missing advantages or features. Image taken from: (Takebe et al., 2017). The images in the subpanels (a-g) are taken or modified by Takebe et.al (Takebe et al., 2017) from following studies: (A) liver organoids (unreported), (B) AngioChip scaffolds (Zhang et al., 2016), (C) brain organoids (Lancaster et al., 2017), (D) lung-on-chip (Huh et al., 2010a), (E) liver organoid (Takebe et al., 2013), (F) AngioChip structure (Zhang et al., 2016), (G) liver organoid (Takebe et al., 2013), (H) microelectrodes on a 96-well plate (unreported), (I) liver organoid, (J) lung-on-chip (Huh et al., 2010a).

PDMS, the structural material of majority of organ-on-chip systems is known to absorb small drug molecules due to its hydrophobic nature. This thwarts the process of careful pharmacokinetic-pharmacodynamic modelling of drug availability inside the organ-on-chip (Meer et al., 2017). Anti-fouling materials such as self-assembled monolayers, polyethylene oxide (PEO) and polyethylene glycol (PEG) that introduce steric repulsion or formation of hydration layer have been used in PDMS devices (Zhang and Chiao, 2015). Such sort of limitations arising in PDMS based culture systems can be avoided by culturing tissue inside hydrogels.

Organ-chip systems based upon co-culture of specific and fewer cell types do not faithfully recapitulate tissue physiology of a complex organ. The multicellular architecture with different cell types is better modelled in organoid systems.

1.13 *In vitro* model systems of UTIs

The potential challenges of performing long-term dynamic studies of IBCs in mouse bladder explants encouraged researchers to build modular and environmentally controlled *in vitro* systems over the past two decades to model early stages of UTI (Andersen et al., 2012; Horsley et al., 2018; Iosifidis and Duggin, 2020; Smith et al., 2006).

1.13.1 Flow chamber model for uroepithelial cell culture

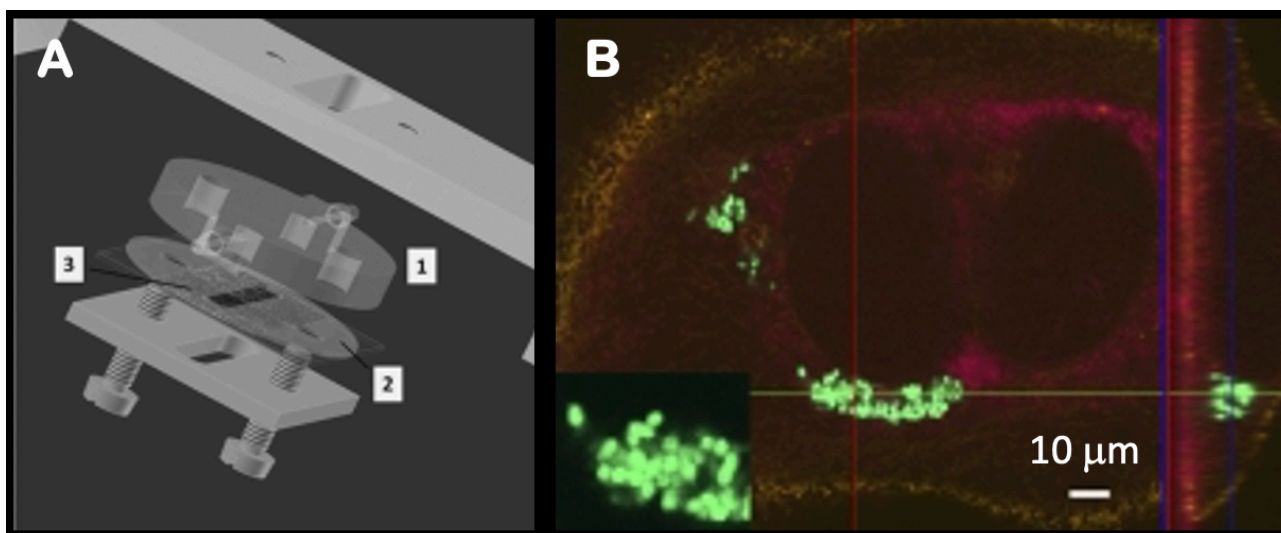


Figure 1.19: Flow-chamber based monoculture model for studying dynamics of intracellular bacterial communities.

(A) The schematic of flow chamber model system for culturing uroepithelial cells. The perfusion inside the flow chamber system was achieved through upper polycarbonate disk (marked as 1) micromachined with inlet/outlet channel with connecting pipes. The flow conditions inside the flow chamber were defined through the spacing between the silicon gasket (marked as 2) and central slit (marked as 3). (B) Orthogonal slice of a binucleate PD07i uroepithelial cell invaded with UTI89-pEGFP. Coccoid bacteria could be visualized in the inset on the lower left side of the image. Image taken from (Andersen et al., 2012).

Andersen et.al (Andersen et al., 2012) developed a human bladder cell infection model in a flow chamber-based system (Figure 1.19A). In this system, a monolayer of PD07i bladder epithelial cells were cultured on a glass plate and the infection dynamics was monitored through the polycarbonate disc. The continuous perfusion of the epithelial nutritional media or urine allowed co-culture of UPEC infected bladder epithelial cell layers for a longer period of time. Invaded bacteria inside the epithelial cells were observed within vesicles and had coccoid morphology (Figure 1.19B). Urine exposure on infected bladder epithelial cells recapitulated conditions faced by UPEC on the superficial

uroepithelial layer. The filamentous bacteria harvested from the flow chamber were shown to convert back to rod-shaped morphology. The degree of UPEC filamentation was shown to be linked to urine concentration. Exposure to urine with high urine specific gravity (USG = 1.02 to 1.03) induced filamentous bacterial growth. However, exposure of diluted urine (USG \leq 1.106) resulted in non-filamentous bacteria.

1.13.2 Microfluidic model for studying the dynamics of IBCs

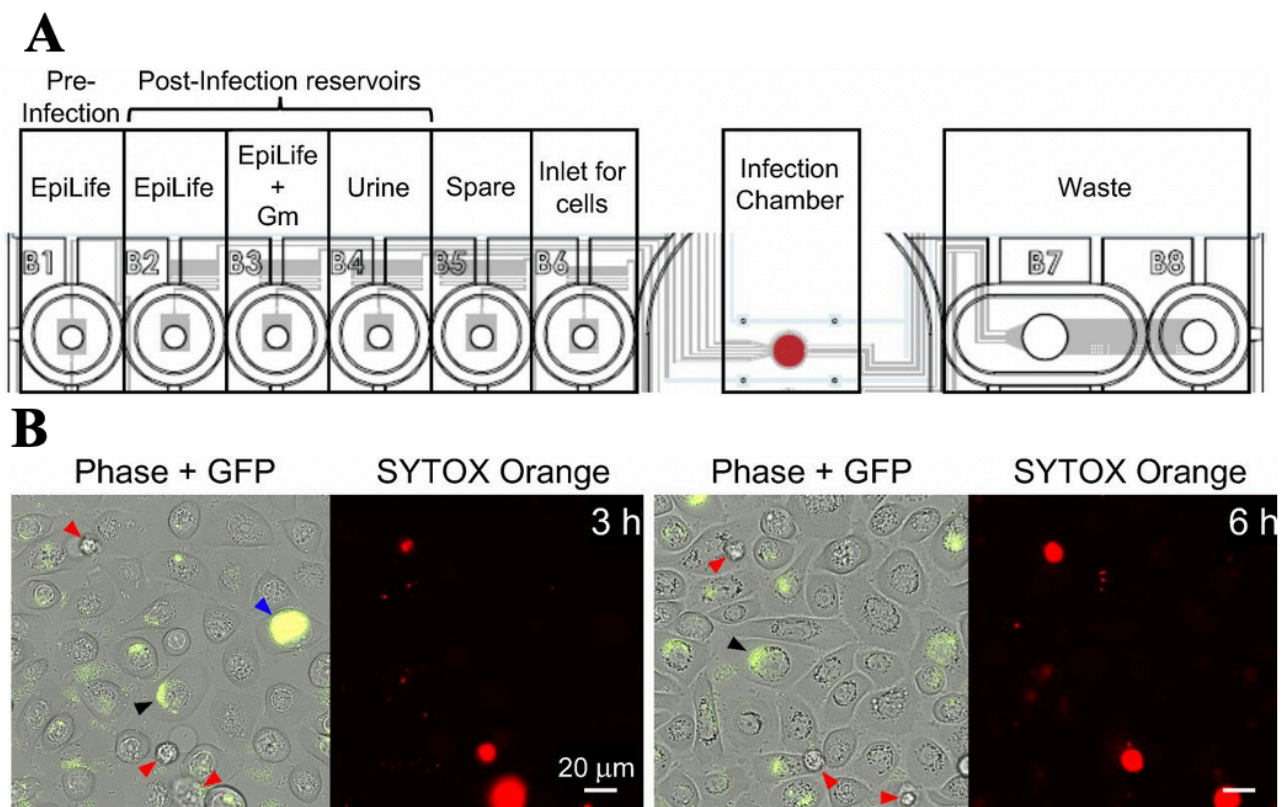


Figure 1.20: Microfluidic monoculture model for studying dynamics of intracellular bacterial communities.

(A) Diagram of the CellASIC Onix microfluidics system showing the different medium reservoirs (B1-B6) that were used to exchange medium in the Infection Chamber and waste was collected in B7, B8 reservoirs. (B) PD07i bladder cells were infected with UTI89/pGI5. Long time-lapse imaging (up to 29 hour) under flow of epithelial cell medium (supplemented with Gentamicin) captured formation of IBCs. SYTOX Orange staining indicated permeability of epithelial cells. Image taken from (Iosifidis and Duggin, 2020).

Recently a microfluidic cell culture model has been developed for studying the dynamics of IBCs in a monolayer of uroepithelial cells using the CellASIC Onix microfluidics system (Iosifidis and Duggin, 2020) (Figure 1.20A). The CellASIC Onix microfluidics system allowed easier switching of epithelial cell medium and urine via medium stored in the separate medium reservoirs. The medium from different medium reservoirs was perfused to the central infection chamber during distinct stages of the experiment. The microfluidics-based infection model system allowed real time imaging of IBC

formation and IBC shedding. The medium exchange from nutritional medium to human urine led to immobilization of bladder epithelial cells. The IBC dispersal events captured with this system showed that some IBCs released filamentous bacteria whereas other IBCs released rod-shaped bacteria. UPEC filamentation was not observed in neutralized and acidified human urine. Instead, human urine with high USG and mildly acidic pH (around 5.3) induced UPEC filamentation.

1.13.3 Organoid model for UPEC infection studies with differentiated urothelial cells

In vitro model systems using 2D monolayers of epithelial cells (1.13.1,1.13.2) have recapitulated important aspects of the host-pathogen interactions revealed by mouse models of UTIs (Hannan et al., 2012). However, various studies have also demonstrated that 2D monoculture systems sometimes fail to recapitulate the important phenotypic and functional responses that are observed in whole-animal infection models (Abbott, 2003; Barrila et al., 2010; Nickerson et al., 2006). In the context of UTIs, it could be linked to the role of transitional urothelial layers as potential harbours for quiescent intracellular populations (Mysorekar and Hultgren, 2006). The monolayer model systems (Andersen et al., 2012; Iosifidis and Duggin, 2020) did not recapitulate stratified uroepithelium which could be important for UPEC pathogenesis. Thus, there was a need for “intermediate” model systems that provide the convenience and experimental power of 2D culture systems while still capturing some of the important aspects of stratified uroepithelium.

The first organoid model for UPEC infection studies was developed by Smith et.al (Smith et al., 2006) (Figure 1.21). The stratified urothelial layers were generated using HTB9 cells adhered and grown on collagen coated beads inside a rotating wall bioreactor (Barrila et al., 2010; Hammond and Hammond, 2001). Cell suspension of HTB9 cells formed stratified organoids over a two-week culture inside the bioreactor (Figure 1.21A,B). The structural comparison via paraffin embedding and Masson’s trichrome staining revealed stratified layers in the organoids that were comparable to that found in human uroepithelium Figure 1.21C). UPEC infection of the organoids led to invasion into the deeper layers of the organoid as early as 2 hours post infection (Figure 1.21D).

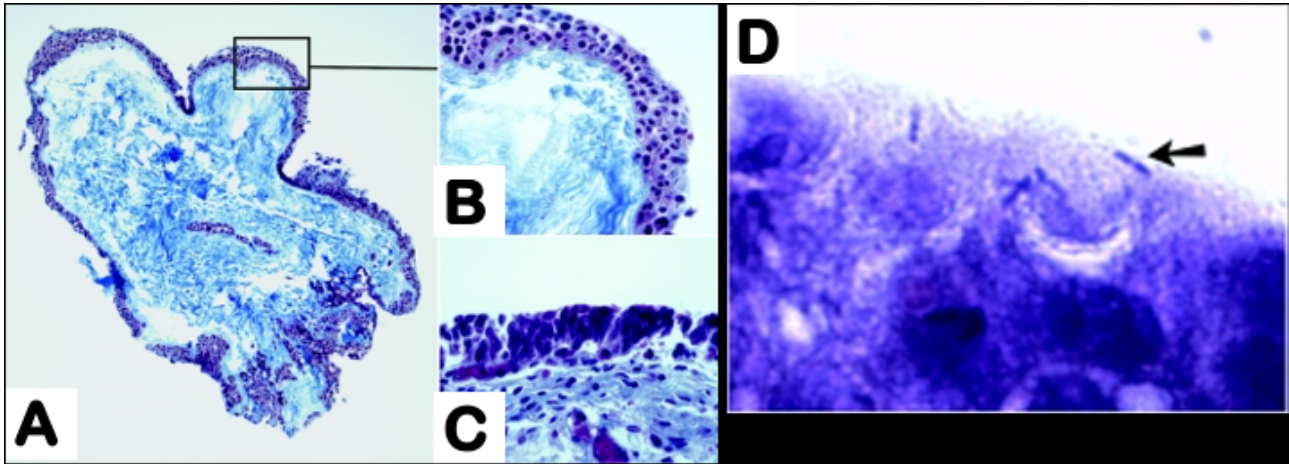


Figure 1.21: Organoid model for UPEC infection studies with terminally differentiated human urothelial cells.

(A) Organoids were formed by HTB9 cells grown on collagen beads (light blue) in a rotating wall vessel bioreactor. (B,C) Morphological comparison of cell layers in human organoids (B) with human uroepithelium (C). (D) Infection of HTB9 organoids with UPEC CP9. Internalized UPEC is marked with a black arrow. All the samples in the images were paraffin embedded and stained with Masson's trichrome. Image taken from: (Smith et al., 2006).

1.13.4 Urine-dependent human urothelial organoid model for infection

A bladder organoid from primary bladder epithelial cells was demonstrated by Horsley et. al (Horsley et al., 2018) (Figure 1.22). The HBLAK primary bladder epithelial cells were cultured on 0.4 μm pore sized transwell inserts. Urine-liquid interface maintained on the apical and basal side of the insert resulted in generation of islands of stratified uroepithelium. The cells in the upper layer of the stratified uroepithelium differentiated into umbrella-like cells with flattened morphology. Human urine was found to be essential for full development and stratification of uroepithelium. *E.faecalis* infection of the organoids showed intracellular bacteria (Figure 1.22C). Intracellular bacteria led to the formation of intracellular microcolonies and infected epithelial cells sloughed off from the epithelial layer.

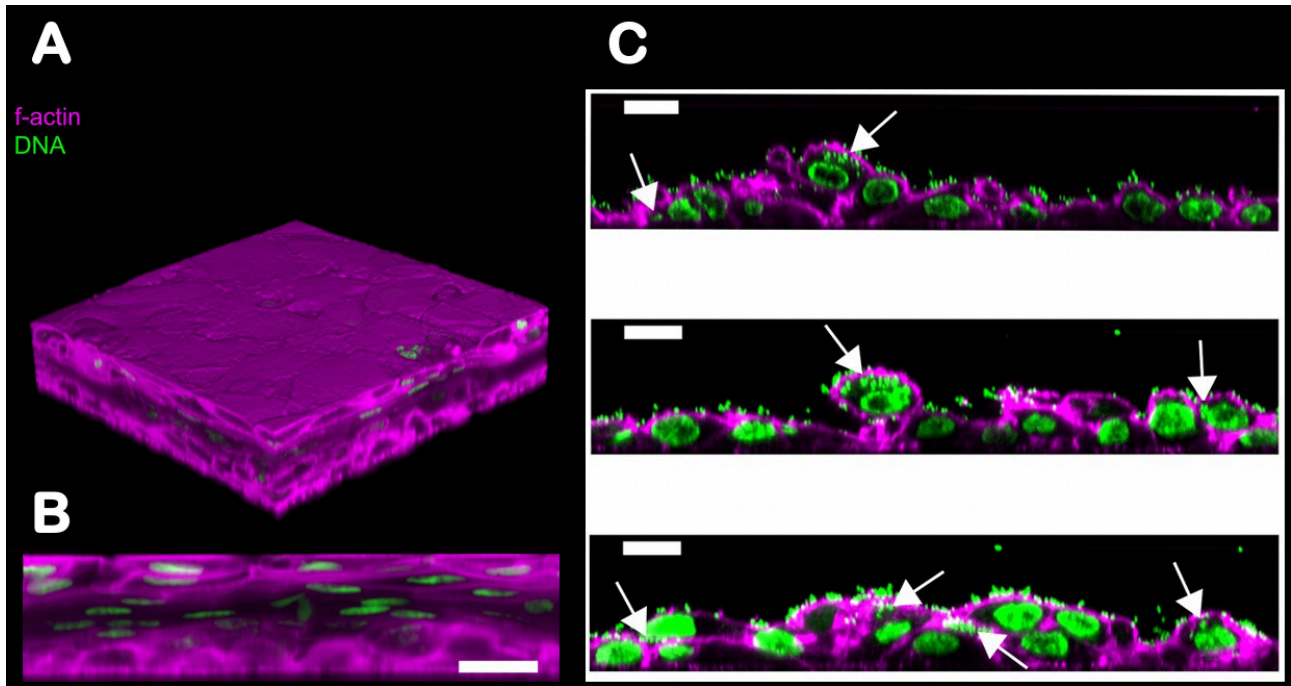


Figure 1.22: Generation of urothelial organoids on transwell inserts.

HBLAK bladder epithelial cells grown under urine exposure on transwell inserts differentiate into urothelial organoids. (B) Orthogonal slice of urothelial organoid shows multiple (5-7) layers with flattened cells in the upper layer. Cells in the bottom layer are more tightly packed and have spheroid shape. (C) Orthogonal slices of HBLAK organoid infected with *E. faecalis*. Instances of intracellular *E. faecalis* within basal and intermediate cells of the HBLAK organoid are shown with white arrows. Image taken from: (Horsley et al., 2018).

1.14 Need for advanced bladder microtissue models

In vitro studies discussed in 1.13.1-1.13.4 have advanced the field of recapitulating early stages of UTI. However, there is still a need for an advanced bladder microtissue model, which can complement the advantages of these developed *in vitro* systems. The novel microtissue model should allow the following functionalities:

- Recapitulation of bladder epithelium co-culture with bladder vasculature
- Mimicking of bladder filling and voiding through stretching and relaxation of the epithelial cells
- Addition of immune cells such as neutrophils to study immune cell-bacteria interactions
- Ability to add and remove antibiotics to study bacterial persistence
- Study persistence of IBCs and QIRs in response to antimicrobial stresses such as antibiotics or neutrophils
- UPEC infection cycle in stratified uroepithelium, recapitulation of IBCs in umbrella cells and QIRs in intermediate cell layers.

1.15 Aims of doctoral thesis

The proposed doctoral thesis aims to develop two distinct and complementary microtissue models: bladder organoids and bladder-chip for studying the dynamics of host-pathogen interactions in the urinary bladder. The bladder microtissue models should recapitulate the stratified bladder architecture within a small volume suitable for live-cell imaging of host-pathogen dynamics with high spatiotemporal resolution. The bladder organoid model with more tissue compatible physiological niche will recapitulate the stratified bladder epithelium with lumen and bladder wall. The bladder-chip model will allow co-culture of epithelial and endothelial cells on with recapitulation of urine and nutritional media interface. The bladder-chip model should be able to recapitulate the mechanics of bladder filling and bladder voiding cycles.

The microtissue model systems will be compatible for multi-position, confocal single-cell time-lapse imaging with the possibility to add or remove antimicrobial stresses. By introducing antibiotics or neutrophils, the survival strategies adapted by the pathogen under stress will also be studied. The microtissue model systems will be developed to study motile and flagellated bacterium Uropathogenic *Escherichia coli* (UPEC) that can grow both extracellularly and intracellularly within bladder epithelial cells as biofilm like communities known as IBCs. Thus, the models should reconstitute both extracellular and intracellular growth of this pathogen. In particular, the intracellular lifestyle of this pathogen either as intracellular bacterial communities (IBCs) and quiescent intracellular reservoirs (QIRs) has been known to cause persistent infection in the bladder epithelium, despite being exposed to host immune cells and antibiotics.

Thus, in thesis doctoral thesis, I plan to achieve following aims:

- (1) Develop a bladder organoid model with differentiated uroepithelium to study the UPEC pathogenesis in the stratified uroepithelium. The model should allow study of bacterial persistence in response to antibiotics and neutrophil mediated stresses.
- (2) Develop a novel bladder-chip model system to recapitulate co-culture of differentiated uroepithelial cells and bladder endothelial cells with distinct urine and nutritional medium perfusion to the respective sides. Moreover, the system should be able to mimic bladder filling and voiding by application of linear strain. This system will specifically look into the dynamics of IBC formation and persistence in response to neutrophil and antibiotic treatment.
- (3) Optimization of conditions for stratification and differentiation of uroepithelial cells.

1.16 References

- Agace, W.W., Hedges, S.R., Ceska, M., and Svanborg, C. (1993). Interleukin-8 and the neutrophil response to mucosal gram-negative infection. *J Clin Invest* 92, 780–785.
- Alon, R., Hammer, D.A., and Springer, T.A. (1995). Lifetime of the P-selectin-carbohydrate bond and its response to tensile force in hydrodynamic flow. *Nature* 374, 539–542.
- Andersen, T.E., Khandige, S., Madelung, M., Brewer, J., Kolmos, H.J., and Møller-Jensen, J. (2012). *Escherichia coli* uropathogenesis in vitro: invasion, cellular escape, and secondary infection analyzed in a human bladder cell infection model. *Infect Immun* 80, 1858–1867.
- Anderson, G.G., Palermo, J.J., Schilling, J.D., Roth, R., Heuser, J., and Hultgren, S.J. (2003). Intracellular Bacterial Biofilm-Like Pods in Urinary Tract Infections. *Science* 301, 105–107.
- Andrews, J.M. (2001). Determination of minimum inhibitory concentrations. *J Antimicrob Chemoth* 48, 5–16.
- Apodaca, G. (2004). The Uroepithelium: Not Just a Passive Barrier. *Traffic* 5, 117–128.
- Avraham, R., and Hung, D.T. (2016). A perspective on single cell behavior during infection. *Gut Microbes* 7, 518–525.
- Baker, B.M., and Chen, C.S. (2012). Deconstructing the third dimension – how 3D culture microenvironments alter cellular cues. *J Cell Sci* 125, 3015–3024.
- Balaban, N.Q., Merrin, J., Chait, R., Kowalik, L., and Leibler, S. (2004). Bacterial Persistence as a Phenotypic Switch. *Science* 305, 1622–1625.
- Balaban, N.Q., Helaine, S., Lewis, K., Ackermann, M., Aldridge, B., Andersson, D.I., Brynildsen, M.P., Bumann, D., Camilli, A., Collins, J.J., et al. (2019). Definitions and guidelines for research on antibiotic persistence. *Nat Rev Microbiol* 17, 441–448.
- Barber, A.E., Norton, J.P., Spivak, A.M., and Mulvey, M.A. (2013). Urinary Tract Infections: Current and Emerging Management Strategies. *Clin Infect Dis* 57, 719–724.
- Barker, N., Es, J.H. van, Kuipers, J., Kujala, P., Born, M. van den, Cozijnsen, M., Haegebarth, A., Korving, J., Begthel, H., Peters, P.J., et al. (2007). Identification of stem cells in small intestine and colon by marker gene *Lgr5*. *Nature* 449, 1003–1007.
- Barker, N., Huch, M., Kujala, P., Wetering, M. van de, Snippert, H.J., Es, J.H. van, Sato, T., Stange, D.E., Begthel, H., Born, M. van den, et al. (2010). *Lgr5*+ve Stem Cells Drive Self-Renewal in the Stomach and Build Long-Lived Gastric Units In Vitro. *Cell Stem Cell* 6, 25–36.
- Barrila, J., Radtke, A.L., Crabbé, A., Sarker, S.F., Herbst-Kralovetz, M.M., Ott, C.M., and Nickerson, C.A. (2010). Organotypic 3D cell culture models: using the rotating wall vessel to study host–pathogen interactions. *Nat Rev Microbiol* 8, 791–801.

- Bartfeld, S. (2016). Modeling infectious diseases and host-microbe interactions in gastrointestinal organoids. *Dev Biol* 420, 262–270.
- Bartfeld, S., and Clevers, H. (2015). Organoids as Model for Infectious Diseases: Culture of Human and Murine Stomach Organoids and Microinjection of *Helicobacter Pylori*. *J Vis Exp Jove*.
- Bédard, P., Gauvin, S., Ferland, K., Caneparo, C., Pellerin, È., Chabaud, S., and Bolduc, S. (2020). Innovative Human Three-Dimensional Tissue-Engineered Models as an Alternative to Animal Testing. *Bioeng* 7, 115.
- Benam, K.H., Villenave, R., Lucchesi, C., Varone, A., Hubeau, C., Lee, H.-H., Alves, S.E., Salmon, M., Ferrante, T.C., Weaver, J.C., et al. (2016a). Small airway-on-a-chip enables analysis of human lung inflammation and drug responses in vitro. *Nat Methods* 13, 151–157.
- Benam, K.H., Novak, R., Nawroth, J., Hirano-Kobayashi, M., Ferrante, T.C., Choe, Y., Prantil-Baun, R., Weaver, J.C., Bahinski, A., Parker, K.K., et al. (2016b). Matched-Comparative Modeling of Normal and Diseased Human Airway Responses Using a Microengineered Breathing Lung Chip. *Cell Syst* 3, 456-466.e4.
- Bhatia, S.N., and Ingber, D.E. (2014). Microfluidic organs-on-chips. *Nat Biotechnol* 32, 760–772.
- Bigger, Joseph W. (1944). TREATMENT OF STAPHYLOCOCCAL INFECTIONS WITH PENICILLIN BY INTERMITTENT STERILISATION. *Lancet* 244, 497–500.
- Bishop, B.L., Duncan, M.J., Song, J., Li, G., Zaas, D., and Abraham, S.N. (2007). Cyclic AMP-regulated exocytosis of *Escherichia coli* from infected bladder epithelial cells. *Nat Med* 13, 625–630.
- Blango, M.G., and Mulvey, M.A. (2010). Persistence of Uropathogenic *Escherichia coli* in the Face of Multiple Antibiotics. *Antimicrob Agents Ch* 54, 1855–1863.
- Blango, M.G., Ott, E.M., Erman, A., Veranic, P., and Mulvey, M.A. (2014). Forced Resurgence and Targeting of Intracellular Uropathogenic *Escherichia coli* Reservoirs. *Plos One* 9, e93327.
- Borregaard, N. (2010). Neutrophils, from Marrow to Microbes. *Immunity* 33, 657–670.
- Brandenberg, N., and Lutolf, M.P. (2016). In Situ Patterning of Microfluidic Networks in 3D Cell-Laden Hydrogels. *Adv Mater* 28, 7450–7456.
- Brandenberg, N., Hoehnel, S., Kuttler, F., Homicsko, K., Ceroni, C., Ringel, T., Gjorevski, N., Schwank, G., Coukos, G., Turcatti, G., et al. (2020). High-throughput automated organoid culture via stem-cell aggregation in microcavity arrays. *Nat Biomed Eng* 1–12.
- Branzk, N., Lubojemska, A., Hardison, S.E., Wang, Q., Gutierrez, M.G., Brown, G.D., and Papanikolaou, V. (2014). Neutrophils sense microbe size and selectively release neutrophil extracellular traps in response to large pathogens. *Nat Immunol* 15, 1017–1025.
- Brinkmann, V., and Zychlinsky, A. (2007). Beneficial suicide: why neutrophils die to make NETs. *Nat Rev Microbiol* 5, 577–582.

- Brinkmann, V., Reichard, U., Goosmann, C., Fauler, B., Uhlemann, Y., Weiss, D.S., Weinrauch, Y., and Zychlinsky, A. (2004). Neutrophil Extracellular Traps Kill Bacteria. *Science* 303, 1532–1535.
- Brubaker, L., and Wolfe, A. (2016). The urinary microbiota. *Curr Opin Obstetrics Gynecol* 28, 407–412.
- Bruns, S., Kniemeyer, O., Hasenberg, M., Aimanianda, V., Nietzsche, S., Thywißen, A., Jeron, A., Latgé, J.-P., Brakhage, A.A., and Gunzer, M. (2010). Production of Extracellular Traps against *Aspergillus fumigatus* In Vitro and in Infected Lung Tissue Is Dependent on Invading Neutrophils and Influenced by Hydrophobin RodA. *Plos Pathog* 6, e1000873.
- Bumann, D. (2015). Heterogeneous Host-Pathogen Encounters: Act Locally, Think Globally. *Cell Host Microbe* 17, 13–19.
- Casadevall, A., and Pirofski, L. (2000). Host-Pathogen Interactions: Basic Concepts of Microbial Commensalism, Colonization, Infection, and Disease. *Infect Immun* 68, 6511–6518.
- Claudi, B., Spröte, P., Chirkova, A., Personnic, N., Zankl, J., Schürmann, N., Schmidt, A., and Bumann, D. (2014). Phenotypic Variation of *Salmonella* in Host Tissues Delays Eradication by Antimicrobial Chemotherapy. *Cell* 158, 722–733.
- Clevers, H. (2016). Modeling Development and Disease with Organoids. *Cell* 165, 1586–1597.
- Clevers, H. (2020). COVID-19: organoids go viral. *Nat Rev Mol Cell Biology* 1–2.
- Cohen, N.R., Lobritz, M.A., and Collins, J.J. (2013). Microbial Persistence and the Road to Drug Resistance. *Cell Host Microbe* 13, 632–642.
- Conover, M.S., Hadjifrangiskou, M., Palermo, J.J., Hibbing, M.E., Dodson, K.W., and Hultgren, S.J. (2016). Metabolic Requirements of *Escherichia coli* in Intracellular Bacterial Communities during Urinary Tract Infection Pathogenesis. *Mbio* 7, e00104-16.
- Coombes, J.L., Charsar, B.A., Han, S.-J., Halkias, J., Chan, S.W., Koshy, A.A., Striepen, B., and Robey, E.A. (2013). Motile invaded neutrophils in the small intestine of *Toxoplasma gondii*-infected mice reveal a potential mechanism for parasite spread. *Proc National Acad Sci* 110, E1913–E1922.
- Cornish, J., Lecomwasam, J.P., Harrison, G., Vanderwee, M.A., and Miller, T.E. (1988). Host defence mechanisms in the bladder. II. Disruption of the layer of mucus. *Brit J Exp Pathol* 69, 759–770.
- Delincé, M.J., Bureau, J.-B., López-Jiménez, A.T., Cosson, P., Soldati, T., and McKinney, J.D. (2016). A microfluidic cell-trapping device for single-cell tracking of host–microbe interactions. *Lab Chip* 16, 3276–3285.
- Dhakal, B.K., and Mulvey, M.A. (2012). The UPEC pore-forming toxin α -hemolysin triggers proteolysis of host proteins to disrupt cell adhesion, inflammatory, and survival pathways. *Cell Host Microbe* 11, 58–69.

- Dhar, N., and McKinney, J.D. (2007). Microbial phenotypic heterogeneity and antibiotic tolerance. *Curr Opin Microbiol* 10, 30–38.
- Dhar, N., McKinney, J., and Manina, G. (2016). Phenotypic Heterogeneity in *Mycobacterium tuberculosis*. *Microbiol Spectr* 4.
- Driehuis, E., and Clevers, H. (2017). CRISPR/Cas 9 genome editing and its applications in organoids. *Am J Physiology Gastrointest Liver Physiology* 312, ajpgi.00410.2016.
- Duinen, V. van, Heuvel, A. van den, Trietsch, S.J., Lanz, H.L., Gils, J.M. van, Zonneveld, A.J. van, Vulto, P., and Hankemeier, T. (2017). 96 perfusable blood vessels to study vascular permeability in vitro. *Sci Rep-Uk* 7, 18071.
- Duraiswamy, S., Chee, J.L.Y., Chen, S., Yang, E., Lees, K., and Chen, S.L. (2018). Purification of Intracellular Bacterial Communities during Experimental Urinary Tract Infection Reveals an Abundant and Viable Bacterial Reservoir. *Infect Immun* 86, e00740-17.
- Duval, K., Grover, H., Han, L.-H., Mou, Y., Pegoraro, A.F., Fredberg, J., and Chen, Z. (2017). Modeling Physiological Events in 2D vs. 3D Cell Culture. *Physiology* 32, 266–277.
- Ettayebi, K., Crawford, S.E., Murakami, K., Broughman, J.R., Karandikar, U., Tenge, V.R., Neill, F.H., Blutt, S.E., Zeng, X.-L., Qu, L., et al. (2016). Replication of human noroviruses in stem cell–derived human enteroids. *Science* 353, 1387–1393.
- Flores-Mireles, A.L., Walker, J.N., Caparon, M., and Hultgren, S.J. (2015). Urinary tract infections: epidemiology, mechanisms of infection and treatment options. *Nat Rev Microbiol* 13, 269–284.
- Forbester, J.L., Goulding, D., Vallier, L., Hannan, N., Hale, C., Pickard, D., Mukhopadhyay, S., and Dougan, G. (2015). Interaction of *Salmonella enterica* Serovar Typhimurium with Intestinal Organoids Derived from Human Induced Pluripotent Stem Cells. *Infect Immun* 83, 2926–2934.
- Foxman, B. (2002). Epidemiology of urinary tract infections: incidence, morbidity, and economic costs. *Am J Medicine* 113, 5–13.
- Foxman, B. (2010). The epidemiology of urinary tract infection. *Nat Rev Urol* 7, 653–660.
- Foxman, B., Gillespie, B., Koopman, J., Zhang, L., Palin, K., Tallman, P., Marsh, J.V., Spear, S., Sobel, J.D., Marty, M.J., et al. (2000). Risk Factors for Second Urinary Tract Infection among College Women. *Am J Epidemiol* 151, 1194–1205.
- Frey, O., Misun, P.M., Fluri, D.A., Hengstler, J.G., and Hierlemann, A. (2014). Reconfigurable microfluidic hanging drop network for multi-tissue interaction and analysis. *Nat Commun* 5, 4250.
- Fuchs, T.A., Abed, U., Goosmann, C., Hurwitz, R., Schulze, I., Wahn, V., Weinrauch, Y., Brinkmann, V., and Zychlinsky, A. (2007a). Novel cell death program leads to neutrophil extracellular traps. *J Cell Biology* 176, 231–241.
- Fuchs, T.A., Abed, U., Goosmann, C., Hurwitz, R., Schulze, I., Wahn, V., Weinrauch, Y., Brinkmann, V., and Zychlinsky, A. (2007b). Novel cell death program leads to neutrophil extracellular traps. *J Exp Medicine* 204, i2–i2.

- Garofalo, C.K., Hooton, T.M., Martin, S.M., Stamm, W.E., Palermo, J.J., Gordon, J.I., and Hultgren, S.J. (2007). *Escherichia coli* from Urine of Female Patients with Urinary Tract Infections Is Competent for Intracellular Bacterial Community Formation ▽. *Infect Immun* 75, 52–60.
- Geerlings, S.E. (2019). Urinary Tract Infections. Undefined 27–40.
- Germanos, G.J., Trautner, B.W., Zoorob, R.J., Salemi, J.L., Drekonja, D., Gupta, K., and Gri-goryan, L. (2019). No Clinical Benefit to Treating Male Urinary Tract Infection Longer than Seven Days: An Outpatient Database Study. *Open Forum Infect Dis* 6, ofz216.
- Gjorevski, N., Sachs, N., Manfrin, A., Giger, S., Bragina, M.E., Ordóñez-Morán, P., Clevers, H., and Lutolf, M.P. (2016). Designer matrices for intestinal stem cell and organoid culture. *Nature* 539, 560–564.
- Gobaa, S., Hoehnel, S., Roccio, M., Negro, A., Kobel, S., and Lutolf, M.P. (2011). Artificial niche microarrays for probing single stem cell fate in high throughput. *Nat Methods* 8, 949–955.
- Griebing, T.L. (2005). UROLOGIC DISEASES IN AMERICA PROJECT. *J Urology* 173, 1288–1294.
- Hakim, A., Fürnrohr, B.G., Amann, K., Laube, B., Abed, U.A., Brinkmann, V., Herrmann, M., Voll, R.E., and Zychlinsky, A. (2010). Impairment of neutrophil extracellular trap degradation is associated with lupus nephritis. *Proc National Acad Sci* 107, 9813–9818.
- Hammond, T.G., and Hammond, J.M. (2001). Optimized suspension culture: the rotating-wall ves-sel. *Am J Physiol-Renal* 281, F12–F25.
- Hannan, T.J., Mysorekar, I.U., Hung, C.S., Isaacson-Schmid, M.L., and Hultgren, S.J. (2010). Early severe inflammatory responses to uropathogenic *E. coli* predispose to chronic and recurrent urinary tract infection. *Plos Pathog* 6, e1001042.
- Hannan, T.J., Totsika, M., Mansfield, K.J., Moore, K.H., Schembri, M.A., and Hultgren, S.J. (2012). Host–pathogen checkpoints and population bottlenecks in persistent and intracellular uro-pathogenic *Escherichia coli* bladder infection. *Fems Microbiol Rev* 36, 616–648.
- Haraoka, M., Hang, L., Frendéus, B., Godaly, G., Burdick, M., Strieter, R., and Svanborg, C. (1999). Neutrophil Recruitment and Resistance to Urinary Tract Infection. *J Infect Dis* 180, 1220–1229.
- Hassell, B.A., Goyal, G., Lee, E., Sontheimer-Phelps, A., Levy, O., Chen, C.S., and Ingber, D.E. (2017). Human Organ Chip Models Recapitulate Orthotopic Lung Cancer Growth, Therapeutic Re-sponses, and Tumor Dormancy In Vitro. *Cell Reports* 21, 508–516.
- Hedges, S., Svensson, M., and Svanborg, C. (1992). Interleukin-6 response of epithelial cell lines to bacterial stimulation in vitro. *Infect Immun* 60, 1295–1301.
- Helaine, S., Thompson, J.A., Watson, K.G., Liu, M., Boyle, C., and Holden, D.W. (2010). Dynam-ics of intracellular bacterial replication at the single cell level. *Proc National Acad Sci* 107, 3746–3751.

- Helaine, S., Cheverton, A.M., Watson, K.G., Faure, L.M., Matthews, S.A., and Holden, D.W. (2014). Internalization of *Salmonella* by Macrophages Induces Formation of Nonreplicating Persisters. *Science* 343, 204–208.
- Heo, I., Dutta, D., Schaefer, D.A., Iakobachvili, N., Artegiani, B., Sachs, N., Boonekamp, K.E., Bowden, G., Hendrickx, A.P.A., Willems, R.J.L., et al. (2018). Modelling Cryptosporidium infection in human small intestinal and lung organoids. *Nat Microbiol* 3, 814–823.
- Hicks, R.M. (1975). THE MAMMALIAN URINARY BLADDERAN ACCOMMODATING ORGAN. *Biol Rev* 50, 215–246.
- Holden, D.W. (2015). Persisters unmasked. *Science* 347, 30–32.
- Homan, K.A., Kolesky, D.B., Skylar-Scott, M.A., Herrmann, J., Obuobi, H., Moisan, A., and Lewis, J.A. (2016). Bioprinting of 3D Convulated Renal Proximal Tubules on Perfusable Chips. *Sci Rep-Uk* 6, 34845.
- Homan, K.A., Gupta, N., Kroll, K.T., Kolesky, D.B., Skylar-Scott, M., Miyoshi, T., Mau, D., Valerius, M.T., Ferrante, T., Bonventre, J.V., et al. (2019). Flow-enhanced vascularization and maturation of kidney organoids in vitro. *Nat Methods* 16, 255–262.
- Hooton, T.M. (2001). Recurrent urinary tract infection in women. *Int J Antimicrob Ag* 17, 259–268.
- Hopke, A., Scherer, A., Kreuzburg, S., Abers, M.S., Zerbe, C.S., Dinauer, M.C., Mansour, M.K., and Irimia, D. (2020). Neutrophil swarming delays the growth of clusters of pathogenic fungi. *Nat Commun* 11, 2031.
- Horsley, H., Dharmasena, D., Malone-Lee, J., and Rohn, J.L. (2018). A urine-dependent human urothelial organoid offers a potential alternative to rodent models of infection. *Sci Rep-Uk* 8, 1238.
- Huch, M., Bonfanti, P., Boj, S.F., Sato, T., Loomans, C.J.M., Wetering, M. van de, Sojoodi, M., Li, V.S.W., Schuijers, J., Gracanin, A., et al. (2013). Unlimited in vitro expansion of adult bi-potent pancreas progenitors through the Lgr5/R-spondin axis. *Embo J* 32, 2708–2721.
- Huh, D., Matthews, B.D., Mammoto, A., Montoya-Zavala, M., Hsin, H.Y., and Ingber, D.E. (2010a). Reconstituting Organ-Level Lung Functions on a Chip. *Science* 328, 1662–1668.
- Huh, D., Matthews, B.D., Mammoto, A., Montoya-Zavala, M., Hsin, H.Y., and Ingber, D.E. (2010b). Reconstituting Organ-Level Lung Functions on a Chip. *Science* 328, 1662–1668.
- Huh, D., Leslie, D.C., Matthews, B.D., Fraser, J.P., Jurek, S., Hamilton, G.A., Thorneloe, K.S., McAlexander, M.A., and Ingber, D.E. (2012). A Human Disease Model of Drug Toxicity–Induced Pulmonary Edema in a Lung-on-a-Chip Microdevice. *Sci Transl Med* 4, 159ra147–159ra147.
- Hui, K.P.Y., Ching, R.H.H., Chan, S.K.H., Nicholls, J.M., Sachs, N., Clevers, H., Peiris, J.S.M., and Chan, M.C.W. (2018). Tropism, replication competence, and innate immune responses of influenza virus: an analysis of human airway organoids and ex-vivo bronchus cultures. *Lancet Respir Medicine* 6, 846–854.

- Hurst, R.E. (1994). Structure, function, and pathology of proteoglycans and glycosaminoglycans in the urinary tract. *World J Urol* *12*, 3–10.
- Ingersoll, M.A. (2017). Sex differences shape the response to infectious diseases. *Plos Pathog* *13*, e1006688.
- Ingersoll, M.A., Kline, K.A., Nielsen, H.V., and Hultgren, S.J. (2008). G-CSF induction early in uropathogenic *Escherichia coli* infection of the urinary tract modulates host immunity. *Cell Microbiol* *10*, 2568–2578.
- Iosifidis, G., and Duggin, I.G. (2020). Distinct Morphological Fates of Uropathogenic *Escherichia coli* Intracellular Bacterial Communities: Dependency on Urine Composition and pH. *Infect Immun* *88*.
- Jacobsen, S.M., Stickler, D.J., Mobley, H.L.T., and Shirtliff, M.E. (2008). Complicated Catheter-Associated Urinary Tract Infections Due to *Escherichia coli* and *Proteus mirabilis*. *Clin Microbiol Rev* *21*, 26–59.
- Jain, N., and Vogel, V. (2018). Spatial confinement downsizes the inflammatory response of macrophages. *Nat Mater* *17*, 1134–1144.
- Jalili-Firoozinezhad, S., Gazzaniga, F.S., Calamari, E.L., Camacho, D.M., Fadel, C.W., Bein, A., Swenor, B., Nestor, B., Cronce, M.J., Tovaglieri, A., et al. (2019). A complex human gut microbiome cultured in an anaerobic intestine-on-a-chip. *Nat Biomed Eng* *3*, 520–531.
- Jang, K.-J., Mehr, A.P., Hamilton, G.A., McPartlin, L.A., Chung, S., Suh, K.-Y., and Ingber, D.E. (2013). Human kidney proximal tubule-on-a-chip for drug transport and nephrotoxicity assessment. *Integr Biol* *5*, 1119–1129.
- Jang, K.-J., Otieno, M.A., Ronxhi, J., Lim, H.-K., Ewart, L., Kodella, K.R., Petropolis, D.B., Kulkarni, G., Rubins, J.E., Conegliano, D., et al. (2019). Reproducing human and cross-species drug toxicities using a Liver-Chip. *Sci Transl Med* *11*, eaax5516.
- Jiménez-Alcázar, M., Rangaswamy, C., Panda, R., Bitterling, J., Simsek, Y.J., Long, A.T., Bilyy, R., Krenn, V., Renné, C., Renné, T., et al. (2017). Host DNases prevent vascular occlusion by neutrophil extracellular traps. *Science* *358*, 1202–1206.
- Justice, S.S., Hung, C., Theriot, J.A., Fletcher, D.A., Anderson, G.G., Footer, M.J., and Hultgren, S.J. (2004). Differentiation and developmental pathways of uropathogenic *Escherichia coli* in urinary tract pathogenesis. *Proc National Acad Sci* *101*, 1333–1338.
- Justice, S.S., Hunstad, D.A., Seed, P.C., and Hultgren, S.J. (2006). Filamentation by *Escherichia coli* subverts innate defenses during urinary tract infection. *Proc National Acad Sci* *103*, 19884–19889.
- Kang, Y.B. (Abraham), Sodunke, T.R., Lamontagne, J., Cirillo, J., Rajiv, C., Bouchard, M.J., and Noh, M. (2015). Liver sinusoid on a chip: Long-term layered co-culture of primary rat hepatocytes and endothelial cells in microfluidic platforms. *Biotechnol Bioeng* *112*, 2571–2582.

- Kansas, G.S. (1996). Selectins and their ligands: current concepts and controversies. *Blood* 88, 3259–3287.
- Kasendra, M., Tovaglieri, A., Sontheimer-Phelps, A., Jalili-Firoozinezhad, S., Bein, A., Chalkiadaki, A., Scholl, W., Zhang, C., Rickner, H., Richmond, C.A., et al. (2018). Development of a primary human Small Intestine-on-a-Chip using biopsy-derived organoids. *Sci Rep-Uk* 8, 2871.
- Khan, F.U., Ihsan, A.U., Khan, H.U., Jana, R., Wazir, J., Khongorzul, P., Waqar, M., and Zhou, X. (2017). Comprehensive overview of prostatitis. *Biomed Pharmacother* 94, 1064–1076.
- Kienle, K., and Lämmermann, T. (2016). Neutrophil swarming: an essential process of the neutrophil tissue response. *Immunol Rev* 273, 76–93.
- Kim, H.J., and Ingber, D.E. (2013). Gut-on-a-Chip microenvironment induces human intestinal cells to undergo villus differentiation. *Integr Biol* 5, 1130–1140.
- Kim, H.J., Li, H., Collins, J.J., and Ingber, D.E. (2016). Contributions of microbiome and mechanical deformation to intestinal bacterial overgrowth and inflammation in a human gut-on-a-chip. *Proc National Acad Sci* 113, E7–E15.
- Kim, J., Koo, B.-K., and Knoblich, J.A. (2020). Human organoids: model systems for human biology and medicine. *Nat Rev Mol Cell Bio* 21, 571–584.
- Klein, R.D., and Hultgren, S.J. (2020). Urinary tract infections: microbial pathogenesis, host-pathogen interactions and new treatment strategies. *Nat Rev Microbiol* 18, 211–226.
- Klein, S.L., and Flanagan, K.L. (2016). Sex differences in immune responses. *Nat Rev Immunol* 16, 626–638.
- Kobel, S., and Lutolf, M.P. (2011). Biomaterials meet microfluidics: building the next generation of artificial niches. *Curr Opin Biotech* 22, 690–697.
- Kolaczowska, E., and Kubes, P. (2013). Neutrophil recruitment and function in health and inflammation. *Nat Rev Immunol* 13, 159–175.
- Kreisel, D., Nava, R.G., Li, W., Zinselmeyer, B.H., Wang, B., Lai, J., Pless, R., Gelman, A.E., Krupnick, A.S., and Miller, M.J. (2010). In vivo two-photon imaging reveals monocyte-dependent neutrophil extravasation during pulmonary inflammation. *Proc National Acad Sci* 107, 18073–18078.
- Lamers, M.M., Beumer, J., Vaart, J. van der, Knoop, K., Puschhof, J., Breugem, T.I., Ravelli, R.B.G., Schayck, J.P. van, Mykytyn, A.Z., Duimel, H.Q., et al. (2020). SARS-CoV-2 productively infects human gut enterocytes. *Sci New York N Y* eabc1669.
- Lämmermann, T., Afonso, P.V., Angermann, B.R., Wang, J.M., Kastenmüller, W., Parent, C.A., and Germain, R.N. (2013). Neutrophil swarms require LTB4 and integrins at sites of cell death in vivo. *Nature* 498, 371–375.

- Lancaster, M.A., Corsini, N.S., Wolfiger, S., Gustafson, E.H., Phillips, A.W., Burkard, T.R., Otani, T., Livesey, F.J., and Knoblich, J.A. (2017). Guided self-organization and cortical plate formation in human brain organoids. *Nat Biotechnol* 35, 659–666.
- Lee, S.W., and Kim, J.H. (2008). The significance of natural bladder filling by the production of urine during cystometry. *Neurourol Urodynam* 27, 772–774.
- Lee, G.Y., Kenny, P.A., Lee, E.H., and Bissell, M.J. (2007). Three-dimensional culture models of normal and malignant breast epithelial cells. *Nat Methods* 4, 359–365.
- Lee, K.K., McCauley, H.A., Broda, T.R., Kofron, M.J., Wells, J.M., and Hong, C.I. (2018a). Human stomach-on-a-chip with luminal flow and peristaltic-like motility. *Lab Chip* 18, 3079–3085.
- Lee, S.H., Hu, W., Matulay, J.T., Silva, M.V., Owczarek, T.B., Kim, K., Chua, C.W., Barlow, L.J., Kandoth, C., Williams, A.B., et al. (2018b). Tumor Evolution and Drug Response in Patient-Derived Organoid Models of Bladder Cancer. *Cell* 173, 515–528.e17.
- Levin, B.R., and Rozen, D.E. (2006). Non-inherited antibiotic resistance. *Nat Rev Microbiol* 4, 556–562.
- Ley, K., Laudanna, C., Cybulsky, M.I., and Nourshargh, S. (2007). Getting to the site of inflammation: the leukocyte adhesion cascade updated. *Nat Rev Immunol* 7, 678–689.
- Liese, J., Rooijackers, S.H.M., Strijp, J.A.G. van, Novick, R.P., and Dustin, M.L. (2012). Intravital two-photon microscopy of host-pathogen interactions in a mouse model of *Staphylococcus aureus* skin abscess formation: Intravital 2-P microscopy of *S. aureus* skin infection. *Cell Microbiol* 15, 891–909.
- Lim, G.B. (2018). DNases prevent clots formed by neutrophil extracellular traps. *Nat Rev Cardiol* 15, 69–69.
- Lloyd, A.L., Rasko, D.A., and Mobley, H.L.T. (2007). Defining Genomic Islands and Uropathogen-Specific Genes in Uropathogenic *Escherichia coli*. *J Bacteriol* 189, 3532–3546.
- Lupo, F., and Ingersoll, M.A. (2019). Is bacterial prostatitis a urinary tract infection? *Nat Rev Urol* 16, 203–204.
- Lüthje, P., Brauner, H., Ramos, N.L., Övregaard, A., Gläser, R., Hirschberg, A.L., Aspenström, P., and Brauner, A. (2013). Estrogen Supports Urothelial Defense Mechanisms. *Sci Transl Med* 5, 190ra80-190ra80.
- Lutolf, M.P., and Hubbell, J.A. (2005). Synthetic biomaterials as instructive extracellular microenvironments for morphogenesis in tissue engineering. *Nat Biotechnol* 23, 47–55.
- Lutolf, M.P., Gilbert, P.M., and Blau, H.M. (2009). Designing materials to direct stem-cell fate. *Nature* 462, 433–441.
- Manina, G., Dhar, N., and McKinney, J.D. (2015). Stress and Host Immunity Amplify *Mycobacterium tuberculosis* Phenotypic Heterogeneity and Induce Nongrowing Metabolically Active Forms. *Cell Host Microbe* 17, 32–46.

- Mariano, L.L., and Ingersoll, M.A. (2020). The immune response to infection in the bladder. *Nat Rev Urology* 1–20.
- Mariano, L.L., Rousseau, M., Varet, H., Legendre, R., Gentek, R., Coronilla, J.S., Bajenoff, M., Perdiguero, E.G., and Ingersoll, M.A. (2020). Functionally distinct resident macrophage subsets differentially shape responses to infection in the bladder. *Sci Adv* 6, eabc5739.
- Markle, J.G., and Fish, E.N. (2014). Sex matters in immunity. *Trends Immunol* 35, 97–104.
- McIlroy, D.J., Jarnicki, A.G., Au, G.G., Lott, N., Smith, D.W., Hansbro, P.M., and Balogh, Z.J. (2014). Mitochondrial DNA neutrophil extracellular traps are formed after trauma and subsequent surgery. *J Crit Care* 29, 1133.e1–1133.e5.
- Meares, E.M., and Stamey, T.A. (1972). THE DIAGNOSIS AND MANAGEMENT OF BACTERIAL PROSTATITIS. *Brit J Urol* 44, 175–179.
- Meer, B.J. van, Vries, H. de, Firth, K.S.A., Weerd, J. van, Tertoolen, L.G.J., Karperien, H.B.J., Jonkheijm, P., Denning, C., IJzerman, A.P., and Mummery, C.L. (2017). Small molecule absorption by PDMS in the context of drug response bioassays. *Biochem Bioph Res Co* 482, 323–328.
- Mejías, J.C., Nelson, M.R., Liseth, O., and Roy, K. (2020). A 96-well format microvascularized human lung-on-a-chip platform for microphysiological modeling of fibrotic diseases. *Lab Chip* 20, 3601–3611.
- Metzler, K.D., Fuchs, T.A., Nauseef, W.M., Reumaux, D., Roesler, J., Schulze, I., Wahn, V., Papanopoulos, V., and Zychlinsky, A. (2011). Myeloperoxidase is required for neutrophil extracellular trap formation: implications for innate immunity. *Blood* 117, 953–959.
- Miao, Y., Bist, P., Wu, J., Zhao, Q., Li, Q., Wan, Y., and Abraham, S.N. (2017). Collaboration between Distinct Rab Small GTPase Trafficking Circuits Mediates Bacterial Clearance from the Bladder Epithelium. *Cell Host Microbe* 22, 330–342.e4.
- Mills, M., Meysick, K.C., and O'Brien, A.D. (2000). Cytotoxic Necrotizing Factor Type 1 of Uropathogenic Escherichia coli Kills Cultured Human Uroepithelial 5637 Cells by an Apoptotic Mechanism. *Infect Immun* 68, 5869–5880.
- Mobley, H.L.T. (2016). Measuring Escherichia coli Gene Expression during Human Urinary Tract Infections. *Pathogens Basel Switz* 5, 7.
- Möller, J., Luehmann, T., Hall, H., and Vogel, V. (2012). The Race to the Pole: How High-Aspect Ratio Shape and Heterogeneous Environments Limit Phagocytosis of Filamentous Escherichia coli Bacteria by Macrophages. *Nano Lett* 12, 2901–2905.
- Monteil, V., Kwon, H., Prado, P., Hagelkrüys, A., Wimmer, R.A., Stahl, M., Leopoldi, A., Garreta, E., Pozo, C.H.D., Prosper, F., et al. (2020). Inhibition of SARS-CoV-2 Infections in Engineered Human Tissues Using Clinical-Grade Soluble Human ACE2. *Cell* 181, 905–913.e7.
- Moore, E.E., Hawes, S.E., Scholes, D., Boyko, E.J., Hughes, J.P., and Fihn, S.D. (2008a). Sexual Intercourse and Risk of Symptomatic Urinary Tract Infection in Post-Menopausal Women. *J Gen Intern Med* 23, 595–599.

- Moore, E.E., Jackson, S.L., Boyko, E.J., Scholes, D., and Fihn, S.D. (2008b). Urinary Incontinence and Urinary Tract Infection. *Obstetrics Gynecol* 111, 317–323.
- Mullenders, J., Jongh, E. de, Brousalı, A., Roosen, M., Blom, J.P.A., Begthel, H., Korving, J., Jonges, T., Kranenburg, O., Meijer, R., et al. (2019). Mouse and human urothelial cancer organoids: A tool for bladder cancer research. *Proc National Acad Sci* 116, 201803595.
- Mulvey, M.A. (2002). Adhesion and entry of uropathogenic *Escherichia coli*. *Cell Microbiol* 4, 257–271.
- Mulvey, M.A., Lopez-Boado, Y.S., Wilson, C.L., Roth, R., Parks, W.C., Heuser, J., and Hultgren, S.J. (1998). Induction and Evasion of Host Defenses by Type 1-Piliated Uropathogenic *Escherichia coli*. *Science* 282, 1494–1497.
- Mulvey, M.A., Schilling, J.D., and Hultgren, S.J. (2001). Establishment of a Persistent *Escherichia coli* Reservoir during the Acute Phase of a Bladder Infection. *Infect Immun* 69, 4572–4579.
- Mysorekar, I.U., and Hultgren, S.J. (2006). Mechanisms of uropathogenic *Escherichia coli* persistence and eradication from the urinary tract. *Proc National Acad Sci* 103, 14170–14175.
- Mysorekar, I.U., Mulvey, M.A., Hultgren, S.J., and Gordon, J.I. (2002). Molecular Regulation of Urothelial Renewal and Host Defenses during Infection with Uropathogenic *Escherichia coli*. *J Biol Chem* 277, 7412–7419.
- Mysorekar, I.U., Isaacson-Schmid, M., Walker, J.N., Mills, J.C., and Hultgren, S.J. (2009). Bone Morphogenetic Protein 4 Signaling Regulates Epithelial Renewal in the Urinary Tract in Response to Uropathogenic Infection. *Cell Host Microbe* 5, 463–475.
- Nagamatsu, K., Hannan, T.J., Guest, R.L., Kostakioti, M., Hadjifrangiskou, M., Binkley, J., Dodson, K., Raivio, T.L., and Hultgren, S.J. (2015). Dysregulation of *Escherichia coli* α -hemolysin expression alters the course of acute and persistent urinary tract infection. *Proc National Acad Sci* 112, E871–E880.
- Nauseef, W.M., and Borregaard, N. (2014). Neutrophils at work. *Nat Immunol* 15, 602–611.
- Nikolaev, M., Mitrofanova, O., Broguiere, N., Geraldo, S., Dutta, D., Tabata, Y., Elci, B., Brandenburg, N., Kolotuev, I., Gjorevski, N., et al. (2020). Homeostatic mini-intestines through scaffold-guided organoid morphogenesis. *Nature* 585, 574–578.
- Nourshargh, S., Hordijk, P.L., and Sixt, M. (2010). Breaching multiple barriers: leukocyte motility through venular walls and the interstitium. *Nat Rev Mol Cell Bio* 11, 366–378.
- O’Brien, V.P., Hannan, T.J., Yu, L., Livny, J., Roberson, E.D.O., Schwartz, D.J., Souza, S., Mendelsohn, C.L., Colonna, M., Lewis, A.L., et al. (2016). A mucosal imprint left by prior *Escherichia coli* bladder infection sensitizes to recurrent disease. *Nat Microbiol* 2, 16196.
- Oliveira, S. de, Rosowski, E.E., and Huttenlocher, A. (2016). Neutrophil migration in infection and wound repair: going forward in reverse. *Nat Rev Immunol* 16, 378–391.

- Öztürk, R., and Murt, A. (2020). Epidemiology of urological infections: a global burden. *World J Urol* 1–11.
- Pak, J., Pu, Y., Zhang, Z.-T., Hasty, D.L., and Wu, X.-R. (2001). Tamm-Horsfall Protein Binds to Type 1 Fimbriated *Escherichia coli* and Prevents *E. coli* from Binding to Uroplakin Ia and Ib Receptors. *J Biol Chem* 276, 9924–9930.
- Papayannopoulos, V. (2017). Neutrophil extracellular traps in immunity and disease. *Nat Rev Immunol* 18, 134–147.
- Papayannopoulos, V., Metzler, K.D., Hakkim, A., and Zychlinsky, A. (2010). Neutrophil elastase and myeloperoxidase regulate the formation of neutrophil extracellular traps. *J Cell Biology* 191, 677–691.
- Park, S.E., Georgescu, A., and Huh, D. (2019). Organoids-on-a-chip. *Sci New York N Y* 364, 960–965.
- Parsons, C.L. (2007). The Role of the Urinary Epithelium in the Pathogenesis of Interstitial Cystitis/Prostatitis/Urethritis. *Urology* 69, S9–S16.
- Peters, N.C., Egen, J.G., Secundino, N., Debrabant, A., Kimblin, N., Kamhawi, S., Lawyer, P., Fay, M.P., Germain, R.N., and Sacks, D. (2008). In Vivo Imaging Reveals an Essential Role for Neutrophils in Leishmaniasis Transmitted by Sand Flies. *Science* 321, 970–974.
- Pilschek, F.H., Salina, D., Poon, K.K.H., Fahey, C., Yipp, B.G., Sibley, C.D., Robbins, S.M., Green, F.H.Y., Surette, M.G., Sugai, M., et al. (2010). A Novel Mechanism of Rapid Nuclear Neutrophil Extracellular Trap Formation in Response to *Staphylococcus aureus*. *J Immunol* 185, 7413–7425.
- Pisu, D., Huang, L., Grenier, J.K., and Russell, D.G. (2020). Dual RNA-Seq of Mtb-Infected Macrophages In Vivo Reveals Ontologically Distinct Host-Pathogen Interactions. *Cell Reports* 30, 335–350.e4.
- Poplimont, H., Georgantzoglou, A., Boulch, M., Walker, H.A., Coombs, C., Papaleonidopoulou, F., and Sarris, M. (2020). Neutrophil Swarming in Damaged Tissue Is Orchestrated by Connexins and Cooperative Calcium Alarm Signals. *Curr Biol* 30, 2761–2776.e7.
- Qian, X., Nguyen, H.N., Jacob, F., Song, H., and Ming, G.-L. (2017). Using brain organoids to understand Zika virus-induced microcephaly. *Dev Camb Engl* 144, 952–957.
- Raz, R., and Stamm, W.E. (1993). A Controlled Trial of Intravaginal Estriol in Postmenopausal Women with Recurrent Urinary Tract Infections. *New Engl J Medicine* 329, 753–756.
- Reátegui, E., Jalali, F., Khankhel, A.H., Wong, E., Cho, H., Lee, J., Serhan, C.N., Dalli, J., Elliott, H., and Irimia, D. (2017). Microscale arrays for the profiling of start and stop signals coordinating human-neutrophil swarming. *Nat Biomed Eng* 1, 0094.
- Robino, L., Scavone, P., Araujo, L., Algorta, G., Zunino, P., and Vignoli, R. (2013). Detection of intracellular bacterial communities in a child with *Escherichia coli* recurrent urinary tract infections. *Pathog Dis* 68, 78–81.

- Robinson, D., Tooze-Hobson, P., and Cardozo, L. (2013). The effect of hormones on the lower urinary tract. *Menopause Int* 19, 155–162.
- Ronald, A.R., Nicolle, L.E., Stamm, E., Krieger, J., Warren, J., Schaeffer, A., Naber, K.G., Hooton, T.M., Johnson, J., Chambers, S., et al. (2001). Urinary tract infection in adults: research priorities and strategies. *Int J Antimicrob Ag* 17, 343–348.
- Rosen, D.A., Hooton, T.M., Stamm, W.E., Humphrey, P.A., and Hultgren, S.J. (2007). Detection of Intracellular Bacterial Communities in Human Urinary Tract Infection. *Plos Med* 4, e329.
- Rosen, D.A., Pinkner, J.S., Jones, J.M., Walker, J.N., Clegg, S., and Hultgren, S.J. (2008). Utilization of an Intracellular Bacterial Community Pathway in *Klebsiella pneumoniae* Urinary Tract Infection and the Effects of FimK on Type 1 Pilus Expression ∇ . *Infect Immun* 76, 3337–3345.
- Rossi, G., Manfrin, A., and Lutolf, M.P. (2018). Progress and potential in organoid research. *Nat Rev Genet* 19, 671–687.
- Roy, V., Magne, B., Vaillancourt-Audet, M., Blais, M., Chabaud, S., Grammond, E., Piquet, L., Fradette, J., Laverdière, I., Moulin, V.J., et al. (2020). Human Organ-Specific 3D Cancer Models Produced by the Stromal Self-Assembly Method of Tissue Engineering for the Study of Solid Tumors. *Biomed Res Int* 2020, 1–23.
- Ruben, F.L., Dearwater, S.R., Norden, C.W., Kuller, L.H., Gartner, K., Shalley, A., Warshafsky, G., Kelsey, S.F., O'Donnell, C., Means, E., et al. (1995). Clinical Infections in the Noninstitutionalized Geriatric Age Group: Methods Utilized and Incidence of Infections. *Am J Epidemiol* 141, 145–157.
- Russell, W.M.S., and Birch, R.L. (1960). The Principles of Humane Experimental Technique. *Med J Australia* 1, 500–500.
- Sachs, N., Ligt, J. de, Kopper, O., Gogola, E., Bounova, G., Weeber, F., Balgobind, A.V., Wind, K., Gracanin, A., Begthel, H., et al. (2018). A Living Biobank of Breast Cancer Organoids Captures Disease Heterogeneity. *Cell* 172, 373–386.e10.
- Sachs, N., Papaspyropoulos, A., Ommen, D.D.Z., Heo, I., Böttinger, L., Klay, D., Weeber, F., Huelsz-Prince, G., Iakobachvili, N., Amatngalim, G.D., et al. (2019). Long-term expanding human airway organoids for disease modeling. *Embo J* 38.
- Säemann, M.D., Weichhart, T., Zeyda, M., Staffler, G., Schunn, M., Stuhlmeier, K.M., Sobanov, Y., Stulnig, T.M., Akira, S., Gabain, A. von, et al. (2005). Tamm-Horsfall glycoprotein links innate immune cell activation with adaptive immunity via a Toll-like receptor-4-dependent mechanism. *J Clin Invest* 115, 468–475.
- Saitoh, T., Komano, J., Saitoh, Y., Misawa, T., Takahama, M., Kozaki, T., Uehata, T., Iwasaki, H., Omori, H., Yamaoka, S., et al. (2012). Neutrophil Extracellular Traps Mediate a Host Defense Response to Human Immunodeficiency Virus-1. *Cell Host Microbe* 12, 109–116.
- Salahudeen, A.A., Choi, S.S., Rustagi, A., Zhu, J., Unen, V. van, O, S.M. de la, Flynn, R.A., Margalef-Català, M., Santos, A.J.M., Ju, J., et al. (2020). Progenitor identification and SARS-CoV-2 infection in human distal lung organoids. *Nature* 588, 670–675.

- Sanden, S.M.G. van der, Sachs, N., Koekkoek, S.M., Koen, G., Pajkrt, D., Clevers, H., and Wolthers, K.C. (2018). Enterovirus 71 infection of human airway organoids reveals VP1-145 as a viral infectivity determinant. *Emerg Microbes Infect* 7, 84.
- Sato, T., Vries, R.G., Snippert, H.J., Wetering, M. van de, Barker, N., Stange, D.E., Es, J.H. van, Abo, A., Kujala, P., Peters, P.J., et al. (2009). Single Lgr5 stem cells build crypt-villus structures in vitro without a mesenchymal niche. *Nature* 459, 262–265.
- Sauer, M.M., Jakob, R.P., Eras, J., Baday, S., Eriş, D., Navarra, G., Bernèche, S., Ernst, B., Maier, T., and Glockshuber, R. (2016). Catch-bond mechanism of the bacterial adhesin FimH. *Nat Commun* 7, 10738.
- Scharff, A.Z., Rousseau, M., Mariano, L.L., Canton, T., Consiglio, C.R., Albert, M.L., Fontes, M., Duffy, D., and Ingersoll, M.A. (2019). Sex differences in IL-17 contribute to chronicity in male versus female urinary tract infection. *Jci Insight* 4.
- Schilling, J.D., Lorenz, R.G., and Hultgren, S.J. (2002). Effect of Trimethoprim-Sulfamethoxazole on Recurrent Bacteriuria and Bacterial Persistence in Mice Infected with Uropathogenic *Escherichia coli*. *Infect Immun* 70, 7042–7049.
- Schiwon, M., Weisheit, C., Franken, L., Gutweiler, S., Dixit, A., Meyer-Schwesinger, C., Pohl, J.-M., Maurice, N.J., Thiebes, S., Lorenz, K., et al. (2014). Crosstalk between sentinel and helper macrophages permits neutrophil migration into infected uroepithelium. *Cell* 156, 456–468.
- Schwank, G., Koo, B.-K., Sasselli, V., Dekkers, J.F., Heo, I., Demircan, T., Sasaki, N., Boymans, S., Cuppen, E., Ent, C.K. van der, et al. (2013). Functional repair of CFTR by CRISPR/Cas9 in intestinal stem cell organoids of cystic fibrosis patients. *Cell Stem Cell* 13, 653–658.
- Schwartz, D.J., Chen, S.L., Hultgren, S.J., and Seed, P.C. (2011). Population Dynamics and Niche Distribution of Uropathogenic *Escherichia coli* during Acute and Chronic Urinary Tract Infection. *Infect Immun* 79, 4250–4259.
- Scott, V.C.S., Haake, D.A., Churchill, B.M., Justice, S.S., and Kim, J.-H. (2015). Intracellular Bacterial Communities: A Potential Etiology for Chronic Lower Urinary Tract Symptoms. *Urology* 86, 425–431.
- Sellgren, K.L., Butala, E.J., Gilmour, B.P., Randell, S.H., and Grego, S. (2014). A biomimetic multicellular model of the airways using primary human cells. *Lab Chip* 14, 3349–3358.
- Serafini-Cessi, F., Malagolini, N., and Cavallone, D. (2003). Tamm-Horsfall glycoprotein: biology and clinical relevance. *Am J Kidney Dis* 42, 658–676.
- Serex, L., Sharma, K., Rizov, V., Bertsch, A., McKinney, J.D., and Renaud, P. (2020). Microfluidic-assisted bioprinting of tissues and organoids at high cell concentrations. *Biofabrication*.
- Servin, A.L. (2014). Pathogenesis of Human Diffusely Adhering *Escherichia coli* Expressing Afa/Dr Adhesins (Afa/Dr DAEC): Current Insights and Future Challenges. *Clin Microbiol Rev* 27, 823–869.

- Shah, P., Fritz, J.V., Glaab, E., Desai, M.S., Greenhalgh, K., Frachet, A., Niegowska, M., Estes, M., Jäger, C., Seguin-Devaux, C., et al. (2016). A microfluidics-based in vitro model of the gastrointestinal human–microbe interface. *Nat Commun* 7, 11535.
- Shin, K., Lee, J., Guo, N., Kim, J., Lim, A., Qu, L., Mysorekar, I.U., and Beachy, P.A. (2011). Hedgehog/Wnt feedback supports regenerative proliferation of epithelial stem cells in bladder. *Nature* 472, 110–114.
- Smith, Y.C., Grande, K.K., Rasmussen, S.B., and O’Brien, A.D. (2006). Novel Three-Dimensional Organoid Model for Evaluation of the Interaction of Uropathogenic *Escherichia coli* with Terminally Differentiated Human Urothelial Cells. *Infect Immun* 74, 750–757.
- Song, J., Duncan, M.J., Li, G., Chan, C., Grady, R., Stapleton, A., and Abraham, S.N. (2007). A Novel TLR4-Mediated Signaling Pathway Leading to IL-6 Responses in Human Bladder Epithelial Cells. *Plos Pathog* 3, e60.
- Stucki, A.O., Stucki, J.D., Hall, S.R.R., Felder, M., Mermoud, Y., Schmid, R.A., Geiser, T., and Guenat, O.T. (2014). A lung-on-a-chip array with an integrated bio-inspired respiration mechanism. *Lab Chip* 15, 1302–1310.
- Subashchandrabose, S., Hazen, T.H., Brumbaugh, A.R., Himpsl, S.D., Smith, S.N., Ernst, R.D., Rasko, D.A., and Mobley, H.L.T. (2014). Host-specific induction of *Escherichia coli* fitness genes during human urinary tract infection. *P Natl Acad Sci Usa* 111, 18327–18332.
- Sundac, L., Dando, S.J., Sullivan, M.J., Derrington, P., Gerrard, J., and Ulett, G.C. (2016). Protein-based profiling of the immune response to uropathogenic *Escherichia coli* in adult patients immediately following hospital admission for acute cystitis. *Pathog Dis* 74, ftw062.
- Takebe, T., Sekine, K., Enomura, M., Koike, H., Kimura, M., Ogaeri, T., Zhang, R.-R., Ueno, Y., Zheng, Y.-W., Koike, N., et al. (2013). Vascularized and functional human liver from an iPSC-derived organ bud transplant. *Nature* 499, 481–484.
- Takebe, T., Zhang, B., and Radisic, M. (2017). Synergistic Engineering: Organoids Meet Organ-on-a-Chip. *Cell Stem Cell* 21, 297–300.
- Tandan, M., Duane, S., Cormican, M., Murphy, A.W., and Vellinga, A. (2016). Reconsultation and Antimicrobial Treatment of Urinary Tract Infection in Male and Female Patients in General Practice. *Antibiotics* 5, 31.
- Thomas, W.E., Trintchina, E., Forero, M., Vogel, V., and Sokurenko, E.V. (2002). Bacterial Adhesion to Target Cells Enhanced by Shear Force. *Cell* 109, 913–923.
- Toniolo, C., Rutschmann, O., and McKinney, J.D. (2021). Do chance encounters between heterogeneous cells shape the outcome of tuberculosis infections? *Curr Opin Microbiol* 59, 72–78.
- Trietsch, S.J., Naumovska, E., Kurek, D., Setyawati, M.C., Vormann, M.K., Wilschut, K.J., Lanz, H.L., Nicolas, A., Ng, C.P., Joore, J., et al. (2017). Membrane-free culture and real-time barrier integrity assessment of perfused intestinal epithelium tubes. *Nat Commun* 8, 262.

- Truschel, S.T., Wang, E., Ruiz, W.G., Leung, S.-M., Rojas, R., Lavelle, J., Zeidel, M., Stoffer, D., and Apodaca, G. (2002). Stretch-regulated Exocytosis/Endocytosis in Bladder Umbrella Cells. *Mol Biol Cell* 13, 830–846.
- Uderhardt, S., Martins, A.J., Tsang, J.S., Lämmermann, T., and Germain, R.N. (2019). Resident Macrophages Cloak Tissue Microlesions to Prevent Neutrophil-Driven Inflammatory Damage. *Cell* 177, 541–555.e17.
- Urban, C.F., Reichard, U., Brinkmann, V., and Zychlinsky, A. (2006). Neutrophil extracellular traps capture and kill *Candida albicans* yeast and hyphal forms. *Cell Microbiol* 8, 668–676.
- Veras, F.P., Pontelli, M.C., Silva, C.M., Toller-Kawahisa, J.E., Lima, M. de, Nascimento, D.C., Schneider, A.H., Caetité, D., Tavares, L.A., Paiva, I.M., et al. (2020). SARS-CoV-2–triggered neutrophil extracellular traps mediate COVID-19 pathology. *J Exp Med* 217.
- Waite, J.C., Leiner, I., Lauer, P., Rae, C.S., Barbet, G., Zheng, H., Portnoy, D.A., Pamer, E.G., and Dustin, M.L. (2011). Dynamic Imaging of the Effector Immune Response to *Listeria* Infection In Vivo. *Plos Pathog* 7, e1001326.
- Wakamoto, Y., Dhar, N., Chait, R., Schneider, K., Signorino-Gelo, F., Leibler, S., and McKinney, J.D. (2013). Dynamic Persistence of Antibiotic-Stressed *Mycobacteria*. *Science* 339, 91–95.
- Wang, Y., Gunasekara, D.B., Reed, M.I., DiSalvo, M., Bultman, S.J., Sims, C.E., Magness, S.T., and Allbritton, N.L. (2017). A microengineered collagen scaffold for generating a polarized crypt-villus architecture of human small intestinal epithelium. *Biomaterials* 128, 44–55.
- Weber, E.J., Chapron, A., Chapron, B.D., Voellinger, J.L., Lidberg, K.A., Yeung, C.K., Wang, Z., Yamaura, Y., Hailey, D.W., Neumann, T., et al. (2016). Development of a microphysiological model of human kidney proximal tubule function. *Kidney Int* 90, 627–637.
- WHO (2020). Global tuberculosis report (World Health Organization).
- Wiles, T.J., Kulesus, R.R., and Mulvey, M.A. (2008). Origins and virulence mechanisms of uropathogenic *Escherichia coli*. *Exp Mol Pathol* 85, 11–19.
- Wistrand-Yuen, E., Knopp, M., Hjort, K., Koskiniemi, S., Berg, O.G., and Andersson, D.I. (2018). Evolution of high-level resistance during low-level antibiotic exposure. *Nat Commun* 9, 1599.
- Yang, E., Chee, J.L.Y., Duraiswamy, S., Chen, S., Lees, K., and Chen, S.L. (2019). Isolation of Single Intracellular Bacterial Communities Generated from a Murine Model of Urinary Tract Infection for Downstream Single-cell Analysis. *J Vis Exp Jove*.
- Yipp, B.G., Petri, B., Salina, D., Jenne, C.N., Scott, B.N.V., Zbytnuik, L.D., Pittman, K., Asaduz-zaman, M., Wu, K., Meijndert, H.C., et al. (2012). Infection-induced NETosis is a dynamic process involving neutrophil multitasking in vivo. *Nat Med* 18, 1386–1393.
- Yousefi, S., Mihalache, C., Kozłowski, E., Schmid, I., and Simon, H.U. (2009). Viable neutrophils release mitochondrial DNA to form neutrophil extracellular traps. *Cell Death Differ* 16, 1438–1444.
- Yu, W. (2007). Umbrella cell mechanotransduction and stretch-regulated exocytosis/endocytosis.

- Yu, L., O'Brien, V.P., Livny, J., Dorsey, D., Bandyopadhyay, N., Colonna, M., Caparon, M.G., Roberson, E.D., Hultgren, S.J., and Hannan, T.J. (2019). Mucosal infection rewires TNF α signaling dynamics to skew susceptibility to recurrence. *Elife* 8, e46677.
- Zang, R., Castro, M.F.G., McCune, B.T., Zeng, Q., Rothlauf, P.W., Sonnek, N.M., Liu, Z., Brulois, K.F., Wang, X., Greenberg, H.B., et al. (2020). TMPRSS2 and TMPRSS4 promote SARS-CoV-2 infection of human small intestinal enterocytes. *Sci Immunol* 5, eabc3582.
- Zhang, H., and Chiao, M. (2015). Anti-fouling Coatings of Poly(dimethylsiloxane) Devices for Biological and Biomedical Applications. *J Med Biol Eng* 35, 143–155.
- Zhang, B., Hirahashi, J., Cullere, X., and Mayadas, T.N. (2003). Elucidation of Molecular Events Leading to Neutrophil Apoptosis following Phagocytosis CROSS-TALK BETWEEN CASPASE 8, REACTIVE OXYGEN SPECIES, AND MAPK/ERK ACTIVATION. *J Biol Chem* 278, 28443–28454.
- Zhang, B., Montgomery, M., Chamberlain, M.D., Ogawa, S., Korolj, A., Pahnke, A., Wells, L.A., Massé, S., Kim, J., Reis, L., et al. (2016). Biodegradable scaffold with built-in vasculature for organ-on-a-chip engineering and direct surgical anastomosis. *Nat Mater* 15, 669–678.
- Zhang, B., Korolj, A., Lai, B.F.L., and Radisic, M. (2018). Advances in organ-on-a-chip engineering. *Nat Rev Mater* 3, 257–278.
- Zheng, Y., Chen, J., Craven, M., Choi, N.W., Totorica, S., Diaz-Santana, A., Kermani, P., Hempstead, B., Fischbach-Teschl, C., López, J.A., et al. (2012). In vitro microvessels for the study of angiogenesis and thrombosis. *Proc National Acad Sci* 109, 9342–9347.
- Zheng, Y., Chen, J., and López, J.A. (2015). Flow-driven assembly of VWF fibres and webs in in vitro microvessels. *Nat Commun* 6, 7858.
- Zhou, J., Li, C., Sachs, N., Chiu, M.C., Wong, B.H.-Y., Chu, H., Poon, V.K.-M., Wang, D., Zhao, X., Wen, L., et al. (2018). Differentiated human airway organoids to assess infectivity of emerging influenza virus. *P Natl Acad Sci Usa* 115, 6822–6827.
- Zhou, J., Li, C., Liu, X., Chiu, M.C., Zhao, X., Wang, D., Wei, Y., Lee, A., Zhang, A.J., Chu, H., et al. (2020). Infection of bat and human intestinal organoids by SARS-CoV-2. *Nat Med* 26, 1077–1083.
- Zhou, M., Ma, H., Lin, H., and Qin, J. (2013). Induction of epithelial-to-mesenchymal transition in proximal tubular epithelial cells on microfluidic devices. *Biomaterials* 35, 1390–1401.
- Zhou, M., Zhang, X., Wen, X., Wu, T., Wang, W., Yang, M., Wang, J., Fang, M., Lin, B., and Lin, H. (2016). Development of a Functional Glomerulus at the Organ Level on a Chip to Mimic Hypertensive Nephropathy. *Sci Rep-Uk* 6, 31771.
- Zhu, N., Zhang, D., Wang, W., Li, X., Yang, B., Song, J., Zhao, X., Huang, B., Shi, W., Lu, R., et al. (2020). A Novel Coronavirus from Patients with Pneumonia in China, 2019. *New Engl J Med* 382, 727–733.

Chapter 2. Bladder organoids as a model system for studying UPEC pathogenesis

Invasion of uropathogenic *Escherichia coli* into the bladder wall generates solitary subpopulations that are protected from killing by antibiotics and neutrophil swarms in an organoid model

Authors: Kunal Sharma¹, Vivek V. Thacker^{1, *#}, Neeraj Dhar^{1*#}, François Signorino-Gelo¹, Maria Clapés Cabrer¹, Anaëlle Dubois¹, Jasper Mullenders², Graham Knott¹, Hans Clevers², John D. McKinney^{1*}

Affiliations:

¹School of Life Sciences, Swiss Federal Institute of Technology in Lausanne (EPFL), 1015 Lausanne, Switzerland.

²Oncode Institute, Hubrecht Institute, Royal Netherlands Academy of Arts and Sciences and University Medical Center, Utrecht, Netherlands.

*Correspondence to: vivekvthacker@gmail.com, neeraj.dhar@epfl.ch, john.mckinney@epfl.ch

These authors contributed equally

2.1 Abstract

Uropathogenic *Escherichia coli* (UPEC) is the most common cause of urinary tract infections (UTIs) and require antibiotic therapy. Recurrent infections, which occur in a quarter of treated individuals, are thought to be caused by existence of intracellular reservoirs that subsequently reinitiate the infection cycle. Here, we present a novel bladder organoid model of UPEC infection that recapitulates the stratified bladder architecture within a small volume suitable for live-cell imaging of host-pathogen dynamics with high spatiotemporal resolution. We confirm that bacteria injected into the organoid lumen rapidly enter superficial epithelial cells and proliferate to form IBCs. We also identified individual “solitary” bacteria that penetrate deeper layers of the organoid wall, where they evade killing by antibiotics and neutrophils. Volumetric serial block face scanning electron microscopy of infected organoids reveals that solitary bacteria may be intracellular or pericellular (sandwiched between uroepithelial cells). Unlike bacteria within IBCs, which are coccoid-shaped and unflagellated, solitary bacteria are rod-shaped and flagellated. Through time-lapse imaging, we demonstrate that solitary bacteria in the bladder organoid wall form independently of IBCs. We conclude that bacterial fluxing from IBCs is not required for establishment of solitary bacterial subpopulations in the bladder wall that resist elimination by antibiotics and the host immune response.

Keywords: bladder organoids, uropathogenic *Escherichia coli* (UPEC), intracellular bacterial communities (IBCs), pericellular bacteria, bacterial persistence, antibiotic treatment, neutrophil swarms, live-cell imaging

2.2 Introduction

Urinary tract infections (UTIs) are among the most common bacterial infections and the second most-common cause for the prescription of antibiotics (Foxman, 2010). Although seldom fatal, UTIs substantially reduce the quality of life and incur enormous healthcare costs. Recurrence, defined as a appearance of 2 episodes of UTI in 6 months or 3 episodes of UTI in 12 months despite the apparently successful completion of antibiotic therapy, occurs in a quarter of all UTIs (Foxman et al., 2000). Women are at particularly high risk, and more than 60% of women will be diagnosed with a UTI at least once in their lifetime (Klein and Hultgren, 2020). Uropathogenic *Escherichia coli* (UPEC) is the causative agent of about 80% of all UTIs, which can be further complicated by dissemination of UPEC from the bladder (cystitis) to the kidneys (nephritis) or into the bloodstream (urosepsis).

Much of our current understanding of UPEC pathogenesis has been derived from experiments in mouse models of infection (Hannan and Hunstad, 2016; Hung et al., 2009), which reveal that UPEC can grow extracellularly in the urine within the bladder or intracellularly in the bladder wall. (Anderson et al., 2003; Justice et al., 2004; Mulvey et al., 2001). Invasion into the bladder wall is preceded by adherence of UPEC to the superficial epithelial cell layer of the bladder, mediated by interactions of the bacterial type I pilus with uroplakin proteins on the surface of the uroepithelium (Martinez et al., 2000; Mulvey et al., 1998). Following bacterial entry into umbrella cells, a subset of bacteria proliferates to form biofilm-like “intracellular bacterial communities” (IBCs) (Anderson et al., 2003; Justice et al., 2004; Mulvey et al., 2000) which may be refractory to clearance by antibiotic treatment or innate immune responses. At later stages of infection, UPEC has been shown to penetrate into deeper layers of the bladder to form “quiescent reservoirs” that may also be responsible for recurrent infection after antibiotic therapy (Mulvey et al., 2000, 2001; Mysorekar and Hultgren, 2006; Schilling et al., 2002). However, these isolated subpopulations have been difficult to characterize in bladder sections, and the relative contribution of IBCs and quiescent reservoirs in the persistence of infection remains unclear (Blango et al., 2014; Mulvey et al., 2001; Scott et al., 2015). The number of bacteria in these three distinct subpopulations (extracellular bacteria, IBCs, and quiescent reservoirs), their relative growth dynamics, and their persistence under attack from antibiotics or immune cells are difficult to characterize *in situ* in animal models. Most studies therefore rely on an examination of bladder explants at specified time points post-infection. However, this technique does not provide information on the underlying dynamics of host-pathogen interactions, nor does it permit the quantification of *in situ* growth of extracellular bacteria (Anderson et al., 2003; Justice et al., 2004). *In vitro* models have been developed to probe specific aspects of UPEC infection, such as the role of the stratified bladder architecture (Horsley et al., 2018) or the effects of micturition on IBC formation (Andersen et al., 2012; Iosifidis and Duggin, 2020). However, these models suffer from limitations in their ability to recreate a stratified epithelium with multiple differentiated cell layers (Andersen et al., 2012) or to reproduce the migration of immune cells into the bladder in response to infection (Horsley et al., 2018). In many of these systems, live-cell imaging remains technically challenging (Horsley et al., 2018; Smith et al., 2006).

In the last decade, organoids have emerged as experimentally tractable biomimetics that recapitulate key physiological and functional features of the cognate organs (Clevers, 2016). These complex 3D multicellular structures are generated from stem cells or organ-specific progenitor cells (Rossi et al., 2018) and have now been established for a number of different organs (Liu et al., 2004; Sachs et al., 2019), including the bladder (Lee et al., 2018b; Mullenders et al., 2019). Recently, organoids have

also emerged as model systems to study host-pathogen interactions during infections caused by bacteria (Bartfeld and Clevers, 2015; Co et al., 2019; Kessler et al., 2019; Pleguezuelos-Manzano et al., 2020; Williamson et al., 2018), viruses (Qian et al., 2017; Sanden et al., 2018; Zhou et al., 2018), or parasites (Heo et al., 2018; Nikolaev et al., 2020).

Bladder organoids offer several distinct advantages as model systems for UTIs. They recapitulate the stratified and differentiated layers of the uroepithelium, possess a lumen that mimics the bladder lumen, and are easier to manipulate than whole-animal infection models. Importantly, the compact volume of individual organoids can be imaged in its entirety with high spatiotemporal resolution using time-lapse confocal microscopy. This makes it possible to follow the rapidly changing dynamics of UTIs and to monitor the responses of host cells and bacterial cell to external perturbations, such as a defined course of antibiotic treatment or the addition of innate immune cells (Neal et al., 2018; Sachs et al., 2019). Compared to conventional *ex vivo* tissue explants (Justice et al., 2004) or *in vitro* infection models (Andersen et al., 2012; Iosifidis and Duggin, 2020), bladder organoids offer a more realistic reconstitution of bladder physiology that is accessible to a wider range of experimental techniques for studies of UPEC pathogenesis.

Here, we establish a new model system to study the early dynamics of UPEC pathogenesis based on recently developed mouse bladder organoids derived from primary cells (Mullenders et al., 2019). We use a combination of time-lapse laser scanning confocal microscopy and serial block face scanning electron microscopy (SBEM) to monitor the dispersal, death, and morphology of UPEC within the bladder organoid lumen and wall in response to attack by antibiotics or host neutrophils with single-cell, sub-micron resolution. We find that isolated “solitary” bacteria are seeded in deeper layers of the bladder epithelium concomitantly with but independently of the formation of IBCs in the superficial umbrella-like cells. Our observations suggest that early invasion of bacteria into the bladder wall may play a more diverse and important role in recurrent infections than was previously assumed.

2.3 Results

2.3.1 Establishment of differentiated mouse bladder organoids

We generated mouse bladder organoids from C57BL/6 wild-type (WT) or mT/mG mice (Muzumdar et al., 2007), which express the red-fluorescent protein tdTomato within cell membranes, following the procedure of Mullenders *et al.*, [Figure 2.1A](#)) (Mullenders et al., 2019). Briefly, mouse bladders were isolated *ex vivo* and epithelial cells extracted from the bladder lumen were cultured in basement membrane extract to generate organoids over a period of 2-3 weeks ([Figure 2.1A](#)). We verified that

these organoids recapitulate the different layers of the stratified mouse uroepithelium by comparative immunofluorescence staining of bladder organoids and explanted mouse bladders. Staining with antibodies directed against uroplakin-3a (UP3a) or cytokeratin 8 (CK8) confirmed the presence of superficial umbrella like-cells in bladder organoids ([Figure 2.1B](#)) and mouse bladder tissue ([Figure 2.1C](#)). CK8 expression was higher in umbrella cells compared to the underlying intermediate and basal cells, as expected (Southgate et al., 1994). The presence of intermediate and basal cell layers in the bladder organoids was confirmed by staining with antibodies directed against cytokeratin 13 (CK13) ([Figure 2.1B, C](#)), p63 ([Figure 2.7](#)), or cytokeratin 7 (CK7) ([Figure 2.7](#)). Bladder organoids therefore recapitulate the stratified architecture of the mouse uroepithelium with high levels of uroplakin expression in the umbrella cell layer, which is important for UPEC adherence and invasion mediated by type I pili (Mulvey et al., 1998).

2.3.2 Invasion of UPEC into the bladder wall provides protection against antibiotics

Intravital imaging of antibiotic treatment and recovery in the infected bladder is extremely challenging (Justice et al., 2004, 2006). We therefore modelled the acute phase of a UTI by microinjecting UPEC expressing yellow fluorescent protein (YFP) into the lumen of individual bladder organoids, which mimics the natural route of infection through the urethra ([Figure 2.2A](#)). The infection cycle was modelled in three stages: stage one (0-165 minutes), an initial period of unimpeded bacterial proliferation; stage two (165-345 minutes), treatment with ampicillin at ten-fold the minimum inhibitory concentration (10X-MIC); stage three (345-525 minutes), bacterial recovery after ampicillin washout. Snapshots from time-lapse imaging of two infected organoids are shown in [Figure 2.2B-E](#) (see [supplementary movie SMov1](#)) and [Figure 2.2F-I](#) (see [supplementary movie SMov2](#)); an additional example is shown in [Figure 2.8A](#) (see [supplementary movie SMov3](#)). Rapid bacterial growth within the organoid is observed soon after microinjection ([Figure 2.2B, C](#) and [Figure 2.2F, G](#)), predominantly within the lumen (indicated by a yellow arrowhead in [Figure 2.2B](#)). As in UTI infections in humans and in animal models of UTI, bacterial growth over time leads to a gradual exfoliation of umbrella cells, as indicated by reduced CK8 levels (cf. [Figure 2.9C](#) and controls in [Figure 2.9A](#)), while the overall structure of the organoid is relatively unaffected (cf. [Figure 2.9D](#) and [Figure 2.9B](#)).

Addition of 10X-MIC ampicillin (64.5 µg/ml, [Figure 2.8C](#)) into the medium surrounding the organoids rapidly reduces the bacterial volume within the organoid ([Figure 2.2D, H](#)), consistent with the bactericidal nature of the antibiotic. In most cases, bacterial growth resumed only after the removal of the antibiotic ([Figure 2.2E](#)). Unexpectedly, in two out of the 124 organoids studied, bacterial growth resumed even in the presence of the antibiotic ([Figure 2.2I](#)). A time-profile for the growth

kinetics of UPEC within the organoids is shown in [Figure 2.2J](#) and captures these two different behaviors in the presence of antibiotic. A plot of bacterial volume over time within infected organoids during the growth phase confirms that growth is exponential ([Figure 2.2K](#)) with a median growth rate of 0.017 min^{-1} ([Figure 2.2M](#)), corresponding to a doubling time of 41.5 min, in agreement with measurements of growth in the mouse bladder (Justice et al., 2004; Scott et al., 2015). During ampicillin treatment, the bacterial volume initially increases before plateauing due to filamentation of the bacteria, consistent with the mode of action of ampicillin ([Figure 2.2L](#)). Both the fluorescence intensity and the intra-organoid bacterial volume subsequently decline, with a median killing rate of 0.019 min^{-1} ([Figure 2.8D](#)). Compared to growth before ampicillin treatment, regrowth after ampicillin washout is significantly slower, with a median growth rate of 0.003 min^{-1} , corresponding to a doubling time of 226.8 min ([Figure 2.2M](#)).

Interestingly, the spatial distribution of bacterial regrowth after ampicillin washout is very different from the luminal growth observed after microinjection (cf. [Figure 2.2E](#) vs [Figure 2.2B, C](#) and [Figure 2.2I](#) vs [Figure 2.2F, G](#)) and is localized to the bladder wall. These results suggest that, whereas the lumen or bladder volume may be the preferred site of growth prior to antibiotic exposure, the bladder wall offers a more protective niche for bacterial survival and regrowth after antibiotic treatment. The small volume of the organoid model allows us to quantify the dynamics of bacterial growth in both these niches (lumen and bladder wall) simultaneously before, during, and after antibiotic treatment.

2.3.3 Neutrophils swarm towards intra-organoid UPEC with three distinct migratory profiles

Organoids are powerful systems to study immune cell responses *in situ* (Nikolaev et al., 2020; Sachs et al., 2019; Yuki et al., 2020), and, in conjunction with long-term live-cell imaging, can be used to visualize the spatiotemporal dynamics of immune cell responses. Peripheral innate immune cells such as neutrophils have been shown to be the first responders in the early phases of bladder infection in the mouse model (Haraoka et al., 1999). We therefore added murine bone marrow-derived neutrophils to the collagen matrix surrounding bladder organoids immediately after microinjection of the organoid lumen with UPEC. Neutrophils were pre-labeled with a CellTracker™ dye to enable identification. Live-cell imaging revealed three distinct patterns of neutrophil dynamics (see [supplementary movie SMov4, SMov5, SMov6](#)). In most cases, neutrophils surrounding an infected organoid migrate towards and accumulate in the lumen, forming aggregates or swarms ([Figure 2.3A1-A3, Figure 2.3B1-B3](#)). Neutrophil migration into the organoid lumen is consistently accompanied by a sharp reduction in bacterial volume ([Figure 2.3A2-A5, Figure 2.3B2-B5, Figure 2.3C2-C5](#)). In some cases,

the neutrophil swarms remain within the lumen for >30 minutes (Figure 2.3A3-A5), characteristic of *persistent swarms* (Kienle and Lämmermann, 2016; Lämmermann et al., 2013). In other cases, the swarm rapidly disaggregates after clearance of bacteria within the organoid (Figure 2.3B3-B5), characteristic of *transient swarms*. In a third category, large intra-organoid aggregates of neutrophils do not form; rather, neutrophil numbers within the organoid fluctuate in response to bacterial numbers. We classified this third category, with fluctuating neutrophil numbers inside the infected organoid, as *dynamic swarms* (Hopke et al., 2020). Additional examples for each type of migratory behaviour are shown in Figure 2.11A-C (see [supplementary movies SMov7, SMov8, SMov9](#)).

Additional verification of the inward migration of neutrophils is afforded by an examination of the shapes of these cells; neutrophils surrounding the organoid are predominantly spherical in shape, whereas migratory neutrophils adopt elongated shapes (Figure 2.12C). Importantly, neutrophils do not migrate towards uninfected “bystander” organoids, as shown in Figure 2.3A, B (colored red), which confirms that neutrophils can discriminate between uninfected and infected organoids and direct their movement specifically towards infected organoids.

These neutrophil dynamics are better understood from time profiles of the neutrophil volume within the organoid (amber), the neutrophil volume surrounding the organoid (blue), and the intra-organoid bacterial volume (green), each normalized by the maximum value attained over the time period of the experiment. Data for each parameter are shown in Figure 2.3D-F, corresponding to Figure 2.3A1-A5, Figure 2.3B1-B5, and Figure 2.3C1-C5, respectively; absolute numbers are shown in Figure 2.10 and Figure 2.11D-I. Infection of bladder organoids therefore successfully reproduces the range of neutrophil migratory responses reported from intravital imaging studies, and bacteria within the lumen are effectively cleared by neutrophils independent of their migratory profile.

2.3.4 Bacteria within the wall of the bladder organoid are refractory to clearance by neutrophils

The rapid clearance of luminal bacteria by migratory neutrophils provides an opportunity to observe niches where bacteria may be protected from neutrophil attacks, such as intracellular bacterial communities (IBCs) (Justice et al., 2004). We observed IBCs in a subset of infected organoids, reinforcing the validity of the organoid model. Figure 2.4A1-A3 shows an example of an IBC that forms and persists despite the presence of a persistent swarm of neutrophils within the organoid that successfully clears the bacteria from the organoid lumen. Live-cell imaging revealed the IBC to be a dynamic, fluctuating structure; for example, in the 15-minute interval between Figure 2.4A3 and Figure 2.4A4

(see [supplementary movie SMov10](#)), the IBC begins to shed bacteria, which are rapidly taken up by nearby neutrophils. The vast majority of the bacteria released from the IBC are processed and killed within 30 minutes, as evidenced by loss of YFP fluorescence ([Figure 2.4A5](#)). In contrast, [Figure 2.4B1-B5](#) (see [supplementary movie SMov11](#)) shows another example of an IBC that forms in the presence of a persistent neutrophil swarm (white arrowhead, [Figure 2.4B1-B2](#)), but in this case the bacteria shed from the IBC are spread by the neutrophils to different regions of the bladder epithelium ([Figure 2.4B3-B4](#), cyan arrowheads). Some of these bacteria persist as isolated bacteria within the organoid wall and resist clearance by neutrophils (cyan arrowheads, [Figure 2.4B5](#)).

Unexpectedly, at early time points we also identified spatially isolated subpopulations of bacteria, comprising individual cells or small clusters (threshold of detection set at $10\ \mu\text{m}^3$), located within the organoid wall (yellow arrowheads, [Figure 2.4B1](#)). Hereafter, we refer to these subpopulations as “solitary” bacteria to distinguish them from “communal” bacteria within IBCs. The high spatiotemporal resolution afforded by confocal imaging allowed us to track three such examples, labelled ‘1’ through ‘3’, over the entire course of the time series shown in [Figure 2.4B1-5](#). Our results confirm that solitary bacteria are located within the organoid wall throughout and are refractory to neutrophil-mediated clearance ([Figure 2.4B5](#), yellow arrowheads and corresponding labels). The number of solitary bacteria was enhanced by the addition of some of the bacteria shed by the IBC (cyan arrowheads in [Figure 2.4B5](#)). Even 15 hours after addition of neutrophils, solitary bacteria persist within some organoids ([Figure 2.4C3-C4](#), [Figure 2.3C](#) and analysis in [Figure 2.3D](#), [Figure 2.3F](#), [Figure 2.10C](#), [Figure 2.11D](#) and [Figure 2.11G](#)), whereas other organoids are successfully sterilized by the neutrophils ([Figure 2.4C1-C2](#), and analysis in [Figure 2.3E](#), [Figure 2.10B](#) and [Figure 2.11E-I](#)). These two outcomes (persistence and sterilization) occur with roughly equal frequency ([Figure 2.4D](#)). Live-cell imaging confirmed that bacteria shed from IBCs contribute only a small portion of these persistent bacteria.

These results demonstrate that niches within the deeper layers of the bladder epithelium, below the superficial umbrella cells containing IBCs, can also harbor subpopulations of bacteria that are resistant to clearance by antibiotics or neutrophils. In the latter case, bacterial persistence is independent of the migratory profile of the neutrophil swarm ([Figure 2.4C3, C4](#)). We attempted to localize these persistent bacteria with greater precision, but the spatial resolution of confocal microscopy proved to be insufficient to identify unambiguously the boundaries of the bladder lumen and the precise location of individual bacteria within the organoid wall. We therefore imaged infected organoids using electron microscopy, which provides much higher spatial resolution than optical microscopy.

2.3.5 Volumetric electron microscopy reveals five distinct bacterial niches within infected organoids

Technical developments in scanning electron microscopy now permit volumetric imaging of large samples using serial block face scanning electron microscopy (SBEM) (Denk and Horstmann, 2004; Hoffman et al., 2020; Maclachlan et al., 2018). High-contrast staining used for the preparation of SBEM samples densely labels cell membranes, which is useful for localizing bacteria within tissue. We used this imaging method to capture an entire infected organoid at ca. 6 hours after microinjection of UPEC and addition of neutrophils. The organoid was imaged with optical microscopy (Figure 2.13A, B) prior to staining and resin embedding. It was then mounted inside the scanning electron microscope and serial images of the entire structure were collected at a lateral resolution of 30 nm with 100 nm sections separating each image. The imaging parameters allowed us to identify cell membranes and to localize all bacteria in the organoid. In addition, the light microscopy imaging prior to embedding provided a 3D map of the organoid in which we could identify fluorescently labelled cells such as neutrophils in the final EM image series. We identified a total of 2,938 bacteria and classified them into five distinct subpopulations according to their locations within the organoid (Figure 2.5A-E, see supplementary movie SMov12).

The majority (62%, n=1,821) of bacteria are extracellular and located within the organoid lumen (Figure 2.5A). Smaller bacterial fractions are located either as solitary bacteria within the cytoplasm of bladder epithelial cells (3.8%, n=111) or within the IBC (13.5%, n=398) (Figure 2.5C, D). The small fraction of bacteria located within neutrophils (4.8%, n=141) is probably an underestimate, since bacteria are typically degraded after phagocytic uptake (Figure 2.5B). Bacteria within the neutrophils have an altered morphology, likely due to exposure to antimicrobial stresses within the neutrophil. Unexpectedly, we identified a fifth subpopulation of solitary bacteria, which we term “pericellular” (15.9%, n=467), that is located in between bladder epithelial cells within the organoid wall (Figure 2.5E). To the best of our knowledge, this pericellular subpopulation of solitary bacteria has not been reported previously, presumably due to the difficulty of whole-bladder imaging with sufficient spatial resolution to identify individual bacteria located between host cell membranes.

A view inside a model of the organoid, created from a 3D map of coordinates of all cells and bacteria, shows the arrangement of the different bacterial classes inside (Figure 2.5F). The bacterial population within the irregularly shaped lumen clusters towards the first quadrant (zoom in Figure 2.5G), likely

indicating the site of injection. Intracellular and pericellular solitary bacteria can be found scattered throughout all areas of the organoid wall (evident in zoom in [Figure 2.5H](#)). Individual neutrophils can be observed in all areas of the organoid wall as well as the lumen ([Figure 2.5H](#)), and some of these neutrophils contain numerous bacteria ([Figure 2.13C](#)). Bacteria within the IBC form a tight cluster below the nucleus of the cell hosting the IBC ([Figure 2.5F](#)). The protection against phagocytic uptake conferred by intracellular localization is evident from the fact that the IBC remains intact despite the infected cell being surrounded by multiple neutrophils. A plot of the shortest distance of each subpopulation to the organoid lumen is shown in [Figure 2.5J](#). It is noteworthy that intracellular and pericellular solitary bacteria are found within the deeper layers of the organoid that express intermediate and basal cell markers ([Figure 2.1C](#)).

We asked whether the intracellular and pericellular solitary subpopulations are phenotypically different from bacteria in the organoid lumen. UPEC has been shown to markedly alter flagellar expression and cell shape during bladder infection (Anderson et al., 2004; Lane et al., 2007; Wright et al., 2007). We therefore used immunofluorescence to probe flagellin expression *in situ*. Because paraformaldehyde fixation tends to degrade the signal of bacterial YFP, we used immunostaining against lipopolysaccharide (LPS) and a mask of the organoid shape to label intra-organoid bacteria (cyan) and bacteria surrounding the organoid (green) in [Figure 2.6A](#). The corresponding image with anti-flagellin immunostaining ([Figure 2.6B](#)) shows that a majority of intra-organoid bacteria have low or no detectable flagellin expression. We applied a threshold on the basis of volume to the intra-organoid bacteria clumps and found that large bacterial clumps (volume greater than $1,000\ \mu\text{m}^3$) express very low flagellin levels ([Figure 2.6D](#)), whereas smaller clusters (volume smaller than $1,000\ \mu\text{m}^3$) and individual bacteria retain intermediate to high levels of flagellin expression ([Figure 2.6C](#), [Figure 2.13B](#)). Thus, bacteria that continue to express flagellin are predominantly single cells or small clusters located within the organoid wall; both observations suggest that these subpopulations correspond to the intracellular or pericellular subpopulations of solitary bacteria identified in serial electron micrographs. This point is strengthened by our observation that bacteria within the IBC have severely reduced flagellar expression (Wright et al., 2007), whereas single bacteria surrounding the IBC retain high-level flagellar expression ([Figure 2.6E](#)).

Scanning electron microscopy (SEM) is a powerful technique to examine surface morphology and overall bacterial shape. We ruptured open an infected organoid using a tungsten needle (Heo et al., 2018) at ca. 6 hours after microinjection with UPEC to gain access to the interior of the organoid ([Figure 2.6F](#)). We found that the majority of bacteria accessible to SEM imaging are located within

tight clusters, suggestive of IBC growth (Figure 2.6G, H). These bacteria are coccoid in shape and are not flagellated (Figure 2.6H), consistent with previous findings (Anderson et al., 2003; Justice et al., 2004). In contrast, we identified a small subpopulation of bacteria in a different spatial location within the organoid that retain flagellar expression (Figure 2.6I, J). These observations are consistent with data in Figure 2.6C, D. We verified that bacteria from a stationary-phase axenic culture retain flagellin expression (Figure 2.6K) and are longer than the coccoid bacteria within IBCs (Figure 2.6L). The bladder organoid model is therefore able to recapitulate characteristic morphological features of bacteria within IBCs. It also reveals that the bladder wall comprises distinct niches, including some in which the bacteria are rod-shaped and retain flagellin expression. These observations highlight the utility of organoids as a tool to obtain a more comprehensive picture of UPEC phenotypic variants that arise in the course of infection.

2.4 Discussion

The mouse model of UPEC infection faithfully reproduces key features of UPEC infections in humans (reviewed in Flores-Mireles *et al.* (Flores-Mireles et al., 2015) and Hung *et al.* (Hung et al., 2009)), but this model is not well suited for live-cell imaging with high spatiotemporal resolution. There is also a paucity of tractable *in vitro* models that capture the complex 3D stratified architecture of the bladder wall and key features of the UPEC pathogenesis cycle, such as bacterial persistence and regrowth after antibiotic treatment. In an early *in vitro* model, Smith *et al.*, (Smith et al., 2006) reported that a human cancer cell line could be induced to establish stratified uroepithelial layers on collagen beads by exposure to shear stress. This model lacks a lumen where bacteria can be introduced in a topologically correct manner. Andersen *et al.* (Andersen et al., 2012; Iosifidis and Duggin, 2020) developed a model in which a virus-immortalized human bladder cell line is cultured under flow to mimic micturition, but this model does not include a stratified uroepithelium or the ability to introduce additional cell components, such as immune cells. More recently, Horsley et al (Horsley et al., 2018) stratified primary human uroepithelial cells on Transwell® inserts, although stratification is non-uniform and it is difficult to reproduce immune cell dynamics or track them using live-cell imaging in this model. Other stratified bladder epithelium models have been reported (Cattan et al., 2011; Chabaud et al., 2017; Suzuki et al., 2019), however to the best of our knowledge, none of these models has been adapted for infection studies.

Here, we show that bladder organoids embedded in a collagen matrix fulfill all these requirements: the ability to simultaneously track bacterial growth dynamics within the organoid wall and in a central lumen that mimics the bladder volume; the ability to add and remove soluble compounds, which we

exploit here for real-time studies of bacterial responses to antibiotic treatment; and the ability to study immune cell migration into the organoids in response to infection. Organoids are amenable to long-term live-cell imaging and offer significantly higher throughput and lower costs than the mouse model, as well as the flexibility to combine different cell types, such as uroepithelial cells and immune cells derived from different strains of genetically modified mice. These combinations are not possible in simple monolayer systems (Andersen et al., 2012; Iosifidis and Duggin, 2020), in previous complex stratified systems (Horsley et al., 2018; Smith et al., 2006), or in experiments with extracted bladder tissue (Justice et al., 2004, 2006).

We leverage these advantages to demonstrate that whereas the bladder organoid lumen is the predominant site of bacterial replication, it is the simultaneous presence of bacteria within the organoid wall that enables infection to resist clearance by antibiotics and neutrophils. Prior to antibiotic treatment, rapid growth of bacteria in the organoid lumen predominates, although widely scattered invasion of bacteria into the bladder wall occurs at the same time. Some of the invading bacteria take up residence within the superficial umbrella-like cells abutting the organoid lumen, where they replicate intracellularly to form IBCs, while others invade into deeper layers of the organoid wall. In contrast to bacteria within IBCs – which are communal, unflagellated, coccoid-shaped, and intracellular, we find that bacteria that invade into deeper layers of the organoid wall are solitary, flagellated, rod-shaped, and may be intracellular or pericellular. Following antibiotic washout, the spatial pattern of bacterial growth is reversed, occurring at scattered sites throughout the organoid wall but only rarely within the lumen; also, regrowth in the organoid wall after antibiotic treatment is significantly slower than growth in the organoid lumen prior to treatment. In rare cases, we found that bacteria within the organoid wall continue to divide even in the presence of antibiotic. This observation could reflect a niche within the organoid wall where antibiotic penetration is poor, emergence of spontaneous antibiotic resistance, or the fact that bacterial responses to antibiotics are heterogeneous and dynamic and may, in some cases, involve balanced division and death (Wakamoto et al., 2013). These dynamic and transient phenotypes are impossible to capture in mouse models or using conventional static measurements of bacterial numbers such as colony forming units. We conclude that early invasion of solitary bacteria into deep layers of the bladder wall, concomitant with invasion of superficial umbrella-like cells and IBC formation, may play an important role in bacterial persistence and relapse following antibiotic treatment.

We observed similar spatially distinct dynamics for bacterial killing by neutrophils. The small volume and spherically symmetric geometry of the organoid model allowed us to capture neutrophil migration

dynamics in a quantitative fashion that is difficult to achieve with other systems. We found that UPEC infection of organoids generates a strong and highly directed neutrophil migration response, with three distinct spatiotemporal patterns (persistent, transient, or dynamic) that are reminiscent of descriptions based on intravital imaging of neutrophil responses to bacterial infections (Kienle and Lämmermann, 2016; Lämmermann et al., 2013; Liese et al., 2012; Shannon et al., 2013). We also found that neutrophils migrate out of the lumen of bladder organoids after resolving infection. Regardless of the neutrophil migration pattern, about half of the organoids that we studied were not completely sterilized by neutrophils even after many hours; in a majority of the cases, bacterial survival was restricted to the organoid wall while luminal bacteria were sterilized. Although both IBCs in superficial umbrella-like cells and solitary bacteria within deeper layers of the organoid wall appear to be relatively refractory to clearance by neutrophils, we found that the bacteria released when IBCs rupture are rapidly taken up and destroyed by patrolling neutrophils. In a subset of organoids where we did not detect any IBCs, solitary bacteria within deeper layers of the uroepithelium were solely responsible for survival during neutrophil attacks. These observations suggest that early and IBC-independent invasion of solitary bacteria into deeper layers of the bladder wall may play an important role in recurrent infections by generating a subpopulation that is refractory to clearance by the host innate immune response.

Solitary bacteria are phenotypically distinct from bacteria within IBCs, inasmuch as they remain rod-shaped and flagellated, whereas bacteria within IBCs are coccoid-shaped and unflagellated. The latter point is interesting because loss of flagellar expression within IBCs has been reported in the study (Wright et al., 2007), whereas flagellar expression has been shown to be important for generating persistent infections in the mouse bladder (Lane et al., 2007; Wright et al., 2007). Our findings suggest that unflagellated bacteria within IBCs and flagellated solitary bacteria seeded throughout deeper layers of the bladder wall may both contribute to survival during antibiotic treatment and neutrophil attacks. Given the relatively small numbers of solitary bacteria, it is unlikely that this subpopulation could be identified by transcriptomic analysis of the total bacterial population within the bladder or by cursory microscopic imaging of bladders from infected mice.

The small volume of the organoid lumen and the lack of bacterial clearance by micturition might accelerate the formation of IBCs relative to the mouse model. Even so, it is noteworthy that spatially distinct IBCs and solitary bacteria within the organoid wall both appear within hours of infection. This contrasts with the current model of UPEC persistence, which postulates that cycles of formation and rupture of IBCs, eventually resulting in exfoliation of superficial umbrella-like cells and exposure

of underlying layers of the stratified epithelium, are a necessary precursor to invasion of bacteria into deeper layers of the uroepithelium, where they generate “quiescent intracellular reservoirs” (Flores-Mireles et al., 2015). It is possible that solitary bacteria may eventually develop into quiescent intracellular reservoirs, but we did not test this possibility within the relatively short timescale of our experiments.

The dynamics of host-pathogen interactions during bladder infections are difficult to capture with high spatiotemporal resolution in conventional animal models. Bladder organoids, being miniaturized and experimentally tractable models of the bladder, are well suited to generate new insights into UPEC pathogenesis. Here, we use time-lapse optical microscopy and electron microscopy to demonstrate the existence of solitary subpopulations of intracellular and pericellular bacteria located within deeper layers of the stratified bladder organoid wall, beneath the superficial layer of umbrella-like cells. These solitary subpopulations appear early in the course of infection, concomitant with the formation of IBCs in the umbrella-cell layer, and they resist elimination by antibiotics and neutrophils. Thus, improved understanding of the physiology of solitary bacteria could contribute to the development of new strategies to eliminate persistent bladder infections.

2.5 Figures

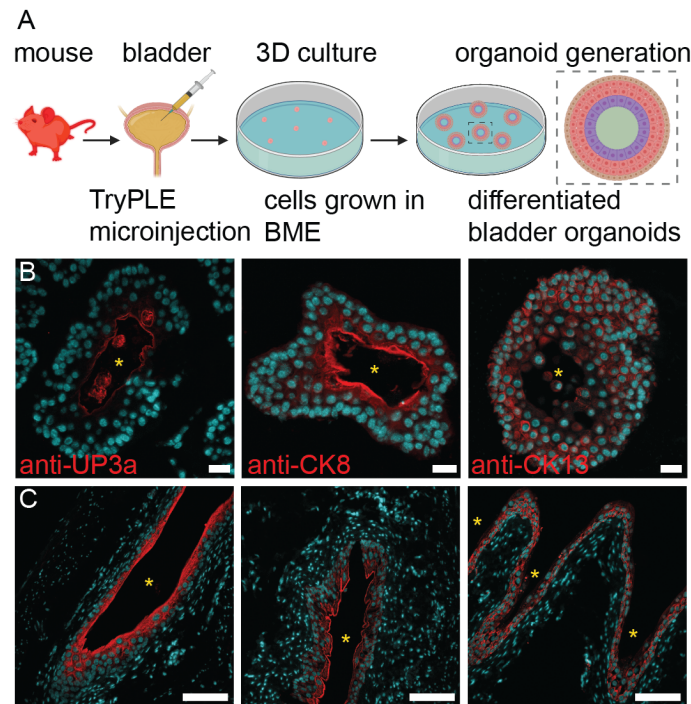


Figure 2.1: Mouse bladder organoids recapitulate the stratification of bladder uroepithelium.

(A) Schematic of the protocol used for generation of mouse bladder organoids. Luminal cells, isolated by microinjection of TryPLE solution into the bladder, are cultured in basement membrane extract (BME) to form differentiated bladder organoids. (B, C) Immunofluorescence staining confirms that bladder organoids (B) recapitulate the stratified layers of the uroepithelium observed in mouse bladder tissue (C). The umbrella cell layer was identified with anti-uropod 3a (anti-UP3a) and anti-cytokeratin 8 (anti-CK8) antibodies. The basal and intermediate cell layers were identified with anti-cytokeratin 13 (anti-CK13) antibody. Cell nuclei were labeled with DAPI (cyan). The lumens of the bladder organoids and mouse bladder slices are indicated by yellow asterisks. Scale bars, 20 μm in (B) and 100 μm in (C).

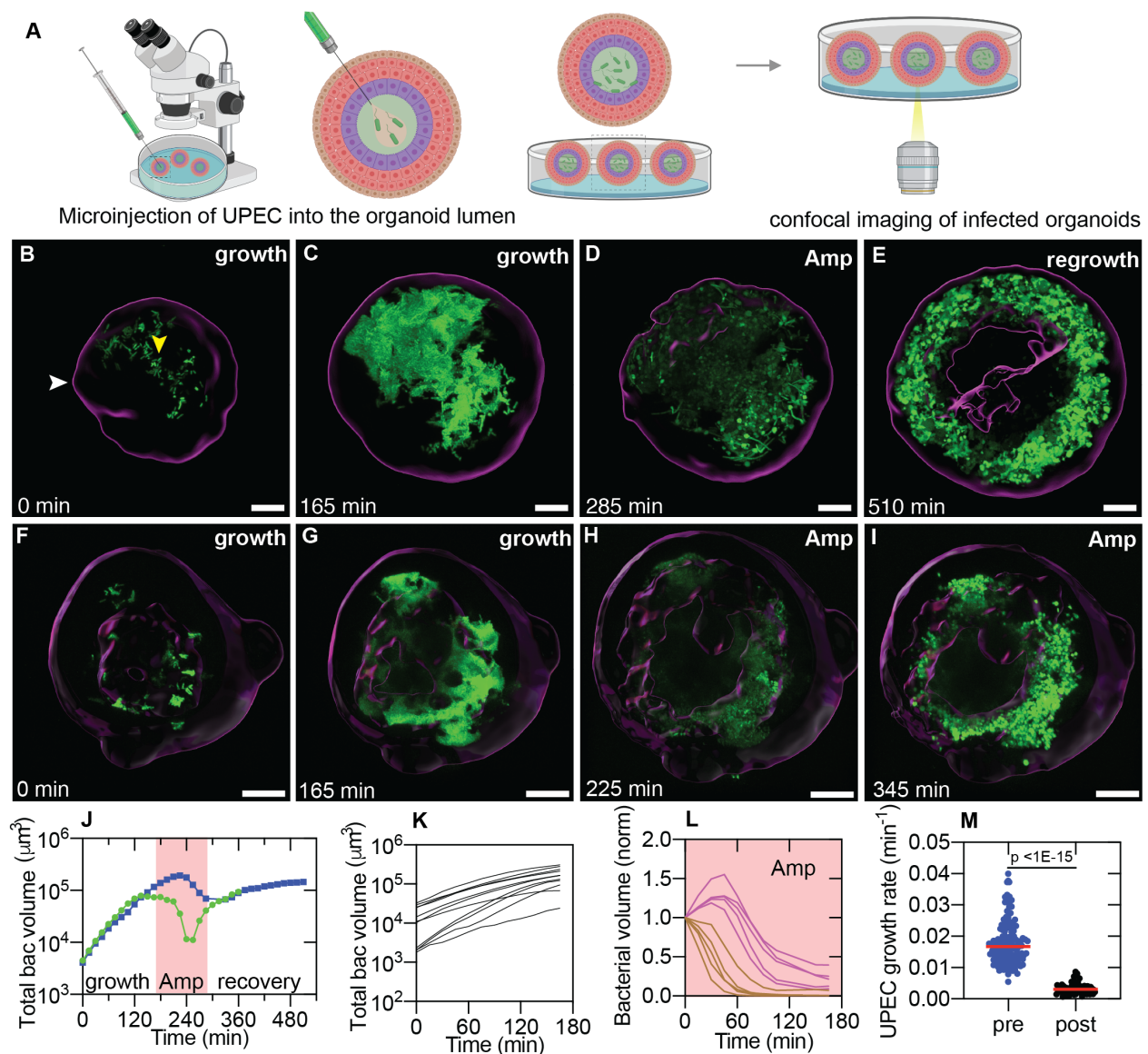


Figure 2.2: Bacteria within the bladder organoid wall are refractory to antibiotic clearance.

(A) Schematic of the microinjection protocol. Bacteria are injected via a glass microcapillary into the lumen of individual organoids and the organoids are resuspended in a collagen matrix for live-cell confocal imaging. (B-E) Snapshots from time-lapse imaging of an infected organoid over 9 hours. (B) White arrowhead indicates the organoid boundary. Yellow arrowhead indicates bacteria in the lumen. The bacterial volume within the organoid increases rapidly during the initial growth phase (B, C, 0-165 min from the start of the experiment) and occurs predominantly within the lumen. At ca. 165 min, a 10X-MIC dose of ampicillin was added to the extracellular growth media. (D) Intra-organoid bacterial volume, quantified by bacterial fluorescence, decreases due to bacterial killing during this period (ca. 165-345 min). Subsequently, the antibiotic was withdrawn (recovery phase ca. 345-525 min) and bacterial regrowth appears to be restricted to the organoid wall (E, see supplementary movie SMov1). In contrast, panels (F-I) highlight an isolated example where bacterial volume initially decreases (compare H vs G) but growth subsequently resumes (I) even in the presence of the antibiotic (see supplementary movie SMov2). (J) Time profiles for intra-organoid bacterial volume over the entire course of the experiment for the organoids in panels B-E (squares) and F-I (circles), respectively. Shaded region represents the period of antibiotic treatment. (K-M) Characterization of bacterial growth dynamics at different stages of infection. (K, L) Representative plots of bacterial volume vs. time reveal that growth is exponential during the pre-ampicillin phase (K, $n = 11$ organoids) and decay is exponential during ampicillin treatment (L, $n = 10$ organoids). In some cases, bacterial volume declines immediately after ampicillin administration (L, brown lines), while in others, growth continues for some time before declining (L, magenta lines). (M) UPEC growth rate (min^{-1}) for pre and post antibiotic treatment. $p < 1\text{E-}15$.

(**M**) Scatter plot for the growth rate of the bacterial volume within the bladder organoids before (n=124 organoids) and after (n=58 organoids) ampicillin exposure. The growth rate before ampicillin treatment is significantly faster than the regrowth rate after ampicillin treatment ($p < 1E-15$, Mann-Whitney Test). Red lines represent the median values. Scale bars, 50 μm in (**B-I**).

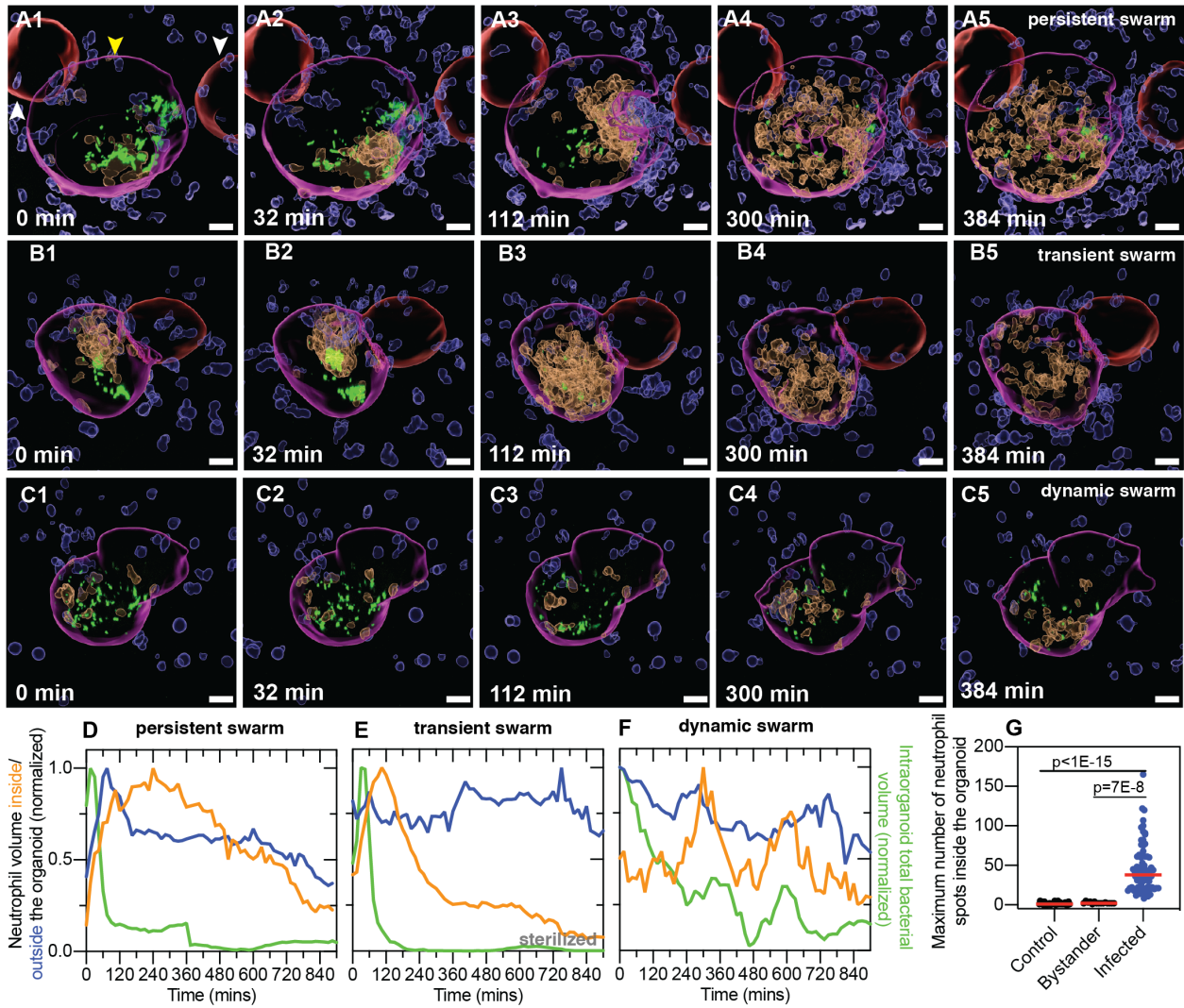


Figure 2.3: Neutrophil swarming dynamics in response to bacterial infection.

Characterization of neutrophil migration dynamics by time-lapse imaging of infected mouse bladder organoids. In all panels, surfaces of intra-organoid (amber) and extra-organoid (blue) neutrophils and infected (magenta) and uninfected (red) organoids were generated using a Bitplane Imaris analysis pipeline. UPEC (green) are shown without processing to identify individual bacteria. (A1-A5) Persistent swarm. Snapshots show the migration of neutrophils into the lumen of an infected organoid (yellow arrowhead) but not the adjacent uninfected organoid (white arrowhead). A neutrophil swarm forms around the bacteria in the lumen and persists over the course of the experiment. Solitary bacteria in the bladder wall (A5) appear to be refractory to clearance. Images are presented in a perspective view. (B1-B5) Transient swarm. The image series shows two consecutive cycles of neutrophil swarm formation and disaggregation in response to intra-organoid bacterial growth. (C1-C5) Dynamic swarm. The image series shows rapidly fluctuating neutrophil numbers within the organoid without the formation of large aggregates. (D-F) Time profiles of the relative volumes of neutrophils within the organoid, neutrophils surrounding the organoid, and bacteria within the organoid for the three profiles presented in (A-C), respectively. In each case, the volume is normalized to the maximum volume during the course of the experiment. Persistent and transient swarms are characterized on the basis of neutrophil reverse migration rates. (G) Scatter plots of the maximum number of intra-organoid neutrophils during the experiment in uninfected control organoids, uninfected bystander organoids, and infected organoids provides clear evidence of directed migration into infected organoids. $P < 1\text{E-}15$ comparing control organoids ($n = 30$) and infected organoids ($n = 75$). $P = 7\text{E-}8$ comparing bystander organoids ($n = 15$) and infected organoids ($n = 75$). P-values were calculated using Kruskal-Wallis ANOVA Test. Red lines represent median values. Scale bars, 20 μm in (A1-C5).

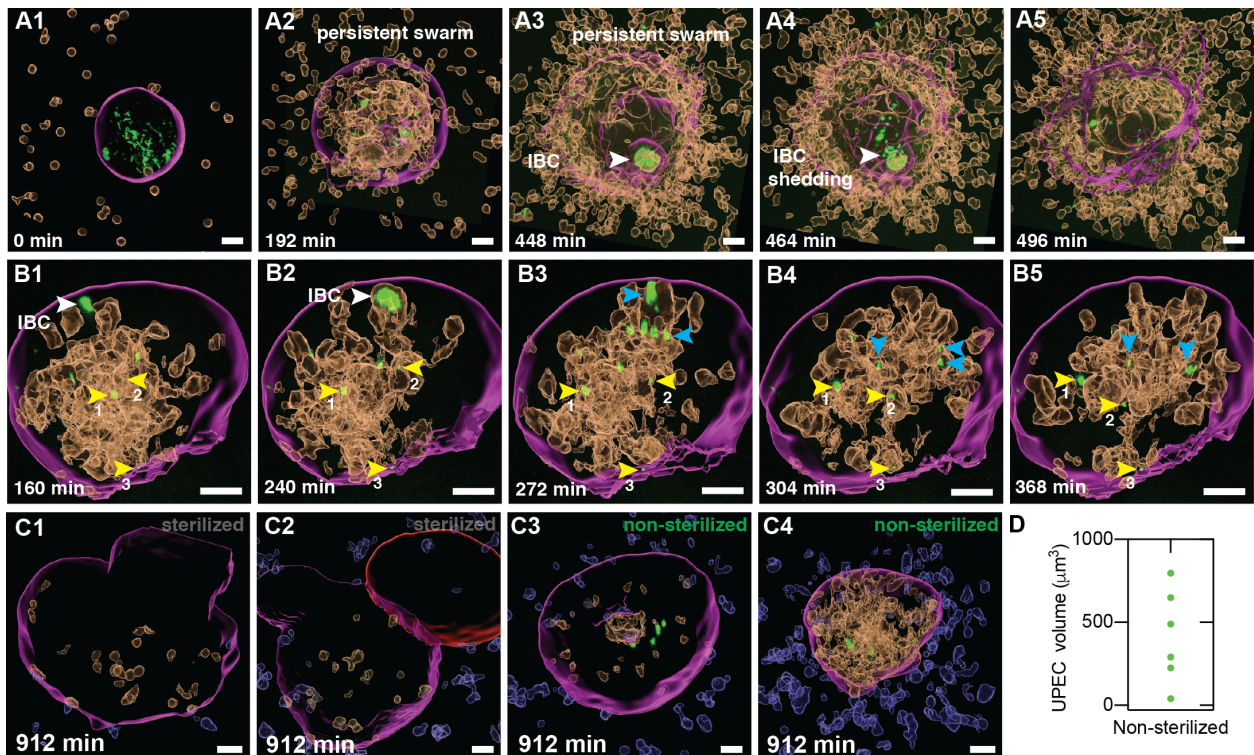


Figure 2.4: Bacteria within the bladder organoid wall are protected from clearance by neutrophil swarms.

(A1-A5, B1-B5) Two examples of IBCs that are protected from neutrophil-mediated clearance. Shedding of bacteria from an IBC (A4, A5 and B2, B3) is followed by two outcomes: phagocytic uptake and rapid clearance (A5), or dispersal to other niches in the bladder epithelium (B5, cyan arrowheads). Three examples of isolated solitary bacteria in the bladder wall (labelled '1', '2' and '3') that are refractory to clearance throughout the time series in (B1-B5) are indicated by yellow arrowheads and tracked within the organoid over this time period. (C1-C4) Snapshots at ca. 15 hours after infection and addition of neutrophils. (C1, C2) Examples of bacterial clearance from organoids following neutrophil treatment. (C3, C4) Examples of bacterial persistence in organoids where the neutrophil swarm disperses (C3) or persists up to 15 hours post-infection (C4). (D) Quantification of the total bacterial volume at 15 hours post-infection in case of non-sterilized organoids (n=6). Scale bars, 20 μm in (A1-A5), (B1-B5), and (C1-C4).

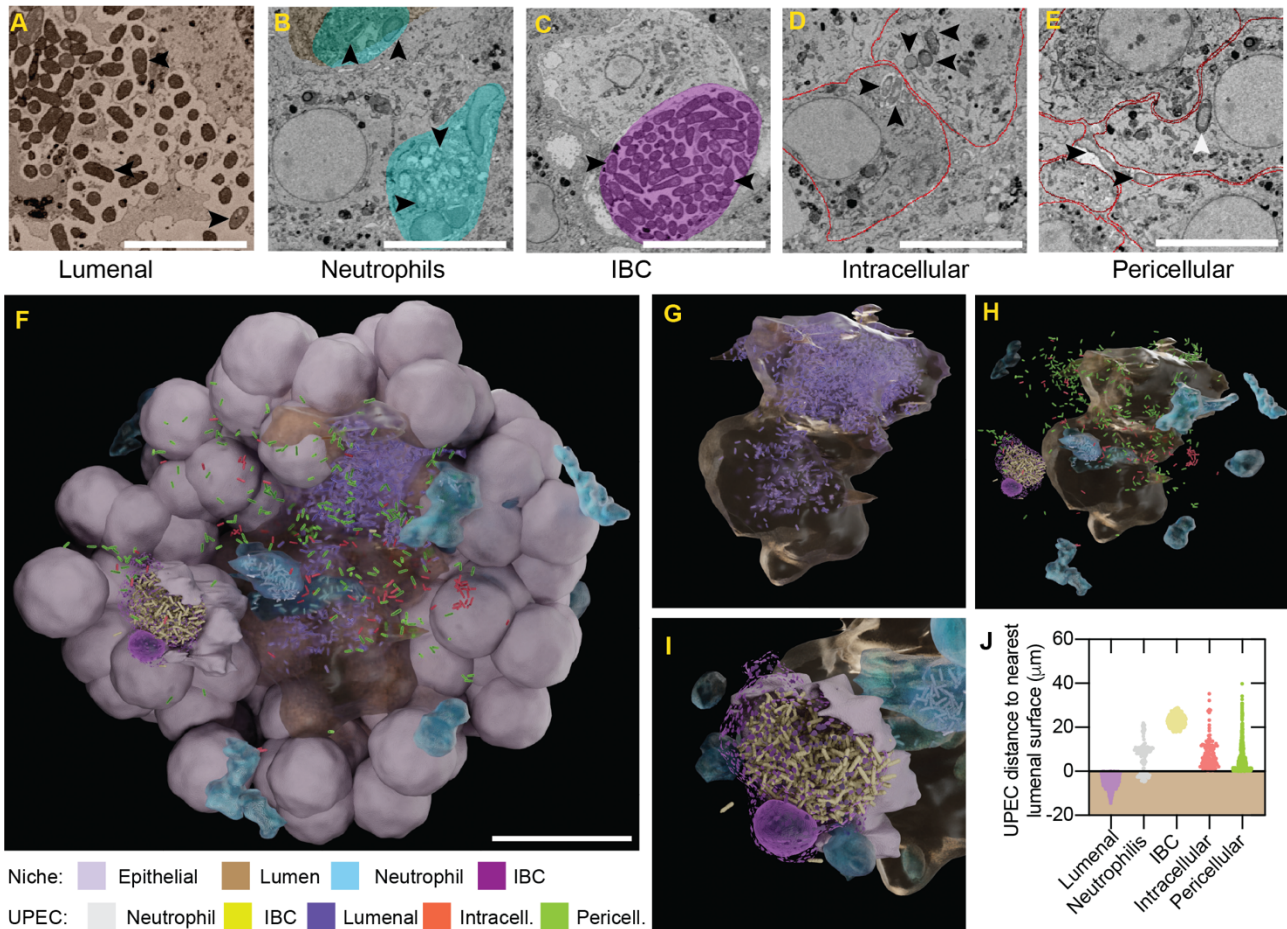


Figure 2.5: Volumetric electron microscopy reveals five distinct bacterial niches within an infected organoid.

(A-E) Serial-block face-scanning electron microscopy (SBEM) snapshots of an infected organoid at ca. 6 hours after microinjection of UPEC and addition of neutrophils. Five distinct niches were identified; bacteria within each niche are indicated by black arrowheads. (A) Extracellular bacteria within the organoid lumen (brown; $n = 1,821$). (B) Bacteria within neutrophils (light cyan) that can be either in the lumen or in the bladder wall ($n = 141$). (C) Bacteria within an IBC ($n = 398$). The area of the IBC is shown in purple. (D) Individual bacteria in the cytoplasm of epithelial cells (cell boundaries in red; $n = 111$). (E) Bacteria located between epithelial cells (cell boundaries in red; $n = 467$). An additional example of an intracellular bacterium is indicated with a white arrowhead. (F) Model derived from the serial electron microscopy images of the entire organoid in which all bacteria and cells were plotted. Image shows the interior of the organoid, revealing the lumen (brown), as well as epithelial cells (grey) and neutrophils (cyan). Bacteria located within the five niches corresponding to (A-E) are colored violet (luminal), grey (neutrophil), yellow (IBC), red (intracellular), and green (pericellular). The width of the organoid is 85 μm . (G) Zoom shows the extracellular bacteria in the lumen (brown). (H) Zoom shows all other bacterial classifications around the lumen. (I) Zoom shows the bacteria within the IBC, which appear to be protected from clearance by the surrounding neutrophils. (J) Scatter plot of the distance of bacteria within each subpopulation from the luminal surface; luminal bacteria are located entirely within the lumen (shaded brown region). Scale bars, 5 μm in (A-E) and 20 μm in F.

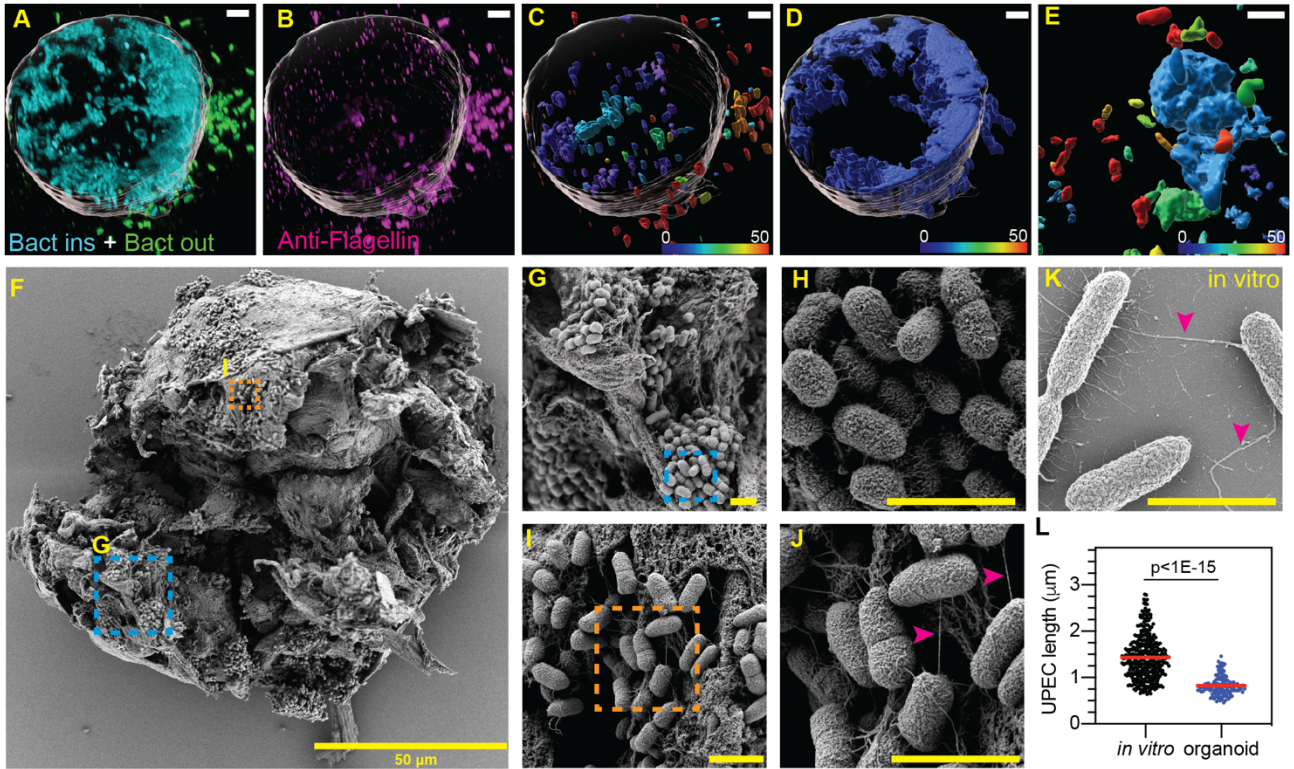


Figure 2.6: Solitary bacteria within the bladder organoid wall are rod-shaped and flagellated, whereas coccoid forms are non-flagellated.

(A-D) Perspective views of an infected organoid (surface indicated in grey) at ca. 6 hours after microinjection with UPEC. (A) Bacteria inside (cyan) and outside (green) the organoid were identified by immunostaining for bacterial LPS. (B) Flagellated bacteria (magenta) were identified by immunostaining for bacterial flagellin. Analysis of co-expression of LPS and flagellin for individual bacteria (C) or large clumps of bacteria, which are predominantly restricted to the lumen (D). Bacteria are color-coded according to the intensity of the flagellin signal. Flagellated bacteria are predominantly observed outside the organoid (C) but can also occur as individual solitary cells within the organoid wall. (E) Bacteria within an IBC have low-level flagellin expression, whereas individual bacteria surrounding the IBC retain high-level flagellin expression. (F) Scanning Electron Microscopy (SEM) image of an infected organoid at 6 hours after microinjection with UPEC. Ruptured organoids reveal multiple areas of bacterial growth. Zooms for two representative areas are shown in (G-J). Bacteria in (I) are loosely packed, rod-shaped, and express flagella (J, magenta arrowheads), whereas bacteria in (G) are tightly packed, coccoid-shaped, and do not express flagella (H). (K) SEM image of UPEC grown in axenic culture, where flagellar expression in rod-shaped bacteria is clearly observed (magenta arrowheads). (L) Size distributions for bacteria grown to stationary phase in axenic culture and bacteria within tightly packed clusters in the organoid. Both populations were imaged by SEM. Bacteria in axenic cultures ($n=370$) are longer than intra-organoid bacteria ($n=136$) ($p<1E-15$, calculated using Mann-Whitney Test). Scale bars, 5 μm in (A-E) and 2 μm in (G-K).

2.6 Supplementary Figures

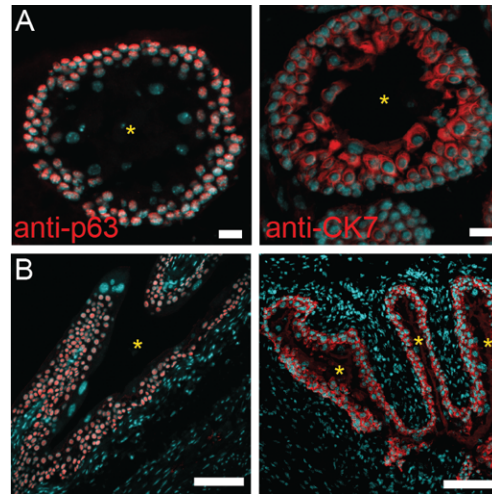


Figure 2.7: Mouse bladder organoids recapitulate the stratification of bladder uroepithelium.

Intermediate and basal layers of the uroepithelium were identified in mouse bladder organoids (A) or explanted mouse bladder tissue (B) by immunofluorescence staining with anti-p63 (left panels) or anti-cytokeratin 7 (anti-CK7, right panels) antibodies. Cell nuclei were labeled with DAPI (cyan). The lumens in the bladder organoid and mouse bladder slices are indicated with yellow asterisks. Scale bars: 20 μm in (A), 100 μm in (B).

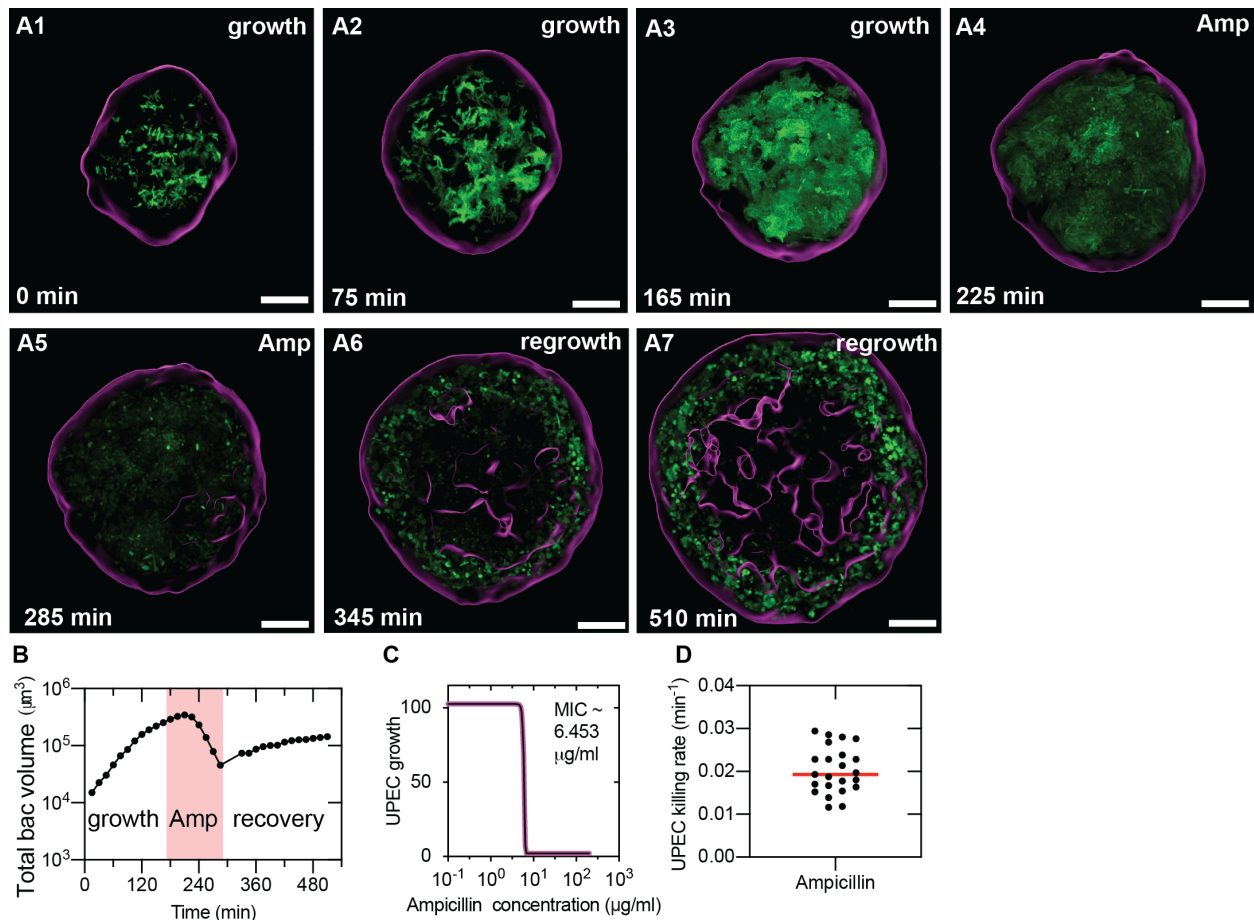


Figure 2.8: Bacteria within the bladder organoid wall are refractory to antibiotic clearance.

(A1-A7) An additional example showing bacterial growth within the organoid lumen, killing upon exposure to ampicillin, and slow regrowth within the organoid wall after ampicillin washout. (B) Corresponding time profiles for intra-organoid bacterial volume for the organoid in panels (A1-A7). (C) Measurement of ampicillin minimum inhibitory concentration (MIC) in mouse bladder organoid medium (DMEM) for the UPEC strain used in these experiments. (D) Scatter plot of the rate of decline of intra-organoid bacterial volume (“killing rate”) during ampicillin treatment, calculated by fitting the portion of the curves in Figure 2.2M, after the maximum volume attained, with a linear fit. Scale bars, 50 μm in (A1-A7).

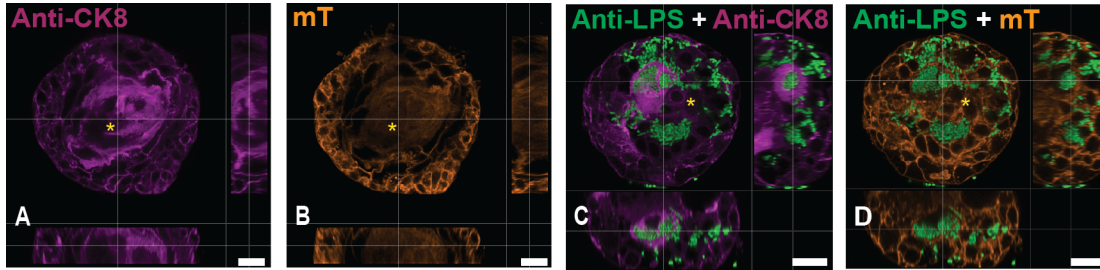


Figure 2.9: Infected organoids have abnormal CK8 expression.

(A,B) Sliced top view of an uninfected organoid. (A) Immunostaining with anti-CK8 antibody to identify umbrella cells. (B) Labelling of all cells in the organoid by td-Tomato expression (amber) surrounding the organoid lumen (yellow asterisk) demonstrates the presence of stratified epithelial cells. (C) Sliced top view of an infected organoid. Bacteria identified with an anti-LPS antibody (green). Infection reduces and significantly alters CK8 expression. (D) Overall integrity of the organoid is maintained during infection. Scale bars, 20 μm in (A-D).

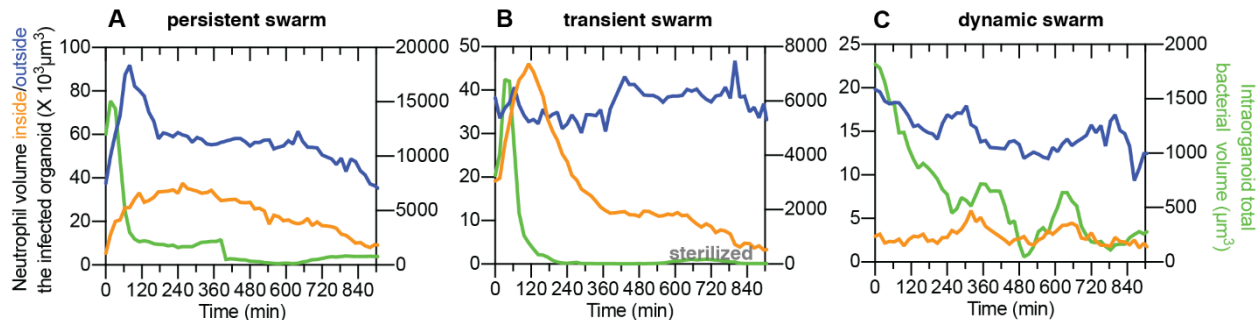


Figure 2.10: Distinct volume profiles of different neutrophil swarms formed inside infected organoids.

(A-C) Time profiles of the absolute volume of neutrophils within the organoid, surrounding the organoid, and the intra-organoid bacterial volume for the three profiles presented in Figure 2.3A-C respectively.

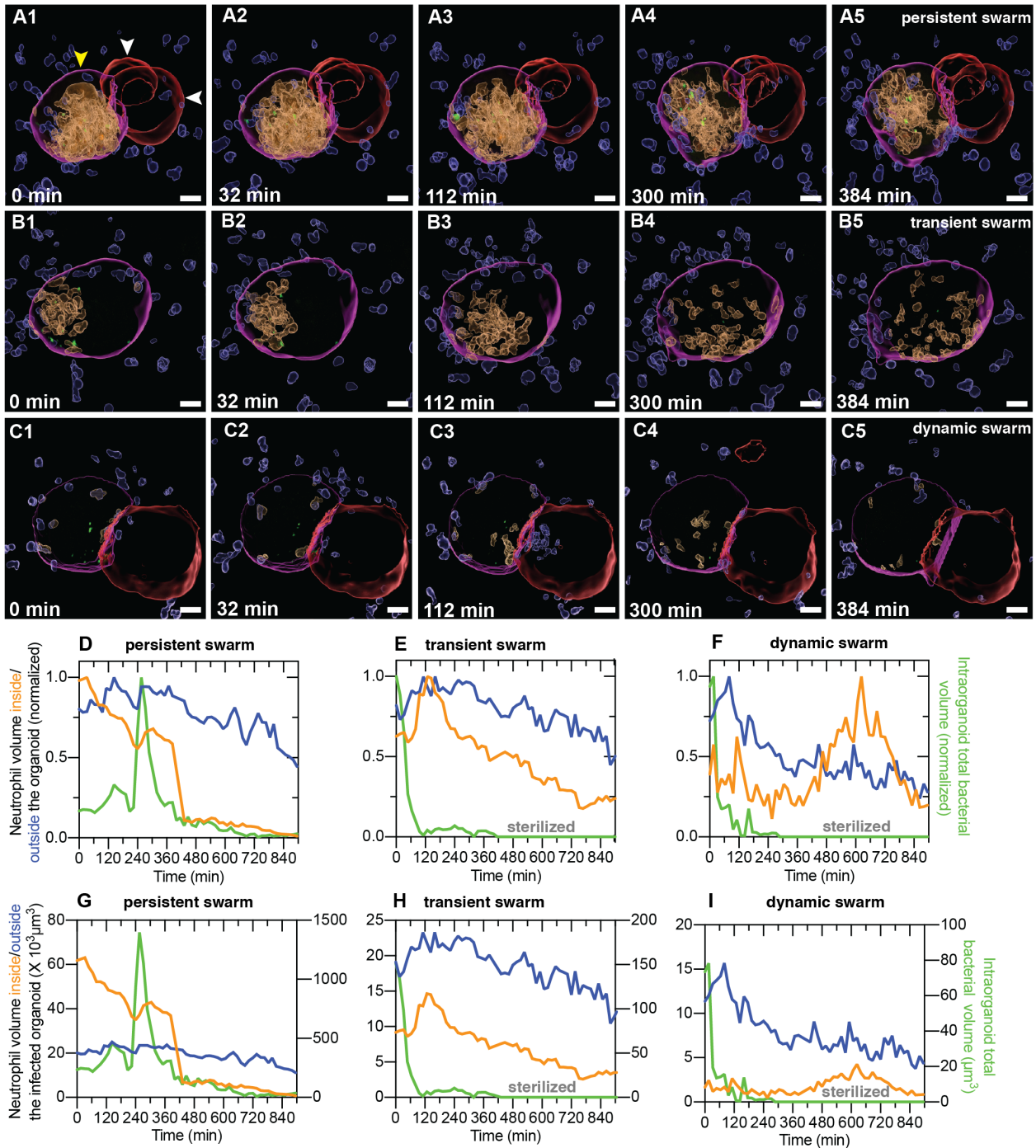


Figure 2.11: Additional examples of snapshots from time-lapse imaging showing the formation of distinct neutrophil swarms.

(A1-A5) a persistent neutrophil swarm, (B1-B5) a transient neutrophil swarm, and (C1-C5) a dynamic neutrophil swarm in response to intra-organoid bacterial infection. In all panels, neutrophil surfaces (intra-organoid, amber; extra-organoid, blue) and organoid surfaces (infected, magenta; uninfected, red) generated via an analysis pipeline using Bitplane Imaris. Bacteria (green) are shown without processing to identify individual cells. (D-I) Time profiles of the volume of neutrophils within the organoid, surrounding the organoid, and the intra-organoid bacterial volume for the three profiles presented in (A-C), respectively. In each case, the volume normalized to the maximum volume during the course of the experiment (D-F) or the absolute volume (G-I) is shown.

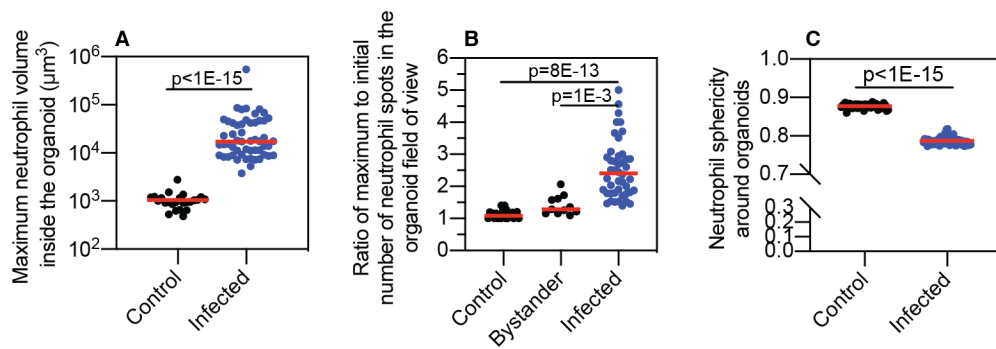


Figure 2.12: Characterization of neutrophil swarm behaviour in infected organoids.

(A) Scatter plot showing the maximum neutrophil volume inside organoids during the experimental time course. Infection significantly increases neutrophil migration. $P < 1E-15$, control (n=24) and infected (n=54), respectively. P-values calculated using a Mann-Whitney test. (B) Forward migration towards organoids also increases the concentration of neutrophils surrounding the organoid for infected organoids but not uninfected bystander organoids or control organoids. $P = 8E-13$ for control (n=24) vs infected (n= 46). $P = 1E-3$ for bystander (n=11) vs infected (n=46). P-values calculated using a Kruskal-Wallis ANOVA test. (C) Migration can also be characterized by a reduction in the sphericity of the shape of neutrophils surrounding infected organoids. $P < 1E-15$ for control (n=64) vs infected (n=66). P-values calculated using a Mann-Whitney test.

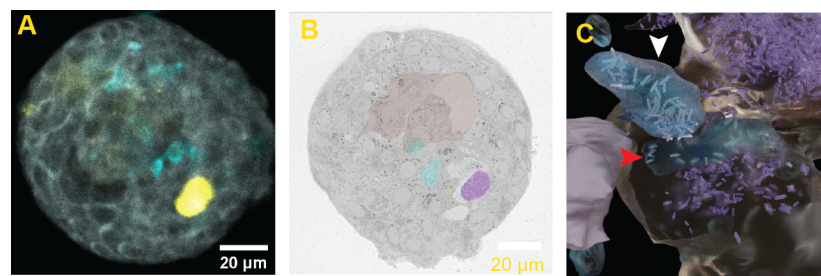


Figure 2.13: Correlative confocal and serial block electron microscopy image of an infected organoid.

(A) A fluorescence image of the infected organoid used for SBEM obtained using a confocal microscope. False coloring indicates epithelial cells (grey), neutrophils (cyan), and IBC (bacteria within the IBC in yellow). (B) Single slice of the corresponding infected organoid acquired from SBEM shows the organoid lumen (brown), IBC (area of IBC is shown in purple), and neutrophils (cyan). (C) Magnified image of the neutrophil (cyan) present inside the lumen (brown) is indicated with red arrowhead. Another neutrophil outside the lumen is indicated with white arrowhead. Bacteria located within different niches are colored violet (luminal) and grey (neutrophil).

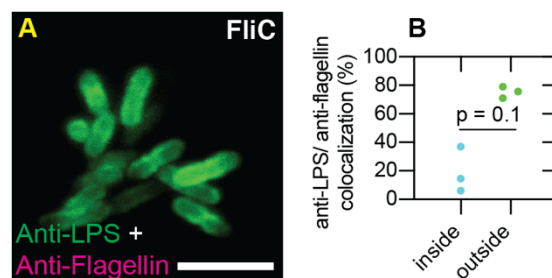


Figure 2.14 : Flagellin expression was attenuated in UPEC found inside the infected organoids.

(A) UPEC fliC mutant does not stain with anti-flagellin antibody. (B) Mander's overlap coefficient a calculated for colocalization of anti-LPS and anti-flagellin staining on bacteria found inside and outside organoids (segmented as shown in Fig. 6A). Data is for n=3 organoids. P-values calculated using Mann-Whitney test.

2.7 Supplementary Movie Legends

Supplementary movie 1

File Name: SMov1, **Description:** **Intra-organoid UPEC growth is refractory to antibiotic clearance** ([Figure 2.2B-E](#)).

UPEC (in green) grows inside the organoid (organoid surface in magenta generated by Bitplane Imaris) for 3 hours during the growth phase (0-165 min). Bacterial growth is predominantly observed in the organoid lumen. Following addition of ampicillin at a concentration ten times the minimum inhibitory concentration (10 X MIC at ca. 165 min) in the extracellular medium, bacterial killing is observed. In response to ampicillin treatment (ca. 165-345 min), UPEC is observed to initially filament followed by lysis. After removal of the antibiotic (recovery phase ca. 345-525 min), bacterial regrowth appears to be restricted to the bladder epithelium or organoid wall.

Supplementary movie 2

File Name: SMov2, **Description:** **UPEC growth could be observed in the presence of the antibiotic** ([Figure 2.2F-I](#)).

UPEC (in green) grows inside the organoid (organoid surface in magenta generated by Bitplane Imaris) for 3 hours during the growth phase (0-165 min). Bacterial growth is predominantly observed in the organoid lumen. Following addition of ampicillin at a concentration ten times the minimum inhibitory concentration (10 X MIC at ca. 165 min) in the extracellular medium, bacterial killing is observed. In response to ampicillin treatment (ca. 165-345 min), UPEC is observed to initially filament followed by lysis. However, during the later stage of the ampicillin treatment (after 240 min), UPEC growth is observed in the bladder epithelium or organoid wall.

Supplementary movie 3

File Name: SMov3, **Description:** **Intra-organoid UPEC growth is refractory to antibiotic clearance** ([Figure 2.8A1-A7](#)). An additional example showing growth of the bacteria within the lumen of an organoid during the growth phase (0-165 min), bacterial killing upon exposure to ampicillin treatment (ca. 165-345 min), and a slow regrowth after the removal of ampicillin (recovery phase ca. 345-525 min).

Supplementary movie 4

File Name: SMov4, **Description:** **Neutrophil form a persistent swarm in response to bacterial infection inside the organoid** ([Figure 2.3A1-A5](#)).

Surfaces of intra-organoid neutrophils (amber), extra-organoid neutrophils (blue) and infected (magenta) and uninfected (red) organoids were generated using a Bitplane Imaris analysis pipeline. UPEC (green) are shown without image processing to identify individual bacteria. During the course of infection, UPEC grows inside the organoid (observed by increase in green fluorescence), and neutrophils migrate into the lumen of an infected organoid (but not the adjacent uninfected organoid (shown in red)). A neutrophil swarm is formed around the bacteria in the lumen and persists over the course of the experiment. The neutrophil swarm kills a majority of the bacteria in the organoid lumen.

Supplementary movie 5

File Name: SMov5, **Description:** **Neutrophil form a transient swarm in response to bacterial infection inside the organoid** ([Figure 2.3B1-B5](#)).

A transient neutrophil swarm (amber) is formed around the bacteria in the organoid. Following the bacterial killing, the neutrophil cluster disaggregates, and neutrophils migrate back out of the organoid to the surrounding collagen matrix.

Supplementary movie 6

File Name: SMov6, **Description:** **Neutrophil form a dynamic swarm in response to bacterial infection inside the organoid** ([Figure 2.3C1-C5](#)).

A dynamic neutrophil swarm (amber) is formed around the bacteria in the organoid. Neutrophils volume inside the organoid is observed to fluctuate during the course of the experiment.

Supplementary movie 7

File Name: SMov7, **Description:** **Neutrophil form a persistent swarm in response to bacterial infection inside the organoid** ([Figure 2.11A1-A5](#)).

Another example of persistent neutrophil swarm formed inside the infected organoid.

Supplementary movie 8

File Name: SMov8, **Description:** **Neutrophil form a transient swarm in response to bacterial infection inside the organoid** ([Figure 2.11B1-B5](#)).

Another example of transient neutrophil swarm formed inside the infected organoid.

Supplementary movie 9

File Name: SMov9, **Description:** **Neutrophil form a dynamic swarm in response to bacterial infection inside the organoid** ([Figure 2.11C1-C5](#)).

Another example of dynamic neutrophil swarm formed inside the infected organoid.

Supplementary movie 10

File Name: SMov10, Description: **Intracellular bacterial community is protected from surrounding neutrophils** ([Figure 2.4A1-A5](#)).

Bacteria inside the IBC (imaging time from start of the experiment: 448 min) are protected from a persistent swarm inside the infected organoid. Following the event of IBC shedding (relative time: 0-60 min, imaging time: 448-496 min), bacteria are killed by the surrounding neutrophils. All the neutrophils (inside and outside the organoid) are shown in amber. Segments during the time period (absolute time: 192-448 min) were out of focus and could not be captured during imaging. All the neutrophils (inside and outside the organoid) are shown in amber.

Supplementary movie 11

File Name: SMov11, Description: **Neutrophil swarms spread the IBC bacteria** ([Figure 2.4B1-B5](#)).

Bacteria inside the IBC (imaging time from start of the experiment: 160-240 min) are protected from a persistent swarm inside the infected organoid. Following the event of IBC shedding (relative time: 0-32 min, imaging time: 240-272 min), majority of the bacteria are killed by the surrounding neutrophil swarm. However, some of the bacteria are spread away by the persistent swarm. Solitary bacterial in the organoid wall did not originate from an IBC. These results demonstrate additional niches within the layers of the bladder epithelium beyond IBCs that can also harbour subpopulations of bacteria that are resistant to clearance by antibiotics or neutrophils. Neutrophils outside the organoid are not shown for clarity.

Supplementary movie 12

File Name: SMov12, Description: **Volumetric electron microscopy reveals five distinct bacterial niches within an infected organoid** ([Figure 2.5F-I](#)).

Model derived from the serial electron microscopy images of the entire organoid in which all bacteria and cells were plotted. Video shows the interior of the organoid, revealing the lumen (brown), and epithelial cells (grey), as well as the neutrophils (cyan). Bacteria located within the five niches corresponding to are colored violet (luminal), grey (neutrophil), lemon yellow (IBC), red (intracellular), and green (pericellular). An IBC is seen surrounded by neutrophils. Solitary intracellular and pericellular bacterial sub-populations are visible around all the quadrants of the whole organoid. The width of this organoid is 85 μm .

2.8 Acknowledgements

V.V.T gratefully acknowledges support by a Human Frontier Science Program (HFSP) Long-Term Fellowship (LT000231/2016-L) and a European Molecular Biology Organization (EMBO) Long-Term Fellowship (921-2015). This research was supported by a grant awarded to J.D.M by the Swiss National Science Foundation (SNSF) (Project Funding, 310030B_176397). K.S wishes to thank the entire team of EPFL Bioimaging & Optics Core Facility for their assistance in confocal live cell imaging and post analysis in Bitplane Imaris, Dr. Devanjali Dutta (EPFL) and Stephanie Rosset (at the EPFL Biological Electron Microscopy Facility) for help in optimizing the protocol for rupturing of infected organoids, Dr. Jessica Sordet-Desimoz and Gian-Filippo Mancini (EPFL Histology Core Facility) for assistance with paraffin-embedded slicing of organoids, Dr. Germann Markus for development of the neutrophil isolation protocol, Mikhail Nikolaev (EPFL) for assistance with the collagen gel polymerization protocol, and Alexandre Marcos (EPFL) for optimizing the protocol for microinjection of bladder organoids. The authors thank and credit BioRender.com for the illustrations and schematics used in this manuscript.

2.9 Author Contributions

| Contributor role | Role definition |
|--------------------------------------|---|
| Conceptualization | K.S., V.V.T., N.D. and J.D.M. |
| Methodology | K.S., V.V.T., N.D. and J.D.M. |
| Software | K.S. and V.V.T. |
| Validation | K.S., V.V.T. and N.D. |
| Formal analysis | K.S., V.V.T. and N.D. |
| Investigation | K.S., N.D., F.S.G., M.C.C., A.D., G.K. and J.D.M. |
| Resources | K.S., V.V.T., N.D., F.S.G., M.C.C., A.D., J.M., G.K., H.C. and J.D.M. |
| Data Curation | K.S. |
| Writing – original draft preparation | K.S. and V.V.T. |
| Writing – review and editing | K.S., V.V.T., N.D., F.S.G., M.C.C., A.D., J.M., G.K., H.C. and J.D.M. |
| Visualization | K.S., V.V.T. and N.D. |
| Supervision | V.V.T., N.D. and J.D.M. |
| Project administration | K.S., V.V.T., N.D. and J.D.M. |
| Funding acquisition | J.D.M |

2.10 Materials and Methods

| Reagent or re-source | Designation | Source or reference | Identifiers | Additional information |
|--|---|--------------------------|------------------------------|--|
| Strain, strain background (Mus musculus, C57BL6) | Gt(ROSA)26Sortm4(ACTB-ttdTomato,-EGFP)Luo/J | Jackson Laboratory | Cat#: 007576; PMID: 17868096 | Female, 6–8 weeks old |
| Strain, strain background (Mus musculus, C57BL6) | | Charles River Laboratory | Cat#: C57BL/6NCrl | Female, 6–8 weeks old |
| strain, strain background | Uropathogenic Escherichia coli (UPEC) strain CFT073 | PMID: 2182540 | NCBI:txid199310 | originally isolated from a pyelonephritis patient and provided by Prof. H.L.T. Mobley, University of Michigan, USA |
| plasmid | pZA32-YFP | PMID: 9092630 | | (Lutz and Bujard, 1997) |
| strain, strain background | CFT073-pZA32-YFP | this paper | | this study |
| other | RPMI-1640 medium | ATCC | Cat#:30-2001 | |
| other | Gibco™ RPMI 1640 Medium, no phenol red | Thermofisher | Cat#:11835063 | |
| other | Gibco™ Fetal Bovine Serum, Premium Plus | Thermofisher | Cat#:A4766801 | |
| other | Gibco™ Antibiotic-Antimycotic (100X) | Thermofisher | Cat#:15240062 | |
| other | Gibco™ Trypsin-EDTA (0.05%), phenol red | Thermofisher | Cat#:25300054 | |
| drug | Chloramphenicol | Sigma-Aldrich | Cat#:C1919-25G | 34 mg/mL in ethanol (stored at -20 °C) |
| drug | Ampicillin | Sigma-Aldrich | Cat#: A9518-5G | 50 mg/mL in ddH ₂ O (stored at -80 °C) |
| other | Phosphate Buffered Saline | Thermofisher | Cat#: 10010056 | |
| other | TrypLE™ Express Enzyme (1X) | Thermofisher | Cat#: 12605010 | |
| other | Gibco™ HEPES | Thermofisher | Cat#: F2006 | |
| other | Invitrogen™ DAPI | Thermofisher | Cat#: D1306 | used at 1µg/mL in PBS from a stock of 5 mg/mL prepared in DMSO |
| other | LB (Luria broth base, Miller's modified) | Sigma-Aldrich | Cat#: L1900-1KG | |
| other | CellTracker™ Deep Red Dye | Thermofisher | Cat#: C34565 | used at 1µM concentration in respective cell medium |
| antibody | Anti-CK7 | abcam | Cat#: ab209599 | used at 1:100 dilution in 1% BSA (with .02% Triton) |
| antibody | Anti-CK8 | abcam | Cat#: ab192468 | used at 1:100 dilution in 1% BSA (with .02% Triton) |
| antibody | Anti-LPS | abcam | Cat#: ab 35654 | used at 1:100 dilution in 1% BSA, conjugated with Donkey anti-Mouse secondary antibody, Alexa Fluor 488 (2µg/mL) in 1%BSA (with .02% Triton) |

| | | | | |
|------------------------------|--|--------------|-----------------|---|
| antibody | Anti-flagellin | abcam | Cat#: ab 93713 | used at 1:100 dilution in 1% BSA, conjugated with Donkey anti-Rabbit secondary antibody, Alexa Fluor 647 (2µg/mL) in 1%BSA (with .02% Triton) |
| antibody | Anti-p63 | abcam | Cat#: ab 735 | used at 1:100 dilution in 1% BSA, conjugated with Donkey anti-Mouse secondary antibody, Alexa Fluor 647 (2µg/mL) in 1%BSA (with .02% Triton) |
| antibody | Anti-Uroplakin3a | Santa Cruz | Cat#: sc-166808 | used at 1:100 dilution in 1% BSA, conjugated with Donkey anti-Mouse secondary antibody, Alexa Fluor 647 (2µg/mL) in 1%BSA (with .02% Triton) |
| antibody | Anti-CK1 | Thermofisher | Cat#: MA1-06312 | used at 1:100 dilution in 1% BSA, conjugated with Donkey anti-Mouse secondary antibody, Alexa Fluor 647 (2µg/mL) in 1%BSA (with .02% Triton) |
| antibody | Donkey anti-Mouse IgG (H+L) Highly Cross-Adsorbed Secondary Antibody, Alexa Fluor 647 | Thermofisher | Cat#: A-31571 | 2 mg/mL |
| antibody | Donkey anti-Rabbit IgG (H+L) Highly Cross-Adsorbed Secondary Antibody, Alexa Fluor 647 | Thermofisher | Cat#: A-31573 | 2 mg/mL |
| antibody | Goat anti-Mouse IgG (H+L) Highly Cross-Adsorbed Secondary Antibody, Alexa Fluor 488 | Thermofisher | Cat#: A-11029 | 2 mg/mL |
| antibody | Donkey anti-Rabbit IgG (H+L) Highly Cross-Adsorbed Secondary Antibody, Alexa Fluor 568 | Thermofisher | Cat#: A10042 | 2 mg/mL |
| antibody | Donkey anti-Mouse IgG (H+L) Highly Cross-Adsorbed Secondary Antibody, Alexa Fluor 568 | Thermofisher | Cat#: A10037 | 2 mg/mL |
| peptide, recombinant protein | Native Collagen, Bovine dermis | AteloCell | Cat#: IAC-50 | 5 mg/mL |
| other | Advanced DMEM/F-12 | Thermofisher | Cat#: 12634010 | supplemented with 1X HEPES and 1X Glutamax |
| other | DMEM/F-12, no phenol red | Thermofisher | Cat#: 21041025 | supplemented with 1X HEPES and 1X Glutamax |
| other | HEPES, 100X | Thermofisher | Cat#:15630106 | used at 1X in DMEM/F12 |
| other | Glutamax, 100X | Thermofisher | | used at 1X in DMEM/F12 |
| peptide, recombinant protein | B27 | Thermofisher | Cat#:17504044 | stored at -20 °C |

| | | | | |
|------------------------------|---|---------------------|--------------------|--|
| peptide, recombinant protein | Human KGF/ FGF7 | Peptotech | Cat#:100-19 | stock at .1mg/ml in 0.1%BSA, used at (100 ng/ml) in DMEM/F12 |
| peptide, recombinant protein | Human FGF10 | Peptotech | Cat#:100-26 | stock at .1mg/ml in 0.1%BSA, used at (100 ng/ml) in DMEM/F12 |
| Other | A8301 | Tocris | Cat#: 2939 | stock at 5mM concentration in DMSO , stored at -20 °C |
| Other | Rhokinase inhibitor, Y-27632 | Abmole Bioscience | Cat#: 2939 | stock at 100mM concentration in ddH ₂ O |
| peptide, recombinant protein | Cultrex PathClear Reduced Growth Factor BME, Type 2 | Bio-Techne | Cat#: 3533-005-02 | stored at -80 °C |
| Other | Glass Pasteur pipettes | VWR | Cat#: 612-1701 | |
| commercial assay or kit | Anti-Ly-6G MicroBead Kit, mouse | Miltenyi Biotec | Cat#: 130-092-332 | |
| software, algorithm | Imaris 9.5.1 | Bitplane | | |
| other | Gas chamber for stages with k-frame insert (160x110mm) - magnetic model with sliding lid. | okolab | Cat#: H201-K-FRAME | |
| other | Flaming/Brown Micropipette Puller | Sutter Instruments | model P-87 | capillaries were pulled with settings: pressure 360, heat=866, velocity =200 |
| other | Capillary glass, 1.0 mm outer diameter, 0.75 mm inner diameter | WPI | TW100F-4 | |
| other | 35mm holder - magnetic | okolab | Cat#:1x35-M | |
| other | μ-Dish 35 mm, high | ibidi | Cat#:81156 | |
| other | Flexible tubing, 0.76X1.65X0.45X15000 | Freudenberg Medical | Cat#:0045634143 | |
| other | 1.00/0.75 x 20mm metallic tubes | Unimed | Cat#:200.010-A | |
| other | Aladdin programmable pump | WPI | Cat#:PUMP-NE-1000 | |
| other | Olympus SZX16 stereo microscope | Olympus | | |
| other | Leica SP8 confocal microscope | Leica | | |
| other | Olympus MVX10 stereo microscope | Olympus | | |

2.10.1 Generation of mouse bladder organoids from mouse bladder uroepithelial cells

Mouse bladder organoids were prepared by selectively isolating luminal cells from the bladder of C57BL/6 mice (Charles River Laboratories) or ROSA^{MT/MG} mice (Jackson Laboratories) by filling the clamped mouse bladder *ex vivo* with TrypLEA, as described (Mullenders et al., 2019). Mice were housed in a specific pathogen-free facility. Animal protocols were reviewed and approved by EPFL's Chief Veterinarian, by the Service de la Consommation et des Affaires Vétérinaires of the Canton of Vaud, and by the Swiss Office Vétérinaire Fédéral.

Mice were euthanized by CO₂ overdose and luminal uroepithelial cells were isolated from three female mice at an age of four months to optimise the number of uroepithelial cells obtained by microinjecting approximately 500 µl TryPLE (Gibco) with a 26G needle (Terumo) and placing the clamped mouse urinary bladder inside a 50 ml Falcon tube surrounded by pre-warmed 20 ml Basal Medium (Advanced DMEM/F-12 medium). The Falcon tube containing the bladder was incubated for 1 hour inside a cell culture incubator at 37°C and 5% CO₂. The bladder was then washed twice with basal medium containing 20% heat-inactivated fetal bovine serum (FBS) to neutralize the effect of TryPLE. The cell suspension was passed through a filter with 40 µm pores (Fisher) and the flow-through cells were collected and pelleted at 0.3 g for 5 minutes. The isolated uroepithelial cells were resuspended in an appropriate volume of Cultrex® Basement Membrane Extract (BME) and seeded as hemispherical domes (40-50 µL volume) in a 24-well plate. The 24-well plate was inverted to promote 3D growth and BME was allowed to polymerize at 37°C for 30 minutes. The solidified hemispherical domes were supplemented with mouse bladder medium (MBM, (Mullenders et al., 2019)) supplemented with 1X antibacterial/antifungal solution (Gibco). MBM medium consists of Advanced DMEM/F-12 medium (Thermofisher), 100 ng/ml of FGF10 (Peprotech), 25 ng/ml of FGF7 (Peprotech), 500 nM of A83-01 (Tocris Bioscience), 2% of B27 (Thermofisher), and 10 µM of Y-27632 ROCK inhibitor (Abmole Bioscience). Over the subsequent 2-3 weeks, the mouse bladder organoids were passaged every 5 days or sheared with a fire polished glass pipette. Organoids were used immediately for infection experiments or cryopreserved in freezing media (60% FBS, 30% Advanced DMEM/F-12, 10% DMSO) at -180°C for later experiments.

2.10.2 UPEC culture and injection of mouse bladder organoids

Uropathogenic *Escherichia coli* (UPEC) strain CFT073 was isolated from a pyelonephritis patient (provided by H.L.T. Mobley). A derivative strain expressing yellow fluorescent protein (YFP) was generated by electroporation of CFT073 with the episomal plasmid PZA32-YFP. To induce expression of type 1 pili, UPEC was grown in LB media containing 25 µg/ml chloramphenicol in non-shaking condition at 37°C for 2 days prior to the experiment.

Cryopreserved tdTomato mouse bladder organoids were thawed and recultured in BME for five days before the experiment. One day before the experiment, organoids were washed twice with ice-cold DMEM (without antibacterial or antifungal) followed by centrifugation at 100 g for 5 minutes to remove the spent BME. They were then seeded in fresh BME inside a 35 mm ibidi µ-Dish in basal medium without antibacterial or antifungal supplementation. On the day of the experiment, stationary-phase UPEC were microinjected into the organoid lumen using a Pneumatic PicoPump (WPI). The micropipettes used for microinjection were prepared by laser pulling of thin wall glass capillary

(TW100F-4 with length 100 mm and diameter 1mm) with Flaming/Brown Micropipette Puller (Sutter Instruments model P-87) set at pressure 360, heat 866, Vel 200. Prior to UPEC microinjection, micropipettes were filled with 10 μ L of 1:1 volume dilution of UPEC culture with a Phenol Red solution (Sigma-Aldrich) using MicroloaderTM flexible tips (Eppendorf) to allow visualization of the injected volume. The micropipettes were broken with a sharp scalpel under a stereomicroscope (Olympus SZX-16). The tip size of the cut micropipette was checked by setting pressure conditions on PicoPump to eject 1 nL volume in mineral oil on thin film of paraffin on a Zeiss coverslide (corresponding to 100 μ m). 1 nL of diluted bacterial volume corresponds to 100-200 UPEC bacilli, enumerated by plating for colony forming units on LB agar. The volume of bacterial inoculum was adjusted according to the size of the organoids. Medium-sized organoids (100-300 μ m in diameter) with a clearly distinguishable lumen were the easiest organoids to inject.

For the experiments with co-culture with mouse neutrophils, injected organoids were removed from fresh BME by pipetting 2 ml of ice-cold Cell Recovery Solution (CorningTM) after removing MBM from ibidi μ -Dish. The BME hydrogel was mechanically dissociated with a P1000 pipette and the resulting liquid gel was placed inside a 15 ml falcon tube pre-coated with a 1% BSA solution. The ibidi μ -Dish was washed twice with additional 1.5 ml of Cell Recovery Solution to collect the organoids, and the resulting 5 ml of Cell Recovery Solution containing organoids inside the 15 ml falcon tube was mechanically dissociated with a non-tapered glass pipette pre-coated with a 1% BSA solution. The cell recovery solution containing infected organoids was kept on ice for 30 minutes to completely liquefy the BME. The cell recovery solution was then exchanged through two washes with 10 ml of basal medium (supplemented with 10% FBS) and the organoids were centrifuged at 100 g for 5 minutes at 4°C to remove the recovery solution. The organoid pellet was then ready to be resuspended in collagen gel.

2.10.3 Isolation of neutrophils and labelling with CellTrackerTM dye

Neutrophils were isolated from bone marrow of three female WT mice (Charles River) per experiment. Mice were euthanized by CO₂ overdose and the femur and tibia were isolated. The isolated bone marrow was crushed with a mortar and pestle and resuspended in 5 ml of cold SM++ solution (HBSS + 2% serum + 25 mM HEPES). The tissue homogenate was then passed through a pre-wet filter with 40 μ m pores. Additional cold SM++ solution was added to the filtered cell suspension to make a total volume of 50 mL and then pelleted down at 0.3 g for 5 minutes. The cell suspension was then processed in batches of 10⁷ cells using positive selection with the Miltenyi Anti-Ly6G kit as described by the supplier. Isolated Ly6G mice neutrophils were stained with CellTrackerTM Deep Red (Thermofisher) in a serum-free RPMI phenol red free medium at 1 μ M and incubated for 30 minutes

in 5 ml cell suspension inside 50 ml falcon tube maintained at 37°C. Neutrophils were labelled with Post-CellTracker™ and subsequently washed twice with 10 ml of 20% FBS in RPMI phenol red free medium to remove the unbound dye. The labelled neutrophils were kept briefly at room temperature before introduction into a co-culture with infected organoids inside the collagen gel.

2.10.4 Co-culture of mouse neutrophils and infected organoids in collagen gels

Collagen gels were used to co-culture infected organoids and mouse neutrophils. The collagen gel master mix buffered at pH 7.0 was made by adding 312 µL of ice-cold native bovine collagen with 4 µL of 1M HEPES, 4 µL of 1M sodium bicarbonate, 40 µL of 1X DMEM/F-12, and 40 µL of 10X DMEM/F-12. The collagen gel mixture was stored on ice before use and care was taken to avoid generating bubbles when pipetting. Freshly isolated neutrophils (10^7) labeled with CellTracker™ were resuspended in 88 µL of a premade mixture of collagen gel master mix (10X DMEM/F-12, 1X DMEM/F-12, HEPES, sodium bicarbonate) without native bovine collagen on ice and then mixed with infected organoids. 156 µL of collagen solution was added twice to the suspension of infected organoids and neutrophils on ice followed by rapid mixing with a P200 pipette. The obtained collagen gel suspension of infected organoids and neutrophils was pipetted on a plasma pre-treated ibidi µ-Dish (Diener) at pressure 60 and time 60 s. Plasma pretreatment makes the µ-Dish surface more hydrophilic, which allows a uniform thin layer (1-2 mm) of collagen gel to be deposited on the dish which is good for imaging with a confocal microscope. The collagen gel was then incubated at 37°C and 5% CO₂ for 30 minutes to allow the collagen gel to polymerize and solidify. Lastly, 1.5 ml of a 25 ng/mL solution of murine Granulocyte Colony Stimulating Factor (G-CSF) was added to the co-culture of infected organoids and neutrophils.

2.10.5 Immunofluorescence of uninfected and infected mouse bladder organoids

Cryopreserved mouse bladder organoids were thawed and maintained in BME culture for five days before the experiment. The cultured uninfected and infected organoids were fixed with 4% paraformaldehyde (PFA) for 6 hours at room temperature with occasional mechanical dissociation with a P1000 pipette. The fixed organoids were washed with PBS and centrifuged at 100 g for 5 minutes in a 15 ml falcon tube pre-coated with 1% BSA. The organoids were washed at least twice with PBS to remove any remaining residues of PFA then resuspended in 50 µL of prewarmed Histogel (ThermoFisher) at 50 °C and pipetted out as a small hemispherical dome inside a 1 cm Tissue-Tek Cryomold. The cryomold was placed on a cold ice plate for solidification. Subsequently, the hemispherical Histogel was processed for paraffin embedding. Organoids embedded in paraffin were cut into 4 µm slices. The thin paraffin sections were deparaffinized and rehydrated by immersing the slides through the following solutions: xylene, three washes for 5 minutes each; 100% ethanol, two washes for 10

minutes each; 95% ethanol, two washes for 10 minutes each; 70% ethanol, two washes for 10 minutes each; 50% ethanol, two washes for 10 minutes each; PBS, three washes for 5 minutes each. Rehydrated slides were then processed for heat induced antigen retrieval using 10 mM citrate buffer, pH =6.0. Slides were washed with 1X PBS, permeabilized with 0.15 % Triton X-100 for 15 minutes, washed twice with 1X PBS, and blocked with 1% BSA in PBS for 1 hour. The boundaries of paraffin sections were marked with a hydrophobic pen and slides were labelled with a permanent ethanol-resistant marker. Primary antibody incubation at a dilution of either 10 µg/ml or 1:100 was performed overnight in an antibody incubation buffer comprising 1% BSA and 0.01% Triton-100 in PBS. Slides were subsequently washed three times with PBS for 10 minutes each. Secondary antibody incubation was performed at 2 µg/ml in antibody incubation buffer for 1 hour at room temperature. Excess antibody was removed by washing three times with PBS for 10 minutes each. Cell nuclei were stained with DAPI (5 µg/ml) for 30 minutes and slides were mounted with Fluoromount-GTM mounting medium (Thermofisher) overnight in a dark chamber.

For immunofluorescence of organoids cultured for 6 hours in collagen gels on Ibidi µ-Dishes, uninfected and infected organoids were fixed with 1 ml of 4% PFA for 1 hour and antibody labelling was performed as described above. Images were deconvolved using SVI Huygens (Quality, 0.05; Iterations, 40).

2.10.6 Time-lapse confocal imaging of infected organoids

All imaging experiments were conducted using a Leica SP8 confocal microscope in the inverted configuration with a temperature-controlled microscope environmental chamber at 37°C and a stage-top chamber that allowed supplementation with 5% CO₂ (OKOlabs). Time-lapse imaging was conducted using a Leica HC FLUOTAR 25X (NA 0.95) multi-immersion objective. Water was pumped to the ring around the water objective at 9 Hz with pumping duration 10 seconds and pumping interval 30 minutes, controlled by SRS software. Microinjected tdTomato-expressing organoids were identified and imaged on two channels (without neutrophils) or three channels (with neutrophils). Laser excitation wavelengths of 500 nm (YFP), 555 nm (tdTomato), and 630 nm (CellTrackerTM Deep Red) were chosen to allow multi-channel imaging within the same sequence with reduced spectral overlap. Images were acquired with a scan speed of 700 Hz and a zoom factor of 2.25 resulting in an XY resolution of 200-450 nm depending on the number of pixels acquired per field of view. Z-stacks were acquired with 0.5 or 1 µm step sizes.

2.10.7 Experimental setup and image analysis for ampicillin treatment experiments

tdTomato organoids suspended in fresh BME were microinjected with UPEC. After UPEC microinjection, MBOs were resuspended in collagen and supplemented with 1.5 ml of MBM medium

following collagen polymerization for 30 minutes. Prior to the experiment, Ibidi μ -Dishes were modified by inserting bent metallic tubes (1.00/0.75 X 20mm, Unimed Catalogue 200.010-A) through the lid and sealing these devices with PDMS cured in an oven at 80°C for 1 hour. Flexible 0.76 mm x 1.65 mm x 1 mm tubing (Mono-Lumen Freudenberg Medical) was connected to these tubes to facilitate medium addition and removal. A setup period of 2 to 3 hours was typically required and is not considered within the time duration of the experiment. Once imaging commenced, bacteria were allowed to grow for a 3-hour “growth phase” (0-165 minutes). The medium in the μ -Dish was then replaced with fresh medium containing ampicillin at 64.5 μ g/ml, corresponding to 10X-MIC. The dynamics of bacterial growth and killing in the presence of ampicillin was then monitored for a 3-hour “treatment phase” (ca. 165-345 minutes), after which ampicillin was removed from the extracellular medium by gentle exchange with fresh MBM media using a 10 ml syringe. Bacterial growth after ampicillin washout was then monitored for a further 3-hour “regrowth phase” (345-525 minutes). The drift in focus was adjusted manually at frequent intervals throughout the experiment.

2.10.8 Image analysis for confocal live-cell imaging

Image analysis was performed with Bitplane Imaris 9.5.1. The time-lapse images have four channels for UPEC (first channel), uroepithelial cells (second channel), neutrophils (third channel), and transmitted light (fourth channel). The organoid surface was generated and tracked over time using the second channel (Threshold, 5 to 15; Smooth Surfaces Detail, 3 μ m). When required, nearby organoids were separated with seed point diameter (depending upon the size of nearby organoids) or adjoining organoid surfaces were orthogonally trimmed with the cut option. The uroepithelial cell channel was subtracted from the neutrophil channel to create a fifth channel (neutrophils-epithelial). This channel subtraction was performed to reduce the crosstalk between the boundaries of the epithelial cells marked by the tdTomato membrane marker and neutrophils labelled cytoplasmically with CellTrackerTM Deep Red. This procedure allowed for a more robust detection of neutrophils inside the organoids. Finally, the organoid surface was used to mask the fifth channel; generate a sixth channel of intra-organoid neutrophils and a seventh channel for extra-organoid neutrophils. These masked sixth and seventh channels were used to detect neutrophil surfaces (Threshold, 10; Smooth Surfaces Detail, 0.5 or 1.0 μ m) inside and outside the organoid respectively. The masked sixth channel was also used to detect neutrophil spots (Size, 8 μ m; Quality, 4 to 8) inside the organoid. Neutrophil spots in the field of view were detected on the neutrophil channel (Size, 8 μ m; Quality, 4 to 8). Neither neutrophil spots nor neutrophil surfaces were tracked over time due to the technical difficulties with imaging speed and amorphous shapes of migrating neutrophils around infected organoids. Average neutrophil sphericity (≥ 0.5) for neutrophils around an organoid was obtained with time-collapsed information

of average neutrophil sphericity for all the neutrophil surfaces per time point. In cases of bigger neutrophil clusters, average neutrophil sphericity was obtained by excluding sphericity of the bigger neutrophil cluster (<0.5). For UPEC volume inside the organoids, the first channel was sufficient to create the surface (Threshold, 15; Smooth Surfaces Detail, 0.5 or 1 μm). In cases of extracellular UPEC growth, organoid surface was used as a mask on UPEC channel to create eighth channel for calculating intra-organoid UPEC growth.

2.10.9 Serial block face-scanning electron microscopy (SBEM) of co-culture of infected organoids with migrating neutrophils

Organoids expressing tdTomato were grown in Ibidi μ -Dishes and microinjected with UPEC, which was allowed to grow within the organoid lumen for six hours. After two hours of bacterial growth, injected organoids were removed from fresh BME by pipetting 2 ml of ice-cold Cell Recovery Solution after removing MBM from the Ibidi μ -Dish. The BME hydrogel was mechanically dissociated with a P1000 pipette and the resulting liquid gel was placed inside a 15ml falcon tube pre-coated with 1% BSA. The Ibidi μ -Dish was washed twice with 1.5 ml of Cell Recovery Solution to collect the organoids and the resulting 5 mL of Cell Recovery Solution containing organoids was occasionally mechanically dissociated with a non-tapered glass pipette pre-coated with 1% BSA. The Cell Recovery Solution containing infected organoids was kept on ice for 30 minutes to completely liquefy the BME. The Cell Recovery Solution was washed twice with 10 ml of basal medium and the organoids were centrifuged at 100 g for 5 minutes at 4°C to remove the recovery solution. The microinjected tdTomato-expressing organoids grown in Ibidi μ -Dishes were co-embedded with freshly isolated LY6G neutrophils labeled with CellTracker™ Deep Red on a plasma-treated MatTek dish with a gridded coverslip. The organoids were fixed 6 hours after addition of MBM supplemented with 25 ng/ml of mouse G-CSF. After 6 hours, organoids were fixed for 1 hour at room temperature in a 15 ml falcon tube containing a mix of 1% glutaraldehyde and 2% paraformaldehyde in 0.1 M phosphate buffer (pH 7.4). Infected organoids were fixed for one hour, washed twice with PBS, and examined using optical microscopy to identify organoids with at least one IBC and neutrophils within the lumen. The selected organoid was then imaged on a confocal Leica Sp8 microscope using a 10X objective. The fluorescent image, acquired with 0.2 μm lateral and 1 μm axial resolution, was used to identify and locate the target organoid on the gridded coverslip for correlative light and SBEM. This fixed organoid was kept overnight at 4°C in the fixative.

The fixed organoids were postfixed in potassium ferrocyanide (1.5%) and osmium (2%), then stained with thiocarbohydrazide (1%) followed by osmium tetroxide (2%) alone. They were finally stained overnight in uranyl acetate (1%) and washed in distilled water at 50°C before staining with lead

aspartate at a pH of 5.5 at the same temperature. The entire cover slip, with the organoids attached, were dehydrated in increasing concentrations of alcohol and then embedded in durcupan resin and hardened at 65°C for 24 hours. The total thickness of the coverslip and resin was minimized to around 1 mm. Once hardened, the coverslip was removed, and the region of resin containing the organoid of interest was cut away from the others with a scalpel blade. This piece was glued, with conductive glue, to an aluminium holder, and then placed inside the scanning electron microscope (Merlin, Zeiss NTS) integrated with an in-chamber ultramicrotome device (3View, Gatan). Serial images, 100 nm apart, were collected from the block face using a beam energy of 1.7 kV and 350 pA of current. Each image contained 6144 x 4608 pixels with a pixel size of 30 nm, and the stack contained 960 serial images. The overall volume imaged was 184.32 x 138.24 x 96 μm^3 .

2.10.10 Labelling of bacteria, epithelial cells, neutrophils, and organoid lumen in SBEM images

Identification and labelling of different features (e.g., lumen boundary, neutrophils, bacteria) was done manually; features whose identity was doubtful were not included in the analysis. All the different bacterial categories were identified on the full stack (960 slices). We identified five different categories of bacteria based on their location: extracellular bacteria in the organoid lumen, bacteria inside neutrophils, bacteria within an IBC, bacteria inside the cytoplasm of a uroepithelial cell, and pericellular bacteria sandwiched between the boundaries of adjacent cells. The injection site could be identified with asymmetry and higher abundance of extracellular luminal bacteria towards one side of the lumen.

The selected IBC-containing cell allowed X,Y alignment of the fluorescent images with the SBEM stack. Boundary of the organoid lumen, organoid coverage, and neutrophil boundaries were marked on a reduced stack (480 z-stacks) with X, Y, Z pixel resolution of 60 nm, 60 nm, and 100 nm, respectively. We also marked the location of uroepithelial cell nuclei. Fluorescent images of neutrophils labeled with CellTrackerTM Deep Red were used to identify and profile individual neutrophils. Neutrophils were identifiable in electron microscope images due to their multi-lobular nuclei and high electron density. Five neutrophils were identified outside, and nine neutrophils were identified inside the organoid. After identifying the multi-lobular nuclei of the neutrophils, bacteria were found in the neutrophil cytoplasm.

2.10.11 3D analysis and modelling of the infected organoid

Serial electron micrographs were imported into the TrakEM2 software operating in FIJI. They were then aligned and the positions of all cells and bacteria were plotted in the image series. The organoid lumen was reconstructed by segmenting it in each of the images in which it appeared, as were the neutrophils and the uroepithelial cell boundaries surrounding the IBC. For ease of manipulating the

large dataset, reconstruction of the lumen and identification of neutrophils and uroepithelial cells was done on a reduced stack of 480 slices with corresponding pixel size of 60 nm and spacing between serial slices of 200 nm.

The segmentations of cells and the organoid lumen, and the coordinates of each mouse cell and bacterial cell, were exported to Blender 3D modeling software. The “proximity tool” in the NeuroMorph toolset (Jorstad et al., 2018) was used to measure the distance of each bacterium to the wall of the lumen, as well as the organoid’s external surface. To visualize the organoid, with all bacteria, the particles system in the Blender software was used to place a single generic model of either a bacterium or a cell at the vertex that marked its 3D coordinate.

2.10.12 Scanning electron microscopy of infected organoids

UPEC-infected tdTomato-expressing organoids were allowed to grow for 6 hours. After 6 hours, organoids were fixed for 1 hour at room temperature in a 15 ml falcon tube containing a mix of 1% glutaraldehyde and 2% paraformaldehyde in 0.1 M phosphate buffer (pH 7.4). The fixed organoids were seeded onto 12 mm poly-L-lysine-coated coverslips and stored overnight in the fixative. The organoids were further fixed with 1% osmium tetroxide in 0.1 M cacodylate buffer, then dehydrated in increasing concentrations of ethanol (50% to 100% in 10% increments) for 10 minutes per incubation. The dehydrated organoids were then dried at the critical point of CO₂ (Leica CPD300) before being manipulated with a 0.125 mm tungsten needle (FST, 10130-05) using a stereomicroscope (Leica M205), and adhered to an aluminium stub using conductive tape (Electron Microscopy Sciences, USA). This holder was coated with 5 nm of gold palladium metal using a Q150 sputter coater (Quorum Ltd, UK), then imaged in a scanning electron microscope (Merlin, Zeiss NTS).

2.11 References:

- Andersen, T.E., Khandige, S., Madelung, M., Brewer, J., Kolmos, H.J., and Møller-Jensen, J. (2012). *Escherichia coli* uropathogenesis in vitro: invasion, cellular escape, and secondary infection analyzed in a human bladder cell infection model. *Infect Immun* 80, 1858–1867.
- Anderson, G.G., Palermo, J.J., Schilling, J.D., Roth, R., Heuser, J., and Hultgren, S.J. (2003). Intracellular Bacterial Biofilm-Like Pods in Urinary Tract Infections. *Science* 301, 105–107.
- Anderson, G.G., Dodson, K.W., Hooton, T.M., and Hultgren, S.J. (2004). Intracellular bacterial communities of uropathogenic *Escherichia coli* in urinary tract pathogenesis. *Trends Microbiol* 12, 424–430.
- Bartfeld, S., and Clevers, H. (2015). Organoids as Model for Infectious Diseases: Culture of Human and Murine Stomach Organoids and Microinjection of *Helicobacter Pylori*. *J Vis Exp Jove*.
- Blango, M.G., Ott, E.M., Erman, A., Veranic, P., and Mulvey, M.A. (2014). Forced Resurgence and Targeting of Intracellular Uropathogenic *Escherichia coli* Reservoirs. *Plos One* 9, e93327.
- Cattan, V., Bernard, G., Rousseau, A., Bouhout, S., Chabaud, S., Auger, F.A., and Bolduc, S. (2011). Mechanical Stimuli-induced Urothelial Differentiation in a Human Tissue-engineered Tubular Genitourinary Graft. *Eur Urol* 60, 1291–1298.
- Chabaud, S., Saba, I., Baratange, C., Boiroux, B., Leclerc, M., Rousseau, A., Bouhout, S., and Bolduc, S. (2017). Urothelial cell expansion and differentiation are improved by exposure to hypoxia. *J Tissue Eng Regen M* 11, 3090–3099.
- Clevers, H. (2016). Modeling Development and Disease with Organoids. *Cell* 165, 1586–1597.
- Co, J.Y., Margalef-Català, M., Li, X., Mah, A.T., Kuo, C.J., Monack, D.M., and Amieva, M.R. (2019). Controlling Epithelial Polarity: A Human Enteroid Model for Host-Pathogen Interactions. *Cell Reports* 26, 2509-2520.e4.
- Denk, W., and Horstmann, H. (2004). Serial Block-Face Scanning Electron Microscopy to Reconstruct Three-Dimensional Tissue Nanostructure. *Plos Biol* 2, e329.
- Flores-Mireles, A.L., Walker, J.N., Caparon, M., and Hultgren, S.J. (2015). Urinary tract infections: epidemiology, mechanisms of infection and treatment options. *Nat Rev Microbiol* 13, 269–284.
- Foxman, B. (2010). The epidemiology of urinary tract infection. *Nat Rev Urol* 7, 653–660.
- Foxman, B., Gillespie, B., Koopman, J., Zhang, L., Palin, K., Tallman, P., Marsh, J.V., Spear, S., Sobel, J.D., Marty, M.J., et al. (2000). Risk Factors for Second Urinary Tract Infection among College Women. *Am J Epidemiol* 151, 1194–1205.
- Hannan, T.J., and Hunstad, D.A. (2016). A Murine Model for *Escherichia coli* Urinary Tract Infection. *Methods Mol Biology Clifton N J* 1333, 159–175.

- Haraoka, M., Hang, L., Frendéus, B., Godaly, G., Burdick, M., Strieter, R., and Svanborg, C. (1999). Neutrophil Recruitment and Resistance to Urinary Tract Infection. *J Infect Dis* 180, 1220–1229.
- Heo, I., Dutta, D., Schaefer, D.A., Iakobachvili, N., Artegiani, B., Sachs, N., Boonekamp, K.E., Bowden, G., Hendrickx, A.P.A., Willems, R.J.L., et al. (2018). Modelling Cryptosporidium infection in human small intestinal and lung organoids. *Nat Microbiol* 3, 814–823.
- Hoffman, D.P., Shtengel, G., Xu, C.S., Campbell, K.R., Freeman, M., Wang, L., Milkie, D.E., Passolli, H.A., Iyer, N., Bogovic, J.A., et al. (2020). Correlative three-dimensional super-resolution and block-face electron microscopy of whole vitreously frozen cells. *Science* 367, eaaz5357.
- Hopke, A., Scherer, A., Kreuzburg, S., Abers, M.S., Zerbe, C.S., Dinauer, M.C., Mansour, M.K., and Irimia, D. (2020). Neutrophil swarming delays the growth of clusters of pathogenic fungi. *Nat Commun* 11, 2031.
- Horsley, H., Dharmasena, D., Malone-Lee, J., and Rohn, J.L. (2018). A urine-dependent human urothelial organoid offers a potential alternative to rodent models of infection. *Sci Rep-Uk* 8, 1238.
- Hung, C.-S., Dodson, K.W., and Hultgren, S.J. (2009). A murine model of urinary tract infection. *Nat Protoc* 4, 1230–1243.
- Iosifidis, G., and Duggin, I.G. (2020). Distinct Morphological Fates of Uropathogenic Escherichia coli Intracellular Bacterial Communities: Dependency on Urine Composition and pH. *Infect Immun* 88.
- Jorstad, A., Blanc, J., and Knott, G. (2018). NeuroMorph: A Software Toolset for 3D Analysis of Neurite Morphology and Connectivity. *Front Neuroanat* 12, 59.
- Justice, S.S., Hung, C., Theriot, J.A., Fletcher, D.A., Anderson, G.G., Footer, M.J., and Hultgren, S.J. (2004). Differentiation and developmental pathways of uropathogenic Escherichia coli in urinary tract pathogenesis. *Proc National Acad Sci* 101, 1333–1338.
- Justice, S.S., Hunstad, D.A., Seed, P.C., and Hultgren, S.J. (2006). Filamentation by Escherichia coli subverts innate defenses during urinary tract infection. *Proc National Acad Sci* 103, 19884–19889.
- Kessler, M., Hoffmann, K., Fritsche, K., Brinkmann, V., Mollenkopf, H.-J., Thieck, O., Costa, A.R.T. da, Braicu, E.I., Sehouli, J., Mangler, M., et al. (2019). Chronic Chlamydia infection in human organoids increases stemness and promotes age-dependent CpG methylation. *Nat Commun* 10, 1194.
- Kienle, K., and Lämmermann, T. (2016). Neutrophil swarming: an essential process of the neutrophil tissue response. *Immunol Rev* 273, 76–93.
- Klein, R.D., and Hultgren, S.J. (2020). Urinary tract infections: microbial pathogenesis, host-pathogen interactions and new treatment strategies. *Nat Rev Microbiol* 18, 211–226.

- Lämmermann, T., Afonso, P.V., Angermann, B.R., Wang, J.M., Kastenmüller, W., Parent, C.A., and Germain, R.N. (2013). Neutrophil swarms require LTB4 and integrins at sites of cell death in vivo. *Nature* *498*, 371–375.
- Lane, M.C., Alteri, C.J., Smith, S.N., and Mobley, H.L.T. (2007). Expression of flagella is coincident with uropathogenic *Escherichia coli* ascension to the upper urinary tract. *Proc National Acad Sci* *104*, 16669–16674.
- Lee, S.H., Hu, W., Matulay, J.T., Silva, M.V., Owczarek, T.B., Kim, K., Chua, C.W., Barlow, L.J., Kandoth, C., Williams, A.B., et al. (2018). Tumor Evolution and Drug Response in Patient-Derived Organoid Models of Bladder Cancer. *Cell* *173*, 515–528.e17.
- Liese, J., Rooijakkers, S.H.M., Strijp, J.A.G. van, Novick, R.P., and Dustin, M.L. (2012). Intravital two-photon microscopy of host-pathogen interactions in a mouse model of *Staphylococcus aureus* skin abscess formation: Intravital 2-P microscopy of *S. aureus* skin infection. *Cell Microbiol* *15*, 891–909.
- Liu, Y., Stein, E., Oliver, T., Li, Y., Brunken, W.J., Koch, M., Tessier-Lavigne, M., and Hogan, B.L.M. (2004). Novel Role for Netrins in Regulating Epithelial Behavior during Lung Branching Morphogenesis. *Curr Biol* *14*, 897–905.
- MacIachlan, C., Sahlender, D.A., Hayashi, S., Molnár, Z., and Knott, G. (2018). Block Face Scanning Electron Microscopy of Fluorescently Labeled Axons Without Using Near Infra-Red Branding. *Front Neuroanat* *12*, 88.
- Martinez, J.J., Mulvey, M.A., Schilling, J.D., Pinkner, J.S., and Hultgren, S.J. (2000). Type 1 pilus-mediated bacterial invasion of bladder epithelial cells. *Embo J* *19*, 2803–2812.
- Mullenders, J., Jongh, E. de, Brousal, A., Roosen, M., Blom, J.P.A., Begthel, H., Korving, J., Jonges, T., Kranenburg, O., Meijer, R., et al. (2019). Mouse and human urothelial cancer organoids: A tool for bladder cancer research. *Proc National Acad Sci* *116*, 201803595.
- Mulvey, M.A., Lopez-Boado, Y.S., Wilson, C.L., Roth, R., Parks, W.C., Heuser, J., and Hultgren, S.J. (1998). Induction and Evasion of Host Defenses by Type 1-Piliated Uropathogenic *Escherichia coli*. *Science* *282*, 1494–1497.
- Mulvey, M.A., Schilling, J.D., Martinez, J.J., and Hultgren, S.J. (2000). Bad bugs and beleaguered bladders: Interplay between uropathogenic *Escherichia coli* and innate host defenses. *Proc National Acad Sci* *97*, 8829–8835.
- Mulvey, M.A., Schilling, J.D., and Hultgren, S.J. (2001). Establishment of a Persistent *Escherichia coli* Reservoir during the Acute Phase of a Bladder Infection. *Infect Immun* *69*, 4572–4579.
- Muzumdar, M.D., Tasic, B., Miyamichi, K., Li, L., and Luo, L. (2007). A global double-fluorescent Cre reporter mouse. *Genesis* *45*, 593–605.
- Mysorekar, I.U., and Hultgren, S.J. (2006). Mechanisms of uropathogenic *Escherichia coli* persistence and eradication from the urinary tract. *Proc National Acad Sci* *103*, 14170–14175.

- Neal, J.T., Li, X., Zhu, J., Giangarra, V., Grzeskowiak, C.L., Ju, J., Liu, I.H., Chiou, S.-H., Salahudeen, A.A., Smith, A.R., et al. (2018). Organoid Modeling of the Tumor Immune Microenvironment. *Cell* 175, 1972–1988.e16.
- Nikolaev, M., Mitrofanova, O., Broguiere, N., Geraldo, S., Dutta, D., Tabata, Y., Elci, B., Brandenberg, N., Kolotuev, I., Gjorevski, N., et al. (2020). Homeostatic mini-intestines through scaffold-guided organoid morphogenesis. *Nature* 585, 574–578.
- Pleguezuelos-Manzano, C., Puschhof, J., Huber, A.R., Hoeck, A. van, Wood, H.M., Nomburg, J., Gurjao, C., Manders, F., Dalmaso, G., Stege, P.B., et al. (2020). Mutational signature in colorectal cancer caused by genotoxic pks⁺E. coli. *Nature* 580, 269–273.
- Qian, X., Nguyen, H.N., Jacob, F., Song, H., and Ming, G.-L. (2017). Using brain organoids to understand Zika virus-induced microcephaly. *Dev Camb Engl* 144, 952–957.
- Rossi, G., Manfrin, A., and Lutolf, M.P. (2018). Progress and potential in organoid research. *Nat Rev Genet* 19, 671–687.
- Sachs, N., Papaspyropoulos, A., Ommen, D.D.Z., Heo, I., Böttinger, L., Klay, D., Weeber, F., Huelsz-Prince, G., Iakobachvili, N., Amatngalim, G.D., et al. (2019). Long-term expanding human airway organoids for disease modeling. *Embo J* 38.
- Sanden, S.M.G. van der, Sachs, N., Koekkoek, S.M., Koen, G., Pajkrt, D., Clevers, H., and Wolthers, K.C. (2018). Enterovirus 71 infection of human airway organoids reveals VP1-145 as a viral infectivity determinant. *Emerg Microbes Infect* 7, 84.
- Schilling, J.D., Lorenz, R.G., and Hultgren, S.J. (2002). Effect of Trimethoprim-Sulfamethoxazole on Recurrent Bacteriuria and Bacterial Persistence in Mice Infected with Uropathogenic *Escherichia coli*. *Infect Immun* 70, 7042–7049.
- Scott, V.C.S., Haake, D.A., Churchill, B.M., Justice, S.S., and Kim, J.-H. (2015). Intracellular Bacterial Communities: A Potential Etiology for Chronic Lower Urinary Tract Symptoms. *Urology* 86, 425–431.
- Shannon, J.G., Hasenkrug, A.M., Dorward, D.W., Nair, V., Carmody, A.B., and Hinnebusch, B.J. (2013). *Yersinia pestis* Subverts the Dermal Neutrophil Response in a Mouse Model of Bubonic Plague. *Mbio* 4, e00170-13.
- Smith, Y.C., Grande, K.K., Rasmussen, S.B., and O'Brien, A.D. (2006). Novel Three-Dimensional Organoid Model for Evaluation of the Interaction of Uropathogenic *Escherichia coli* with Terminally Differentiated Human Urothelial Cells. *Infect Immun* 74, 750–757.
- Southgate, J., Hutton, K.A., Thomas, D.F., and Trejdosiewicz, L.K. (1994). Normal human urothelial cells in vitro: proliferation and induction of stratification. *Laboratory Investigation J Technical Methods Pathology* 71, 583–594.
- Suzuki, K., Koyanagi-Aoi, M., Uehara, K., Hinata, N., Fujisawa, M., and Aoi, T. (2019). Directed differentiation of human induced pluripotent stem cells into mature stratified bladder urothelium. *Sci Rep-Uk* 9, 10506.

Wakamoto, Y., Dhar, N., Chait, R., Schneider, K., Signorino-Gelo, F., Leibler, S., and McKinney, J.D. (2013). Dynamic Persistence of Antibiotic-Stressed Mycobacteria. *Science* 339, 91–95.

Williamson, I.A., Arnold, J.W., Samsa, L.A., Gaynor, L., DiSalvo, M., Cocchiaro, J.L., Carroll, I., Azcarate-Peril, A., Rawls, J.F., Allbritton, N.L., et al. (2018). A High-Throughput Organoid Microinjection Platform to Study Gastrointestinal Microbiota and Luminal Physiology. *Cell Mol Gastroenterology Hepatology* 6, 301–319.

Wright, K.J., Seed, P.C., and Hultgren, S.J. (2007). Development of intracellular bacterial communities of uropathogenic *Escherichia coli* depends on type 1 pili. *Cell Microbiol* 9, 2230–2241.

Yuki, K., Cheng, N., Nakano, M., and Kuo, C.J. (2020). Organoid Models of Tumor Immunology. *Trends Immunol* 41, 652–664.

Zhou, J., Li, C., Sachs, N., Chiu, M.C., Wong, B.H.-Y., Chu, H., Poon, V.K.-M., Wang, D., Zhao, X., Wen, L., et al. (2018). Differentiated human airway organoids to assess infectivity of emerging influenza virus. *P Natl Acad Sci Usa* 115, 6822–6827.

Chapter 3. Bladder-chip as a model system for studying UPEC pathogenesis

Dynamic persistence of intracellular bacterial communities of uropathogenic *Escherichia coli* in a human bladder-chip model of urinary tract infections

Authors: Kunal Sharma, Neeraj Dhar*&, Vivek V. Thacker*&, Thomas M. Simonet, François Signorino-Gelo, Graham Knott, John D. McKinney*

Affiliations:

School of Life Sciences, Swiss Federal Institute of Technology in Lausanne (EPFL), 1015 Lausanne, Switzerland.

& These authors contributed equally

*Correspondence to: neeraj.dhar@epfl.ch, vivekvthacker@gmail.com , john.mckinney@epfl.ch

3.1 Abstract

Uropathogenic *Escherichia coli* (UPEC) proliferate within superficial bladder umbrella cells to form intracellular bacterial communities (IBCs) during early stages of urinary tract infections. However, the dynamic responses of IBCs to host stresses and antibiotic therapy are difficult to assess *in situ*. We develop a human bladder-chip model wherein umbrella cells and bladder microvascular endothelial cells are co-cultured under flow in urine and nutritive media respectively, and bladder filling and voiding mimicked mechanically by application and release of linear strain. Using time-lapse microscopy, we show that rapid recruitment of neutrophils from the vascular channel to sites of infection leads to swarm and neutrophil extracellular trap formation but does not prevent IBC formation. Subsequently, we tracked bacterial growth dynamics in individual IBCs through two cycles of antibiotic administration interspersed with recovery periods which revealed that the elimination of bacteria within IBCs by the antibiotic was delayed, and in some instances, did not occur at all. During the recovery period, rapid proliferation in a significant fraction of IBCs reseeded new foci of infection through bacterial shedding and host cell exfoliation. These insights reinforce a dynamic role for IBCs as harbours of bacterial persistence, with significant consequences for non-compliance with antibiotic regimens.

Keywords: bladder-chip, uropathogenic *Escherichia coli* (UPEC), intracellular bacterial communities (IBCs), bacterial persistence, antibiotic treatment, neutrophil swarms, neutrophil extracellular traps, shear stress, stretching, confocal live-cell imaging

3.2 Introduction

Urinary tract infections (UTIs), the second most-common cause for the prescription of antibiotics (Foxman, 2010) are characterized by the high frequency of recurrence, defined as a reappearance of infection within 12 months despite the apparently successful completion of antibiotic therapy. Recurrence occurs in about 25% of all UTIs (Foxman et al., 2000) and strongly impacts the cost of healthcare and reduces the quality of life, particularly since more than 60% of women are diagnosed with a UTI at least once in their lifetime (Klein and Hultgren, 2020). Uropathogenic *Escherichia coli* (UPEC), the causative agent for the majority of UTIs, exhibits a complex lifestyle in the bladder, with planktonic sub-populations within the urine co-existing with intracellular bacteria. UPEC invasion of the urinary bladder generates substantial changes to bladder morphology and a robust immune response. Much of our current understanding of early stages of UTI and the intracellular lifestyle is derived from studies in the mouse model (Anderson et al., 2003; Duraiswamy et al., 2018; Hannan et al., 2012; Hung et al., 2009; Justice et al., 2004; Schwartz et al., 2011; Yang et al., 2019). Examinations of mouse bladder explants via microscopy have revealed the formation of intracellular bacterial communities (IBCs) composed of thousands of bacteria within individual superficial uroepithelial cells (Justice et al., 2004). IBCs also play a prominent role in clinical infection and have also been harvested from the urine of cystitis patients (Robino et al., 2013; Rosen et al., 2007). These structures are considered to have a linear progression from an early stage of colonization by single bacteria to an intermediate stage of biofilm-like communities culminating in the release of bacteria at the late stage. However, long-term imaging of infected animals or of explant-tissue is technically challenging and therefore it has been difficult to capture the dynamic changes that underlie the formation of these structures and their impact on infection and clearance by subsequent antibiotic treatment.

In addition, the bladder is an extremely complex organ; it has a stratified architecture with well-differentiated cell types; a lumen filled with urine whose composition and chemical properties can vary depending on the physiological state of the individual and is subjected to periodic and large changes in organ volume and surface area (Korkmaz and Rogg, 2007). These features may play important roles in infection, but they have been hitherto hard to capture outside of a whole animal model, where they are present in their entirety and cannot be dissected in a modular manner.

Organotypic models are well-suited to address these outstanding questions. A key strength of advanced organotypic models such as organs-on-chip (Benam et al., 2016a; Huh et al., 2010b; Jang et al., 2013, 2019; Kim et al., 2016; Novak et al., 2020; Zhou et al., 2016) or organoids (Cakir et al., 2019; Clevers, 2016; Rossi et al., 2018; Sato et al., 2009) is that they increasingly recapitulate the complexity of host physiology. Organ-on-chip models have been developed for several organs either in isolation or in combination (Novak et al., 2020; Ronaldson-Bouchard and Vunjak-Novakovic,

2018). These systems are increasingly being used to model infectious diseases including viral and bacterial infections of the respiratory tract (Nawroth et al., 2020; Si et al., 2020; Thacker et al., 2020b, 2020a), gut (Jalili-Firoozinezhad et al., 2019; Kim et al., 2016; Shah et al., 2016; Tovaglieri et al., 2019), kidney (Wang et al., 2019), and liver (Kang et al., 2017). Recently, bladder organoids that mimic the stratified architecture of the uroepithelium have been used to study infections (Horsley et al., 2018; Smith et al., 2006; Sharma et al., 2020). However, the organoid model suffers from certain shortcomings inherent to the 3-D architecture such as the lack of vasculature, the inability to manipulate the cells mechanically, and the constrained volume of the lumen. In contrast, organ-on-chip models offer a complementary approach that does not suffer from these limitations. However, to our knowledge, there have been no reports of a bladder-on-chip model. Although there are studies that have developed *in vitro* bladder models that recreate the stratified architecture of the bladder epithelium (Horsley et al., 2018; Smith et al., 2006; Suzuki et al., 2019), they have not been used to recapitulate the multiple stages of IBC formation. Similarly, while a few studies have visualized different stages of IBC development by culturing human bladder cells under urine flow, these models are restricted to monoculture experiments (Andersen et al., 2012; Iosifidis and Duggin, 2020). Furthermore, the lack of vasculature in these models restricts the extent to which immune cell components or drugs can be introduced in a physiologically relevant manner and none of the systems reported to date offer the possibility of mimicking the mechanics of filling and voiding in a functioning bladder (Andersen et al., 2012; Horsley et al., 2018; Iosifidis and Duggin, 2020; Smith et al., 2006).

Here we report the development and characterization of a bladder-chip model that mimics the bladder architecture by co-culture of a well-characterized human bladder epithelial cell line with bladder microvascular endothelial cells in a device geometry that allows the two cell types to be exposed to urine and nutritive cell culture media, respectively. The flow rates in the apical and vascular channels can be controlled independently, and multiple rounds of micturition are recreated via the application of a linear strain to the PDMS membrane that serves as the substrate for co-culture. Using this model, we show that diapedesis of neutrophils to sites of infection on the epithelial side can lead to the formation of neutrophil swarms and neutrophil extracellular traps (NETs), and that IBCs offer substantial protection to bacteria from antibiotic clearance. Our observations suggest that the role of IBCs in reseeding bladder infections upon cessation of antibiotic treatment or failure to complete a course of antibiotics might be more important than previously assumed and therefore strategies aimed towards eradication of IBCs are very crucial for treatment efficacy.

3.3 Results

3.3.1 Reconstitution of bladder uroepithelium and bladder vasculature

We established a bladder-chip infection model by co-culturing HTB9 bladder epithelial cells (epithelial cells) and HMVEC-Bd primary human bladder microvascular endothelial cells (endothelial cells) in a novel bladder-chip approach (Figure 3.1A). Immunostaining verified that the epithelial and endothelial cells formed confluent monolayers (cell densities in Table 1) with high expression of junction markers such as epithelial cell adhesion molecule (EpCAM) in the epithelial cell layer, and platelet endothelial cell adhesion molecule-1 (PECAM-1) and VE-cadherin in the endothelial cell layer (Figure 3.1B, C, additional images in Figure 3.5A-H). Expression of these and other junction markers such as E-cadherin and zonula occludens-1 (ZO-1) was consistent across monocultures (Figure 3.6A-G).

Similarly, a majority of the epithelial cells expressed cytokeratin 7 (CK7), a general uroepithelial marker and cytokeratin 8 (CK8), a differentiated uroepithelial marker both in monoculture (Figure 3.6I, J) and on-chip (Figure 3.1B, Figure 3.5B, F). Some endothelial cells were also CK7+ (Figure 3.1C, Figure 3.6H). Co-culture of bladder epithelial and bladder endothelial cells in the human bladder-chip therefore did not alter the cellular expression patterns of these markers as compared to monocultures. We further characterized the HTB9 cell line in monoculture for markers for urothelial differentiation. HTB9 cells showed high expression of uroplakin-3a (UP3a) which has been shown to be essential for UPEC infection (Figure 3.6K) (Martinez et al., 2000; Mulvey et al., 1998) but only a small proportion of epithelial cells were positive for the basal cell marker cytokeratin1 (CK1), in agreement with the umbrella cell nature of the HTB9 cell line (Figure 3.6L, M) (Duncan et al., 2004; Smith et al., 2006). Overall, these observations confirmed that the bladder-chip is populated with cells that mimic the physiology of the bladder vasculature and the superficial urothelial cell layer. Further, the chip design enables the flow of media with different compositions through the epithelial and vascular channels. We used this feature to mimic bladder physiology by perfusion of diluted pooled human urine on the epithelial side and endothelial cell medium on the vascular side.

3.3.2 Modelling bladder filling and bladder voiding in the bladder-chip

The human bladder experiences vast changes in volume and surface area on a periodic basis. The first phase of this cycle, (*'filling bladder state'*), occurs through a slow and gradual increase in bladder volume due to addition of urine from kidney via the ureters, resulting in a large increase in bladder volume (Figure 3.1D). At the level of the uroepithelium, these changes manifest as a 2-dimensional biaxial stretch of the bladder tissue. *Ex vivo* studies in rat bladders report that a maximum strain of

90% and 130% can be applied to bladder explants in the circumferential and longitudinal directions (Gloeckner et al., 2002; Parekh et al., 2010), although micturition *in vivo* is likely triggered before this maximum value is reached. Subsequently, volume growth slows, and the bladder attains a relatively constant volume, with the bladder epithelium in a corresponding state of maximal stretch, (*'filled bladder state'*). Voiding of the bladder through urination rapidly reduces bladder volume, (*'voiding bladder state'*) and removes the strain experienced by the bladder cells. The bladder epithelium, as a viscoelastic material, responds to the removal of strain and relaxes over the subsequent period (Pascalis et al., 2018) where the bladder volume remains low (*'voided bladder state'*) (Figure 3.1D).

The architecture of the bladder-chip device allows for a linear strain to be applied to the porous membrane via negative pressure in the channels adjacent to the main channel of the device (*'the vacuum channels'*) (Grassart et al., 2019; Huh et al., 2010a) (Figure 3.1A). We characterized the linear strain experienced by epithelial cells due to application of negative pressure (Figure 3.7). A plot of applied pressure vs. strain was linear, and we could achieve a dynamic range of linear strain (0 to 19 %) by application of negative pressure (0 to -900 mbar). High levels of applied strain were incompatible with long-term time-lapse microscopy as it generated a significant drift in the axial position of the membrane. We therefore limited the linear strain applied to a maximum of 10%, which is nevertheless a significant proportion of the typical strain experienced by the bladder tissue *in vivo*. We then modelled the bladder filling and voiding over a 6-hour duty cycle with different states: *filling bladder* (0 to 2 hours, 0 to 10% strain), *filled bladder* (2 to 4 hours, 10% strain), *voiding bladder* over a period of 2 minutes (4 hours to 4:02 hours, 10% to 0% strain) and *voided bladder* (4:02 hours to 6 hours, 0% strain) (Figure 3.1D). This 6-hour duty cycle was then repeated for the remaining duration of each experiment. Overall, the bladder-chip model enables co-culture of two cell-types in nutritionally different microenvironments with a physiologically relevant level of applied strain that mimics bladder filling and voiding cycles.

3.3.3 UPEC infection of the epithelial layer under flow in the bladder-chip model

UPEC attachment and invasion of bladder epithelial cells has been shown to be sensitive to fluidic shear stress (Andersen et al., 2012; Zalewska-Piątek et al., 2020). Although UPEC infection in the bladder can occur with or without the presence of shear stress, we infected the epithelial layer on the bladder-chip under flow conditions. The small volumes of the microfluidic chip motivated this approach, as rapid bacterial growth in the diluted human urine could lead to acidification of the medium. We therefore maintained a flow rate of 1.2 ml/hour for a period of 1.5 - 2 hours during infection of the epithelial layer of the bladder-chips with UPEC. Under flow conditions, an overwhelming

majority of bacteria did not attach to the epithelial cells. Time-lapse microscopy showed that bacterial attachment to the epithelial cells increased steadily over this period, but that the typical infectious dose at the end of this period was low (<1 bacterium per epithelial cell, [Figure 3.8](#)).

Accordingly, we established a 28-hour live-cell imaging experimental protocol as shown in the schematic in [Figure 3.1E](#) and described in greater detail in the subsequent sections and in the Materials and Methods. Briefly, this consisted of an initial period of acclimatization, followed by UPEC infection, introduction of neutrophils, and two consecutive cycles of antibiotic treatment and recovery to monitor IBC dynamics at the single-cell level. This experimental protocol therefore mimicked key aspects of the host-pathogen interactions in early stages of UTIs as well as the response to antibiotic treatment.

3.3.4 Diapedesis of neutrophils across the epithelial-endothelial barrier in response to UPEC infection in the bladder-chip

The bladder-chip platform enables continuous imaging while maintaining flow in both epithelial and vascular channels and mechanically stretching the membrane as part of the bladder voiding cycle. At the start of each live-cell imaging experiment, bladder epithelial cells in an initial relaxed state were perfused with sterile pooled human urine diluted in PBS on the epithelial side and endothelial cell medium on the vascular side respectively ([Figure 3.2A1, B1, Figure 3.9A1](#)). The epithelial side was inoculated with a low dose of UPEC in diluted urine and infection was performed under flow ([Figure 3.2A2, B2, Figure 3.9A2](#)) for ca. 1.5 to 2 hours. The first bladder duty cycle also initiated at this timepoint. We maintained the optical focus of the microscope on the epithelial layer over the subsequent course of infection. UPEC attachment was evident during this infection phase by visual inspection ([Figure 3.2B2, Figure 3.9A2](#)).

After this period of infection, unattached bacteria in the epithelial channel were removed by perfusion of diluted urine. Our aim was to study the interaction of UPEC with host cells, therefore this perfusion was maintained throughout the experiment. Continuous perfusion reduced the accumulation of bacteria in the urine and enabled imaging of intracellular bacteria without large background noise in the fluorescence channels from planktonic bacteria. We subsequently performed a series of interventions that mimic the course of UTI infections and used time-lapse imaging to monitor the simultaneous changes in host-pathogen interaction dynamics. To mimic the host response, immune cells were introduced into the vascular channel. Among innate immune cells, neutrophils are the first line of defense in UTIs (Haraoka et al., 1999). We isolated neutrophils from human blood and verified that the isolation procedure yielded neutrophils with a high degree of purity (Son et al., 2017) through

immunostaining for CD15, a neutrophil specific marker (Zahler et al., 1997) (Figure 3.10). To enable identification and tracking of neutrophils, they were pre-labelled with CellTracker™ Deep Red dye, which stains the cytoplasm of these cells.

Neutrophils were subsequently introduced in the bladder-chip devices through the vascular channel, mimicking the natural route of immune cell migration into the bladder (schematic in Figure 3.2A3-A5, snapshots in Figure 3.2B3-B5, Figure 3.9A3-A5). We used a cell concentration of ca. 2 million cells/ml similar to the neutrophil concentration in human blood (Hsieh et al., 2007). During this period, the flow rate through the vascular channel was increased to 3ml/hour to provide a shear stress $\eta = 1 \text{ dyne/cm}^2$, which aids neutrophil attachment to endothelial cells (Alon et al., 1995). In uninfected control chips, neutrophil attachment to the endothelial layer was minimal (Figure 3.11A, B) and diapedesis of neutrophils to the epithelial layer was rare (Figure 3.2C, Figure 3.12A). In stark contrast, infection of the epithelial layer with UPEC elicited a robust attachment of neutrophils to endothelial cells (Figure 3.11C, D), along with rapid diapedesis across to the epithelial side (Figure 3.2B2-B4, Figure 3.9A2-A4, Figure 3.12C). We confirmed that neutrophil diapedesis was also stimulated in the absence of infection, upon exposure to a gradient of pro-inflammatory cytokines that are typically upregulated during UTIs (Agace et al., 1993; Hedges et al., 1992; Nagamatsu et al., 2015; Song et al., 2007) (interleukin-1 α , interleukin-1 β , interleukin-6 and interleukin-8 each at 100 ng/ml) across the epithelial-endothelial barrier (Figure 3.12B). However, neutrophil diapedesis was more robust upon infection as compared to the cytokine gradient, with a higher number of neutrophils observed across multiple fields of view on the epithelial side (Figure 3.12B-D). These results suggest that infection on-chip generates a strongly pro-inflammatory environment locally and that neutrophil diapedesis is further stimulated by the presence of UPEC (Agace et al., 1995; Oliveira et al., 2016).

Using time-lapse imaging, we were also able to quantify the kinetics of neutrophil migration with a temporal resolution of up to 7.5 minutes. Neutrophil diapedesis to the epithelial sites of infection was detected as early as ca. 15-17 minutes post-introduction into the vascular channel (Figure 3.2B3, Figure 3.9A3, supplementary movie SMov1, SMov2). Neutrophils that migrated to the epithelial side aggregated on the epithelial cells (Figure 3.2B4-B5, Figure 3.9A4-A5, supplementary movie SMov1, SMov2). In some cases, these neutrophils were able to control bacterial growth (Figure 3.2B4-B5, solid yellow boxes) whereas in others, bacterial growth was uncontrolled (Figure 3.2B4-B5, dashed white boxes). Diapedesis was observed in every field of view examined across n=4 infected chips, whereas diapedesis occurred infrequently in uninfected controls (Figure 3.2C). Furthermore, the size of these aggregates was significantly larger in infected bladder-chips vs. uninfected controls, with the aggregates in case of infected-chips exhibiting the characteristic features of neutrophil swarms (Isles

et al., 2019; Kienle and Lämmermann, 2016; Kreisel et al., 2010; Lämmermann et al., 2013; Poplimont et al., 2020; Uderhardt et al., 2019). We quantified the size of the swarms formed by either estimating the maximum number of neutrophils observed in fields of view on the epithelial side (Figure 3.2D) or by measuring the total volume occupied by neutrophils normalized to the volume of a 3D field of view (Figure 3.2E). Using either metric, infection generated large swarms that did not occur in uninfected bladder-chips. The dynamics of swarm formation across n=51 and n=40 fields of view in two infected bladder-chips are shown in Figure 3.2F. In infected bladder-chips, swarm formation was rapid, and swarms reached their maximum size typically between 60- and 90-minutes post-introduction of neutrophils (Figure 3.2G).

3.3.5 Neutrophil extracellular traps (NETs) formation in response to UPEC infection

Neutrophils have complex responses to infections (Oliveira et al., 2016), including the formation of neutrophil extracellular traps (NETs) that occur by the release of cytosolic azurophilic granules around a scaffold of decondensed chromatin and potentially serves to trap and kill extracellular bacteria (Brinkmann et al., 2004). NETs have been shown to consist of antimicrobial granules such as myeloperoxidase (Metzler et al., 2011) and neutrophil elastase (Papayannopoulos et al., 2010) and have been observed in urine harvested from UTI patients (Yu et al., 2017). Interestingly, we observed NET formation by neutrophils in the infected bladder-chip. We verified the formation of NETs on the epithelial layer through immunostaining of infected bladder-chips at 3.5 hours post-infection and 2 hours post-introduction of neutrophils in the vascular channel using antibodies against neutrophil myeloperoxidase (Figure 3.2H, S9A1-A3) and neutrophil elastase (Figure 3.2I, Figure 3.13B1-B3). In each case, areas on the epithelial layer with strong immunostaining were observed (Figure 3.2H3, I3). Neutrophils in these areas were typically in large numbers, characteristic of swarms. In addition, by this stage of the experiment, neutrophils that had high levels of myeloperoxidase or elastase typically did not retain strong expression of the cytoplasmic CellTracker dye used for identification of neutrophils in live imaging (cf. Figure 3.2H2 and Figure 3.2H3, Figure 3.2I2 and Figure 3.2I3). For each example, a zoomed-in image clearly shows long filament-like structures that extend between cells and are either myeloperoxidase positive (Figure 3.2H5) or neutrophil elastase positive (Figure 3.2I5), strongly suggestive of NETs (Brinkmann et al., 2004; Metzler et al., 2011; Papayannopoulos et al., 2010). NET formation was also observed in some instances by neutrophils in some locations on the endothelial channel, although large swarms did not form here (Figure 3.13B1-B3).

To further characterize these structures, we imaged the epithelial layer of uninfected and infected bladder-chips with or without the addition of neutrophils using scanning electron microscopy (SEM). Representative images of the epithelial layers of uninfected bladder-chip controls (Figure 3.14A)

contrast with those from infected bladder-chips after neutrophil diapedesis (Figure 3.2J1-J4, Figure 3.14C) and clearly highlight the distinctive features of NET formation. In Figure 3.2J1, neutrophils on the surface of the epithelial layer are clearly distinguishable by their distinctive spherical morphology and size (amber arrowheads). Thick bundles consisting of many thinner NETs formed between these neutrophils are shown by white arrowheads and appear to extend between adjacent neutrophils, as is also evident in Figure 3.14C. A majority of the epithelial cells have a characteristic flattened morphology with cell appendages that can extend between cells (cyan arrowheads); an example of a highly infected epithelial cell that is spherical in shape and with bacteria attached to its surface is indicated with a purple arrowhead (Figure 3.2J1). A series of higher-magnification images in Figure 3.2J2-J4 show the structure of NETs in greater detail. Many individual UPEC bacteria (green arrowheads) are captured in these NETs (Figure 3.2J2-J4), which are themselves composed of many individual thinner fibers (indicated by yellow arrowheads in Figure 3.2J2-J4). These structures did not form in infected bladder-chips without the introduction of neutrophils (Figure 3.14B), confirming their identity as structures identified as NETs via immunofluorescence (Figure 3.2H, I). NET formation was a direct response to UPEC and not caused by hyperactivation of neutrophils due to experimental handling. To verify this, we collected the neutrophils that passed through an infected bladder-chip without attachment. Even upon infection, an overwhelming majority of the cells perfused into the chip flow out without adhering, because of the geometry of the channels in the device. NET formation in these samples was not observed unless the neutrophils were themselves infected by UPEC shed from the bladder-chip (Figure 3.15). The bladder-chip model is therefore able to recapitulate key aspects of the host response to the early stages of UPEC infection while demonstrating that intracellular bacteria were substantially protected from neutrophil-mediated killing.

3.3.6 Heterogenous dynamics of intracellular bacterial communities within urothelial cells

Urinary tract infections that do not resolve upon intervention by the host immune system often require treatment with antibiotics. Antibiotics have complex pharmacokinetic and pharmacodynamic profiles *in vivo*, which we attempted to model through two successive rounds of high dose administration of antibiotics (ampicillin at 40x MIC, Figure 3.16A), on both the epithelial and vascular side, interrupted by periods with no antibiotic (schematics in Figure 3.3A, Figure 3.1E). Continuous time-lapse imaging over this entire period allowed us to capture the responses of bacteria to this simplified model of antibiotic profiles and to study the persistence of UPEC upon antibiotic treatment in the different physiological niches (Figure 3.3 and Figure 3.4).

A consequence of the first cycle of antibiotic administration under flow was the elimination of planktonic bacterial growth in the media in the apical channel, as is observed within the lumen of the

bladder *in vivo*. Many bacteria that were still intact at the end of the antibiotic treatment intact did not regrow after the antibiotic was removed (Figure 3.16B). Regrowth commenced in only a small fraction of bacteria (Figure 3.16C) after a variable lag phase (Figure 3.16D) and rapid regrowth was highly correlated with intracellular location of bacteria within epithelial cells. These subsequently proceeded to form intracellular bacterial communities (IBCs), with a variable lag period. An example of an early stage of the IBC formation is shown in the timeseries in Figure 3.3B1-B5, supplementary movie SMov3. This IBC was initially seeded with few bacteria that are present in Figure 3.3B1 and clearly visible in Figure 3.3B2. At the end of the timeseries, the entire host cell was packed with bacteria (Figure 3.3B5). The exponential increase in bacterial numbers frequently led to the saturation of the 8-bit images in the bacterial channel. We therefore examined similar structures in separate bladder-chips via immunofluorescence (Figure 3.3C, Figure 3.17) staining. Zooms of two of the four IBCs highlighted in Fig. 3C show numerous tightly packed bacteria within epithelial cells that are both CK7+ (Figure 3.3C) and CK8+ (Figure 3.17). These bacterial morphologies are highly similar to early-stage IBCs observed in the bladder (Anderson et al., 2003; Duraiswamy et al., 2018; Justice et al., 2004). Higher resolution images of the biofilm-like structures within IBCs obtained via correlative light (Figure 3.3D) and transmission electron microscopy (Figure 3.3E) showed that bacteria in IBCs can be either coccoid or rod shaped, which is also evident in scanning electron micrographs of bacteria within IBCs (Figure 3.3F). IBCs within bladder-chip model therefore show many of the distinctive morphological features reported from images of infected bladders in the mouse model (Anderson et al., 2003; Hunstad and Justice, 2010).

Numerous reports from the mouse model of infection have shown IBCs to be dynamic structures; growth in IBCs eventually culminates in bacterial shedding or the complete exfoliation of the IBC. The underlying dynamics of these phenotypes is hard to capture in the mouse model, but the bladder-chip model allowed us to track the dynamics of bacterial growth within individual IBCs over extended periods of time, providing information on bacterial dynamics within so-called early, middle, and late-stage IBCs. An example of the heterogeneity in growth rates is evident from the timeseries for three IBCs in Figure 3.3G1-G5, supplementary movie SMov4. IBCs#1 and 2 subsequently began to shed individual bacteria (Figure 3.3G4), a phenotype not observed in IBC#3. At a later timepoint (Figure 3.3G5) the fates of all three IBCs were dramatically different – the cell containing IBC#1 had completely exfoliated and was removed from the field of the view by flow in the epithelial channel, IBC#2 continued to shed bacteria, whereas growth remained slow in IBC#3. We monitored the eventual fate of n=100 IBCs during the first and the second growth cycles which confirmed that shedding and exfoliation were not mutually exclusive. While some IBCs only shed bacteria (n=28) and others

exfoliated without shedding (n=27), a substantial fraction of IBCs showed shedding prior to exfoliation (n=31) and some IBCs displayed neither phenotype (n=14). Furthermore, in addition to the coccoid and rod-shaped morphologies highlighted in [Figure 3.3C-F](#), time-lapse imaging also enabled us to capture morphotypes that occurred relatively rarely such as the intracellular growth of filamentous forms of UPEC ([Figure 3.3H1-H5](#), [Figure 3.18](#), [supplementary movie SMov5](#), [SMov6](#)). In this time series, a filamentous bacterium can be seen and appears to encircle the inner boundary of the cell ([Figure 3.3H1-H4](#)) before filling the volume entirely ([Figure 3.3H5](#)). Overall, time-lapse imaging confirms that a significant fraction of bacteria within IBCs can survive the first round of antibiotic treatment and are the source for reseeding of both the extracellular bacterial populations as well as the subsequent growth of IBCs in newly infected cells.

3.3.7 Dynamic persistence of intracellular bacterial communities within uroepithelial cells

A subsequent round of antibiotic treatment provided an opportunity to study the dynamic persistence of bacteria within IBCs in response to an antibiotic profile that was a closer mimic of the periodic antibiotic exposures *in vivo*. Furthermore, at this stage of the experiment, we were also able to study the responses of bacteria in intermediate and mature late-stage IBCs to antibiotic treatment, which was not possible during the first round of antibiotic administration early in the course of infection. In the examples highlighted in [Figure 3.4A1-A5](#) and [supplementary movie SMov7](#), bacterial growth after the first round of antibiotic treatment resulted in the formation of many large IBCs with tightly packed bacteria ([Figure 3.4A1-A2](#)). Many of the bacteria within each of the four IBCs were eliminated by the antibiotic, but a substantial proportion of bacteria in each IBC nevertheless survived the antibiotic treatment ([Figure 3.4A3](#)). Each of these IBCs subsequently regrows when the antibiotic is removed ([Figure 3.4A4-A5](#)), and two additional IBCs are seeded during this time (white arrowheads in [Figure 3.4A5](#)). Overall, the second round of antibiotic administration led to a sharp decline in instances of subsequent bacterial regrowth ([Figure 3.16C](#)). In all instances, regrowth either occurred directly within IBCs, or was caused by the shedding of bacteria from IBCs to repopulate the extracellular niche and seed new IBCs, highlighting the dynamic stability of this niche and its importance in establishing persistent infection. We therefore performed a careful analysis to quantify bacterial growth rate within IBCs. Growth within IBCs across different time periods was exponential ([Figure 3.4B](#)). We were able to track a subset of IBCs across two growth cycles (examples in [Figure 3.4C](#)). In a majority of instances these revealed exponential growth in the absence of antibiotic, delayed response to antibiotic, and a lag phase after the antibiotic was removed. In general, bacterial growth in IBCs in the second growth cycle was slower than in the first ([Figure 3.4D](#)). However, this population level statistic may be influenced by the fact that many of the IBCs monitored in the second growth

cycle had been exposed to two rounds of antibiotic treatment. For this sub-population, in $n=16$ out of $n=18$ IBCs, growth was slower after the second round of antibiotic administration (Figure 3.4E). Next, we examined the dynamics of bacterial growth within IBCs during the period of antibiotic treatment in greater detail. In the IBC shown in the timeseries in (Figure 3.4F1-F5, Figure 3.19A1-A5, supplementary movie SMov8, SMov9), growth before antibiotic administration (Figure 3.4F1-F2) continued for a considerable period after the antibiotic was administered (Figure 3.4F3-F4, Figure 3.19A1-A3). Eventually, a reduction in bacterial volume towards the end of the antibiotic administration period was observed (Figure 3.4F5, Figure 3.19A4-A5). In contrast, the relatively smaller IBC in the timeseries in Figure 3.4G1-G5, Figure 3.19B2-B5, supplementary movie SMov10, SMov11 continued to grow throughout the period of antibiotic administration. These different dynamics are also captured in the plot of bacterial volume for multiple IBCs before, during, and after the antibiotic treatment (Figure 3.4H). In all cases, bacterial volume continues to increase during a significant period of antibiotic administration and in 2 out of 18 cases, there was no decrease in bacterial volume throughout this period (Figure 3.4H). In contrast, extracellular bacteria likely adherent on the epithelial cells but not internalized within them were rapidly eliminated by combination of antibiotic treatment and flow (Figure 3.4I), in all cases the bacterial volume reduced immediately upon antibiotic administration. This differential killing resulted in a significantly higher proportion of extracellular population of bacteria being killed (Figure 3.4J). Elimination of bacteria within IBCs was highly heterogeneous. Another consequence of this differential killing was that after the second round of antibiotic treatment, regrowth was observed in only a very small fraction of non-IBC UPEC (Figure 3.16C). Protection of bacteria within IBCs therefore has a direct outcome of enabling the reseeding of infection at other locations within the epithelial monolayer.

Lastly, we sought to determine if the bladder duty cycle altered the dynamics of UPEC infection. A comparison between infected bladder-chips with and without the duty cycle (Figure 3.4K, L, Figure 3.20) revealed a significant increase in the bacterial burden when the duty cycle was implemented (Figure 3.4M). These results suggest that the bladder filling and voiding cycle influence the uptake and proliferation of UPEC, possibly through physiological changes in the epithelial cells in response to applied strains (Apodaca, 2004; Carattino et al., 2013; Truschel et al., 2002; Wang et al., 2005). In turn, they suggest a deeper connection between the physiology of mechanically active organs such as the bladder and the processes of infection, which can be characterized in detail using this bladder-chip model.

3.4 Discussion

In our human bladder-chip model, we focused on recapitulating the key aspects of bladder physiology relevant to the study of the earliest stages of UPEC infection and IBC formation. Therefore, superficial bladder epithelial cells, the first cell-type usually infected by UPEC, were cultured both under flow in diluted pooled urine and in co-culture with bladder microvascular endothelial cells. The ability to apply a cyclic mechanical stretch to the PDMS membrane, originally designed to mimic the breathing motion in the lung (Huh et al., 2010a) or the peristaltic motion in the gut (Kim and Ingber, 2013), has been adapted here to mimic the slow expansion and rapid contraction of bladder volume. We demonstrate the ability to perform multiple duty cycles while simultaneously imaging the infected device via long-term time-lapse imaging, a technical advance that is difficult to achieve with bladder explants (Justice et al., 2004) or other *in vitro* studies of UPEC infection of bladder epithelial cells (Andersen et al., 2012; Horsley et al., 2018; Iosifidis and Duggin, 2020; Smith et al., 2006). Using this approach, we found that the total bacterial burden inside infected bladder-chips was significantly higher at a late stage of infection if a duty cycle was applied, unlike the non-significant influence of cyclic stretching on *Shigella* infection of intestinal-chips under flow conditions (Grassart et al., 2019). The exact mechanisms underlying this phenomenon remain to be explored, but there is an increasing understanding of the role of mechanical forces in regulating innate immune function (Solis et al., 2019). Our results showcase the ability of the bladder-chip model to capture these interactions between mechanical function, physiology, and infection, unlike other infection models reported thus far.

A primary focus of *in vitro* models developed so far has been to probe specific aspects of UPEC infection, such as the role of the stratified bladder architecture (Horsley et al., 2018) or the effects of micturition on IBC formation (Andersen et al., 2012; Iosifidis and Duggin, 2020). However, the migration of immune cells into the bladder is difficult to reproduce in these models, and in many of these systems, live-cell imaging remains technically challenging (Horsley et al., 2018; Smith et al., 2006). Furthermore, the models do now allow mechanical manipulations of the cellular co-culture. In that sense, the bladder-chip model complements these existing approaches by providing these additional functionalities. Further development, potentially through the combination of organoid and organ-on-chip approaches, could lead to the development of a fully stratified uroepithelium on-chip.

Neutrophils are the first responders to UPEC infection (Abraham and Miao, 2015; Haraoka et al., 1999), and neutrophil migration involves a series of steps that commences with attachment to the endothelium under flow, migration on the endothelial surface, diapedesis across the epithelial-endothelial cell barrier and movement towards the site of infection (Ley et al., 2007; Nourshargh et al.,

2010). Perfusion of the vascular channel with CD15+ neutrophils isolated from human blood shows that the bladder-chip model recapitulates all these phenotypes, with rapid diapedesis of neutrophils to sites of infection. There, neutrophils aggregate to form swarms (Hopke et al., 2020; Isles et al., 2019; Kienle and Lämmermann, 2016; Lämmermann et al., 2013; Poplimont et al., 2020; Reátegui et al., 2017; Uderhardt et al., 2019) and subsequently, the formation of NETs (Branzk et al., 2014; Brinkmann et al., 2004; Metzler et al., 2011; Papayannopoulos et al., 2010) around extracellular bacteria is observed. Characterization of these structures via SEM shows that they can extend across many tens of microns and stain positive for myeloperoxidase (Metzler et al., 2011) and neutrophil elastase (Papayannopoulos et al., 2010), indicative of potent anti-microbial activity. However, neutrophil control of infection on-chip is partial; this is possibly due to the unrestricted growth of large numbers of extracellular bacteria and in some instances, exacerbated by the loss of some neutrophils due to flow in the channel. Another contributing factor could potentially be the architecture of the PDMS membrane, which permits neutrophil diapedesis only at fixed spatial locations on-chip. Neutrophil migration may also be impacted by the relative stiffness of the PDMS membrane. Nevertheless, the demonstration of NET formation is consistent with the occurrence of these structures both in the mouse model (Ermer et al., 2009) as well as in the urine of infected patients (Yu et al., 2017) and suggests that the model is able to recapitulate important aspects of disease. It is also an important advance for the use of organ-on-chip approaches to recapitulate neutrophil swarm and NET formation in infectious diseases.

IBC formation begins immediately after infection and is already underway upon neutrophil administration. However, clear demonstration of IBCs with a high degree of confidence was only possible after an initial treatment with a high dose of antibiotic that eliminated extracellular planktonic bacteria and improved the optical imaging of bacteria attached to or within epithelial cells. It enabled us to capture the full cycle of IBC growth from few bacteria to a large biofilm and subsequent release via shedding and filamentation. Importantly, the compact nature of the device allowed us to image multiple IBCs concurrently on the same chip with a high temporal resolution while simultaneously mimicking the bladder filling and voiding cycles, which is difficult to achieve in bladder explants (Justice et al., 2004) or bladder monoculture *in vitro* model systems (Andersen et al., 2012; Iosifidis and Duggin, 2020). Our observations reiterate the highly dynamic nature of these structures; growth was asynchronous and heterogenous and outcomes included bacterial shedding, exfoliation and filamentation (Hunstad and Justice, 2010; Justice et al., 2004; Scott et al., 2015). Notably, shedding and exfoliation were not mutually exclusive for the time-period of our observations – we report examples of IBCs that shed bacteria and contract in volume before exfoliation.

While IBCs are clearly acknowledged as critical players in early infection, the contribution towards promoting persistence is not completely understood. For example, Blango *et al.*, (Blango and Mulvey, 2010) showed that incubation of bladder explants containing IBCs with a high dose of antibiotics for a period of 18 hours resulted in a substantial sterilization of these structures and concluded that other populations, notably quiescent reservoirs (Mysorekar and Hultgren, 2006) might play a greater role in the establishment of persistent populations. However, the pharmacokinetic profiles of most antibiotics in the host are not time invariant. In case of ampicillin, a standard regimen of ampicillin treatment is typically a bolus of 250-500 mg of antibiotic administered every 6 hours. Within the serum, ampicillin concentration peaks at a $C_{\max} \sim 3\text{-}40 \mu\text{g/ml}$, which is between 1.5 to 20-fold the MIC as measured in human serum (Bryskier, 2020; Putrinš et al., 2015). We therefore chose concentrations that captured these antibiotic exposures (we used ampicillin at 40x MIC measured in the endothelial cell medium perfused in the vascular channel). Ampicillin concentrations in the blood rapidly decay with a half-life of between 60 and 90 minutes with a characteristic pharmacokinetic/pharmacodynamic profile. This period is modelled well by our experimental protocol where phases with high concentration of ampicillin are interspersed with periods with no antibiotic. We are therefore able to model the delivery of two consecutive doses of antibiotic and find that IBCs offer substantial protection against sterilization by a short duration of a high-dose antibiotic treatment and in many instances, bacterial regrowth after two successive rounds of antibiotic administration. Notably, in smaller ‘early IBCs’, bacterial growth continues throughout the period of ampicillin administration, suggesting that the intact nature of the cell membrane likely diminishes the effect of the drug. Our results suggest that, IBCs may continue to play a role in reseeding sites of infection for a considerable period after the commencement of antibiotic treatment. This has particularly important implications with regard to the compliance of antibiotic use as proliferating IBCs could rapidly re-seed sites of infection throughout the bladder if antibiotic doses are missed. These unique capabilities of the bladder-chip to realistically model antibiotic treatment regimens for IBCs can be leveraged in the future to screen compounds (Spaulding et al., 2017) and identify optimal antibiotic treatments regimens that can eliminate persistent bacterial populations in IBCs or alter the host-pathogen interaction dynamic in UTIs.

In summary, the bladder-chip model incorporates aspects of bladder physiology highly relevant to early UPEC infection in a platform amenable to long-term live-cell imaging as well as for the administration of antibiotics and therapeutics in a physiologically relevant manner. Our results establish the suitability of this model for immunological and drug-delivery studies and show that IBCs are highly

dynamic structures that offer substantial protection from antibiotic clearance for an extended period of time.

3.5 Figures

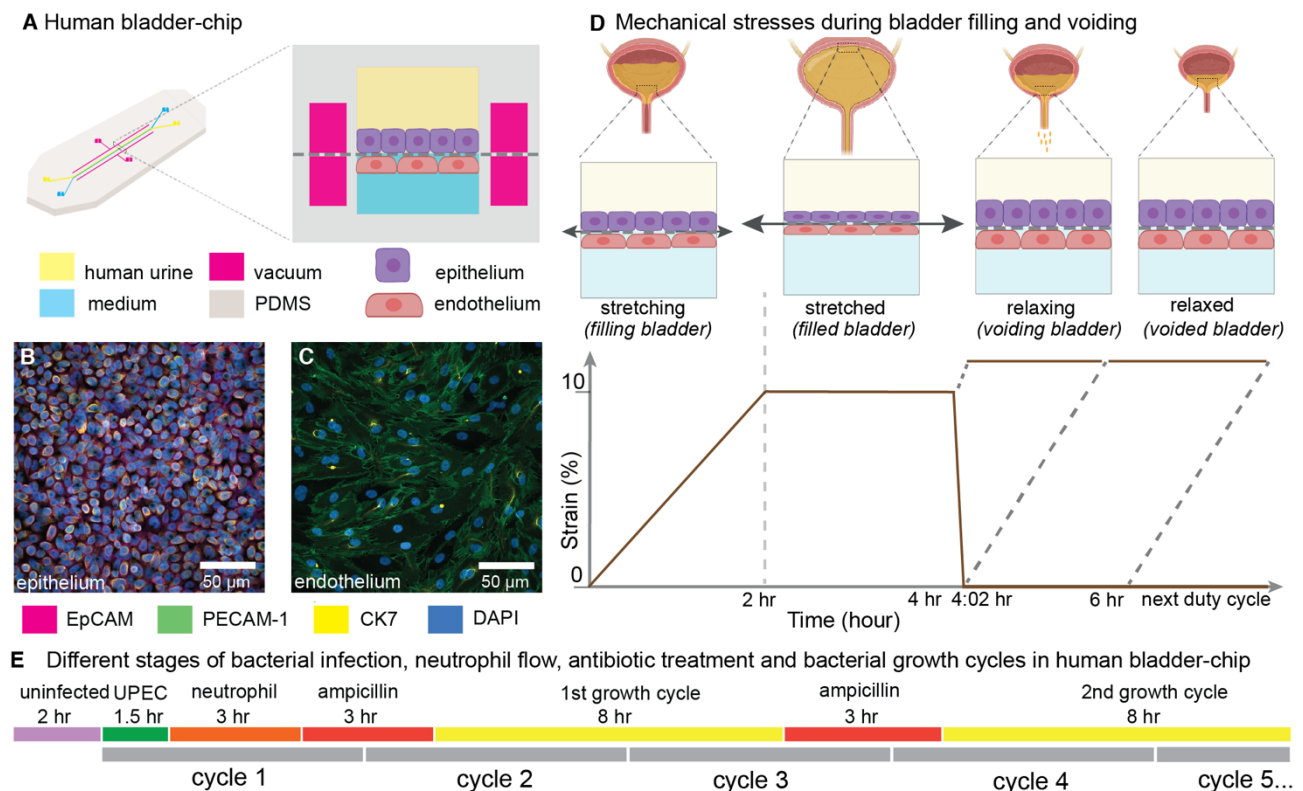


Figure 3.1: Human Bladder-chip model of UTI recapitulates the physiology of bladder filling and voiding.

(A) Schematic of the human bladder-chip with co-culture of the HTB9 human bladder epithelial cell line (epithelium, top) and primary human bladder microvascular endothelial cells (endothelial, bottom) on either side of the stretchable and porous membrane. Pooled human urine diluted in PBS and endothelial cell medium were perfused in the apical and vascular channels respectively to mimic bladder physiology. A negative pressure in the ‘vacuum’ channels (magenta) on either side of the main channel was applied to stretch the porous membrane to mimic stretching of the bladder. (B, C) Immunofluorescence staining of confluent epithelial and endothelial cell monolayers (anti-EpCAM (magenta) and anti-CK7 (yellow) for the epithelial cells and anti-PECAM-1 (green) for the endothelial cells) in an uninfected control chip. Some endothelial cells also stained positive for CK7. Cell nuclei were labeled with DAPI (azure). (D) Schematic of the reconstitution of the bladder filling and voiding cycle via stretching of the membrane with a duty cycle of 6 hours. The cycle consisted of a linear increase in strain through stretching of the membrane (*filling bladder*, 0 to 2 hours), maintenance of the membrane under stretch (*filled bladder*, 2 to 4 hours), a quick relaxation of applied strain over 2 minutes (*voiding bladder*, 4:02 hours) and maintenance without applied strain (*voided bladder*, 4:02 hours to 6 hours). (E) An overview of the timeline of the experimental protocol including infection, addition of neutrophils via the vascular channel, and two cycles of antibiotic treatment interspersed by two bacterial growth cycles. The consecutive bladder duty cycles are indicated.

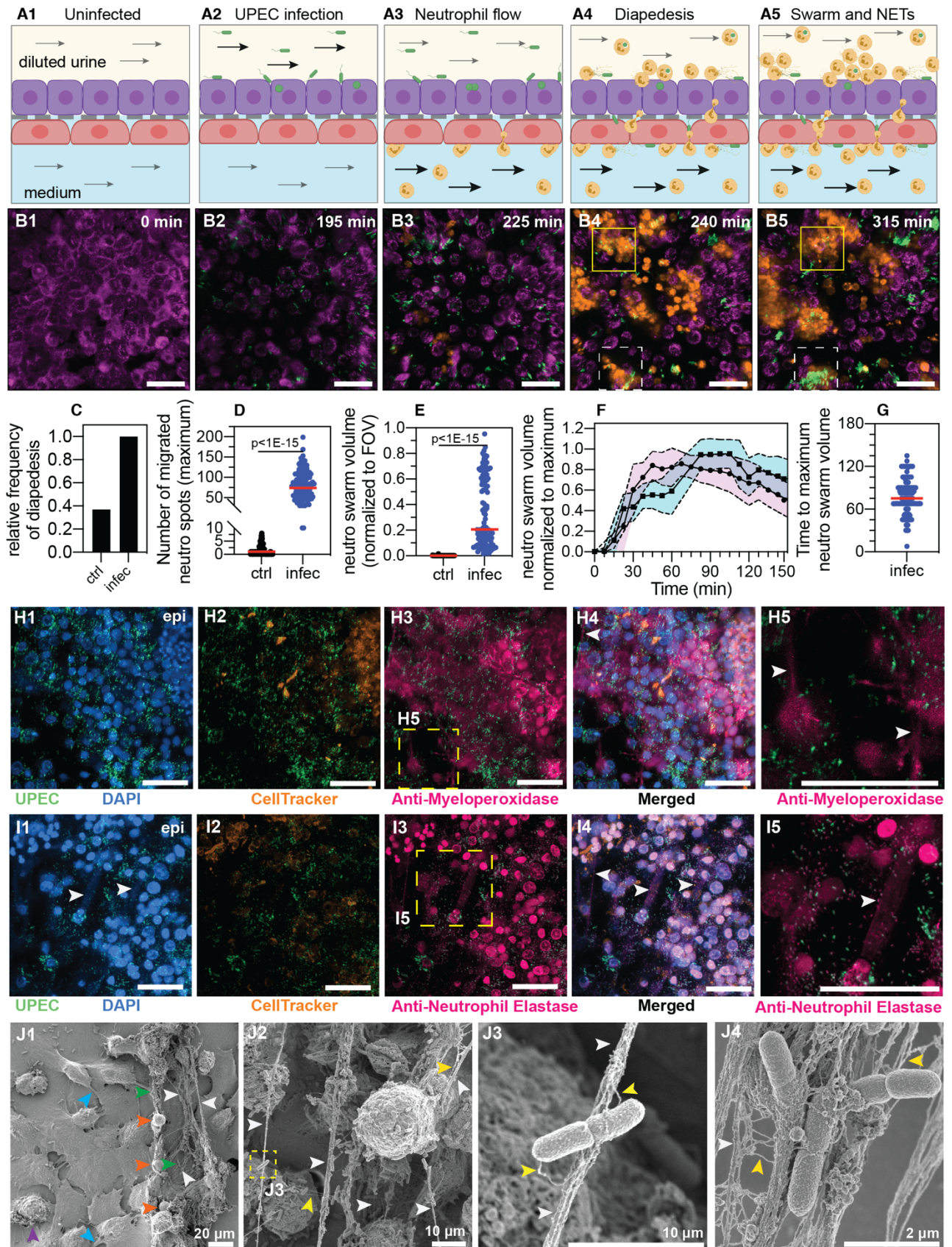


Figure 3.2: Neutrophil diapedesis and NET formation on-chip.

(A1-A5) Schematic of the UPEC infection, introduction of neutrophils and diapedesis of neutrophils across the epithelial-endothelial barrier to sites of infection. Flow in the epithelial and endothelial channels is indicated by arrows; the flow rate was increased upon introduction of neutrophils in the vascular channel to

increase attachment. Increased flow rate in the epithelial and endothelial channel is indicated by black arrows. **(B1-B5)** Snapshots from time-lapse imaging highlighting each stage in the infection cycle shown in **(A1-A5)**. Bladder epithelial cells (magenta) and neutrophils (amber) were identified with membrane (Cell Mask Orange) and cytoplasmic (Cell Tracker Deep Red) dyes, respectively. UPEC identified via constitutive expression of YFP are shown in green. Neutrophil swarms could either control bacterial growth (yellow dashed square, compare **B4** vs **B5**) or did not manage to restrict bacterial growth (white dashed square, compare **B4** vs **B5**). **(C)** Bar charts for relative frequency of neutrophil diapedesis (black) in $n=3$ uninfected control bladder-chips and $n=4$ infected bladder-chips. Data obtained from $n=95$ and $n=116$ fields of view, each of which was $206 \times 206 \mu\text{m}^2$. **(D)** Quantification of the number of neutrophils detected on the epithelial layer, in control and infected bladder-chips. The red bar represents the median value, $p < 1\text{E-}15$. In many instances in the uninfected control bladder-chips, no neutrophil diapedesis is detected. Data obtained from $n=95$ and $n=130$ across $206 \times 206 \mu\text{m}^2$ fields of view. **(E)** A plot of the maximum neutrophil swarm volume on the epithelial layer normalized to the total volume for $n=67$ and $n=118$ fields of view on $n=3$ uninfected control and $n=3$ infected bladder-chips. The red bar represents the median value. $p < 1\text{E-}15$. **(F)** A plot of neutrophil swarm volume on the epithelial layer over time for $n=51$ and $n=40$ fields of view for $n=2$ technical replicates indicated by squares and circles. For each time profile, the volume is normalized to the maximum volume attained over the timeseries and $t=0$ refers to the timepoint at which neutrophils are introduced into the vascular channel **(G)** Plot of the time to reach the maximum swarm volume in $n=154$ fields of view across $n=4$ infected bladder-chips. **(H1-H5, I1-I5)** NET formation by neutrophils on the epithelial layer. The neutrophils are identified by a cytoplasmic dye (CellTracker Deep Red, false coloured in amber) **(H2, I2)** and immunostaining with an anti-myeloperoxidase antibody **(H3, zooms in H5)** or an anti-neutrophil elastase antibody **(I3, zooms in I5)**. Merged images in each case are shown in **H4** and **I4**. UPEC identified via YFP expression is shown in spring green. Nuclear labelling with DAPI is shown in azure. **(H5)** NETs, identified via anti-myeloperoxidase staining or anti-elastase staining are indicated with white arrows in **(H5)** and **(I5)** respectively. **(J1-J4)** Scanning electron micrographs of the epithelial layer of an infected bladder-chip 2 hours after the introduction of neutrophils in the endothelial channel. **(J1)** Neutrophils (amber arrowheads) are visible above a layer of epithelial cells. Thick bundles consisting of many thinner NET structures between neutrophils are indicated by white arrowheads, and examples of individual UPEC bacteria within the NETs are indicated by green arrowheads. A heavily infected epithelial cell with UPEC visible on the epithelial cell (purple arrowhead), and appendages between epithelial cells (cyan arrowheads) are also visible. **(J2)** Micrographs showing thick bundles consisting of many thinner NET structures (white arrowheads) that extend between cells and trap many individual bacteria. Thinner NET fibers (yellow arrowheads) are also visible. **(J3)** Zooms of the regions in **J2** identified by a yellow dashed square. Two bacteria held by a thick bundle composed of many thinner NET fibers are shown. **(J4)** Micrograph highlighting multiple bacteria trapped between NET bundles. p -values in **D** and **E** were calculated using a Mann-Whitney test. Scale bar = $50 \mu\text{m}$ in **B1-B5, H1-H5, I1-I5**.

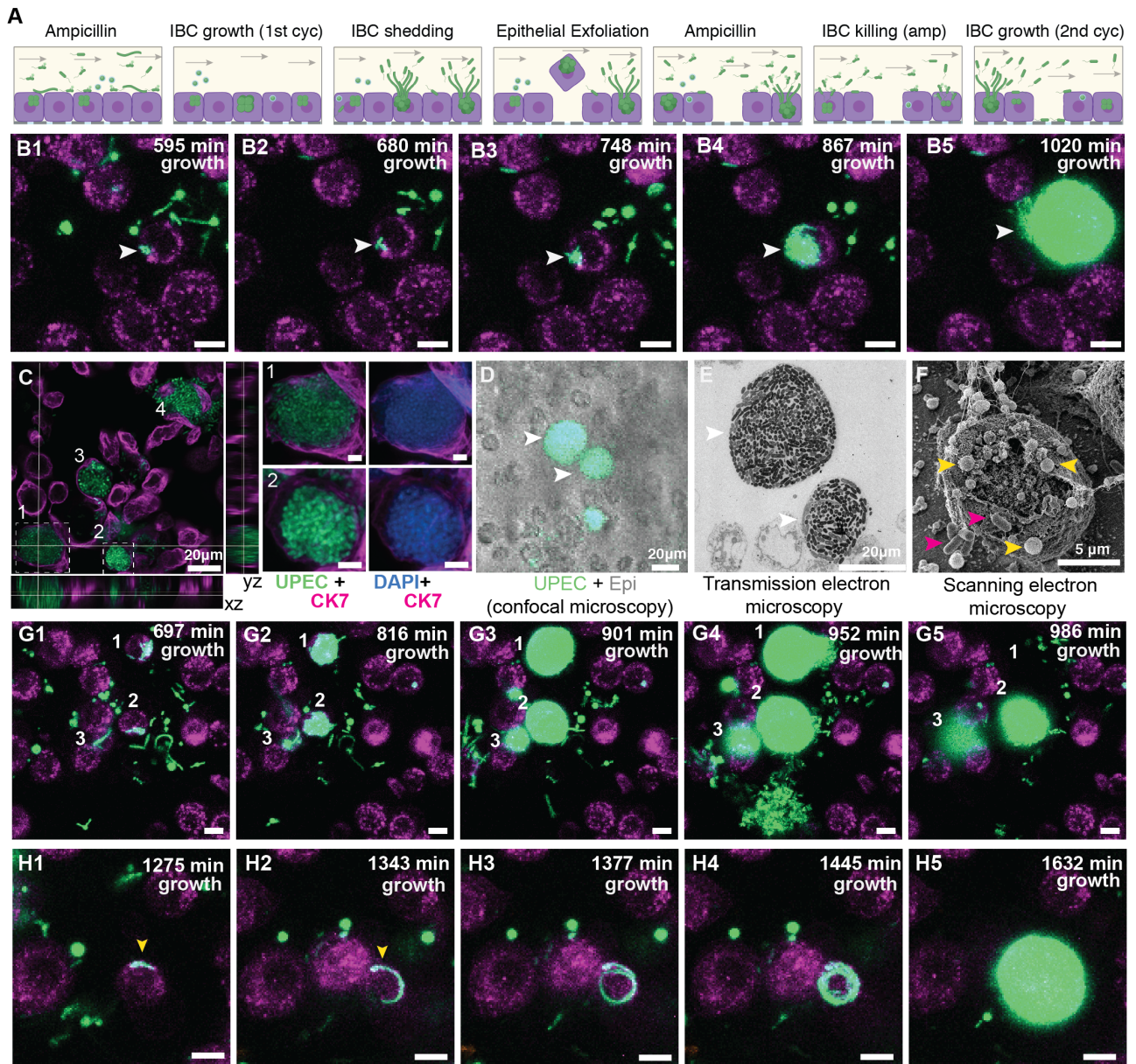


Figure 3.3: Bladder-chip reveals dynamics of IBC growth, shedding and exfoliation.

(A) Schematics of the host-pathogen interactions within IBCs between successive rounds of antibiotic treatment with outcomes including shedding of bacteria and cell exfoliation shown. (B1-B5) Timeseries for the growth of an IBC from few bacteria (white arrowhead) after the first round of ampicillin treatment. Bacteria grow to completely fill the cell volume (B5). (C) Immunofluorescence characterization of two IBCs; the intracellular nature of growth is confirmed with staining with an anti-CK7 antibody. Correlative light (D) and transmission electron micrographs (E) show two IBCs filled with both rod-shaped and coccoid-shaped bacteria. (F) Coccoid-shaped bacteria (yellow arrowheads) and rod-shaped bacteria (magenta arrowheads) are also visible in a scanning electron micrograph of an infected epithelial cell. IBCs on infected bladder-chips shown in C-F were fixed ca. 13.5 hours after UPEC infection and 6 hours into the first growth cycle. (G1-G5) Three examples of IBC growth, labelled 1 – 3 with differing outcomes. Unrestricted bacterial growth is observed within all IBCs. In IBC#1 at timepoint (G4) the IBC begins to shed bacteria into the surrounding medium. The cell exfoliates in the time interval between (G4 and G5). In IBC#2, bacterial shedding is visible at (G4) and shedding continues until end of the timeseries with a reduction in bacterial volume. In contrast, growth within IBC#3 is slower and neither shedding nor exfoliation occurs within the timeseries. (H1-H5) Timeseries highlighting an example of filamentous UPEC growth within an IBC. Scale bars, 10 μ m in B1-B5, G1-G5 and H1-H5.

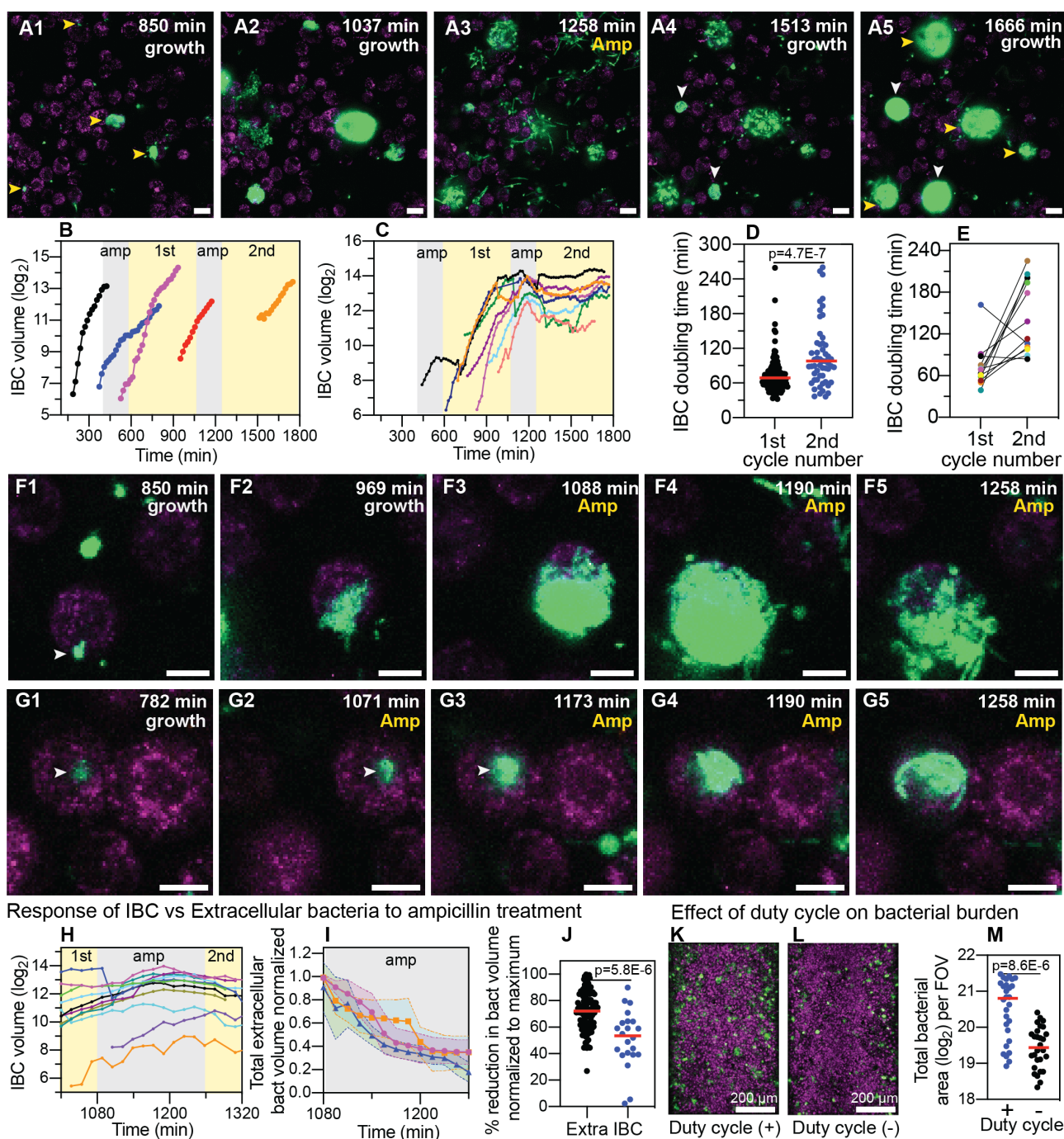


Figure 3.4: IBCs offer a semi-protective niche that delays clearance of bacteria by antibiotics.

(A1-A5) Bacteria persist and grow in IBCs despite antibiotic treatment. Snapshots show the growth of four IBCs with variable growth rates (A1-A2). Ampicillin treatment eliminates some but not all of the bacteria within each IBC (A3). Growth resumes at all sites in (A4, A5), formation of new IBCs in the second growth cycle is indicated by white arrowheads. (B) Plots of logarithm of bacterial volume within five separate IBCs demonstrates exponential bacterial growth. IBCs are seeded dynamically; growth can occur either in the first or second growth cycle, or prior to the administration of antibiotic, or in few cases continues in the presence of the antibiotic. (C) Plots of the logarithm of bacterial volume vs. time for $n=8$ IBCs tracked across two growth phases with an intermediate period of ampicillin treatment. In the growth phases, growth is exponential and bacterial volume continues to increase for up to ca. 120 minutes after administration of antibiotic before declining due to loss of bacteria. In each case, growth resumes after the antibiotic is removed. (D) Scatter plots of the doubling time of bacterial volume in IBCs as measured in the first growth cycle ($n=102$) and the second growth cycle ($n=59$). Growth in the second cycle is significantly slower ($p=4.7E-7$), red line represents the median value. (E) Doubling time of bacterial volume in IBCs in the first and second growth cycle for some of

the IBCs in **(D)** that survived the antibiotic treatment. In $n=16$ out of 18 instances, growth is slower in the second growth cycle. **(F1-F5)** High resolution time-series that highlights bacterial growth within an IBC prior to **(F1, F2)** and after **(F3-F5)** administration of ampicillin. Some bacteria within this IBC are subsequently eliminated **(F5)**. **(G1-G5)** High resolution time-series that highlights bacterial growth within an IBC prior to **(G1, G2)** and after **(G3-G5)** administration of ampicillin. The bacterial volume within this IBC is not diminished by antibiotic treatment **(G5)**. **(H)** Plots of logarithm of bacterial volume within $n=11$ IBCs before, during, and after the second round of antibiotic treatment. **(I)** Plot of the volume of extracellular bacteria upon antibiotic administration from $n=103$ across $206 \times 206 \mu\text{m}^2$ field of view from $n=3$ bladder-chips. The bacterial volumes are normalized to the volume immediately prior to the antibiotic administration. **(J)** Scatter plot of the extracellular bacterial volume ($n=105$) and bacterial volume within IBCs ($n=22$) after antibiotic treatment as a fraction of the maximum bacterial volume prior to antibiotic treatment. Red line represents the median value, $p=5.8\text{E-}6$ as calculated by Mann-Whitney test. **(K, L)** Representative images from the epithelial face of the infected bladder-chips with or without duty cycle. **(M)** Scatter plots of the logarithm of the total bacterial area across $n=14$ from infected bladder-chips with ($n=2$) and without ($n=2$) duty cycle, $p=8.6\text{E-}6$. Infected bladder-chips shown in K, L were fixed ca. 13.5 hours after UPEC infection and 6 hours into the first growth cycle. p-values calculated using a Mann-Whitney test. Scale bars, $10 \mu\text{m}$ in panels **A1-A5, F1-F5, and G1-G5**.

| Cell type | Cell density/ $10^4\mu\text{m}^2$ |
|-------------|-----------------------------------|
| Epithelial | 31.7 ± 5.1 |
| Endothelial | 4.0 ± 0.6 |

Table 2: Characterization of epithelial and endothelial cell densities from a total of n=18 fields of view in both the epithelial and endothelial layers from n=2 bladder-chips.

3.6 Supplementary Figures

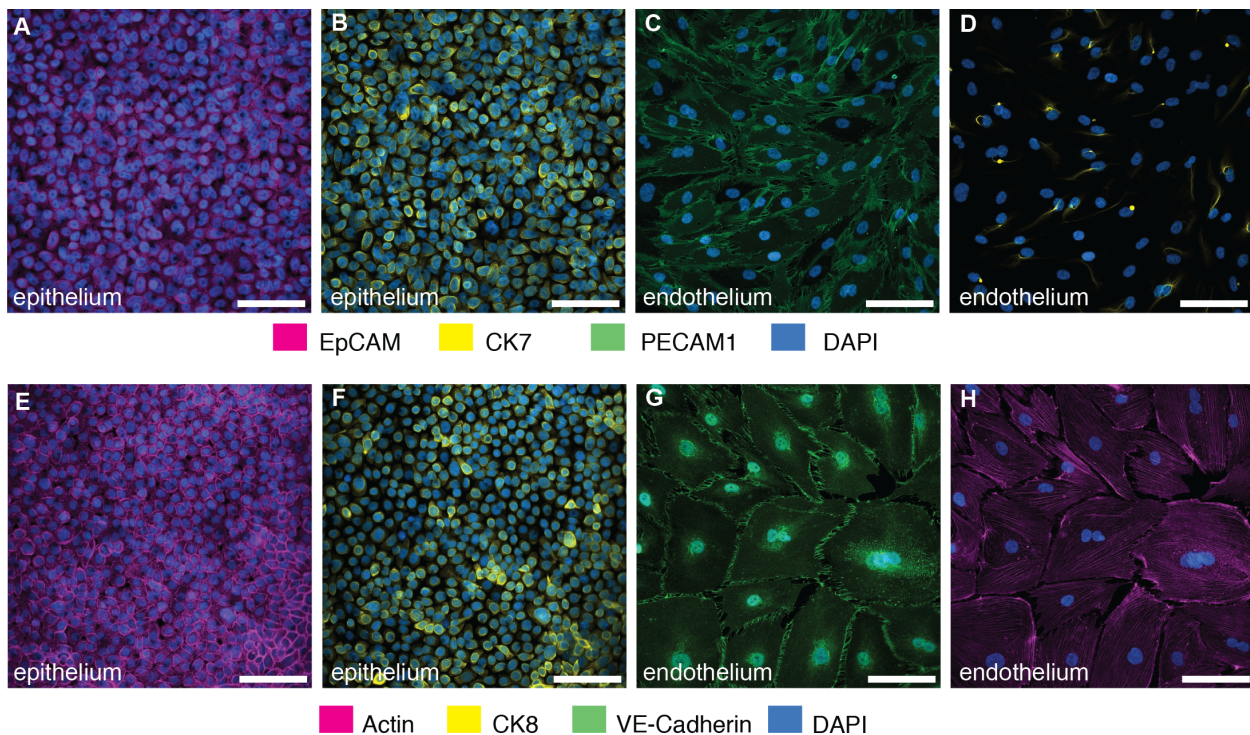


Figure 3.5: Characterization of co-cultures of bladder epithelial cells and bladder endothelial cells in bladder-chip.

Immunofluorescence characterization of HTB9 bladder epithelial cells in bladder-chip for Epithelial Cell Adhesion Molecule (EpCAM) (A), cytokeratin 7 (CK7) (B), and cytokeratin 8 (CK8), a marker for differentiated urothelial cells (F). Immunofluorescence characterization of primary human bladder microvascular endothelial cells in bladder-chip for tight junction markers such as Platelet Endothelial Cell Adhesion Molecule-1 (PECAM-1) (C) and vascular endothelial cadherin (VE-cadherin) (G). Some endothelial cells also express CK7 (D). Filamentous actin staining for epithelial (E) and endothelial (H) cells. Cell nuclei were labeled with DAPI (azure) in all panels. Scale bars, 50 μm in all panels.

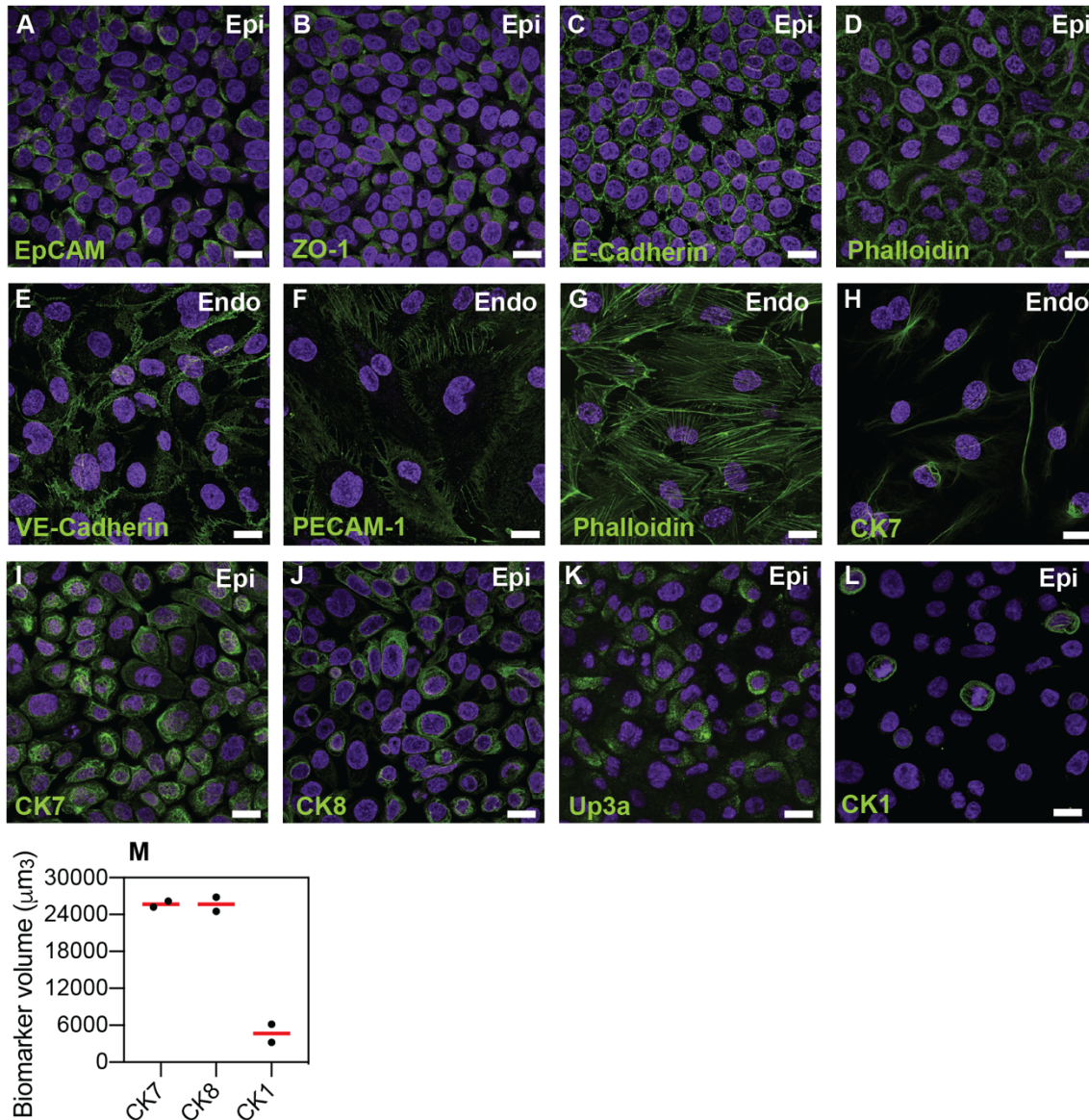


Figure 3.6: Characterization of monocultures of HTB9 bladder epithelial cells and HMVEC-Bd bladder microvascular endothelial cells.

Characterization of the HTB9 bladder epithelial cells for epithelial tight junction markers such as Epithelial Cell Adhesion Molecule (EpCAM) (A), epithelial cadherins (E-cadherin) (B), Zonula Occludens-1 (ZO-1) (C), and filamentous actin (Phalloidin) (D). Bladder endothelial cells express tight junction markers such as vascular, Platelet Endothelial Cell Adhesion Molecule-1 (PECAM-1) (E), endothelial cadherin (VE-cadherin) (F) and filamentous actin (Phalloidin) (G). Some endothelial cells also showed staining for CK7 (H). Characterization of the HTB9 bladder epithelial cell line for the uroepithelial cell marker cytokeratin 7 (CK7) (I), for umbrella cell specific markers cytokeratin 8 (CK8) (J) and uroplakin 3a (Up3a) (K), and the basal cell marker cytokeratin 1 (CK1) (L). CK1 expression was sparse and lower than CK7 and CK8, data obtained from 2 fields of view in an ibidi m-Slide 8 well (M). Red lines represent the median value. Epithelial and endothelial cells were grown to ca. 75-90% confluence in ibidi 8-wells. Cell nuclei were labeled with DAPI (cyan). Scale bars, 10 μm in (A-L).

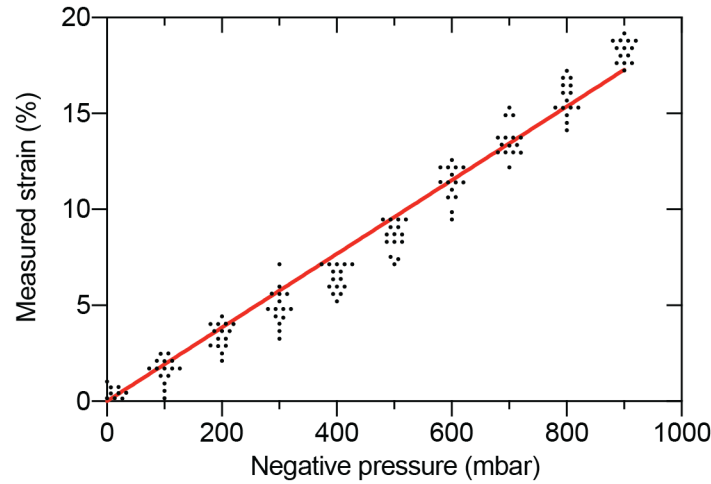


Figure 3.7: Quantification of the linear strain in the PDMS membrane as a function of applied negative pressure in the vacuum channels of the bladder-chip.

Pore-to-pore distance was measured in the PDMS membrane ($n=14$) on human bladder chip under different values of applied pressure and used to calculate the linear strain ($\Delta l = \frac{l_s - l_r}{l_r}$). l_s and l_r refer to the pore-to-pore distance in the stretched (l_s) and relaxed state (l_r).

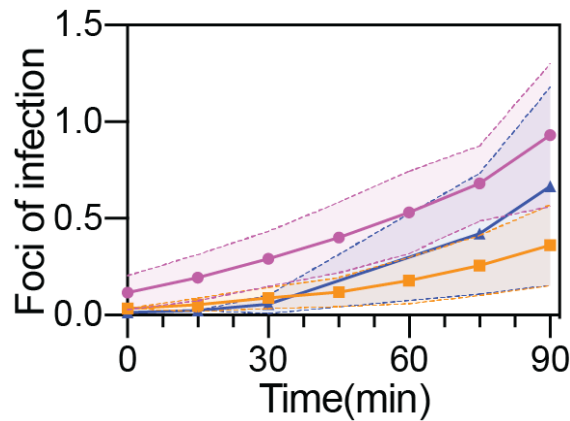


Figure 3.8: Quantification of UPEC attachment to bladder epithelial cells on-chip under flow.

Ratio of number of attached UPEC to the average number of epithelial cells in $n=25$ (magenta line), $n=38$ (orange line) and $n=34$ (blue line) fields of view, each $206 \times 206 \mu\text{m}^2$ across on the epithelial layer of $n=3$ infected bladder-chips. In each case, the protocol results in less than 1 focus of infection per epithelial cell at the end of the 90-minute infection period. The dotted lines and the shaded regions represent the standard deviation.

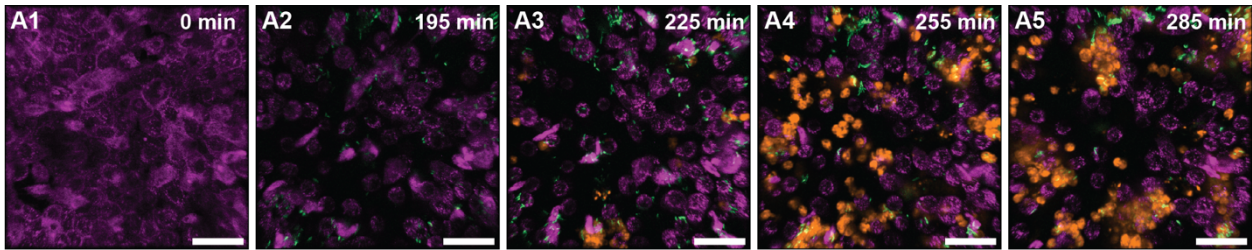


Figure 3.9: Timeseries highlighting neutrophil diapedesis and swarm formation.

Additional images that highlight the diapedesis of neutrophils across the epithelial-endothelial barrier and the formation of neutrophil swarms. Bladder epithelial cells (magenta) and neutrophils (amber) were identified with membrane (Cell Mask Orange) and cytoplasmic (Cell Tracker Deep Red) dyes, respectively. UPEC identified via constitutive expression of YFP are shown in green. In all images, scale bar = 50 μm .

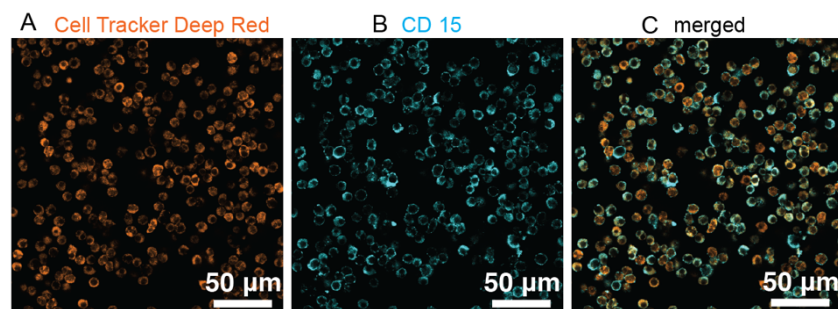


Figure 3.10: Neutrophils isolated from human blood are CD15+.

Images of neutrophils isolated via negative depletion from human blood and labelled with a cytoplasmic dye (Cell Tracker Deep Red) (**A**) and immunostained with an anti-CD15 antibody (**B**). (**C**) Merged image for both channels confirms that all neutrophils are CD15+.

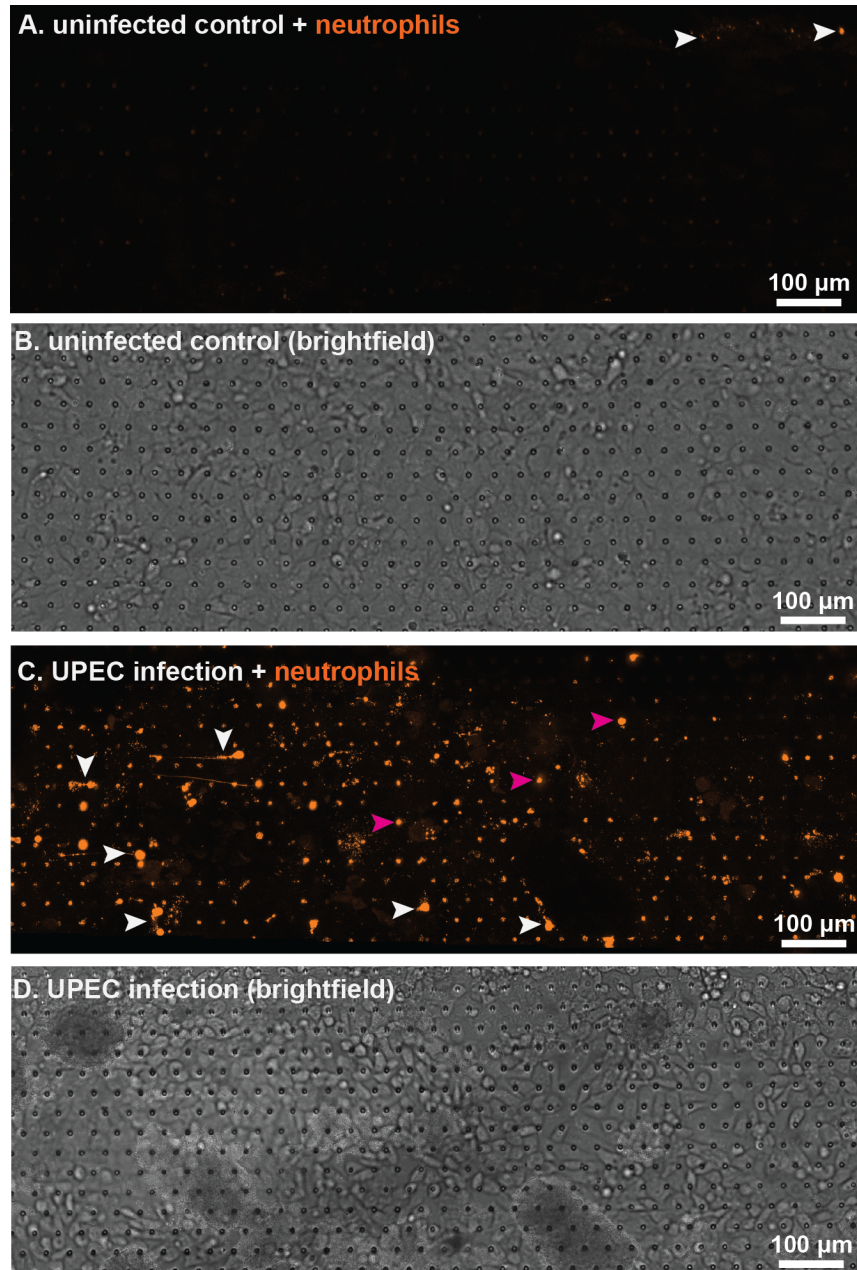


Figure 3.11: Neutrophil attachment to endothelial cells is enhanced upon bacterial infection.

Fluorescent (A) and brightfield (B) imaging of the endothelial layer of an uninfected bladder-chip. The few neutrophils (identified by CellTracker Deep Red, amber) attached to the endothelial layer are indicated by white arrowheads. Fluorescent (C) and brightfield (D) imaging of the endothelial layer of an infected bladder-chip, 1.5 hours after infection of the epithelial layer. Neutrophils attached to the endothelial layer are marked by white arrowheads and examples of diapedesis through the PDMS pores to the epithelial layer are marked with magenta arrowheads. In all panels, neutrophils (amber) were introduced into the vascular channel of the bladder-chip under a flow rate of 3 ml/hour corresponding to a shear stress $\eta=1$ dyne/cm².

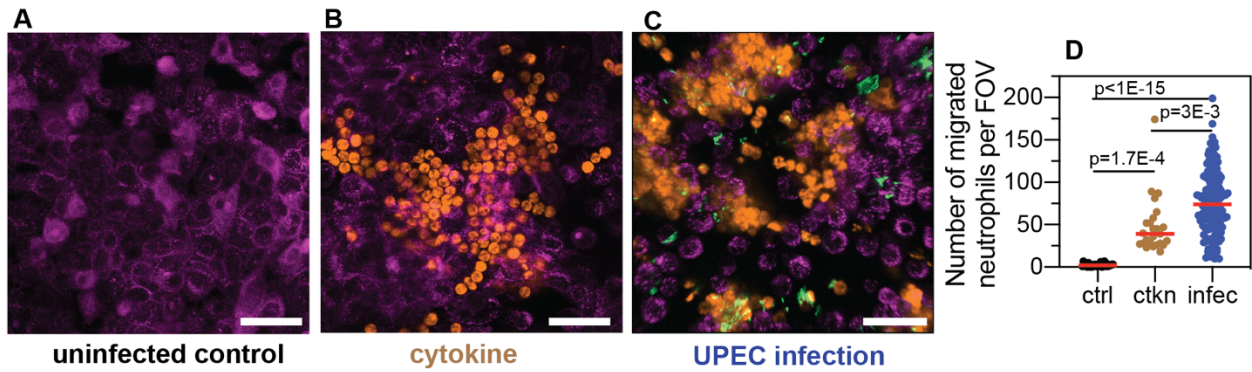


Figure 3.12: Neutrophil diapedesis is stimulated by a pro-inflammatory cytokine gradient across the epithelial-endothelial barrier.

(A) Representative images of the epithelial layer of an uninfected control bladder-chip, 2 hours after the introduction of neutrophils in the endothelial channel. No neutrophil diapedesis is observed. (B) Representative image of the epithelial layer of an uninfected control bladder-chip exposed to a cocktail of pro-inflammatory cytokines (Interleukin-1 α , Interleukin-1 β , Interleukin-6 and Interleukin-8, each at 100 ng/ml) added to the diluted urine on the epithelial side and maintained under flow for 2 hours. Epithelial cells (magenta, identified via CellMask Orange) and neutrophils (amber, identified via CellTracker Deep Red) are shown. (C) Representative image of the epithelial layer of an infected bladder-chip 2 hours after the introduction of neutrophils in the endothelial channel. (D) Scatterplot of maximum number of neutrophils detected in 206 x 206 μm^2 fields of view under control (n= 26), cytokine stimulation (n=26) and infection (n=130). P-values were calculated using Kruskal-Wallis ANOVA Test. Red lines represent median values. Scale bars, 50 μm .

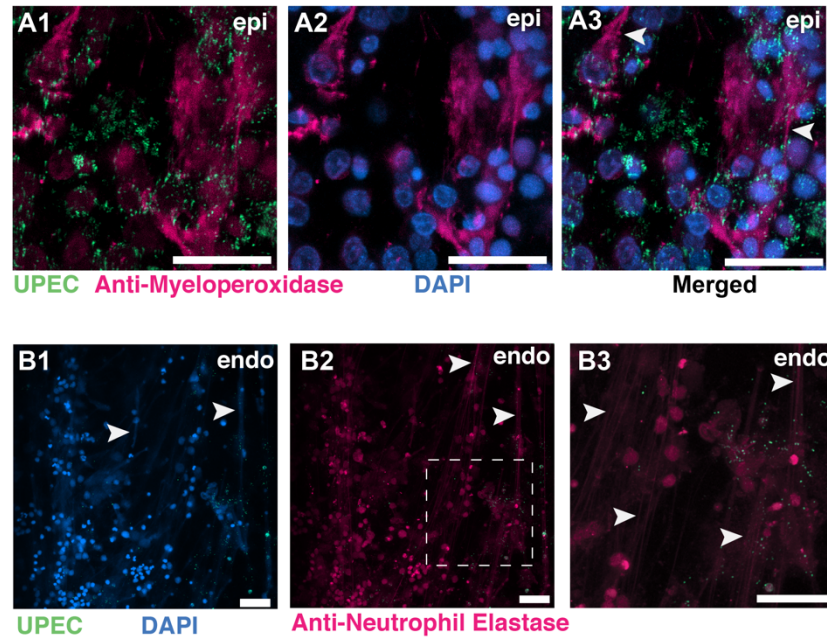


Figure 3.13: NETs formation on the epithelial and endothelial layers of an infected bladder-chip.

(A1-A3) Additional example of NETs formation by neutrophils on the epithelial layer (epi) of an infected bladder-chip. Neutrophils are identified via immunostaining with an anti-myeloperoxidase antibody (A1-A2). UPEC identified via YFP expression are shown in spring green (A1). Nuclear labelling with DAPI is shown in azure (A2). A merged image is shown in A3. (B1-B3) An example of NETs formation by neutrophils on the endothelial layer (endo) of an infected bladder-chip. UPEC identified via YFP expression are shown in spring green and nuclear labelling with DAPI is shown in azure (B1). Neutrophils are identified via immunostaining with an anti-neutrophil elastase antibody (B2). A zoomed image corresponding to the white dashed box in B2 is shown in B3. In all images, scale bar = 50 μ m.

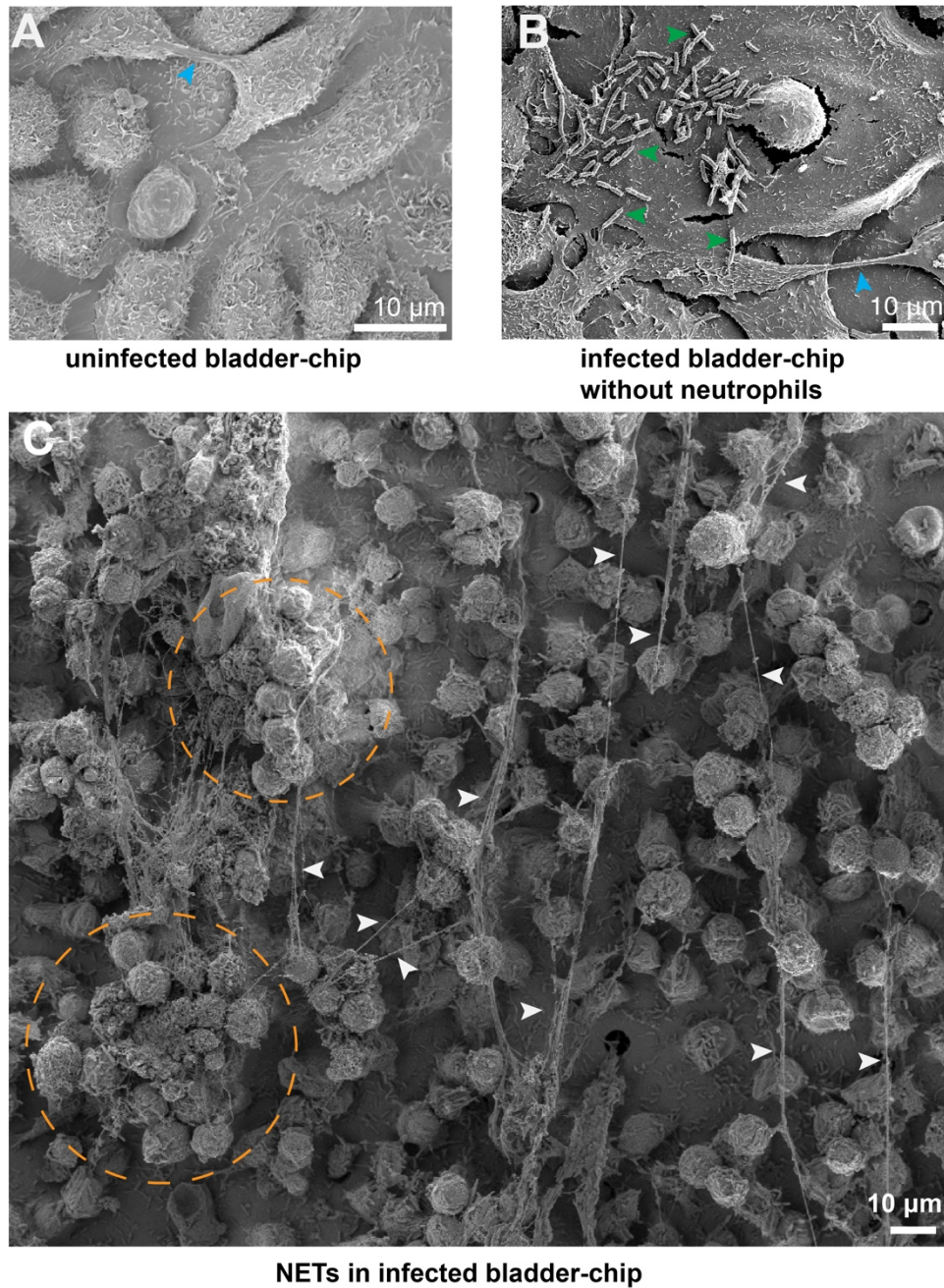


Figure 3.14: SEM characterization of uninfected and infected bladder-chips.

(A) SEM image of the confluent epithelial layer of an uninfected bladder-chip. Appendages between epithelial cells are indicated by cyan arrowheads. (B) Example from an infected bladder-chip without the addition of neutrophils. Long filaments characteristic of NET formation is not observed. Individual UPEC on the surface of the epithelial cells are indicated by green arrowheads. Appendage between epithelial cells is indicated by a cyan arrowhead (C) Additional example of formation of NETs by a large swarm of neutrophils on the epithelial layer of an infected bladder-chip. NETs are indicated by white arrowheads, and large clusters of neutrophils are indicated by dashed amber circles.

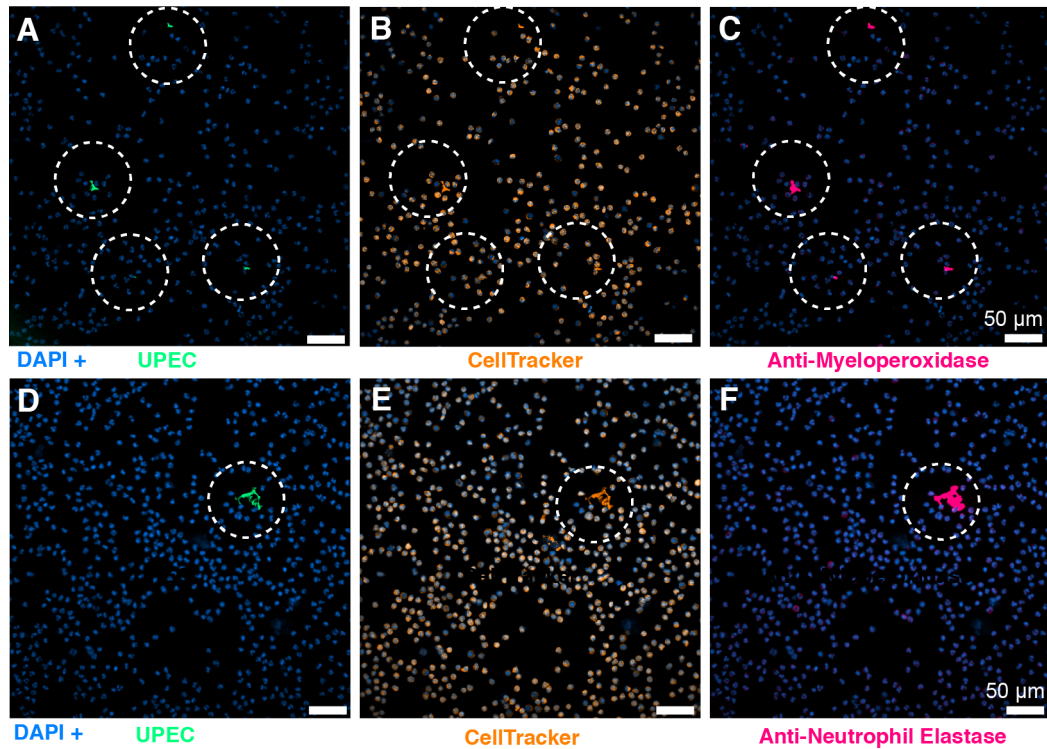


Figure 3.15: Neutrophils do not form NETs in response to shear stress in the bladder-chip.

Neutrophils infused through the vascular channel of an infected bladder-chip were collected and characterized via immunofluorescence for myeloperoxidase (A-C) and neutrophil elastase expression (D-F) to identify the formation of NETs, indicated by dotted white circles. All neutrophils are labelled by the cytoplasmic CellTracker dye (shown in amber in B, E). Both myeloperoxidase expression (marked with dotted white circles in C) and elastase expression (marked with dotted white circles in F) coincide with infected neutrophils (A, D). UPEC are identified via YFP expression and colored spring green, nuclear labelling is indicated in azure. Scale bars, 50 μm in all panels.

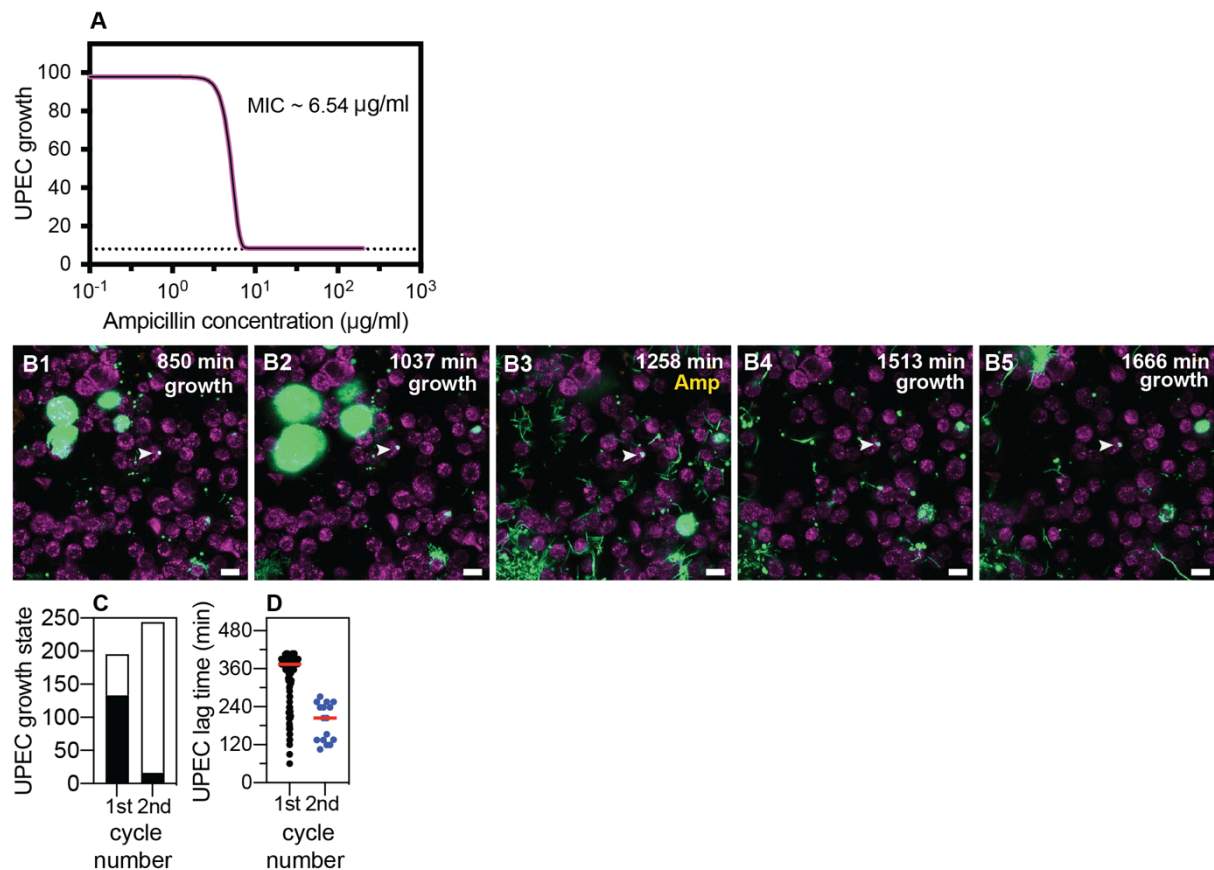


Figure 3.16: Non growing UPEC in response to ampicillin administration in the bladder-chip.

(A) Measurement of ampicillin minimum inhibitory concentration (MIC) in endothelial cell medium for the UPEC strain used in these experiments. (B1-B5) Example of a non-growing clump of UPEC within an epithelial cell following the first growth cycle (indicated by white arrowheads in all images). The bacteria are non-growing throughout the first growth cycle (B1, B2), the second cycle of ampicillin treatment (B3) and subsequently after the removal of antibiotic (B4, B5). (C) Classification of the growth state of intracellular bacterial microcolonies as growing (black) or non-growing (white) across $n=108$ fields of view in total from $n=3$ infected bladder chips during the first and second growth periods. (D) Scatter plot for the distribution of lag time (measured as the time taken to resume growth after removal of antibiotic) for intracellular bacterial microcolonies during the first ($n=133$) and second ($n=16$) growth cycles. Red line represents the median value. Scale bars, 10 μm in B1-B5.

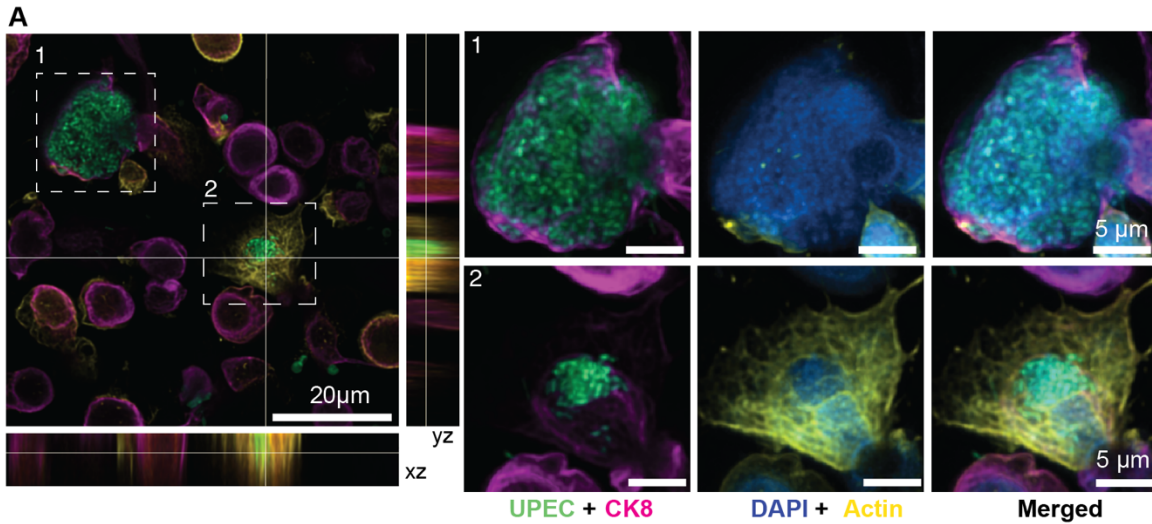


Figure 3.17: Immunofluorescence characterization of IBC formation.

(A) Confocal images of two IBCs within epithelial cells with different morphologies. UPEC are labelled in spring green, anti-CK8 staining is shown in magenta, F-actin labelling is shown in yellow, and nuclear labelling with DAPI is shown in azure. IBCs on the infected bladder chip were fixed 13.5 hours after UPEC infection and 6 hours into the 1st growth cycle.

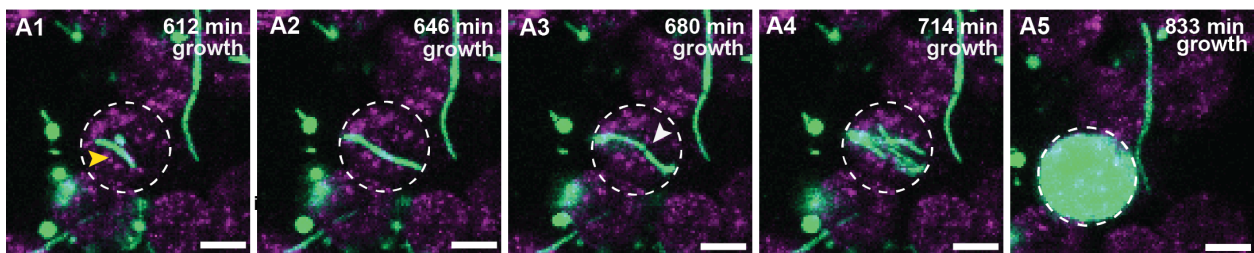


Figure 3.18: IBC formation from filamentous UPEC.

(A1-A5) Additional example of intracellular growth of filamentous UPEC that develops into an IBC. The growing filament (A1-A2) is eventually restricted by the cellular volume and bends (A3) before reductive division (marked by white arrowhead in A3) and IBC formation occurs. Scale bars, 10 μm in A1-A5.

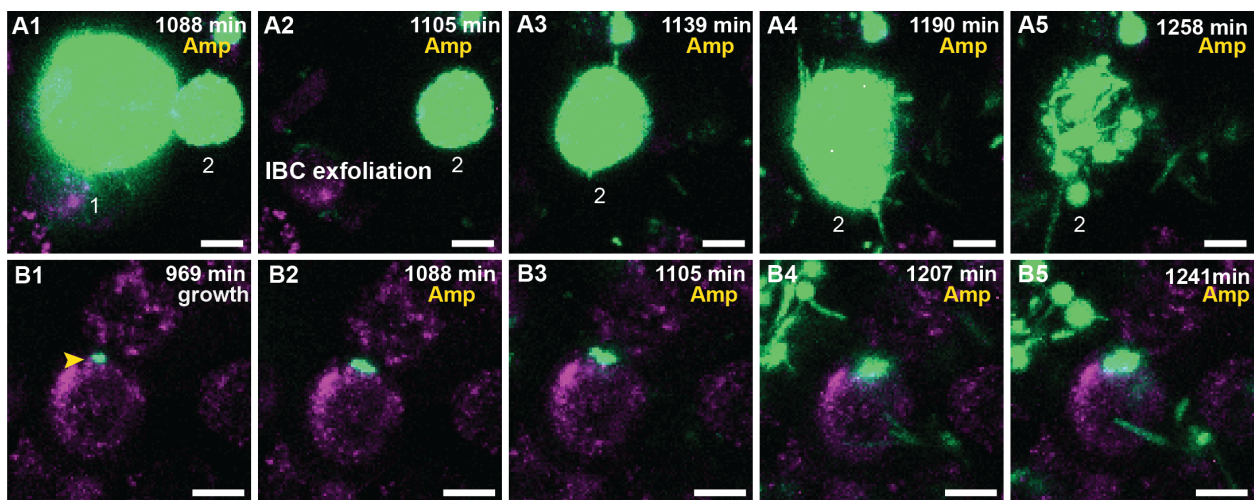


Figure 3.19: UPEC growth in IBCs during ampicillin treatment.

(A1-A5) Additional examples of UPEC growth during ampicillin treatment. (A1) Two IBCs (marked 1 and 2) at the start of ampicillin treatment. The IBC marked 1 exfoliates (A2) whereas the remaining IBC-2 continues to grow (A1-A3). Towards the end of this period, the bacteria filament (A4) before killing due to the antibiotic is observed (A5). (B1-B5) High resolution time-series that highlights bacterial growth within an IBC prior to (B1) and during (B2-B5) administration of ampicillin. The bacterial volume within this IBC is not diminished by antibiotic treatment (B5). Scale bars, 10 μ m in all the panels.

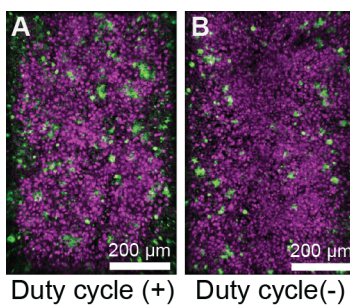


Figure 3.20: UPEC infection leads to a higher bacterial burden in bladder-chips perturbed with duty cycle.

Additional examples of UPEC growth in infected bladder chips with (A) and without (B) duty cycle.

3.7 Supplementary Movie Legends

Supplementary movie 1

File Name: **SMov1** Description: Infection of bladder-chip with UPEC, diapedesis of neutrophils across the epithelial-endothelial barrier and formation of swarms ([Figure 3.2B1-B5](#)).

Stage 1: Prior to infection, the uninfected cells of the epithelial layer (magenta) are imaged (0-120 mins).

Stage 2: UPEC (green) are introduced into the epithelial channel via flow and infection proceeds under flow for 120-210 min.

Stage 3: Neutrophils (amber) are introduced into the vascular channel of the infected bladder-chip via flow (210 min onwards).

Stage 4: Neutrophils undergo diapedesis within 15-30 minutes and are visible on the epithelial side (210-240 min). UPEC can be seen internalized by neutrophils.

Stage 5: Neutrophils aggregate and form a neutrophil swarm (240 min onwards) on the epithelial side.

Supplementary movie 2

File Name: **SMov2**, Description: Neutrophil diapedesis and swarm formation on the epithelial side of UPEC infection ([Figure 3.9A1-A5](#)).

Stage 1: Prior to infection, the uninfected cells of the epithelial layer (magenta) are imaged (0-120 mins).

Stage 2: UPEC (green) are introduced into the epithelial channel via flow and infection proceeds under flow for 120-210 min.

Stage 3: Neutrophils (amber) are introduced into the vascular channel of the infected bladder-chip via flow (210 min onwards).

Stage 4: Neutrophils undergo diapedesis within 15 minutes and are visible on the epithelial side (210-240 min). UPEC can be seen internalized by neutrophils.

Stage 5: Neutrophils aggregate and form a neutrophil swarm (240 min onwards) on the epithelial side.

Supplementary movie 3

File Name: **SMov3**, Description: Formation of intracellular bacterial community inside epithelial cell arising from few bacteria ([Figure 3.3B1-B5](#)).

An intracellular bacterial community is seeded inside a bladder epithelial cell (magenta, stained with Cell Mask Orange) by few UPEC (green) to form an intracellular bacterial community during the first growth cycle (578-1054 min, ca. 8 hr.). During subsequent ampicillin treatment (1071-1258 min, ca. 3 hr.), the IBC shed bacteria and eventually exfoliated from the epithelial layer.

Supplementary movie 4

File Name: **SMov4**, Description: IBC shedding and exfoliation ([Figure 3.3G1-G5](#)).

UPEC (green) divide and proliferate intracellularly in three epithelial cells (magenta, stained with Cell Mask Orange) to form IBCs. Two late-stage IBCs shed bacteria (ca. 935-969 min). One of these two IBCs subsequently exfoliated (ca. 986 min) whereas the other IBC shrank in volume due to the loss of shed bacteria. The third IBC did not shed bacteria during the first growth cycle (578-1054 min, ca. 8 hr.).

Supplementary movie 5

File Name: **SMov5**, Description: Filamentous bacterial growth within an IBC ([Figure 3.3H1-H5](#)).

Filamentous UPEC (green) grow intracellularly in an epithelial cell (magenta, stained with Cell Mask Orange) to form an IBC during the second growth cycle (1275 min onwards). Shedding of bacteria, some of which appear filamentous was subsequently observed later in the time series (ca. 1649-1768 min).

Supplementary movie 6

File Name: **SMov6**, Description: Filamentous bacterial growth within an IBC ([Figure 3.18A1-A5](#)).

Filamentous UPEC (green) grow intracellularly in an epithelial cell (magenta, stained with Cell Mask Orange) to form an IBC during the first growth cycle (578-1054 min, ca. 8 hr.). The IBC eventually exfoliates during the time series.

Supplementary movie 7

File Name: **SMov7**, Description: Bacteria within an IBC can persist and grow within an IBC despite the antibiotic treatment ([Figure 3.4A1-A5](#)).

Proliferation of UPEC (green) within four epithelial cells (magenta, stained with Cell Mask Orange) during the 1st growth cycle (578-1054 min, ca. 8 hr.) leads to the formation of IBCs. The bacteria within the four IBCs persist during the (~40x MIC) ampicillin treatment (1071-1258 min, ca. 3 hr.) In each case, bacterial killing was observed during the ampicillin treatment, but all four IBCs persisted over the course of the treatment. Bacterial growth subsequently resumed within all four IBCs post

ampicillin washout during the second growth cycle (1275 min onwards). Two new IBCs were formed during the second growth cycle (1275 min onwards). IBC fluxing and filamentation could be observed towards the end of time series.

Supplementary movie 8

File Name: **SMov8**, Description: Ampicillin mediated bacterial killing is delayed within an IBC (Figure 3.4F1-F5).

Proliferation of UPEC (green) within an epithelial cell (magenta, stained with Cell Mask Orange) during the 1st growth cycle (578-1054 min, ca. 8 hr.) to form an IBC. The bacteria within the IBC persisted during the (~40x MIC) ampicillin treatment (1071-1258 min, ca. 3 hr.). Bacterial proliferation continued during the first two hours of the ampicillin treatment (1071-1190 min, ca. 2 hr.). Bacterial killing was subsequently observed later during the ampicillin treatment (1190-1258, ca. 1 hr.). Some bacteria within the IBC persisted throughout the ampicillin treatment and resumed proliferation during the second growth cycle (1275 min onwards).

Supplementary movie 9

File Name: **SMov9**, Description: Ampicillin mediated bacterial killing is delayed within an IBC (Figure 3.19A1-A5).

Proliferation of UPEC (green) within two epithelial cells prior to the ampicillin treatment during the 1st growth cycle (578-1054 min, ca. 8 hr.). IBC#1 exfoliates from the epithelial layer (ca. 1105 min). Bacteria within IBC#2 continued to proliferate during the first two hours of the ampicillin treatment (1071-1190 min, ca. 2 hr.). Bacterial killing was subsequently observed later during the ampicillin treatment (1190-1258, ca. 1 hr.). IBC#2 eventually exfoliated from the epithelial layer towards the end of the time series (1292 min).

Supplementary movie 10

File Name: **SMov10**, Description: Bacteria can continue growing within an IBC for the entire duration of ampicillin treatment (Figure 3.4G1-G5).

Proliferation of UPEC (green) within an epithelial cell (magenta, stained with Cell Mask Orange) during the 1st growth cycle (578-1054 min, ca. 8 hr.) to form an IBC. Bacterial growth within the intact IBC continued both during the ampicillin treatment (~40x MIC, 1071-1258 min, ca. 3 hr.) as well as after the ampicillin was washed out during the 2nd growth cycle (1275 min onwards). Eventually, the IBCs shed bacteria (1700-1751 min, ca. 1hr) towards the end of time series.

Supplementary movie 11

File Name: **SMov11**, Description: Bacteria can continue growing within an IBC during the ampicillin treatment ([Figure 3.19B1-B5](#)).

Proliferation of UPEC (green) within an epithelial cell (magenta, stained with Cell Mask Orange) during the 1st growth cycle (578-1054 min, ca. 8 hr.) to form an IBC. Bacterial growth within the intact IBC continued both during the ampicillin treatment (~40x MIC, 1071-1258 min, ca. 3 hr) as well as after the ampicillin was washed out during the 2nd growth cycle (1275 min onwards). The late-stage IBC eventually shed bacteria and filamentous bacterial growth (1632-1717 min, ca. 1.5 hr) was also observed towards the end of time series.

3.8 Acknowledgements

V.V.T gratefully acknowledges support by a Human Frontier Science Program (HFSP) Long-Term Fellowship (LT000231/2016-L) and a European Molecular Biology Organization (EMBO) Long-Term Fellowship (921-2015). This research was supported by a grant awarded to J.D.M by the Swiss National Science Foundation (SNSF) (Project Funding, 310030B_176397) and the National Centre of Competence in Research AntiResist (51NF40_180541), funded by the SNSF. The authors thank the entire team of EPFL Bioimaging & Optics Core Facility for their assistance in confocal live cell imaging and post analysis in Bitplane Imaris. The authors also acknowledge Marie Croisier at the EPFL Biological Electron Microscopy Facility for help in optimizing the protocol for TEM of infected bladder-chip. The authors thank and credit BioRender.com for the illustrations and schematics used in this manuscript.

3.9 Author Contributions

| Contributor role | Role definition |
|--------------------------------------|---|
| Conceptualization | K.S., V.V.T., N.D. and J.D.M. |
| Methodology | K.S., V.V.T., N.D. and J.D.M. |
| Software | K.S. and V.V.T. |
| Validation | K.S., V.V.T. and N.D. |
| Formal analysis | K.S., V.V.T. and N.D. |
| Investigation | K.S., V.V.T., N.D., T.S., F.S.G., G.K. and J.D.M. |
| Resources | K.S., V.V.T., N.D., T.S., F.S.G., G.K. and J.D.M. |
| Data Curation | K.S. |
| Writing – original draft preparation | K.S. and V.V.T. |
| Writing – review and editing | K.S., V.V.T., N.D., T.S., F.S.G. and J.D.M. |
| Visualization | K.S., V.V.T. and N.D. |
| Supervision | V.V.T., N.D. and J.D.M. |
| Project administration | K.S., V.V.T., N.D. and J.D.M. |
| Funding acquisition | J.D.M |

3.10 Materials and Methods

| Reagent or resource | Designation | Source or reference | Identifiers | Additional information |
|---------------------------|---|-------------------------|------------------|--|
| strain, strain background | Uropathogenic Escherichia coli (UPEC) strain CFT073 | PMID: 2182540 | NCBI: txid199310 | originally isolated from a pyelonephritis patient and provided by Prof. H.L.T. Mobley, University of Michigan, USA |
| plasmid | pZA32-YFP | PMID: 9092630 | | (Lutz and Bujard, 1997) |
| strain, strain background | CFT073-pZA32-YFP | this paper | | this study |
| cell line (human) | HTB-9™ bladder epithelial cells | ATCC | Cat#:5637 | |
| Primary cells (human) | HMVEC-Bd – Human Bladder Microvascular Endothelial Cells | Lonza | Cat#:7016 | |
| other | RPMI-1640 medium | ATCC | Cat#:30-2001 | |
| other | Gibco™ RPMI 1640 Medium, no phenol red | Thermofisher | Cat#:11835063 | |
| other | Gibco™ Fetal Bovine Serum, Premium Plus | Thermofisher | Cat#: A4766801 | |
| other | EGM™-2 MV Microvascular Endothelial Cell Growth Medium-2 BulletKit™ | Lonza | Cat#:CC-3202 | |
| other | EBM-PRF Endothelial Medium Phenol-red free, 500 ml | Lonza | Cat#:CC-3129 | |
| other | EGM™-2 Endothelial SingleQuots™ Kit | Lonza | Cat#:CC-4176 | |
| other | Gibco™ Antibiotic-Antimycotic (100X) | Thermofisher | Cat#:15240062 | |
| other | Gibco™ Trypsin-EDTA (0.05%), phenol red | Thermofisher | Cat#:25300054 | |
| drug | Chloramphenicol | Sigma-Aldrich | Cat#:C1919-25G | 34 mg/ml in ethanol (stored at -20 °C) |
| drug | Ampicillin | Sigma-Aldrich | Cat#: A9518-5G | 50 mg/ml in ddH ₂ O (stored at -80 °C) |
| other | pooled human female urine | Golden West Diagnostics | Cat#: OH2010-pH | |
| other | Phosphate Buffered Saline | Thermofisher | Cat#: 10010056 | |
| other | Gibco™ HEPES | Thermofisher | Cat#: F2006 | |
| other | Invitrogen™ DAPI | Thermofisher | Cat#: D1306 | 5 mg/ml in DMSO |
| other | LB (Luria broth base, Miller's modified) | Sigma-Aldrich | Cat#: L1900-1KG | |
| other | Organ-chips (Standard Research Kit - 24 per Pack) | Emulate | RE1000001024 | Emulate, Inc. 27 Drydock Ave, 5th Floor Boston, MA 02210 |
| other | CellMask™ Orange Plasma membrane Stain | Thermofisher | Cat#: C10045 | used at 1µM in respective cell medium |
| other | HCS CellMask™ Deep Red Stain | Thermofisher | Cat#: H32721 | used at 2µM in PBS |

| | | | | |
|----------|--|---------------|---------------------------------|--|
| other | CellTracker™ Deep Red Dye | Thermofisher | Cat#: C34565 | used at 1µM in respective cell medium |
| other | Elveflow® OB1 Pressure Controller OB1 Base MkIII+ | Elveflow | Cat#: OB1MKIII+-MIX- | connected to 6bar compressed air channel |
| other | Elveflow® OB1 Pressure Controller OB1 MkIII Channel-900/1000 | Elveflow | Cat#: OB1-Dual- | connected to Elveflow® OB1 Pressure Controller OB1 Base MkIII+ |
| other | Diaphragm moist gas vacuum pump | KNF Neuberger | Cat#:LABO-PORT® UN 820.3 FT.40P | connected to Elveflow® OB1 Pressure Controller OB1 MkIII Channel-900/1000 |
| antibody | Anti-EpCAM | abcam | Cat#: ab71916 | used at 1:100 dilution in 1% BSA, conjugated with Donkey anti-Rabbit secondary antibody, Alexa Fluor 647 (2µg/ml) and Alexa Fluor 568 (2µg/ml) in 1%BSA |
| antibody | Anti-PECAM1 or Anti-CD31 | abcam | Cat#: ab24590 | used at 1:100 dilution in 1% BSA, conjugated with Donkey anti-Mouse secondary antibody, Alexa Fluor 647 (2µg/ml) and Goat anti-Mouse Alexa Fluor 488 (2µg/ml) in 1%BSA |
| antibody | Anti-CK7 | abcam | Cat#: ab209599 | used at 1:100 dilution in 1% BSA |
| antibody | Anti-CK8 | abcam | Cat#: ab192468 | used at 1:100 dilution in 1% BSA |
| other | Alexa Fluor™ 555 Phalloidin | Thermofisher | Cat#: A34055 | used at 1µM concentration in PBS |
| antibody | Anti-VE-Cadherin | abcam | Cat#: ab33168 | used at 1:100 dilution in 1% BSA, conjugated with Donkey anti-Rabbit secondary antibody, Alexa Fluor 647 (2µg/ml) and Alexa Fluor 488 (2µg/ml) in 1%BSA |
| antibody | Anti-Uroplakin3a | Santa Cruz | Cat#: sc-166808 | used at 1:100 dilution in 1% BSA, conjugated with Donkey anti-Mouse secondary antibody, Alexa Fluor 647 (2µg/ml) in 1%BSA |
| antibody | Anti-CK1 | Thermofisher | Cat#: MA1-06312 | used at 1:100 dilution in 1% BSA, conjugated with Donkey anti-Mouse secondary antibody, Alexa Fluor 647 (2µg/ml) in 1%BSA |

| | | | | |
|------------------------------|--|---------------|-----------------|--|
| antibody | Anti-E-Cadherin | Thermofisher | Cat#: MA5-14408 | used at 1:100 dilution in 1% BSA, conjugated with Donkey anti-Mouse secondary antibody, Alexa Fluor 647 (2µg/ml) in 1%BSA |
| antibody | Anti-ZO-1 | abcam | Cat#: ab216880 | used at 1:100 dilution in 1% BSA, conjugated with Donkey anti-Rabbit secondary antibody, Alexa Fluor 647 (2µg/ml) in 1%BSA |
| antibody | Anti-myeloperoxidase | abcam | Cat#: ab9535 | used at 1:100 dilution in 1% BSA, conjugated with Donkey anti-Rabbit secondary antibody, Alexa Fluor 568 (2µg/ml) in 1%BSA |
| antibody | Anti-neutrophil elastase | abcam | Cat#: ab68672 | used at 1:100 dilution in 1% BSA, conjugated with Donkey anti-Rabbit secondary antibody, Alexa Fluor 568 (2µg/ml) in 1%BSA |
| antibody | Anti-CD15 | abcam | Cat#: ab665 | used at 1:100 dilution in 1% BSA, conjugated with Donkey anti-Mouse secondary antibody, Alexa Fluor 568 (2µg/ml) in 1%BSA |
| antibody | Donkey anti-Mouse IgG (H+L) Highly Cross-Adsorbed Secondary Antibody, Alexa Fluor 647 | Thermofisher | Cat#: A-31571 | 2 mg/ml |
| antibody | Donkey anti-Rabbit IgG (H+L) Highly Cross-Adsorbed Secondary Antibody, Alexa Fluor 647 | Thermofisher | Cat#: A-31573 | 2 mg/ml |
| antibody | Goat anti-Mouse IgG (H+L) Highly Cross-Adsorbed Secondary Antibody, Alexa Fluor 488 | Thermofisher | Cat#: A-11029 | 2 mg/ml |
| antibody | Donkey anti-Rabbit IgG (H+L) Highly Cross-Adsorbed Secondary Antibody, Alexa Fluor 568 | Thermofisher | Cat#: A10042 | 2 mg/ml |
| antibody | Donkey anti-Mouse IgG (H+L) Highly Cross-Adsorbed Secondary Antibody, Alexa Fluor 568 | Thermofisher | Cat#: A10037 | 2 mg/ml |
| peptide, recombinant protein | Fibronectin from human plasma | Sigma-Aldrich | Cat#: F1056 | 500 µg/ml in ddH ₂ O |

| | | | | |
|-------------------------------|---|-----------------|-----------------------|--------------|
| peptide, re-combinant protein | Native Collagen, Bovine dermis | AteloCell | Cat#: IAC-50 | 5 mg/ml |
| peptide, re-combinant protein | Human IL-1 α , research grade | Miltenyi Biotec | Cat#:130-093-894 | 1 μ g/ml |
| peptide, re-combinant protein | Human IL-1 β , research grade | Miltenyi Biotec | Cat#:130-093-895 | 1 μ g/ml |
| peptide, re-combinant protein | Human IL-6, research grade | Miltenyi Biotec | Cat#:130-093-929 | 1 μ g/ml |
| peptide, re-combinant protein | Human IL-8, research grade | Miltenyi Biotec | Cat#:130-122-354 | 1 μ g/ml |
| commercial assay or kit | MACSxpress® Whole Blood Neutrophil Isolation Kit, human | Miltenyi Biotec | Cat#:130-104-434 | |
| software, algorithm | Imaris 9.5.1 | Bitplane | | |
| other | Gas chamber for stages with k-frame insert (160x110mm) - magnetic model with sliding lid. | okolab | Cat#: H201-K-FRAME | |
| other | Custom holder for 24mm x 60mm coverslip | okolab | Cat#:1x24by60-M | |
| other | μ -Slide 8 Well | ibidi | Cat#:80826 | |
| other | Masterflex PharMed tubing, 0.89mm ID, 100 ft | Cole-Palmer | Cat#:GZ-95709-26 | |
| other | Masterflex® Transfer Tubing, Tygon® 0.76mm ID | Cole-Palmer | Cat#:GZ-06419-03 | |
| other | 1.30 x 0.75 x 10 mm metallic tubes | Unimed | Cat#:9084 / 200.010-A | |
| other | 1.00/0.75 x 20mm metallic tubes | Unimed | Cat#:200.010-A | |
| other | Aladdin programmable pump | WPI | Cat#: PUMP-NE-1000 | |

3.10.1 Cell culture of human bladder epithelial and bladder endothelial cells

The HTB9 human bladder epithelial carcinoma cell line (procured from ATCC, 5637) was cultured in RPMI 1640 medium supplemented with 10% Fetal Bovine Serum (FBS) as recommended by the supplier. Human Bladder Microvascular Endothelial cells (HMVEC-Bd) (procured from Lonza, CC-7016) were cultured in Lonza EGM-2 MV BulletKit medium. Both the epithelial and endothelial cells were generally cultured in their respective medium supplemented with 1X Antibiotic-Antimycotic. Epithelial cells were passaged by detachment with 0.05% Trypsin at 37°C for 3-5 minutes followed by neutralization of trypsin with RPMI 1640 medium/10% FBS. Bladder endothelial cells were passaged and split as recommended by the supplier. The cells used in all the experiments were at ten passages or fewer. The cell lines were tested routinely for mycoplasma contamination during passaging.

3.10.2 UPEC culture for infection of bladder epithelial cells in the bladder-chip

Uropathogenic *Escherichia coli* (UPEC) strain CFT073 was originally isolated from a pyelonephritis patient (Mobley et al., 1990) and provided by Prof. H.L.T. Mobley, University of Michigan, USA. A derivative strain expressing yellow fluorescent protein (YFP) was generated by electroporation of CFT073 with the episomal plasmid pZA32-YFP (Lutz and Bujard, 1997), as described earlier (Dhar et al., 2015). To induce expression of type 1 pili, UPEC was grown in LB media containing 25 µg/ml chloramphenicol under non-shaking conditions at 37 °C for 2 days prior to the experiment, to achieve a stationary phase culture ($OD_{600}=1.5$ and corresponding to a concentration of 1.5×10^9 bacteria/ml). The bacteria were diluted 10-fold to a final concentration of 1.5×10^8 cells/ml) and resuspended in a solution of pooled human female urine (procured from Golden West Diagnostics Catalogue OH2010-pH) diluted 10-fold in Phosphate Buffered Saline.

3.10.3 Recapitulation of human bladder physiology in human bladder-on-a-chip device

Bladder-chip devices made of polydimethylsiloxane (PDMS) were purchased from Emulate (Boston, USA). The dimensions of the microfluidic device were as follows: width of the channels- 1000 µm, height of the upper channel- 1000 µm, lower channel – 250 µm). For extracellular matrix (ECM) coating, a coating solution consisting of the ER-1 compound (Emulate) dissolved in ER-2 solution at 0.5 mg/ml (Emulate) was introduced in both apical and vascular channels and the chips were subsequently activated by exposing the bladder-chip for 20 minutes under UV light. The channels were then rinsed with fresh coating solution and the protocol was repeated once. The channels of the bladder-chip were then washed thoroughly with PBS before incubation with an ECM solution of 150 µg/ml bovine collagen type I and 30 µg/ml fibronectin from human plasma in PBS buffered with 15 mM HEPES solution for 1-2 hours at 37°C as described previously (Thacker et al., 2020b). If not used directly, coated chips were stored at 4°C and pre-activated before use by incubation for 30 minutes with the same ECM solution at 37°C. Three days before the day of the experiment, HMVEC-Bd cells were seeded into lower channel of the inverted bladder-chip device at 0.5 million cells/ml. Two days before the experiment, HTB9 cells were seeded into upper channel at 5 million cells/ml. Prior to the infection experiment, bladder endothelial and bladder epithelial cells were cultured in their respective medium supplemented with the 1X Antibiotic-Antimycotic solution. The antibiotics were removed prior to the experiment.

3.10.4 Characterization and immunostaining of human bladder epithelial and human bladder epithelial cells in ibidi wells and human bladder-chip

Human bladder epithelial and bladder endothelial cells were cultured inside ibidi μ -Slide 8 wells for one day. The cells were subsequently fixed with 4% paraformaldehyde (PFA) for 1 hour at room temperature. Fixed cells were then washed three times with 200 μ l of PBS to remove residues of PFA, permeabilized with 0.15 % Triton X-100 for 15 minutes; washed three times with 200 μ l of PBS to remove residues of detergent and then incubated in a blocking solution of 1% BSA in PBS for 1 hour. The cells were then incubated with primary antibodies (anti-EpCAM, anti-PECAM-1, anti-CK7, anti-CK8, anti-VE-Cadherin, anti-Uroplakin3a, anti-CK1, anti-E-Cadherin, anti-ZO-1, anti-myeloperoxidase, anti-neutrophil elastase, anti-CD15) at a dilution of 1:100 in an antibody incubation buffer comprising 1% BSA and 0.01% Triton-100 in PBS. The ibidi 8-wells were subsequently washed three times with PBS for 10 minutes each. Incubation with secondary antibody (Donkey anti-Mouse Alexa Fluor 647, Donkey anti-Mouse Alexa Fluor 568, Goat anti-Mouse Alexa Fluor 488, Donkey anti-Rabbit Alexa Fluor 647, Donkey anti-Rabbit Alexa Fluor 568, Donkey anti-Rabbit Alexa Fluor 488) at a concentration of 2 μ g/ml in antibody incubation buffer was subsequently performed for 1 hour at room temperature. Excess antibody was removed by washing three times with PBS for 10 minutes each. Cell nuclei were stained with DAPI (5 μ g/ml) for 30 minutes. Ibidi 8-wells were washed three times to remove unbound DAPI. Cells were covered with appropriate volume of PBS until imaging. Cells were imaged with 63X oil objective on Leica SP8 confocal microscope. Images were deconvolved using SVI Huygens (Quality, 0.05; Iterations, 40).

For characterization of the cell types on-chip, bladder-chips with co-culture of bladder epithelial and bladder endothelial cells were kept under pooled diluted urine and EBM2 medium using P200 pipette tips for 2 days prior to PFA fixation. The cells in the bladder-chip were then immunostained following the protocol described above. Images were acquired with Leica HC FLUOTAR 25X (NA 0.95) multi-immersion objective on Leica SP8 confocal microscope.

3.10.5 Characterization of strain-pressure curve in the bladder-chip model

Elveflow OB1 MK3 – Microfluidic flow control system was used to control the negative pressure applied to the human bladder-chip. The control system was connected to the compressed air line (6 bar) for the positive pressure and diaphragm vacuum pump for the negative pressure. A negative pressure (0 to -900 mbar) with a step function of -100mbar was subsequently applied to the vacuum channels in the bladder-chip using a Pressure Controller (Elveflow OB1 pressure controller). For these experiments, both bladder epithelial and endothelial cells were seeded on the respective sides

in the devices. This experiment was performed with the chip maintained on the stage of the microscope and a brightfield image was acquired at each step increase of -100mbar, on Leica SP8 confocal microscope. The PDMS inter-pore-to-pore distance was measured for 14 pore-to-pore combinations at each input of negative pressure. Linear fitting was performed using GraphPad Prism (version 9).

3.10.6 Mimicking bladder filling and voiding cycle in human bladder-chip

The stretching of the human bladder-chip was done using the Elveflow OB1 MK3 – Microfluidic flow control system connected to the compressed air line (6 bar) for the positive pressure and diaphragm vacuum pump for the negative pressure. Human bladder-chip in the relaxed (*voided bladder*, 0% strain) state was slowly perturbed with a linear ramp function to reach a stretched (*filled bladder*, 10% strain) state over a period of 2 hours. Linear strain of 10% strain was achieved by application of ca. 520-530 mbar negative pressure in the vacuum channels. This period corresponded to the *filling bladder* state in [Figure 1D](#). Bladder-chip was kept under stretched (*filled bladder*, 10% strain) state over the subsequent 2 hours. Micturition or urination was recapitulated by rapidly reducing the applied strain on the bladder-chip from the stretched (*filled bladder*, 10% strain) state to relaxed (*voided bladder*, 0% strain) state over a period of 2 minutes. Subsequently, the bladder-chip was maintained with no negative pressure applied in the vacuum channel under relaxed (*voided bladder*, 0% strain) state from (4:02 hours to 6 hours). This 6-hour bladder filling and voiding cycle was repeated continuously for the rest of the experiment.

3.10.7 Experimental setup and imaging parameters for time lapse imaging for UPEC infection in the human bladder-chip devices

The medium perfusion inside the bladder-chip device was achieved with the Aladdin syringe pumps. The syringes with respective media were connected to the bladder-chip via gas impermeable PharMed® tubing (inner diameter =0.89 mm, Cole palmer GZ-95809-26) along with longer transparent Tygon tubings (internal diameter of 0.76mm, Masterflex transfer tubing, Cole palmer). The Harmed® tubing was connected to the inlet and outlet of the bladder-chip with 1.30 x 0.75 x 10 mm metallic tubes (Unimed) and transparent tubing with 1.00/0.75 x 20mm metallic tubes (Unimed). The bladder-chip connected to external sources of flow was then mounted onto a 24 x 60 mm No. 1 glass coverslip for microscopy imaging. When required for stretching experiments, tubing was also connected to the stretching channels on either side of the main channel. The connected device was subsequently assembled inside a temperature-controlled microscope environmental chamber at 37°C supplemented with 5% CO₂ (OKO labs). Time-lapse imaging was conducted using a Leica HC FLUOTAR 25X (NA 0.95) multi-immersion objective within custom made environmental chamber set at 37°C for infusion with syringe pumps. Water was pumped to the ring around the water objective

at 9 Hz with pumping duration of 9 seconds and pumping interval 30 minutes, controlled by SRS software (HRZ=9, VPP=95). The autofocus mode (best focus, steps =9, range = 30 μm) was used to maintain the optical focus on the apical side of the PDMS membrane. The experiments were monitored frequently to ensure that the optical focus was maintained, and the experiment was halted and restarted if the focus was lost.

To enable rapid 3-D imaging across multiple spatial locations on-chip, we utilized the capability of the white light laser on the Leica SP8 confocal microscope to image at multiple wavelengths simultaneously. The excitation wavelengths were grouped into two sequences to minimize the spectral overlap. In the first sequence, laser emission at 555 nm was used to excite the Calmest Orange stain in the bladder epithelial cells. In the second laser excitation sequence, laser emission at 500 nm and 630 nm were used to excite the YFP within the bacteria and the cytoplasmic CellTrackerTM Deep Red in the human neutrophils. Images were acquired with a scan speed of 400-700 Hz and a zoom factor of 2.25 (206.67 μm x 206.67 μm) resulting in an XY resolution of 450 nm depending on the number of pixels acquired per field of view. Z-stacks were acquired with 1 μm step sizes. Time lapse images were acquired with interval duration of ca. 15-17 minutes, in a subset of experiments this was further reduced to 7.5 minutes by imaging with the second sequence only at a z-step size of 2 μm .

3.10.8 Time lapse imaging for UPEC infections in the human bladder-chip devices

Pre-infection stage

The time-course of the entire experimental protocol is shown in a schematic in [Figure 1](#). The bladder-chip device was perfused with diluted urine in the apical channel and EBM Endothelium phenol-red free medium supplemented with EGM-2 endothelial SingleQuots kit in the vascular channel. Prior to the commencement of infection, the chip was maintained at homeostasis and the epithelial cells were imaged for a period of two hours.

Infection stage

Stationary phase UPEC in diluted pooled urine at a concentration of 150 million cells/ml were flowed through the apical channel of the device at 1200 $\mu\text{l}/\text{hour}$ for 1.5 hours. During this period, EBM2 media was flowed through the endothelial channel at 600 $\mu\text{l}/\text{hour}$.

Bacterial washout and neutrophil introduction stage

Next, the syringe connected to the apical channel was replaced with a fresh syringe containing pooled diluted urine, this solution was then flowed in the apical channel over the epithelial layer of the chip at a flow rate of 600 $\mu\text{l}/\text{hour}$ over the next 3 hours. This allowed for the continuous removal of

extracellular planktonic bacteria in the apical channel. At the same time, human neutrophils were introduced into the endothelial channel of the bladder-chip via flow. A solution of human neutrophils at a density of 2 million cells/ml isolated via negative selection was flowed through the vascular channel for 2 hours in EBM2 medium with at higher shear stress of $\eta=1.0$ dyne/cm² to enhance neutrophil attachment to endothelial cells.

Neutrophil diapedesis stage

Diapedesis of human neutrophils to epithelial side and subsequent interactions of neutrophils with UPEC was observed for the subsequent 3 hours since introduction of neutrophils into the vasculature side of the chip. During this period, the flow rate in the apical and vascular channels were maintained at 600 μ l/hour and 3000 μ l/hour, respectively. During this period, in a subset of experiments, only the channels that were part of the second laser scanning sequence were imaged. Images of the CellTracker Orange dye for epithelial cell identification were not acquired (first laser scanning sequence). This enabled a number of fields of view to be captured with an enhanced temporal resolution and a frame rate of up to 7.5 minutes. For experiments studying the formation of NETs, the experiment was halted at this stage and the infected chips were fixed, permeabilized, blocked, and immunostained with anti-myeloperoxidase (abcam) or anti-neutrophil elastase (abcam) antibodies using the procedure described earlier. For all other experiments, live imaging continued to the subsequent antibiotic treatment phase, Immunofluorescence for anti-myeloperoxidase and anti-neutrophil elastase was done as the procedure described previously.

Antibiotic treatment and growth cycles

Thereafter, syringes connected to both apical and vascular channels were changed and ampicillin at 250 μ g/ml (used at \sim 40-fold over the minimum inhibitory concentration (MIC) of ampicillin against UPEC grown in EBM2 medium) was introduced in the diluted urine and the EBM2 media perfused into the apical and vascular channels, respectively, for 3 hours at a flow rate of 600 μ l/hour. This was the first ampicillin treatment cycle; whose purpose was to eliminate extracellular bacteria in the apical channel and allow intracellular bacterial colonies (IBCs) to be identified. The medium was subsequently switched with antibiotic-free medium for next 8 hours to allow for IBC growth within epithelial cells. During this period, the flow within the apical channel was maintained, to remove bacteria that grew extracellularly either because they survived the antibiotic treatment or that were released from infected epithelial cells. The ampicillin and growth cycle were then repeated, to allow the

assessment of the response of bacteria within IBCs to antibiotic treatment as well as characterize the subsequent regrowth.

3.10.9 Image analysis of confocal live-cell images

Image analysis was performed with Bitplane Imaris 9.5.1. The time-lapse imaging stack included five channels: uroepithelial cells (epithelial channel), transmitted light (bright field channel), UPEC (bacterial channel), neutrophils (neutrophil channel), and transmitted light (bright field channel). Neutrophils were identified via the spot detection algorithm in Imaris used on the images from the neutrophil channel with the following parameters (Size, 8 μm ; Quality, 4 to 8).

Swarms of neutrophils generate dense aggregates that are ill-suited to quantification with the spot detection algorithm. To quantify the size of the swarms, we therefore segmented images in the neutrophil channel to generate surfaces via the automatic segmentation tool in Imaris with the following parameters (Threshold, 10; Smooth Surfaces Detail, 0.5 or 1.0 μm). Unfortunately, the time resolution was insufficient to track individual neutrophils over time particularly since neutrophils formed small clumps and rapidly changed their cell shapes.

For UPEC volume inside IBCs, necessary 3D volume was cropped in Imaris to ease image analysis. Total bacterial volume inside IBC was detected by creating the surface (Threshold, 15; Smooth Surfaces Detail, 0.5 or 1 μm) on UPEC channel.

In cases of measuring extracellular UPEC growth, surface was generated (Threshold, 15; Smooth Surfaces Detail, 0.5 or 1 μm) on UPEC channel to calculate total extracellular volume in the field of view.

3.10.10 Isolation and Labelling of human neutrophils from fresh human blood

Primary human neutrophils were isolated via negative depletion method from human blood with MACSxpress® Whole Blood Neutrophil Isolation Kit (Miltenyi Biotec), following the manufacturer's instructions. Isolation was performed without the use of a density-based centrifugation method. Isolated human neutrophils were then incubated with a 1 μM solution CellTracker™ Deep Red in a serum free RPMI phenol red free medium for 30 minutes in a cell culture incubator maintained at 37 C and 5% CO₂. Labelled human neutrophils were then washed with 10ml of 20% FBS in RPMI phenol red free medium twice to remove the unbound dye. The human neutrophils were suspended in Lonza EBM2 medium at a cell density of 1 million cells/ml. In some instances, labelled human neutrophils were passed through a filter with 40 μm pores to remove neutrophil clusters that may have formed during the isolation process.

3.10.11 Scanning electron microscopy of human bladder-chip

UPEC within infected human bladder-chips were allowed to proliferate for 6 hours (14 hours from start of UPEC infection) until the end of the first IBC growth cycle. After 6 hours, human bladder-chip was fixed at room temperature for 1 hour with a mix of 1% glutaraldehyde and 2% paraformaldehyde in 0.1 M phosphate buffer (pH 7.4). The fixed bladder-chip was kept in the fixative overnight (at 4°C). Post overnight fixation, human bladder-chip was cut open from the apical channel side. A scalpel was used to cut approximately in the middle of the apical channel side (height=1mm) to expose the bladder epithelial cells. The fixed chip was further fixed for 30 minutes in 1% osmium tetroxide in 0.1 M cacodylate buffer followed by washing with the distilled water. Next, the bladder-chip was dehydrated in a graded alcohol series and dried by passing them through the supercritical point of carbon dioxide (CPD300, Leica Microsystems). Finally, the bladder-chip was attached to an adhesive conductive surface followed by coating with a 3 – 4 nm thick layer of gold palladium metal (Quorum Q Plus, Quorum Technologies). Images of the cells were captured using a field emission scanning electron microscope (Merlin, Zeiss NTS).

Uninfected human bladder-chip controls were fixed at the same time point (14 hours from start of the experiment). For the case of NETs formed on epithelial layer, an uninfected human bladder-chip was fixed 2 hours after the introduction of neutrophils into the vascular channel of the chip.

3.10.12 Preparation for transmission electron microscopy (TEM)

UPEC within infected human bladder-chips were allowed to proliferate for 6 hours (14 hours from start of UPEC infection) during the first IBC growth cycle. After 6 hours, human bladder-chip was fixed at room temperature for 1 hour with a mix of 1% glutaraldehyde and 2% paraformaldehyde in 0.1 M phosphate buffer (pH 7.4). The fixed bladder-chip was kept in the fixative overnight (at 4°C). Post overnight fixation, human bladder-chip was cut open from the apical channel side. A scalpel was used to cut approximately in the middle of the apical channel side (height=1mm) to expose the bladder epithelial cells. The bladder-chip was then washed in cacodylate buffer (0.1M, pH 7.4), postfixed for 40 minutes in 1.0 % osmium tetroxide with 1.5% potassium ferrocyanide, and then fixed again with 1.0% osmium tetroxide alone. The bladder-chip was finally stained for 30 minutes in 1% uranyl acetate in water before being dehydrated through increasing concentrations of alcohol and then embedded in Durcupan ACM (Fluka, Switzerland) resin. The bladder-chip was then placed in Petri dishes so that approximately 1 mm of resin remained above the cells, and the dish than left in an

oven at 65°C for 24 hours. Regions on interest, and corresponding to structures imaged with light microscopy were trimmed from the rest of the device, once the resin had hardened, and thin, 50 nm-thick sections were cut with a diamond knife, and collected onto single-slot copper grids with a pioloform support film. These were contrasted with lead citrate and uranyl acetate, and images taken with a transmission electron microscope at 80 kV (Tecnai Spirit, FEI Company with Eagle CCD camera).

Data availability statement

The datasets generated during and analyzed during the current study are available from the corresponding authors on reasonable request and will be uploaded to Zenodo prior to publication.

3.11 References

- Abraham, S.N., and Miao, Y. (2015). The nature of immune responses to urinary tract infections. *Nat Rev Immunol* 15, 655–663.
- Agace, W.W., Hedges, S.R., Ceska, M., and Svanborg, C. (1993). Interleukin-8 and the neutrophil response to mucosal gram-negative infection. *J Clin Invest* 92, 780–785.
- Agace, W.W., Patarroyo, M., Svensson, M., Carlemalm, E., and Svanborg, C. (1995). *Escherichia coli* induces transuroepithelial neutrophil migration by an intercellular adhesion molecule-1-dependent mechanism. *Infect Immun* 63, 4054–4062.
- Alon, R., Hammer, D.A., and Springer, T.A. (1995). Lifetime of the P-selectin-carbohydrate bond and its response to tensile force in hydrodynamic flow. *Nature* 374, 539–542.
- Andersen, T.E., Khandige, S., Madelung, M., Brewer, J., Kolmos, H.J., and Møller-Jensen, J. (2012). *Escherichia coli* uropathogenesis in vitro: invasion, cellular escape, and secondary infection analyzed in a human bladder cell infection model. *Infect Immun* 80, 1858–1867.
- Anderson, G.G., Palermo, J.J., Schilling, J.D., Roth, R., Heuser, J., and Hultgren, S.J. (2003). Intracellular Bacterial Biofilm-Like Pods in Urinary Tract Infections. *Science* 301, 105–107.
- Apodaca, G. (2004). The Uroepithelium: Not Just a Passive Barrier. *Traffic* 5, 117–128.
- Benam, K.H., Villenave, R., Lucchesi, C., Varone, A., Hubeau, C., Lee, H.-H., Alves, S.E., Salmon, M., Ferrante, T.C., Weaver, J.C., et al. (2016). Small airway-on-a-chip enables analysis of human lung inflammation and drug responses in vitro. *Nat Methods* 13, 151–157.
- Blango, M.G., and Mulvey, M.A. (2010). Persistence of Uropathogenic *Escherichia coli* in the Face of Multiple Antibiotics. *Antimicrob Agents Ch* 54, 1855–1863.
- Branzk, N., Lubojemska, A., Hardison, S.E., Wang, Q., Gutierrez, M.G., Brown, G.D., and Papanikolaou, V. (2014). Neutrophils sense microbe size and selectively release neutrophil extracellular traps in response to large pathogens. *Nat Immunol* 15, 1017–1025.
- Brinkmann, V., Reichard, U., Goosmann, C., Fauler, B., Uhlemann, Y., Weiss, D.S., Weinrauch, Y., and Zychlinsky, A. (2004). Neutrophil Extracellular Traps Kill Bacteria. *Science* 303, 1532–1535.
- Bryskier, A. (2020). Antimicrobial Agents: Antibacterials and Antifungals. In *Undefined*, pp. 113–162.
- Cakir, B., Xiang, Y., Tanaka, Y., Kural, M.H., Parent, M., Kang, Y.-J., Chapeton, K., Patterson, B., Yuan, Y., He, C.-S., et al. (2019). Engineering of human brain organoids with a functional vascular-like system. *Nat Methods* 16, 1169–1175.
- Carattino, M.D., Prakasam, H.S., Ruiz, W.G., Clayton, D.R., McGuire, M., Gallo, L.I., and Apodaca, G. (2013). Bladder filling and voiding affect umbrella cell tight junction organization and function. *Am J Physiol-Renal* 305, F1158–F1168.

- Clevers, H. (2016). Modeling Development and Disease with Organoids. *Cell* 165, 1586–1597.
- Dhar, N., Dubée, V., Ballell, L., Cuinet, G., Hugonnet, J.-E., Signorino-Gelo, F., Barros, D., Arthur, M., and McKinney, J.D. (2015). Rapid Cytolysis of *Mycobacterium tuberculosis* by Faropenem, an Orally Bioavailable β -Lactam Antibiotic. *Antimicrob Agents Ch* 59, 1308–1319.
- Duncan, M.J., Li, G., Shin, J.-S., Carson, J.L., and Abraham, S.N. (2004). Bacterial Penetration of Bladder Epithelium through Lipid Rafts. *J Biol Chem* 279, 18944–18951.
- Duraiswamy, S., Chee, J.L.Y., Chen, S., Yang, E., Lees, K., and Chen, S.L. (2018). Purification of Intracellular Bacterial Communities during Experimental Urinary Tract Infection Reveals an Abundant and Viable Bacterial Reservoir. *Infect Immun* 86, e00740-17.
- Ermer, D., Urban, C.F., Laube, B., Goosmann, C., Zychlinsky, A., and Brinkmann, V. (2009). Mouse Neutrophil Extracellular Traps in Microbial Infections. *J Innate Immun* 1, 181–193.
- Foxman, B. (2010). The epidemiology of urinary tract infection. *Nat Rev Urol* 7, 653–660.
- Gloeckner, D.C., SACKS, M.S., FRASER, M.O., SOMOGYI, G.T., GROAT, W.C. de, and CHANCELLOR, M.B. (2002). Passive Biaxial Mechanical Properties of the Rat Bladder Wall After Spinal Cord Injury. *J Urology* 167, 2247–2252.
- Grassart, A., Malardé, V., Gobba, S., Sartori-Rupp, A., Kerns, J., Karalis, K., Marteyn, B., Sansonetti, P., and Sauvonnnet, N. (2019). Bioengineered Human Organ-on-Chip Reveals Intestinal Microenvironment and Mechanical Forces Impacting *Shigella* Infection. *Cell Host Microbe* 26, 435–444.e4.
- Hannan, T.J., Totsika, M., Mansfield, K.J., Moore, K.H., Schembri, M.A., and Hultgren, S.J. (2012). Host–pathogen checkpoints and population bottlenecks in persistent and intracellular uropathogenic *Escherichia coli* bladder infection. *Fems Microbiol Rev* 36, 616–648.
- Haraoka, M., Hang, L., Frendéus, B., Godaly, G., Burdick, M., Strieter, R., and Svanborg, C. (1999). Neutrophil Recruitment and Resistance to Urinary Tract Infection. *J Infect Dis* 180, 1220–1229.
- Hedges, S., Svensson, M., and Svanborg, C. (1992). Interleukin-6 response of epithelial cell lines to bacterial stimulation in vitro. *Infect Immun* 60, 1295–1301.
- Hopke, A., Scherer, A., Kreuzburg, S., Abers, M.S., Zerbe, C.S., Dinauer, M.C., Mansour, M.K., and Irimia, D. (2020). Neutrophil swarming delays the growth of clusters of pathogenic fungi. *Nat Commun* 11, 2031.
- Horsley, H., Dharmasena, D., Malone-Lee, J., and Rohn, J.L. (2018). A urine-dependent human urothelial organoid offers a potential alternative to rodent models of infection. *Sci Rep-Uk* 8, 1238.
- Hsieh, M.M., Everhart, J.E., Byrd-Holt, D.D., Tisdale, J.F., and Rodgers, G.P. (2007). Prevalence of Neutropenia in the U.S. Population: Age, Sex, Smoking Status, and Ethnic Differences. *Ann Intern Med* 146, 486.

- Huh, D., Matthews, B.D., Mammoto, A., Montoya-Zavala, M., Hsin, H.Y., and Ingber, D.E. (2010a). Reconstituting Organ-Level Lung Functions on a Chip. *Science* 328, 1662–1668.
- Huh, D., Matthews, B.D., Mammoto, A., Montoya-Zavala, M., Hsin, H.Y., and Ingber, D.E. (2010b). Reconstituting Organ-Level Lung Functions on a Chip. *Science* 328, 1662–1668.
- Hung, C.-S., Dodson, K.W., and Hultgren, S.J. (2009). A murine model of urinary tract infection. *Nat Protoc* 4, 1230–1243.
- Hunstad, D.A., and Justice, S.S. (2010). Intracellular Lifestyles and Immune Evasion Strategies of Uropathogenic *Escherichia coli*. *Annu Rev Microbiol* 64, 203–221.
- Iosifidis, G., and Duggin, I.G. (2020). Distinct Morphological Fates of Uropathogenic *Escherichia coli* Intracellular Bacterial Communities: Dependency on Urine Composition and pH. *Infect Immun* 88.
- Isles, H.M., Loynes, C.A., Hamilton, N., Muir, C.F., Kadochnikova, A., Henry, K.M., Kadirkamanathan, V., Renshaw, S.A., and Elks, P.M. (2019). Non-apoptotic pioneer neutrophils initiate an endogenous swarming response in a zebrafish tissue injury model. *Biorxiv* 521450.
- Jalili-Firoozinezhad, S., Gazzaniga, F.S., Calamari, E.L., Camacho, D.M., Fadel, C.W., Bein, A., Swenor, B., Nestor, B., Crouce, M.J., Tovaglieri, A., et al. (2019). A complex human gut microbiome cultured in an anaerobic intestine-on-a-chip. *Nat Biomed Eng* 3, 520–531.
- Jang, K.-J., Mehr, A.P., Hamilton, G.A., McPartlin, L.A., Chung, S., Suh, K.-Y., and Ingber, D.E. (2013). Human kidney proximal tubule-on-a-chip for drug transport and nephrotoxicity assessment. *Integr Biol* 5, 1119–1129.
- Jang, K.-J., Otieno, M.A., Ronxhi, J., Lim, H.-K., Ewart, L., Kodella, K.R., Petropolis, D.B., Kulkarni, G., Rubins, J.E., Conegliano, D., et al. (2019). Reproducing human and cross-species drug toxicities using a Liver-Chip. *Sci Transl Med* 11, eaax5516.
- Justice, S.S., Hung, C., Theriot, J.A., Fletcher, D.A., Anderson, G.G., Footer, M.J., and Hultgren, S.J. (2004). Differentiation and developmental pathways of uropathogenic *Escherichia coli* in urinary tract pathogenesis. *Proc National Acad Sci* 101, 1333–1338.
- Kang, Y.B. (Abraham), Rawat, S., Duchemin, N., Bouchard, M., and Noh, M. (2017). Human Liver Sinusoid on a Chip for Hepatitis B Virus Replication Study. *Micromachines-Basel* 8, 27.
- Kienle, K., and Lämmermann, T. (2016). Neutrophil swarming: an essential process of the neutrophil tissue response. *Immunol Rev* 273, 76–93.
- Kim, H.J., and Ingber, D.E. (2013). Gut-on-a-Chip microenvironment induces human intestinal cells to undergo villus differentiation. *Integr Biol* 5, 1130–1140.
- Kim, H.J., Li, H., Collins, J.J., and Ingber, D.E. (2016). Contributions of microbiome and mechanical deformation to intestinal bacterial overgrowth and inflammation in a human gut-on-a-chip. *Proc National Acad Sci* 113, E7–E15.

- Klein, R.D., and Hultgren, S.J. (2020). Urinary tract infections: microbial pathogenesis, host-pathogen interactions and new treatment strategies. *Nat Rev Microbiol* 18, 211–226.
- Korkmaz, I., and Rogg, B. (2007). A simple fluid-mechanical model for the prediction of the stress-strain relation of the male urinary bladder. *J Biomech* 40, 663–668.
- Kreisel, D., Nava, R.G., Li, W., Zinselmeyer, B.H., Wang, B., Lai, J., Pless, R., Gelman, A.E., Krupnick, A.S., and Miller, M.J. (2010). In vivo two-photon imaging reveals monocyte-dependent neutrophil extravasation during pulmonary inflammation. *Proc National Acad Sci* 107, 18073–18078.
- Lämmermann, T., Afonso, P.V., Angermann, B.R., Wang, J.M., Kastenmüller, W., Parent, C.A., and Germain, R.N. (2013). Neutrophil swarms require LTB4 and integrins at sites of cell death in vivo. *Nature* 498, 371–375.
- Ley, K., Laudanna, C., Cybulsky, M.I., and Nourshargh, S. (2007). Getting to the site of inflammation: the leukocyte adhesion cascade updated. *Nat Rev Immunol* 7, 678–689.
- Lutz, R., and Bujard, H. (1997). Independent and Tight Regulation of Transcriptional Units in *Escherichia Coli* Via the LacR/O, the TetR/O and AraC/I1-I2 Regulatory Elements. *Nucleic Acids Res* 25, 1203–1210.
- Martinez, J.J., Mulvey, M.A., Schilling, J.D., Pinkner, J.S., and Hultgren, S.J. (2000). Type 1 pilus-mediated bacterial invasion of bladder epithelial cells. *Embo J* 19, 2803–2812.
- Metzler, K.D., Fuchs, T.A., Nauseef, W.M., Reumaux, D., Roesler, J., Schulze, I., Wahn, V., Papanopoulos, V., and Zychlinsky, A. (2011). Myeloperoxidase is required for neutrophil extracellular trap formation: implications for innate immunity. *Blood* 117, 953–959.
- Mobley, H.L., Green, D.M., Trifillis, A.L., Johnson, D.E., Chippendale, G.R., Lockatell, C.V., Jones, B.D., and Warren, J.W. (1990). Pyelonephritogenic *Escherichia coli* and killing of cultured human renal proximal tubular epithelial cells: role of hemolysin in some strains. *Infect Immun* 58, 1281–1289.
- Mulvey, M.A., Lopez-Boado, Y.S., Wilson, C.L., Roth, R., Parks, W.C., Heuser, J., and Hultgren, S.J. (1998). Induction and Evasion of Host Defenses by Type 1-Piliated Uropathogenic *Escherichia coli*. *Science* 282, 1494–1497.
- Mysorekar, I.U., and Hultgren, S.J. (2006). Mechanisms of uropathogenic *Escherichia coli* persistence and eradication from the urinary tract. *Proc National Acad Sci* 103, 14170–14175.
- Nagamatsu, K., Hannan, T.J., Guest, R.L., Kostakioti, M., Hadjifrangiskou, M., Binkley, J., Dodson, K., Raivio, T.L., and Hultgren, S.J. (2015). Dysregulation of *Escherichia coli* α -hemolysin expression alters the course of acute and persistent urinary tract infection. *Proc National Acad Sci* 112, E871–E880.
- Nawroth, J.C., Lucchesi, C., Cheng, D., Shukla, A., Ngyuen, J., Shroff, T., Varone, A., Karalis, K., Lee, H.-H., Alves, S., et al. (2020). A Microengineered Airway Lung Chip Models Key Features of Viral-induced Exacerbation of Asthma. *Am J Resp Cell Mol* 63, 591–600.

- Nourshargh, S., Hordijk, P.L., and Sixt, M. (2010). Breaching multiple barriers: leukocyte motility through venular walls and the interstitium. *Nat Rev Mol Cell Bio* 11, 366–378.
- Novak, R., Ingram, M., Marquez, S., Das, D., Delahanty, A., Herland, A., Maoz, B.M., Jeanty, S.S.F., Somayaji, M.R., Burt, M., et al. (2020). Robotic fluidic coupling and interrogation of multiple vascularized organ chips. *Nat Biomed Eng* 4, 407–420.
- Oliveira, S. de, Rosowski, E.E., and Huttenlocher, A. (2016). Neutrophil migration in infection and wound repair: going forward in reverse. *Nat Rev Immunol* 16, 378–391.
- Papayannopoulos, V., Metzler, K.D., Hakkim, A., and Zychlinsky, A. (2010). Neutrophil elastase and myeloperoxidase regulate the formation of neutrophil extracellular traps. *J Cell Biology* 191, 677–691.
- Parekh, A., Cigan, A.D., Wognum, S., Heise, R.L., Chancellor, M.B., and Sacks, M.S. (2010). Ex vivo deformations of the urinary bladder wall during whole bladder filling: Contributions of extracellular matrix and smooth muscle. *J Biomech* 43, 1708–1716.
- Pascalis, R.D., Parnell, W.J., Abrahams, I.D., Shearer, T., Daly, D.M., and Grundy, D. (2018). The inflation of viscoelastic balloons and hollow viscera. *Proc Royal Soc* 474, 20180102.
- Poplimont, H., Georgantzoglou, A., Boulch, M., Walker, H.A., Coombs, C., Papaleonidopoulou, F., and Sarris, M. (2020). Neutrophil Swarming in Damaged Tissue Is Orchestrated by Connexins and Cooperative Calcium Alarm Signals. *Curr Biol* 30, 2761-2776.e7.
- Putrinš, M., Kogermann, K., Lukk, E., Lippus, M., Varik, V., and Tenson, T. (2015). Phenotypic Heterogeneity Enables Uropathogenic *Escherichia coli* To Evade Killing by Antibiotics and Serum Complement. *Infect Immun* 83, 1056–1067.
- Reátegui, E., Jalali, F., Khankhel, A.H., Wong, E., Cho, H., Lee, J., Serhan, C.N., Dalli, J., Elliott, H., and Irimia, D. (2017). Microscale arrays for the profiling of start and stop signals coordinating human-neutrophil swarming. *Nat Biomed Eng* 1, 0094.
- Ronaldson-Bouchard, K., and Vunjak-Novakovic, G. (2018). Organs-on-a-Chip: A Fast Track for Engineered Human Tissues in Drug Development. *Cell Stem Cell* 22, 310–324.
- Rossi, G., Manfrin, A., and Lutolf, M.P. (2018). Progress and potential in organoid research. *Nat Rev Genet* 19, 671–687.
- Sato, T., Vries, R.G., Snippert, H.J., Wetering, M. van de, Barker, N., Stange, D.E., Es, J.H. van, Abo, A., Kujala, P., Peters, P.J., et al. (2009). Single *Lgr5* stem cells build crypt-villus structures in vitro without a mesenchymal niche. *Nature* 459, 262–265.
- Schwartz, D.J., Chen, S.L., Hultgren, S.J., and Seed, P.C. (2011). Population Dynamics and Niche Distribution of Uropathogenic *Escherichia coli* during Acute and Chronic Urinary Tract Infection. *Infect Immun* 79, 4250–4259.
- Scott, V.C.S., Haake, D.A., Churchill, B.M., Justice, S.S., and Kim, J.-H. (2015). Intracellular Bacterial Communities: A Potential Etiology for Chronic Lower Urinary Tract Symptoms. *Urology* 86, 425–431.

- Shah, P., Fritz, J.V., Glaab, E., Desai, M.S., Greenhalgh, K., Frachet, A., Niegowska, M., Estes, M., Jäger, C., Seguin-Devaux, C., et al. (2016). A microfluidics-based in vitro model of the gastrointestinal human–microbe interface. *Nat Commun* 7, 11535.
- Si, L., Bai, H., Rodas, M., Cao, W., Oh, C.Y., Jiang, A., Nurani, A., Zhu, D.Y., Goyal, G., Gilpin, S.E., et al. (2020). Human organs-on-chips as tools for repurposing approved drugs as potential influenza and COVID19 therapeutics in viral pandemics. *Biorxiv* 2020.04.13.039917.
- Smith, Y.C., Grande, K.K., Rasmussen, S.B., and O'Brien, A.D. (2006). Novel Three-Dimensional Organoid Model for Evaluation of the Interaction of Uropathogenic *Escherichia coli* with Terminally Differentiated Human Urothelial Cells. *Infect Immun* 74, 750–757.
- Solis, A.G., Bielecki, P., Steach, H.R., Sharma, L., Harman, C.C.D., Yun, S., Zoete, M.R. de, Warnock, J.N., To, S.D.F., York, A.G., et al. (2019). Mechanosensation of cyclical force by PI-EZO1 is essential for innate immunity. *Nature* 573, 69–74.
- Song, J., Duncan, M.J., Li, G., Chan, C., Grady, R., Stapleton, A., and Abraham, S.N. (2007). A Novel TLR4-Mediated Signaling Pathway Leading to IL-6 Responses in Human Bladder Epithelial Cells. *Plos Pathog* 3, e60.
- Spaulding, C.N., Klein, R.D., Ruer, S., Kau, A.L., Schreiber, H.L., Cusumano, Z.T., Dodson, K.W., Pinkner, J.S., Fremont, D.H., Janetka, J.W., et al. (2017). Selective depletion of uropathogenic *E. coli* from the gut by a FimH antagonist. *Nature* 546, 528–532.
- Suzuki, K., Koyanagi-Aoi, M., Uehara, K., Hinata, N., Fujisawa, M., and Aoi, T. (2019). Directed differentiation of human induced pluripotent stem cells into mature stratified bladder urothelium. *Sci Rep-Uk* 9, 10506.
- Thacker, V.V., Sharma, K., Dhar, N., Mancini, G.-F., Sordet-Dessimoz, J., and McKinney, J.D. (2020a). Rapid endothelial infection, endothelialitis and vascular damage characterise SARS-CoV-2 infection in a human lung-on-chip model. *Biorxiv* 2020.08.10.243220.
- Thacker, V.V., Dhar, N., Sharma, K., Barrile, R., Karalis, K., and McKinney, J.D. (2020b). A lung-on-chip model of early *M. tuberculosis* infection reveals an essential role for alveolar epithelial cells in controlling bacterial growth. *Elife* 9, e59961.
- Tovaglieri, A., Sontheimer-Phelps, A., Geirnaert, A., Prantil-Baun, R., Camacho, D.M., Chou, D.B., Jalili-Firoozinezhad, S., Wouters, T. de, Kasendra, M., Super, M., et al. (2019). Species-specific enhancement of enterohemorrhagic *E. coli* pathogenesis mediated by microbiome metabolites. *Microbiome* 7, 43.
- Truschel, S.T., Wang, E., Ruiz, W.G., Leung, S.-M., Rojas, R., Lavelle, J., Zeidel, M., Stoffer, D., and Apodaca, G. (2002). Stretch-regulated Exocytosis/Endocytosis in Bladder Umbrella Cells. *Mol Biol Cell* 13, 830–846.
- Uderhardt, S., Martins, A.J., Tsang, J.S., Lämmermann, T., and Germain, R.N. (2019). Resident Macrophages Cloak Tissue Microlesions to Prevent Neutrophil-Driven Inflammatory Damage. *Cell* 177, 541-555.e17.

- Wang, E.C.Y., Lee, J.-M., Ruiz, W.G., Balestreire, E.M., Bodungen, M. von, Barrick, S., Cockayne, D.A., Birder, L.A., and Apodaca, G. (2005). ATP and purinergic receptor–dependent membrane traffic in bladder umbrella cells. *J Clin Invest* 115, 2412–2422.
- Wang, J., Wang, C., Xu, N., Liu, Z.-F., Pang, D.-W., and Zhang, Z.-L. (2019). A virus-induced kidney disease model based on organ-on-a-chip: Pathogenesis exploration of virus-related renal dysfunctions. *Biomaterials* 219, 119367.
- Yang, E., Chee, J.L.Y., Duraiswamy, S., Chen, S., Lees, K., and Chen, S.L. (2019). Isolation of Single Intracellular Bacterial Communities Generated from a Murine Model of Urinary Tract Infection for Downstream Single-cell Analysis. *J Vis Exp Jove*.
- Yu, Y., Kwon, K., Tsitrin, T., Bekele, S., Sikorski, P., Nelson, K.E., and Pieper, R. (2017). Characterization of Early-Phase Neutrophil Extracellular Traps in Urinary Tract Infections. *Plos Pathog* 13, e1006151.
- Zahler, S., Kowalski, C., Brosig, A., Kupatt, C., Becker, B.F., and Gerlach, E. (1997). The function of neutrophils isolated by a magnetic antibody cell separation technique is not altered in comparison to a density gradient centrifugation method. *J Immunol Methods* 200, 173–179.
- Zalewska-Piątek, B., Olszewski, M., Lipniacki, T., Błoński, S., Wieczór, M., Bruździak, P., Skwarska, A., Nowicki, B., Nowicki, S., and Piątek, R. (2020). A shear stress micromodel of urinary tract infection by the *Escherichia coli* producing Dr adhesin. *Plos Pathog* 16, e1008247.
- Zhou, M., Zhang, X., Wen, X., Wu, T., Wang, W., Yang, M., Wang, J., Fang, M., Lin, B., and Lin, H. (2016). Development of a Functional Glomerulus at the Organ Level on a Chip to Mimic Hypertensive Nephropathy. *Sci Rep-Uk* 6, 31771.

Chapter 4. Experimental *in vitro* approaches to generate stratified uroepithelium

4.1 Need for stratified uroepithelium

The uroepithelium is a stratified epithelial tissue that comprises of three distinct layers: basal cells, intermediate cells, and umbrella cells (Figure 1.5). In the current mouse model of UPEC pathogenesis, IBCs and QIRs form respectively in the superficial umbrella cell layer and intermediary transitional cell layers (Figure 1.6). However, *in vivo*, it is technically challenging to study underlying spatiotemporal dynamics of IBCs and QIRs formation using the animal models. In this direction, *in vitro* models of stratified bladder tissue have emerged as a promising approach to complement findings from animal models.

4.2 *In vitro* systems with stratified uroepithelium

Several studies have tried to recapitulate stratified uroepithelium. Southgate et.al (Southgate et al., 1994) demonstrated that culture of primary human uroepithelial cells under increased calcium concentration (.09 to 4mM) induced stratification and enhanced expression of E-cadherin. However, the upper layer of this stratified uroepithelium did not show any features of the umbrella cell layer (Southgate et al., 1994). Follow up studies by Southgate and co-workers achieved terminal differentiation in uroepithelium treated with PPAR- γ agonist, troglitazone (Varley et al., 2004). Hypoxia stress has also been shown to improve urothelial cell expansion compared to normoxic conditions (Chabaud et al., 2017).

In another approach, urothelial cells cultured on liquid-liquid interface (LLI) were found to achieve better stratification than air-liquid interface (ALI). The urothelial stratification was achieved both in the presence or absence of Ca^{2+} (Višnjar and Kreft, 2013). However, with urine-liquid interface (ULI) maintained on transwell inserts, uroepithelial formed islands of stratified uroepithelium as shown by Rohn and co-workers (Horsley et al., 2018).

Human uroepithelial cells cultured on 3T3-J2 fibroblasts culture system (Rheinwald and Green, 1975) proliferated to form islands of differentiated uroepithelium (Larsson et al., 2014). However, it was previously shown that application of shear stress on uroepithelial cell monolayers grown on top of γ -irradiated fibroblasts resulted in uniform stratification and differentiation (Cattan et al., 2011). Compressed tubular collagen scaffolds have also been used to achieve differentiation of human urothelial cells and smooth muscle cells under shear stress conditions (Vardar et al., 2015). Another approach with collagen-derived scaffold used a balloon to construct the hollow bladder tissue (Bouhout et al., 2019). Bladder epithelial cells were cultured on the luminal surface whereas bladder mesenchymal cells were embedded in the surrounding collagen scaffold. Using a PPAR- γ agonist, troglitazone and an EGFR inhibitor PD153035, human induced pluripotent stem cells have also been used to achieve stratified and differentiated uroepithelium (Suzuki et al., 2019). Mature uroepithelium has been demonstrated in bladder organoids, achieved via collagen beads (Smith et al., 2006), urine-liquid interface on porous substrates (Horsley et al., 2018) and matrigel (Mullenders et al., 2019).

4.3 Stratification and differentiation of human uroepithelial cells

HTB-9 uroepithelial cells were cultured under many different conditions that were previously shown to induce stratification and are briefly described below.

1) Different doses of CaCl_2

HTB-9 cells were cultured to a confluent monolayer in a 12 well plate pre-coated with 50 $\mu\text{g}/\text{ml}$ Collagen-1. Thereafter, cells were treated with different concentrations of CaCl_2 reconstituted in RPMI/FBS 10% for 1 week. Cells incubated with 0.4, 1 and 4 mM Ca^{2+} did not show any significant morphological change in cell size and cell shape compared to untreated control. Occasionally HTB-9 cells were observed to form spherical ball of cells like HTB-9 spheroids in 4 mM Ca^{2+} . However, cells treated with higher dose i.e 40 mM Ca^{2+} started exfoliating and dying in 2 days after high Ca^{2+} treatment. In all of the cases with different concentration Ca^{2+} , cells did not show any sign of stratification.

2) Reducing serum concentration

HTB-9 cells were typically grown as a confluent monolayer in a 12 well plate pre-coated with 50 $\mu\text{g}/\text{ml}$ Collagen-1 in 10% FBS as per the recommendations of the supplier. FBS concentration was reduced to 1, 2.5 and 5% on a confluent monolayer. The effect of the serum was found to be detrimental while culturing cells with 1% FBS over a week compared to other concentrations of the serum.

Also, diminishing the serum concentration did not induce stratification on a confluent monolayer of cells.

3) Seeding cells on an established monolayer of cells

HTB-9 cells express markers of differentiated uroepithelial cells (Martinez et al., 2000; Mulvey et al., 1998). Primary human uroepithelial cells (PHUC, a kind gift from Dr. Mattias Larsson, EPFL) did not express markers of UP3a, a marker of differentiated uroepithelium. The rationale behind this approach was to test whether differentiated cells could attach and form tight junctions with already confluent monolayer of undifferentiated PHUC cells in a 12 well plate pre-coated with 50 µg/ml Collagen-1. HTB-9 cells were seeded on both confluent monolayer of HTB9 cells and PHUCs in separate experiments. HTB-9 cells could adhere within 2-4 hrs after seeding but failed to proliferate and establish another confluent layer on top of already established monolayer of cells.

4) Culturing with serum free medium

Southgate et al (Southgate et al., 1994) have shown that growing PHUCs in serum free medium i.e Keratinocyte serum free medium (KSFM) with Ca^{2+} can induce stratification. Both HTB-9 cells and PHUCs were grown as a confluent monolayer in a 12 well plate pre-coated with 50 µg/ml Collagen-1. Both HTB-9 cells and PHUCs were incubated in KSFM medium with and without Ca^{2+} . PHUCs cells were observed to stratify in 0.4-2 mM Ca^{2+} as reported by Southgate et al (Southgate et al., 1994). However, HTB-9 cells failed to stratify under similar conditions.

5) Culturing cells under shear stress in ibidi slides

Studies have shown that different cell types such as human uroepithelial cells (Cattan et al., 2011) and intestinal epithelial cell line such as Caco-2 cells (Kim and Ingber, 2013) can differentiate in a mechanically induced environment such as under shear stress. HTB-9 cells were cultured to a confluent monolayer in ibidi µ-Slide VI^{0.4} (dimensions: height- 0.4 mm, width- 3.8 mm and length -17 mm) and put under .02 dyne/cm² shear stress which corresponded to a flow rate of 960 µL/h. HTB-9 cells failed to stratify and differentiate under this level of shear stress over a period of 2 weeks. However, we have to specify that there were differences between our experimental setup and that used by Cattan et al (Cattan et al., 2011), who co-cultured human uroepithelial cells with irradiated human fibroblasts and were able to subject their cells to 5-fold higher levels of shear stress.

6) Cell imprinted substrates

Smart micro-nano environments have been used to induce differentiation in fibroblasts and chondrocytes through cell imprinted substrates (Bonakdar et al., 2016). Application of cell-imprinted topography to cell substrates can induce changes in cell morphology and control stem cell fate. HTB-9 cells were cultured in tissue culture treated T-75 flasks to a 75% confluence. Cell imprinting process was done by pouring PDMS on already 4% PFA fixed cells. PDMS curing process was done at 37°C for 24h. Subsequently cured PDMS was peeled off gently and washed twice in 1M NaOH solution at 37 °C. The washing process was done to remove residues of PDMS. This cell imprinted PDMS substrate was cut into small pieces. HTB-9 cells were cultured on these substrates with and without pre-coating with 50 µg/ml Collagen-1. Cultured cells did form a monolayer on printed substrates but did not show any sign of stratification over a period of 1-2 weeks when cultured in epithelial cell media supplemented with 10% FBS.

7) Supplementation with PPAR γ agonists

The path to terminal differentiation of uroepithelium is affected by PPAR γ signaling (Varley et al., 2004). This differentiation program was shown to be enhanced by simultaneous upon treatment with PPAR γ agonists : rosiglitazone or troglitazone and by inhibition of epidermal growth factor receptor (EGFR) signaling through treatment with PD153035 (Varley et al., 2004). HTB-9 cells were generally grown as a confluent monolayer in a 12 well plate pre-coated with 50 µg/ml Collagen-1. Subsequently cells to different combinations of 1 µM rosiglitazone or troglitazone with and without PD153035 in different media: RPMI (supplemented with 10% FBS) and keratinocyte serum free medium (KSFM). However, we failed to induce any stratification in these HTB-9 cells. Moreover, cells were found to undergo exfoliation when higher concentrations (5 µM) of these compounds were used.

8) Air-Liquid interface (ALI)

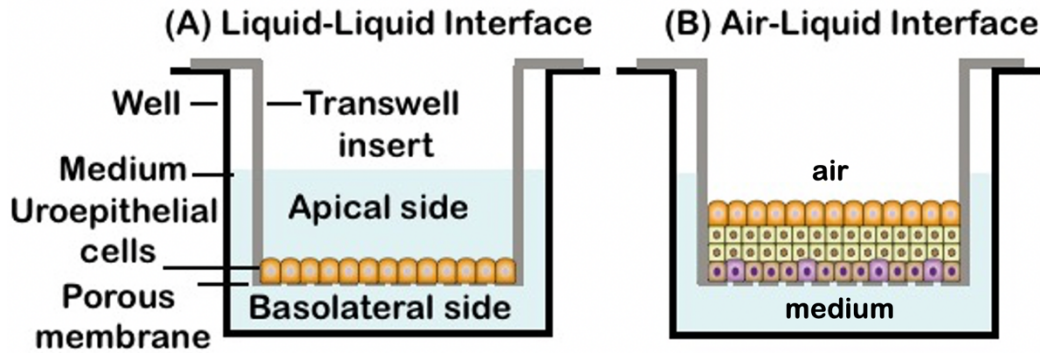


Figure 4.1: Schematic for generation of islands of stratified uroepithelium under air-liquid interface on transwell inserts.

HTB-9 cells were grown to form a monolayer on 0.4 μm pore size Corning Transwell Inserts (detailed protocol is described in 4.10.1). Post-confluence, cells were incubated with and without 2 mM Ca^{2+} in different media: RPMI/10% FBS. Cells were observed to undergo stratification in all of these conditions. Generally, cells were observed to undergo proliferation as early as 2-3 days after introduction of ALI. Two weeks after incubation in ALI, cells proliferated to form patchy islands of 3-4 layers surrounded by a monolayer of cells. This patchy growth was observed in all conditions under ALI and was independent of incubation with or without 2 mM Ca^{2+} as also reported previously (Višnjar and Kreft, 2013). The stratification of uroepithelial cells on bigger pore sized: 3.0 or 5.0 μm transwell inserts did not occur. For epithelial cells cultured on 3.0 or 5.0 μm transwell inserts, the medium was found to diffuse through the pores to reach the apical side of the insert. Thus, the ALI interface was never perfectly maintained on epithelial cell layers grown on 3.0 or 5.0 μm pore size transwell inserts.

The islands of stratified uroepithelial layers on 0.4 μm pore size transwell inserts were fixed 3 weeks after the cell culture. Prior to the paraformaldehyde (4% PFA) fixation, the uroepithelial layers were stained for the plasma membrane with Cell Mask Orange (false coloured in green, Figure 4.2(a-d)). Immunofluorescence staining of the stratified layers revealed islands with 3-4 cell layers (identified with nuclear staining). The upper layer of the stratified uroepithelium were stained for umbrella-cell specific markers, identified by staining for anti-uroplakin3a (UP3a, Figure 4.2a), anti-uroplakin2a (UP2a, Figure 4.2b), anti-cytokeratin-20 (CK20, Figure 4.2c). All the layers of the stratified uroepithelium were stained for general epithelial cell marker cytokeratin-7 (CK7, Figure 4.2d).

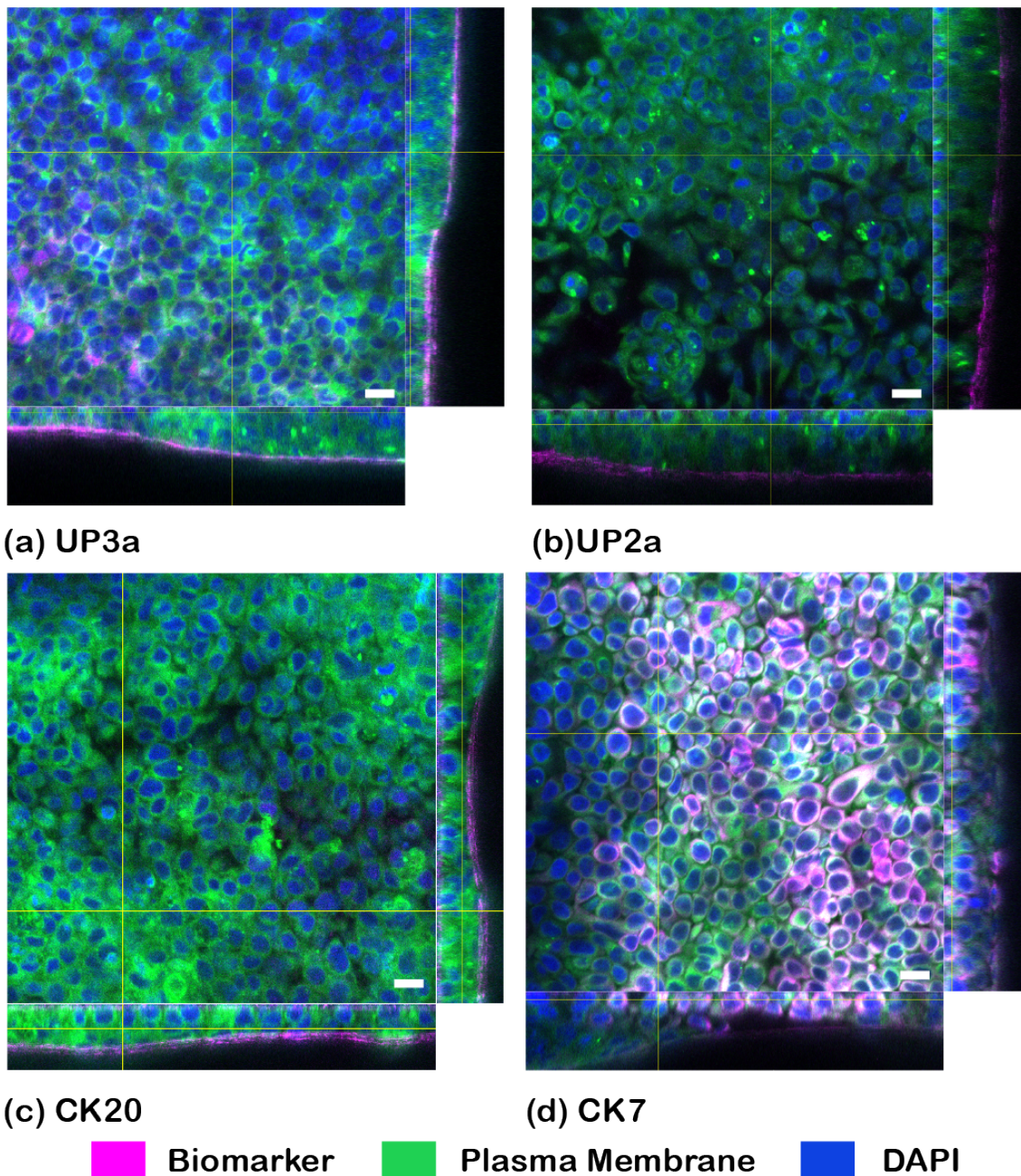


Figure 4.2: HTB9 cells undergo non-uniform stratification in air-liquid interface on transwell inserts. Multiple layers were stained for different cellular markers of differentiation: (a) UP3a, (b) UP2a and (c) CK20. The epithelial layer was checked for stratification through general uroepithelial cell marker: (d) CK 7 and with plasma membrane staining done with Cell Mask Orange. Scale bar is 20 μm in all the panels.

9) Co-culture with bladder endothelial cells in high Ca^{2+} and human urine

The next step for improving the stratification of uroepithelium was motivated from stratification of HBLAK bladder epithelial cells (procured from CELLnTEC) under urine-liquid interface (ULI) on transwell inserts by Horsley et al. (Horsley et al., 2018). Therefore, we tried ULI on the stratified uroepithelial layers that were achieved from ALI. However, we kept the epithelial-endothelial layer

tissue physiology on the apical and basal sides of the insert. The detailed schematic (Figure 4.3) and protocol for the stratification is mentioned in 4.10.1.

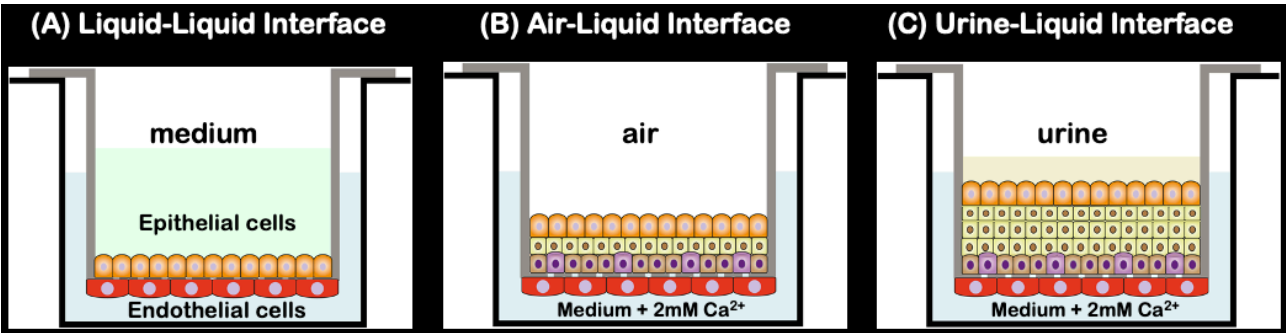


Figure 4.3: Schematic for generation of uniform stratification in bladder epithelial cells on 0.4 μm pore transwell inserts.

Co-culture of monolayer of bladder epithelial cells with bladder endothelial cells in (A) liquid-liquid interface becomes stratified over a period of 5-7 days in (B) air-liquid interface achieves uniform stratification in high calcium on basolateral and urine on apical side in (C) urine-liquid interface.

Horsley et al. (Horsley et al., 2018) cultured HBLAK bladder epithelial cells only under ULI to induce islands of stratified uroepithelium. The experimental protocol optimized for HTB9 bladder epithelial cells induced stratification only when ULI was preceded by ALI. The data for HBLAK bladder epithelial cells is not shown in this thesis. This difference in results could be attributed to the difference in the sources of the cell lines (bladder carcinoma for HTB9 vs normal bladder epithelium for HBLAK cells).

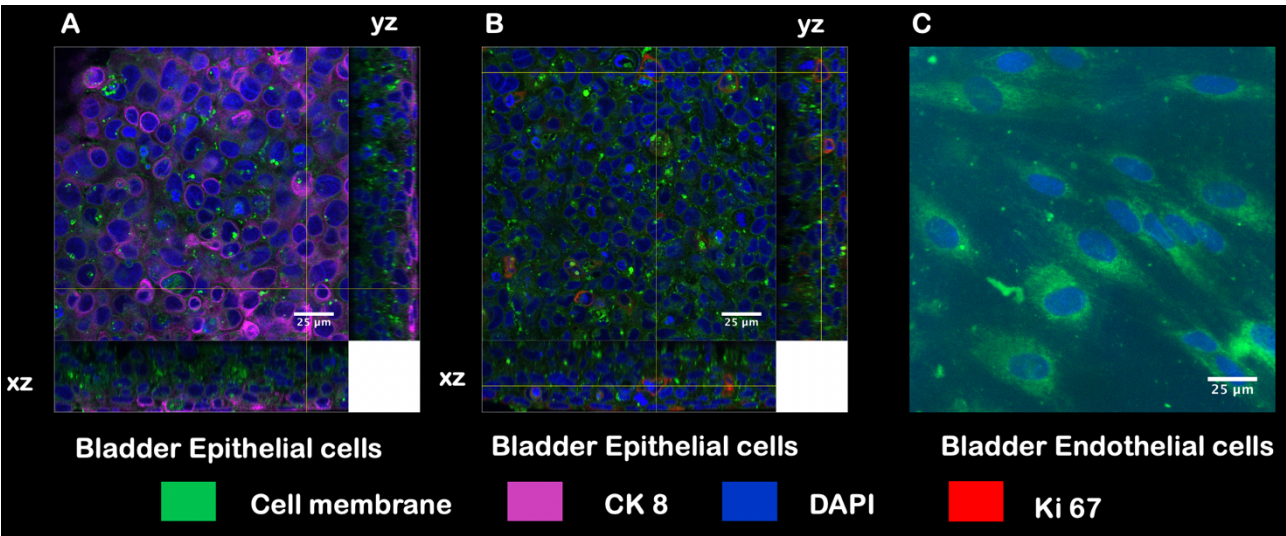


Figure 4.4: Uniform stratification of epithelial cells under urine-liquid interface maintained across epithelium-endothelium on transwell inserts. Orthogonal slices of stratified uroepithelium shows higher CK8 expression on the upper layer. The proliferative cells identified with anti-Ki 67 staining were sparsely populated throughout the stratified epithelium. Cell nuclei were identified with DAPI

staining. The bottom part of the insert was populated with confluent layer of bladder endothelial cells. Scale bar is 25 μm in all the panels.

Culture of HTB9 bladder epithelial cells under ALI for one week followed by ULI for two weeks led to the generation of uniformly stratified uroepithelium. The bladder endothelial cells were cultured on the basal side of the medium with endothelial cell medium supplemented with 2 mM Ca^{2+} . The upper layer of the uniformly stratified uroepithelium stained positive for cytokeratin 8 (CK8, Figure 4.4A). Proliferating cells inside the stratified epithelium were identified with anti-Ki 67 staining (Ki 67, Figure 4.4B). The confluent layer of the endothelial cells on the bottom of the insert were identified with plasma membrane dye (Cell Mask Orange, false coloured in green, Figure 4.4C).

We also confirmed the generation of uniformly stratified uroepithelium by paraffin embedding and imaging of cut thin slices (4 μm) of uroepithelial layers grown on transwell inserts. The uroepithelial layers on transwell inserts were isolated by cutting the PETE membrane around the rim of the insert. The isolated PETE membrane with uroepithelial layers were placed orthogonally in the paraffin block. The thin slicing process resulted in detachment of the uroepithelial layers from the PETE membrane. However, the integrity of the multiple uroepithelial layers was maintained during the process (Figure 4.5A-C). The nuclear staining with DAPI revealed uniformly stratified epithelium consisting of 4-6 layers as found *in vivo* within human uroepithelium (Apodaca, 2004).

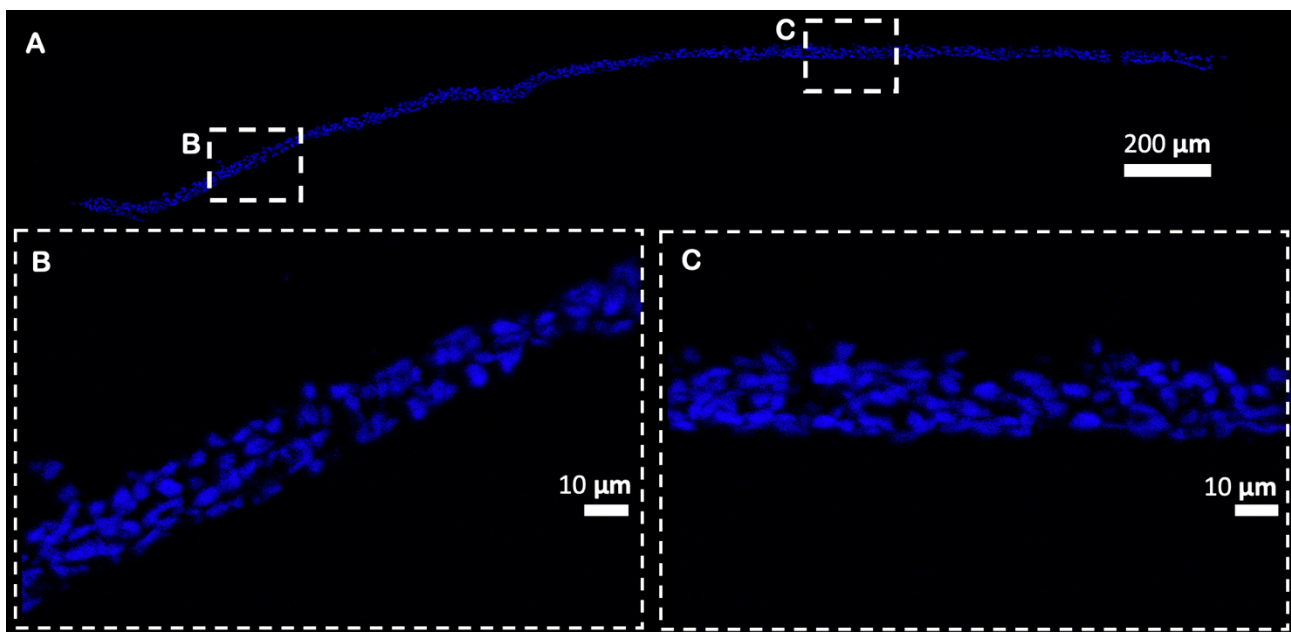


Figure 4.5: Long sheets of uniformly stratified uroepithelium on transwell inserts. (A) Merged tilescan of large field of view (16X4) shows the presence of uniform stratified uroepithelium on transwell inserts. Zooms of two regions (B and C) show 4-5 cell layers identified with DAPI staining (shown in blue) of the nuclei.

The orthogonal slice of the uroepithelium revealed that cell nuclei in the upper layer of the transwell insert were bigger than the lower and middle layers (compare Figure 4.6C vs Figure 4.6A-B) of the stratified uroepithelium. Few instances of binucleate epithelial cells, a marker of umbrella cells (Apo-daca, 2004) were observed in the upper layer of the uroepithelium.

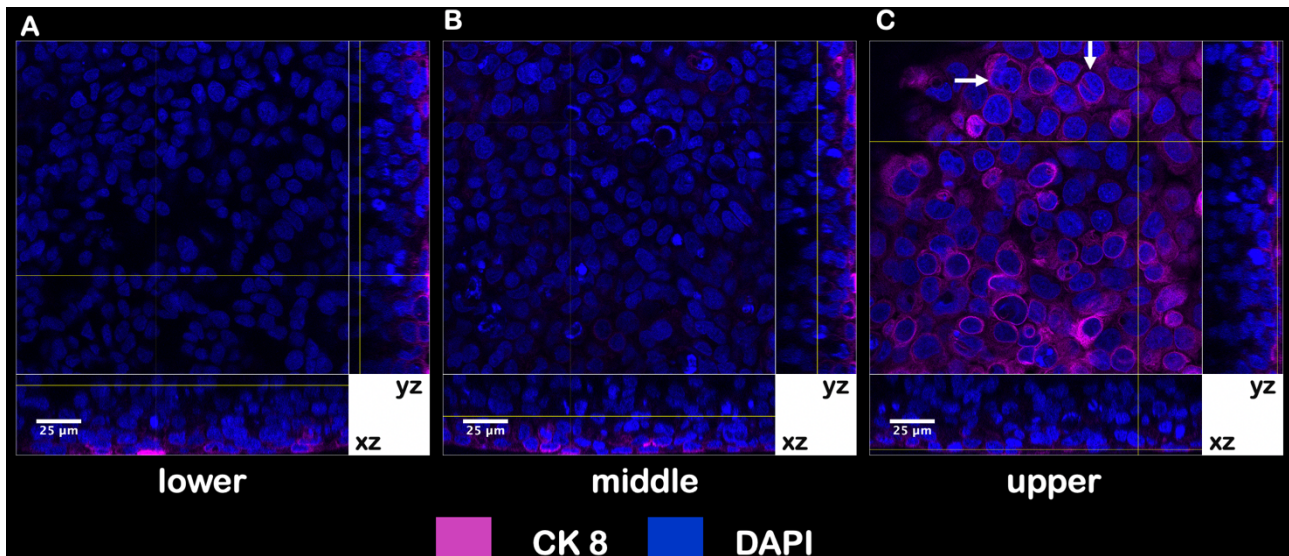


Figure 4.6: Uroepithelial cells in the upper layer of the uniformly stratified epithelium had bigger nuclei. The cells in the lower (A) and middle (B) layers of uniformly stratified uroepithelium had smaller nuclei compared to those found in the upper layer (C). Few cases of binucleate uroepithelial cells (marked with white arrows) were identified in the upper layer. For all panels, scale bar is 25µm.

In summary, after many trials, the only method that appeared to be promising was growing human uroepithelial cells under an air-liquid interface. My results from the various methodologies attempted are summarized in [Table 3](#).

| | Experiment | Conditions | Incubation time | Observations |
|---|---|--|-----------------|--|
| 1 | Different doses of CaCl ₂ | 0.4-40mM | 1 week | no stratification |
| 2 | Reducing serum concentration | 1-10% | 1 week | no stratification |
| 3 | Seeding differentiated epithelial cells on an established monolayer of undifferentiated cells | HTB-9-on-primary human uroepithelial cells | 1 week | Cells did not stick to established confluent monolayer |

| | | | | |
|---|---|---|-----------|---------------------------|
| 4 | Culturing with serum free medium | Keratinocyte serum free medium | 2 weeks | no stratification |
| 5 | Shear stress in ibidi slides | .02 dyne/cm ² | 2 weeks | no stratification |
| 6 | Cell imprinted substrates | RPMI%10 FBS | 1 week | no stratification |
| 7 | Rosiglitazone and retinoic acid | 1 μ M in RPMI%10 FBS | 1 week | no stratification |
| 8 | Air-Liquid Interface | Air/RPMI%10 FBS | 2-8 weeks | islands of stratification |
| 9 | Co-culture with bladder endothelial cells in high Ca ²⁺ medium and human urine | 2mM Ca ²⁺ in endothelial cell medium | 2-8 weeks | uniform stratification |

Table 3: Different methodologies used to induce stratification and differentiation in uroepithelial cells.

4.4 Stratification of bladder epithelial cells inside bladder-chip devices with plastic and PDMS membranes

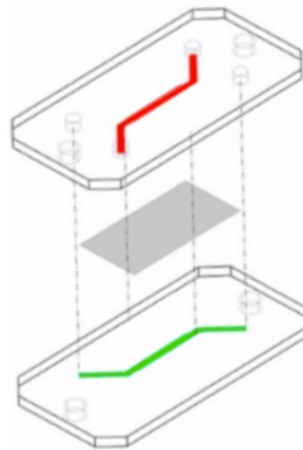


Figure 4.7: Schematic diagram of the bladder-chip device with sandwiched membrane.

The bladder-chip consisted of upper PDMS slab, sandwiched membrane and lower PDMS slab. The schematic shows the upper channel (red), polyester (PETE) or PDMS membrane (grey) and the lower channel (green). Image taken from lab immersion report of Isabelle Heimgartner, Master Student, EPFL.

The bladder-chip is composed of an upper channel, a lower channel and a sandwiched membrane in between the upper and lower channels (Figure 4.7). Both the upper and lower channels were made from PDMS base that was mixed with a crosslinker (curing agent) in 10:1 (weight by weight) ratio. The PDMS base-curing agent mixture was injected inside a lab-made micromachined polycarbonate

mold. For the sandwiched membrane between the upper and lower channels, we used either 0.4 μm Polyester (PETE) membrane filters (Sterlitech, diameter: 47 mm), or 2 μm PDMS membrane (BI/OND, Netherlands).

Both the upper and lower channels in each device were designed with 20 mm length and 1 mm width. The height for the upper and lower channel was chosen to be 1 mm and 250 μm respectively. The plastic membrane was cut (20 mm length and 10 mm width) with a scissor. The plasma treatment of the polyester membrane and PDMS channels was not sufficient to produce robust binding of the plastic membrane to the PDMS. We then resorted to plastic-PDMS bonding at room temperature done by the amine-epoxy chemical bond formation at the plastic-PDMS interface (Tang and Lee, 2010) (Figure 4.8). This chemical bonding was done via the silane coupling reaction of the amine-terminated silane groups on the PDMS substrate with the epoxy-terminated silane groups on the plastic substrate. Both the PDMS upper, lower channels and plastic membrane were treated with air-plasma (Diener, Power= 60 W, time =80 sec). The PDMS upper and lower channels were treated with freshly prepared 1% solution of (3-Aminopropyl) triethoxysilane (APTES) solution in ddH₂O. The plastic membranes were functionalized with 1% freshly prepared solution of (3-Glycidyloxypropyl) triethoxysilane (GPTES) solution. The PDMS channels and plastic membrane was then washed with ddH₂O water, dried with a nitrogen gun and brought into conformal surface contact with one another. We reinforced the chemical bonding by applying a constant pressure throughout, using a small weight (500 g, 5cm X 5cm) on the PDMS-plastic assembly for at least 8 hours.

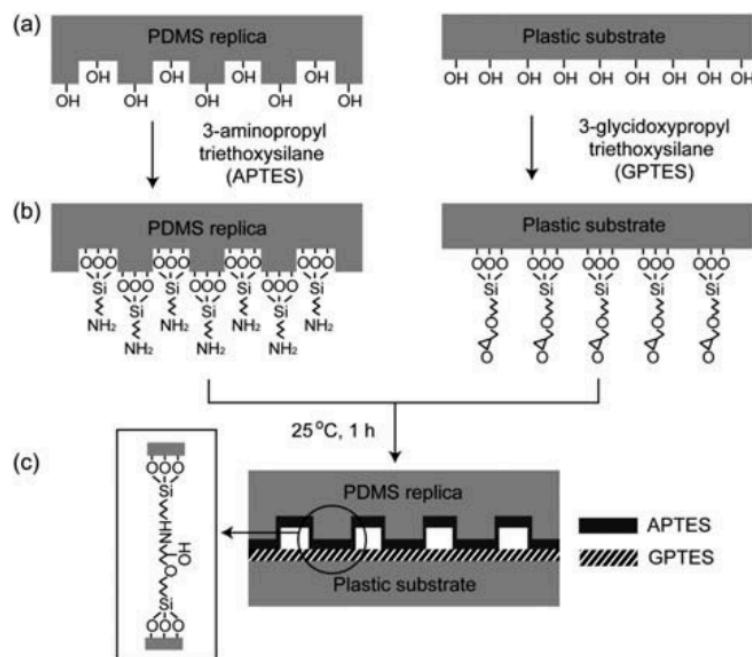


Figure 4.8: PDMS-plastic bonding at room temperature by the formation of amine-epoxy bond at the PDMS-plastic interface.

(a) Plasma treatment of PDMS and plastic substrates generate hydroxyl groups. (b) Aminosilane and epoxysilane functional groups on the oxygen plasma treated PDMS and plastic substrates. Amine-epoxy bond formation by PDMS-plastic surface contact at room temperature for one hour. Image taken from Tang et al (Tang and Lee, 2010).

The bladder-chip devices with sandwiched 2 μm porous PDMS membrane (length-20 mm, width-10 mm, height-5 μm) were assembled post air-plasma treatment (Diener, Power = 60 W) of upper, lower channels and the PDMS membrane. All the bladder-chip devices were coated with extracellular matrix containing 100 $\mu\text{g}/\text{ml}$ of native bovine dermis collagen (Atelocollagen), 50 $\mu\text{g}/\text{ml}$ fibronectin (Gibco), 10 mM HEPES buffer solution (Gibco). The cocktail of extracellular matrix solution was introduced with 200 μL pipette tips inside the bladder-chip devices and incubated inside the cell culture incubator at 37°C for 3 hours. The extracellular coated bladder-chip devices were stored at 4°C until needed for the experiments.

4.4.1 Stratification of bladder epithelial cells inside bladder-chip devices with small pores

Human Bladder Microvascular Endothelial cells (HMVEC-Bd, procured from Lonza) and HTB9 bladder epithelial cells were seeded on each side of the membrane in bladder-chip. The bladder endothelial cells are significantly larger in size (ca. 10X, data not shown) compared to bladder epithelial cells. Thus, we decided to reduce the seeding density for endothelial cells. The lower channel was seeded with endothelial cells at 0.5 million cells/ml prior to seeding of the upper channel with bladder epithelial cells at 5 million cells/ml each in their respective cell culture medium. The monolayer

confluency of the endothelial cells was assured by repeating the seeding process. Both the endothelial cell medium as well as the diluted pooled urine (10 times in PBS) were supplemented with 1X Antibiotic-Antimycotic solution (Gibco).

4.4.2 Direct exposure of bladder epithelial cells to flow of diluted pooled urine

Confluent monolayer of epithelial cells in the upper channel was exposed to pooled urine (diluted ten times in PBS) at a flow rate of 60 $\mu\text{L/hr}$ (shear stress=0.001 dyne/cm²). Simultaneously confluent monolayer of endothelial cells were exposed to endothelial cell medium supplemented with 2 mM Ca^{2+} under flow of 60 $\mu\text{L/hr}$ (shear stress=0.02 dyne/cm²). The bladder-chip was kept inside the incubator at 37°C, 95% humidity and 5% CO_2 for 2-3 weeks. The flow of urine and medium on the epithelial and endothelial sides, respectively allowed us to remove dead exfoliated cells and cellular waste products produced over time. Epithelial cells did tolerate the flow of diluted pooled urine; however, we did not observe any stratification in epithelial layer (Figure 4.9A).

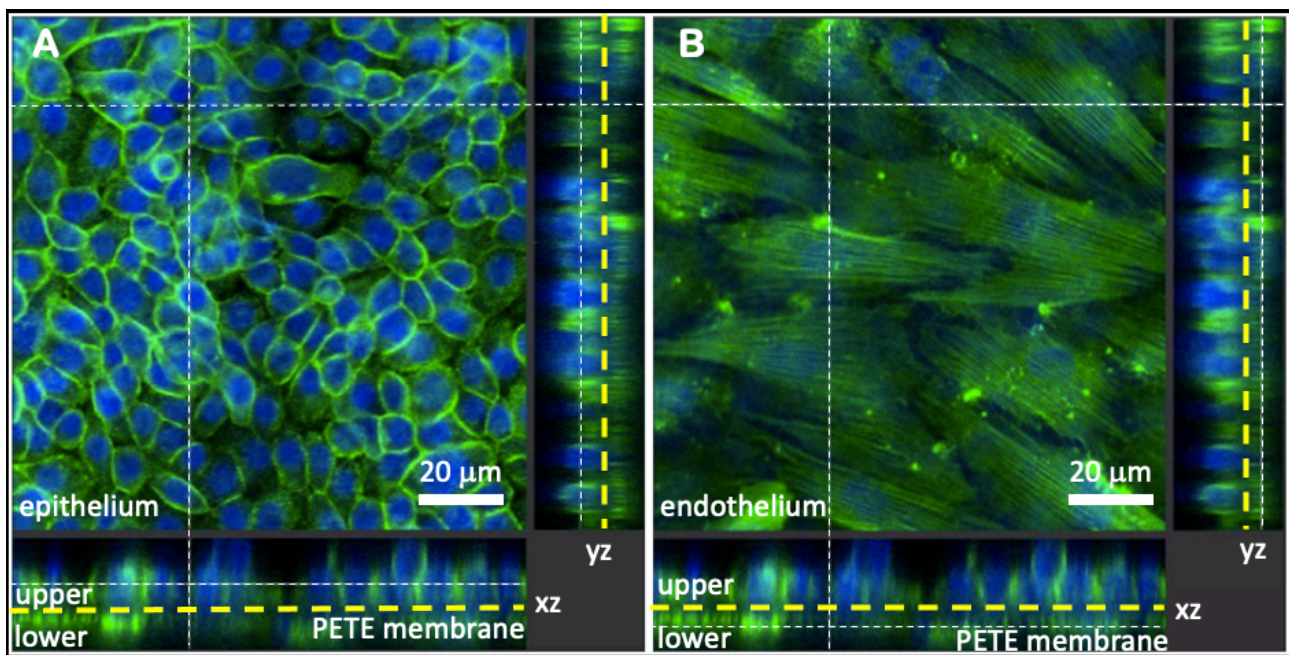


Figure 4.9: Flow of urine on epithelial side and medium supplemented with 2 mM Ca^{2+} on the endothelial side did not induce stratification in epithelial cells. Orthogonal slice of the confluent monolayer of epithelial cells in the upper channel (left) and confluent layer of endothelial cells (right). 0.4 μm PETE membrane is marked with dotted yellow lines. Actin filaments (green) are stained with Phalloidin and cell nuclei are stained with DAPI (blue). Image was acquired by mechanically isolating the PETE membrane from the bladder-chip.

4.4.3 Air-liquid interface in the bladder-chip followed by urine exposure

The flow of urine did not induce stratification in HTB9 bladder epithelial cells. Then we decided to incubate confluent monolayer of epithelial cells under ALI for one-two weeks. The endothelial side

was perfused with endothelial cell medium supplemented with 2 mM Ca^{2+} at flow rate of 60 $\mu\text{L/hr}$. We observed islands of stratified epithelium after one week of ALI. The islands of stratified epithelium became larger with exposure to static urine on the epithelial side for the next 1-2 weeks. The cellular waste products and dead exfoliated epithelial cells were flushed out and replaced with fresh urine every 3-4 days. The islands of stratified uroepithelium were 40-50 μm in thickness and we estimated that to be 3-5 cell layers of thickness based upon the total thickness and nuclear staining with DAPI. These stratified epithelial layers with islands of 3-5 cell layers were comparable to the 3-6 cell layers reported in human uroepithelium (Jost et al., 1989). We could not identify binucleate umbrella cells in our bladder-chip system as widely present in the human uroepithelium (Apodaca, 2004; Jost et al., 1989). However, this could be attributed to the origins of this cell line, which is derived from a biopsy of a bladder cancerous tissue. The immunofluorescence staining with anti-cytokeratin 7 revealed its expression throughout all the stratified layers as reported in normal human uroepithelium (Hustler et al., 2018). However, we did not manage to achieve uniformly stratified uroepithelium as observed on 0.4 μm transwell inserts. The islands of stratified epithelium were similar in size on 0.4 μm pore size PETE membrane (data not shown) and 2 μm pore size PDMS membrane (Figure 4.10 A-B, data from two different bladder-chips). The imaging of stratified epithelium was better in PDMS membranes compared to PETE membrane. Imaging of the PETE membrane at 1 mm distance from the lower PDMS channel required mechanical isolation of the PETE membrane from the bladder-chip. This process was tedious and led to disruption of the stratified epithelium. However, imaging of the stratified uroepithelium at 1 mm distance from the lower channel was always better in PDMS membrane due to better optical transparency in the PDMS membrane compared to the PETE membrane.

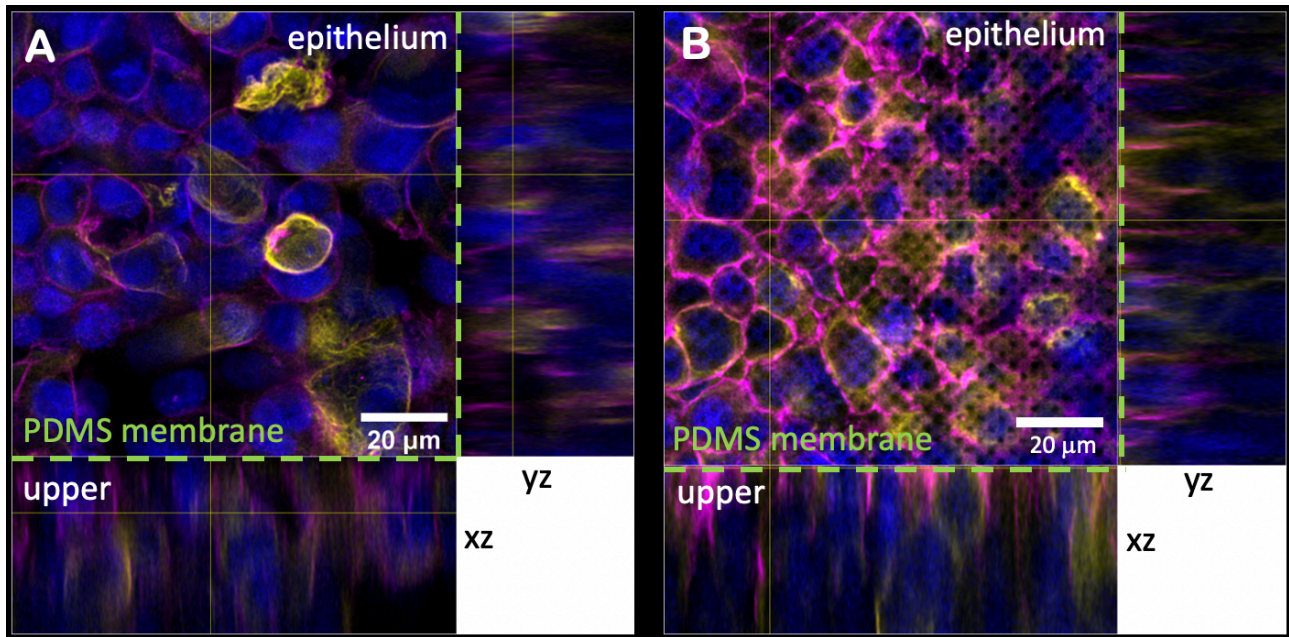


Figure 4.10: Island of stratified uroepithelium in bladder-chip.

(A,B) Example of stratified uroepithelial layers in two separate bladder-chips. Exposure of epithelial cells to a sequence of air-liquid interface followed by exposure to static urine led to islands of stratified epithelium with 3-5 cell layers. Epithelial side was exposed to static urine whereas endothelial side was exposed to flowing endothelial cell medium supplemented with 2 mM Ca^{2+} . Actin filaments (magenta), cytokeratin-7 (yellow) staining shows epithelial cells in the stratified uroepithelium. Cell nuclei are stained with DAPI (blue). 2 μm PDMS membrane is marked with dotted green lines. Image of the stratified uroepithelium was acquired inside the intact bladder-chip.

4.5 Infection of stratified uroepithelium in bladder-chip

The protocol for stratified uroepithelium in bladder-chip required 3-4 weeks of epithelial and endothelial cell culture in urine-endothelial cell medium supplemented with an anti-bacterial/anti-fungal (1X). Still, we lost many bladder-chip devices due to fungal contamination. In the uncontaminated devices, we removed the antibacterial/antifungal 12 hours prior to the experiment. We then performed UPEC infection in the islands of stratified uroepithelium in bladder-chip. UPEC inoculum was introduced as a flow (1200 $\mu\text{L/hr}$) at a cell concentration of 150 million cells/ml in pooled urine (diluted ten times in PBS) for about 1.5-2 hours. The endothelial side of the bladder-chip was always perfused with endothelial cell medium at flow rate of 600 $\mu\text{L/hr}$. Post UPEC infection on the epithelial side, ampicillin treatment (250 $\mu\text{g/ml}$ ~ 40X MIC) was done on both the epithelial and endothelial side for 3 hours to kill UPEC. Ampicillin was washed away, and bladder-chip was perfused with diluted pooled urine and endothelium cell medium at flow rate of 600 $\mu\text{L/hr}$ for next 6 hours. Then, the bladder-chip was fixed and analyzed with immunofluorescence staining. UPEC infection under flow resulted in UPEC attachment to middle (Figure 4.11A) and upper layers (Figure 4.12B) of the stratified uroepithelium. In these experiments, we could not ascertain whether UPEC infection from the upper layer led to the UPEC infection of the middle layers. However, time-lapse imaging of the

stratified uroepithelium could answer this question. As the long protocol (3-4 weeks) for stratified uroepithelium did not result in uniform stratification and many bladder-chip devices were lost due to fungal contamination, we decided to put an end to this project. However, it must be noted that we did achieve islands of stratified uroepithelium in bladder-chips.

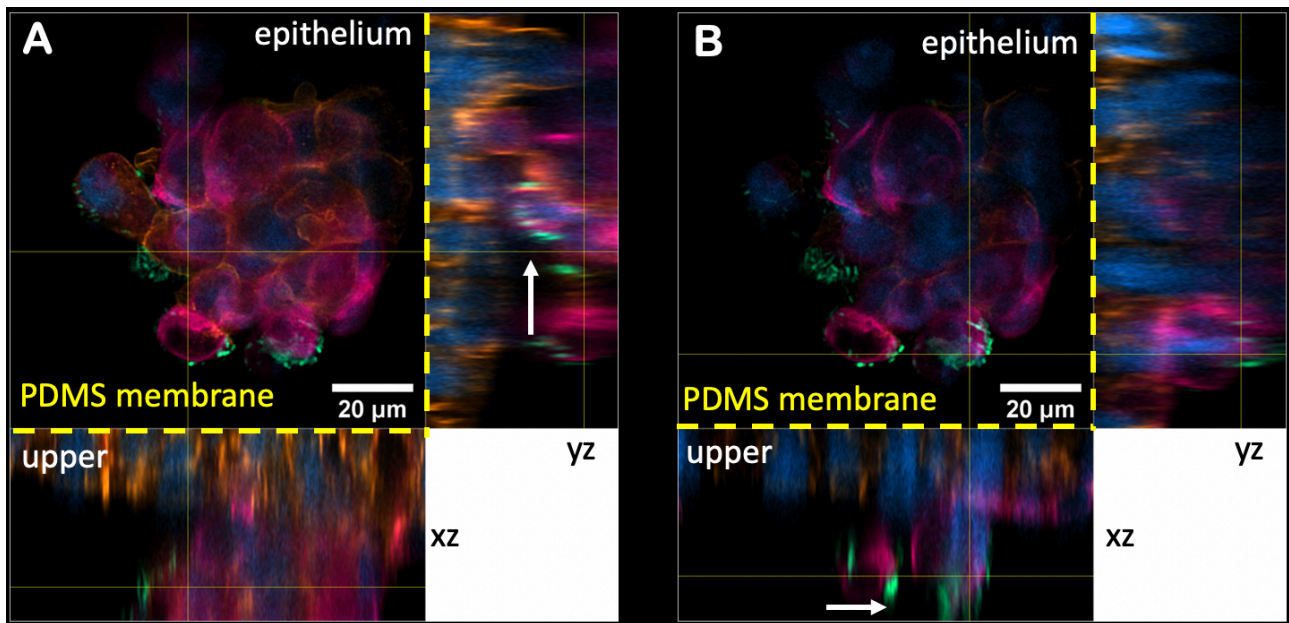


Figure 4.11: UPEC infection of an island of stratified uroepithelium in bladder-chip.

(A) UPEC (spring green) infection of the middle layer of stratified epithelium (shown by white arrow). (B) shows the UPEC infection of the upper layer of the stratified uroepithelium. Actin filaments (amber) and cytokeratin-7 (bright pink) staining shows epithelial cells in the stratified uroepithelium. Cell nuclei are stained with DAPI (blue). 2 μ m PDMS membrane is marked with dotted yellow lines.

4.6 Stratified uroepithelium from dissociated bladder organoids splayed on transwell inserts

We also tried generating multiple layers of uroepithelium on a two-dimensional substrate by seeding stratified mouse bladder organoids on 0.4 μ m pore size transwell inserts. The detailed protocol is mentioned in 4.10.2. The bladder organoids were sheared with a fire polished glass pipette and seeded on transwell inserts under liquid-liquid interface. The epithelial layers of the bladder organoids unfolded and adhered to form islands of stratified uroepithelium over a period of one-two weeks (Figure 4.12). The attached stratified uroepithelium still expressed markers for umbrella cell layer as shown with CK8 staining on transwell insert (Figure 4.12). The CK8 expression was similar as seen on cells inside intact bladder organoids (compare with Figure 2.1). The nuclei of the epithelial cells in the upper layer were bigger than lower and middle layers of the stratified uroepithelium (compare Figure 4.13C vs Figure 4.13A-B). We did not observe any binucleate cells in the upper layer of the stratified uroepithelium (Figure 4.13).

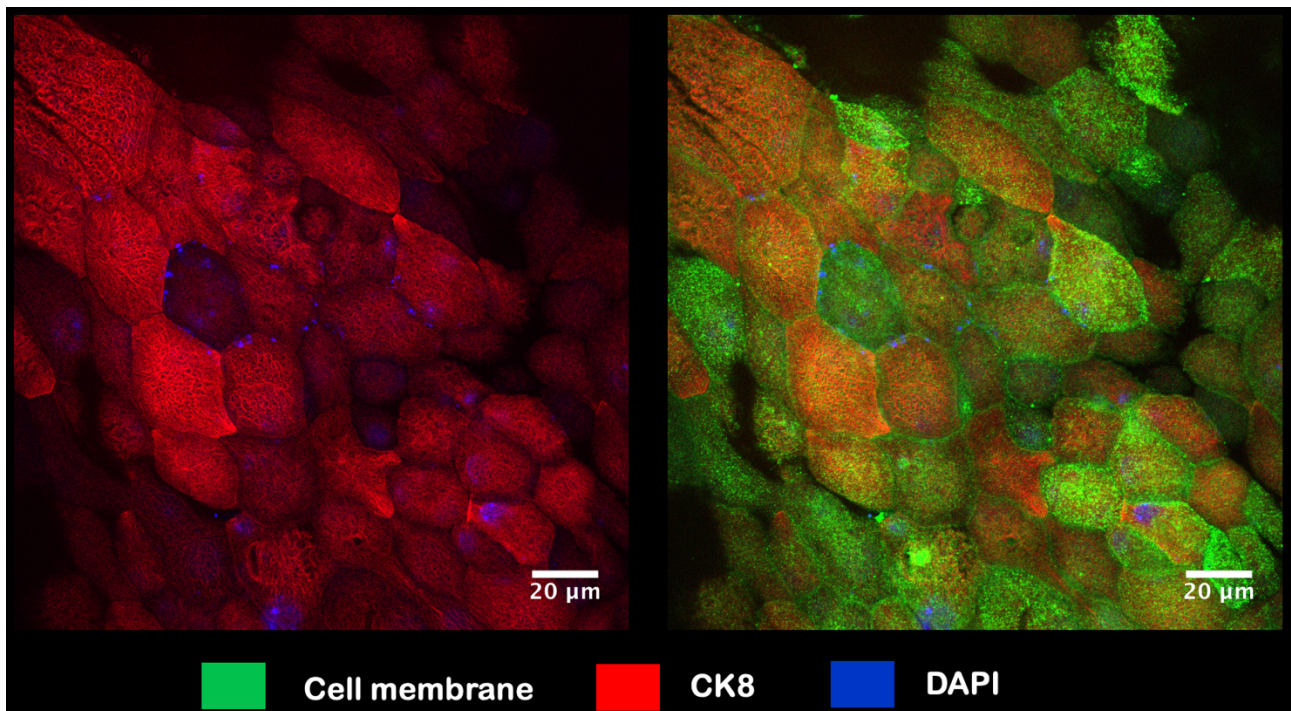


Figure 4.12: Bladder organoids back to 2D culture in liquid-liquid interface on transwell inserts.

The cell membrane of bladder organoids express TdTomato (false coloured in green). CK8 expression was still visible in splayed over organoids. Cell nuclei were identified with DAPI staining.

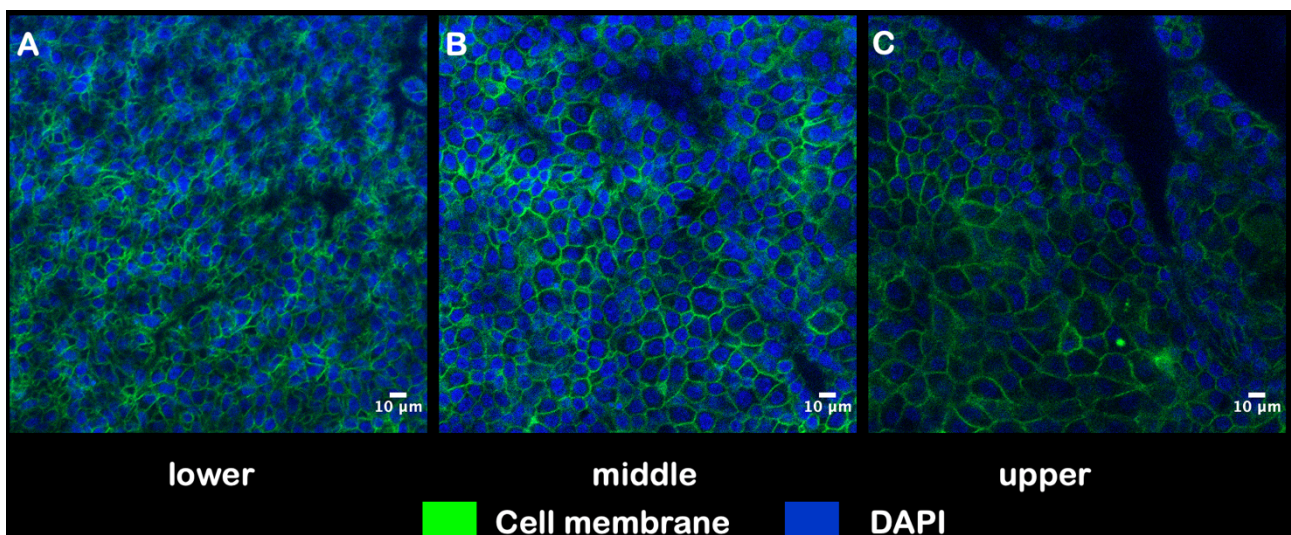


Figure 4.13: Cells in upper layers of the splayed bladder organoids were bigger in size compared to the cells in the lower and middle layers of the splayed bladder organoid.

The cell membrane of bladder organoids express TdTomato (false coloured in green). Cell nuclei were identified with DAPI staining. For all panels, scale bar is 10 µm.

4.7 Splaying up isolated mouse bladder for *ex vivo* UPEC infection

Infected mouse bladder has been used for studying the maturation of IBCs (Justice et al., 2004). This was made possible by immobilizing and stretching the bladder tissue mounted on the microscope stage with four single-axis microtranslators (Figure 4.14). The incubation chamber was filled with RPMI 1640 medium supplemented with 10% FBS. This set up was used for 3-12 hours bladder imaging post removal from the mice.

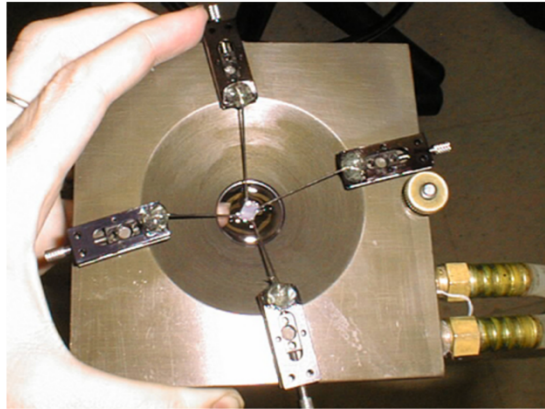


Figure 4.14: Modified incubation chamber for studying infected bladder.

Image taken from Justice et al 2004 (Justice et al., 2004).

In order to study spatio-temporal dynamics of IBCs in mouse bladders, we also explored different ways of isolating the mouse bladder. We first tried immobilizing the stretched mouse bladder with an animal retraction system (Fine Science Tools) (Figure 4.15A). The freshly isolated mouse bladder was either cut into half with a scalpel or with a vibrating microtome (Figure 4.16). The isolated bladder was then stretched using a combination of three blunt retractor tips connected to the fixators with locking jaws (Figure 4.15B). Magnets inside the fixators allowed stability on the steel base plate. The fixators were kept approximately 120° apart to equally balance the forces on the stretched bladder. The steel wire connecting the retractor tips to the fixators was used to slowly stretch the bladder with the help of locking jaws. The bladder was kept initially submerged in PBS and then in RPMI phenol-red free medium 1640/10% FBS. However, it was difficult to maintain the humidity around the stretched bladder with this setup. Also, too many separate components used to immobilize the bladder made it difficult to move and establish this setup on microscope stage.

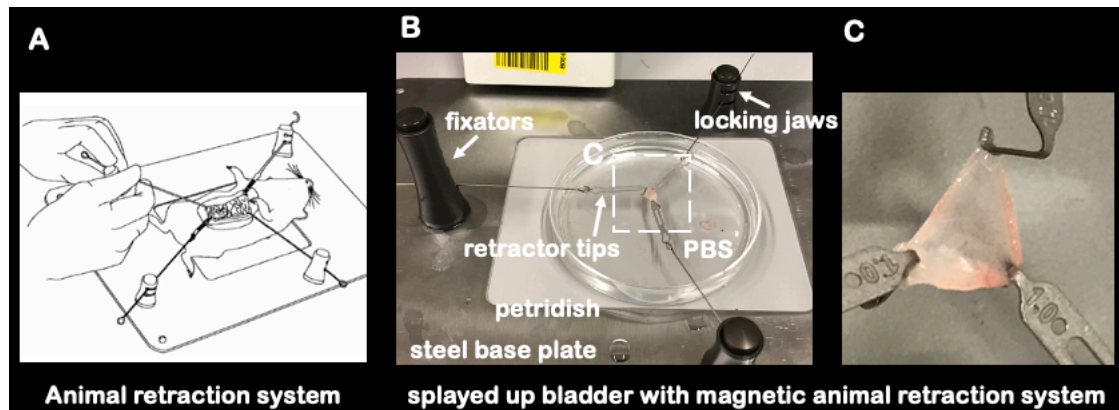


Figure 4.15: Animal retraction system with magnets used for immobilizing stretched bladder.

(A) shows the schematic of animal retraction system. (B) The mouse bladder was immobilized using a combination of retractor tips connected to the fixators with the locking jaws. The whole setup was kept stable with magnetic fixators fixed to the steel base plate. The bladder was kept submerged in PBS during the immobilization. (C) shows magnified image of the stretched mouse bladder. Schematic shown in A is taken from small animal retraction system documentation (Fine Science Tools).

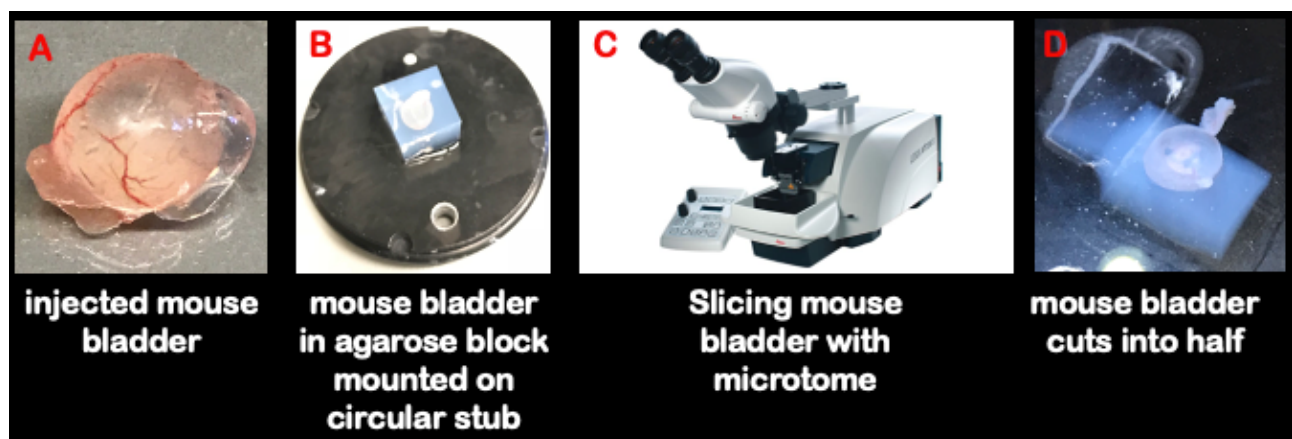


Figure 4.16: Isolation and mounting of mouse bladder in a block of low melting agarose.

(A) Isolated mouse bladder is swollen up by injection with 2% low melting agarose. (B) Swollen up mouse bladder is embedded inside low melting agarose block (white in color) and fixed on steel stub. (C) Vibrating microtome is used to cut the bladder. (D) Cut and open mouse bladder.

Then, we followed up with a different approach of mounting the bladder. Bladder is a soft and stretchable organ like lung. There have been reports on precisely cutting lung slices with microtome (Bennett et al., 2014; Carranza-Rosales et al., 2017). We took inspiration from these studies to try and cut the bladder with microtome. We used 2% Ultrapure low melting point agarose (Thermofisher) to swell up the bladder before slicing. Low melting agarose was melted at 65 °C and then placed inside a 37°C bath to cool down and kept in the liquid state. Then the mouse bladder was clamped and injected with 100-200 μ L of 2% low melting point agarose. Upon solidification of the low melting agarose in the bladder, the bladder was isolated from the mice (Figure 4.16A). The isolated bladder was then surrounded by block with a volume of 3-4 ml of 2% low melting point agarose in the TissueTek

Cryomold. The process of agarose gelification was sped up by placing the block inside the refrigerator at 4 °C for 15 minutes. The agarose block was removed from the cryomold by cutting the cryomold with a scalpel. The block was then glued to the stage of the vibrating microtome (Leica) with few drops of quick glue (Figure 4.16B). The block was then submerged in PBS and cut with the vibrating microtome. (Settings: sectioning speed-1 mm/s, oscillation amplitude-1 mm, oscillation frequency-100 Hz) (Figure 4.16C). The bladder was cut to keep approximately 50-60% of the bladder volume in the agarose block (Figure 4.16D). The cutting process of the bladder resulted in exposing the luminal layer of bladder as the injected solid agarose blob could be removed with a plastic tweezer. The bladder-agarose block was then again submerged in low melting agarose block inside 35 mm Fluorodish (Figure 4.17A). The bladder-block was then submerged in RPMI/10% FBS. The ex vivo bladder was stained with either 1 μ M of Cell Mask Deep Red or 1 μ M of Sir-Actin for one hour to stain plasma membrane or Actin filaments respectively. The remaining cell labelling dye was removed by washing with 2 ml of the medium three times.

The UPEC infection was performed at bacterial concentration of 150 million cells /ml in PBS by pipetting 50 μ L of UPEC inoculum in the center of the bladder for 1.5 hours. The surrounding RPMI/10% FBS medium was removed to just cover the hemispherical dome of the bladder. The extracellular bacteria were killed by treatment with high concentrations (100 μ g/ml) of gentamicin. The infected bladder was then kept submerged inside medium supplemented with lower concentration (15 μ g/ml) of gentamicin. Figure 4.17A shows the experimental setup of the isolated bladder inside FluoroDish placed on the Zeiss LSM 700 Upright Microscope. The imaging was performed with a dipping objective (20X, NA= 0.50). The FluoroDish was placed inside a 50 mm plastic petridish to avoid any spill over on the microscope (Figure 4.17A). The whole setup was then surrounded by 2-3 tissue wipes soaked in PBS and kept around the FluoroDish in plastic petridish to maintain the humidity and prevent the medium from drying up. Imaging was performed with a sequence of 488 nm and 639 nm laser lines and green and far-red filter cubes respectively. The green and far-red filter cubes were used to collect emitted light from UPEC expressing yellow fluorescent protein (YFP) and bladder stained with plasma membrane (Cell Tracker) or actin labelling (Sir-Actin) with fluorescence in far-red.

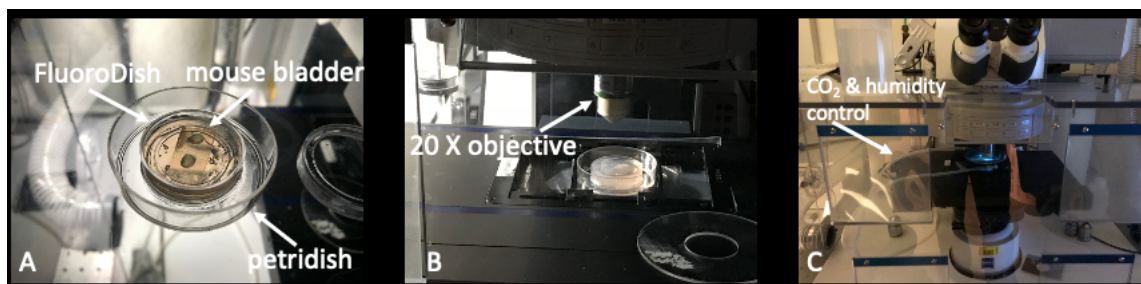


Figure 4.17: Imaging *ex vivo* infected mouse bladder with upright confocal microscope.

(A) The bladder was placed inside FluoroDish kept inside 50mm petridish. B shows the FluoroDish with 20X water dipping objective. C shows the complete imaging setup with CO₂ and humidity control.

The cell membrane labelling was more useful in looking at cellular features compared to actin-filament staining (Figure 4.18). The cell membrane staining also revealed the microvascular channels inside the bladder. We performed live imaging experiments in infected bladder with 10% and 1% laser intensities for the green and far-red laser lines. The hemispherical dome shape of the bladder required multi-z-stack imaging (~100-150 μm with 1 μm step-size). We managed to achieve single bacterium resolution inside the infected bladder uroepithelium (Figure 4.18). However, we did not identify significant UPEC growth in these bladder hemispherical domes nourished with RPMI 1640/10% FBS supplemented with lower concentration (15 $\mu\text{g}/\text{ml}$) of gentamicin. We performed 2 separate experiments of infected bladder with 12 hours of imaging. In both the experiments, the bladder tissue retracted and collapsed slightly which made imaging the same field of view harder to achieve. This technical problem in keeping the bladder tissue under stretched state can be solved either by micro translator setup used by Justice et al (Justice et al., 2004) (Figure 4.14) or by advancing the bladder retraction system tried in our lab (Figure 4.15). Also, the contribution of phototoxicity on bacterial multiplication in our imaging setup cannot be ruled out (Figure 4.17). The isolation of the bladder epithelium using the microtome and mounting of the bladder uroepithelium inside the low melting agarose might also have influenced the viability of bladder epithelium. However, in few instances, we did observe biofilm communities in infected bladder domes ca. 6-8 hours after UPEC infection. These infected bladder-tissues were housed inside the cell culture incubator with humidity and CO₂ control.

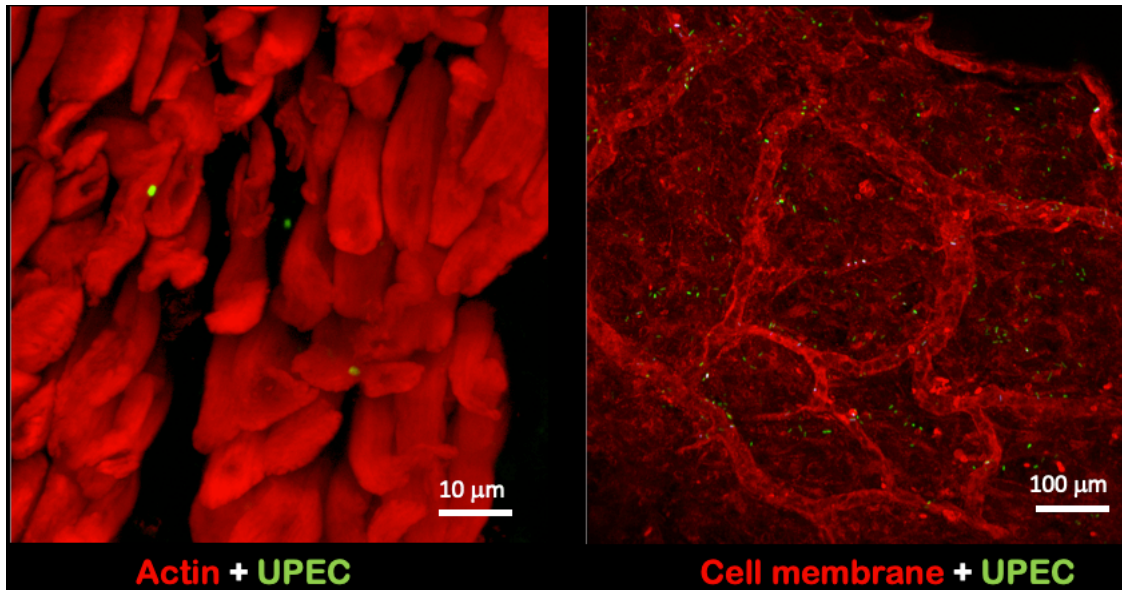


Figure 4.18: Infected bladder tissue stained for actin and cell membrane

UPEC (in green) could be seen inside the uroepithelial cells. Bladder microvascular network could be seen with cell membrane staining.

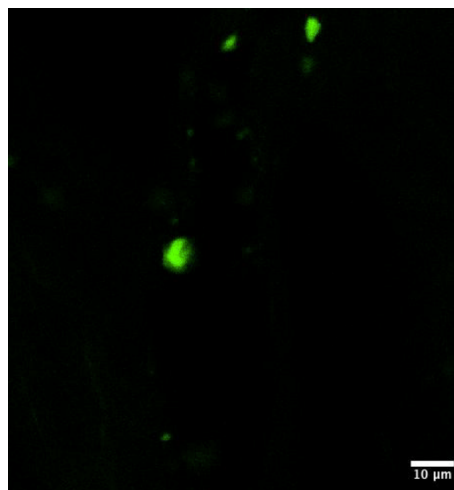


Figure 4.19: Biofilm like communities in infected bladder tissue housed inside cell culture incubator. Scale bar is 10μm.

4.8 Transwell insert as a model system for studying UPEC infection in epithelial monolayer

HTB9 bladder epithelial cells were cultured to confluent monolayers on 0.4 μm transwell inserts precoated with collagen 50 $\mu\text{g/ml}$ (Figure 4.20A). The epithelial cells were seeded 36 hours before the experiment. The epithelial cells were cultured in epithelial cell media RPMI1640/10 % FBS. Prior to the experiment, the transwell insert was cut from the middle by using a scalpel heated with a flame. The epithelial cell layer was stained for cell membrane with 1 μM solution of Cell Mask Deep Red for 30 minutes. The epithelial cell layer was then washed three times to remove the unbound cell membrane dye. The cut transwell insert was then immobilized on a thin layer of 1% solution of low melting agarose inside FluoroDish (Figure 4.20B). 500 μl of liquified low melting agarose at 37 $^{\circ}\text{C}$ was pipetted on the FluoroDish. The cut transwell insert was placed on the thin layer of low melting agarose. Upon solidification of the agarose, 1.5 ml of RPMI medium was added on the sides of the transwell insert immobilized inside the FluoroDish (Figure 4.20C). The transwell insert model provided considerable advantage over epithelial monolayers in ibidi petridishes or ibidi slides. Epithelial cells formed better tight junctions, moved less under infection conditions. Furthermore, different media i.e urine and cell media could be applied respectively on the apical and basal side of the insert.

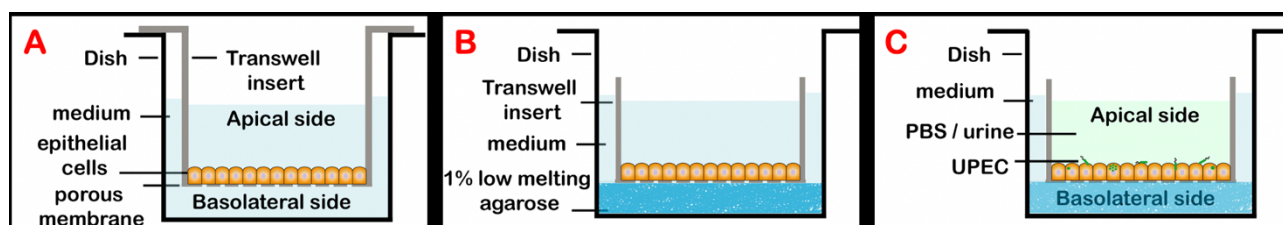


Figure 4.20: Transwell insert model for studying the dynamics of UPEC infection in epithelial monolayers. (A) Bladder epithelial cells were grown to form a confluent monolayer on apical side of the transwell insert. (B) Transwell insert was cut horizontally into half and mounted on a FluoroDish with 1% low melting agarose. (C) Upon agarose solidification, epithelial cell medium was added on the basal side. UPEC infection in urine diluted ten times with PBS was performed from the apical side.

UPEC infection was done by adding 100 μl of inoculum in urine (diluted ten times with PBS) at a concentration of 150 million bacteria/ml on epithelial cells (MOI ~ 15). The UPEC attachment to epithelial cells was done for ca. 1.5-2 hours and typical infectious dose at the end of this period was low (<1 bacterium per epithelial cell, Figure 4.21A). The unattached bacteria were removed by washing three times with 500 μl of PBS. The PBS washing was done gently, and the washing media was removed from the side of the inserts. The apical side of the insert was then kept either in 100 μl of PBS or urine. The attached UPEC started growing inside and between epithelial cells as shown in (Figure 4.21A-B). Eventually UPEC dispersal from infected epithelial cells was observed ca. 3-6

hours (Figure 4.21C) after infection. Subsequently we also added ampicillin 20XMIC (125 $\mu\text{g/ml}$, calculated in epithelial cell media) for 3 hours to kill susceptible bacteria and study persistence of intracellular bacteria. The ampicillin was added on both sides of the insert in the respective media. Antibiotic was removed by washing three times each with 500 μl of diluted urine and epithelial cell media on the apical and basal sides of the insert. 500 μl of fresh urine and epithelial cell media was added to the respective sides of the insert. However, in these experiments, post-ampicillin washout, we never observed regrowth of any surviving UPEC over a period of 12 hours post-washout (data not shown). From axenic culture experiments carried out in McKinney lab and other previously reported experiments (Putrinš et al., 2015; Wang et al., 2014), we do anticipate survival and regrowth when starting from such high numbers of bacteria. Therefore, we inferred that this non-recovery of UPEC was probably due to technical limitations in completely washing out the ampicillin in transwell insert system. These results eventually motivated us further to perform these infection experiments in bladder-chip devices where medium perfusion and washout can be performed continuously and efficiently.

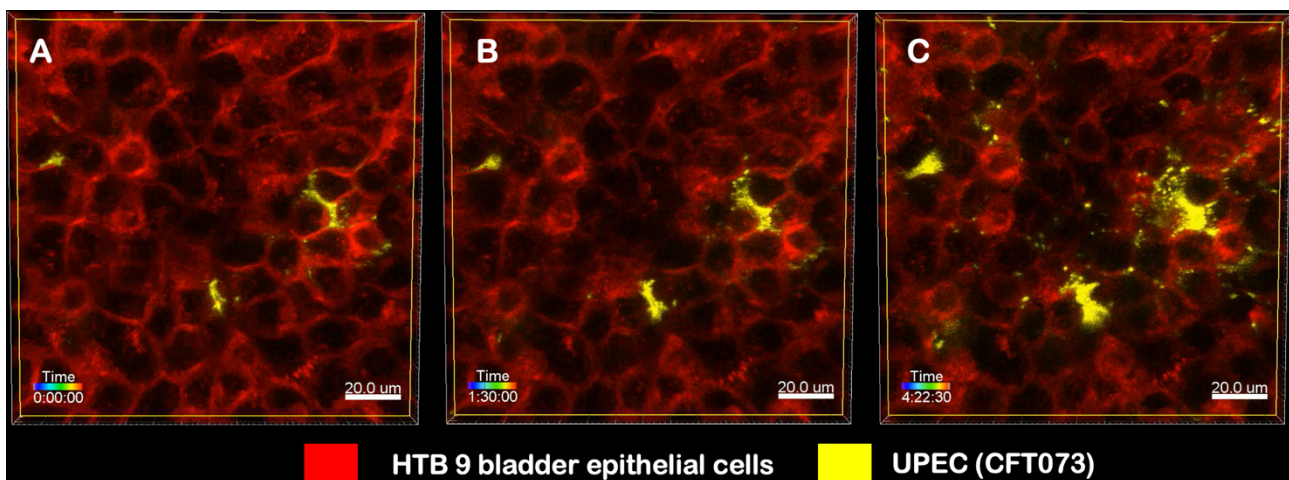


Figure 4.21: Time lapse imaging of infected epithelial cells on the transwell inserts. UPEC (yellow) infection of bladder epithelial cells (red) on transwell inserts resulted in UPEC attachment and growth close to epithelial cell tight junctions. (A) Small foci of UPEC infection in epithelial layer (time = 0 hr). (B) UPEC growth between epithelial cells (time = 1.30 hr). (C) UPEC dispersal from infected epithelial cells. Bladder epithelial cells were stained for plasma membrane with cell mask deep red dye. For all panels, scale bar is 20 μm .

4.9 Conclusions

- Stratification of bladder epithelial cells can be achieved with growing the cells on porous substrates under air-liquid interface.
- Bladder epithelial cells can undergo uniform stratification under co-culture with bladder endothelial cells with urine and endothelium cell medium interface. Application of urine and medium supplemented with 2mM Ca^{2+} enhanced the stratification process.
- *Ex vivo* infection experiments with isolated mouse bladders can be technically challenging.
- Bladder-chip devices can be fabricated using sandwiched plastic and PDMS membranes
- Air-liquid interface followed by urine-liquid interface resulted in islands of stratified uroepithelium in bladder-chip devices.
- Preliminary experiments with stratified uroepithelium in bladder-chips revealed that different layers can be infected with UPEC.
- Monolayer of uroepithelial cells grown on transwell inserts with urine-medium interface can be used as a model system for studying UPEC pathogenesis.

4.10 Materials and Methods

4.10.1 Protocol for stratification of bladder epithelial cells on the transwell inserts

Epithelial and endothelial cell culture:

HTB9 bladder epithelial cells (5637 (ATCC[®] HTB-9[™], ATCC 30-2001) were grown in T75 flasks in RPMI medium containing 10% FBS, supplemented with 1X antibacterial and 1X antifungal solution. The HTB9 bladder epithelial cells were passaged and diluted to a fifth or a tenth depending upon the experimental need. The Human bladder microvascular endothelial cells (HMVEC-Bd, Lonza Catalog #: CC-7016) were cultured in Lonza EGM-2 MV BulletKit (CC-4147+CC-3156) medium. HBLAK bladder epithelial cells (CELLnTEC) were proliferated in Cnt57 Basal medium (CELLnTEC).

The epithelial and endothelial cells were cultured in T75 plates with the reagents recommended by the supplier. For one set of 12 well transwell inserts, we used two T75 flasks of each epithelial and endothelial cells. Epithelial and endothelial cells were grown, passaged as recommended by the supplier. Lonza did not suggest freezing the endothelial cells. However, we found that endothelial cells can be recovered quite easily from cryostocks. Both epithelial and endothelial cells were frozen in 60% FBS, 30% medium (RPMI and Lonza EBM-2 for epithelial and endothelial cells respectively).

We have cultured HTB9 and HBLAK bladder epithelial cells (Horsley et. al 2018) in 1X Antimicrobial/Antifungal for 3-5 weeks. It is highly recommended to add the antimicrobial/antifungal for avoiding bacterial/fungal contamination. We have used a pre-warmed medium and PBS for this protocol.

Day 1: Collagen coating on transwell inserts

1. Take out the lid of the 12 well plate with transwell inserts and perform air plasma treatment (Diener electronics Plasma Surface Technology) with Power=6 W, Time=60 seconds.
2. Post plasma treatment, the plastic surface of the transwell insert should be hydrophilic and flip the insert in a glass petridish (Corning) upside down and put 100-200 µl of native collagen (AteloCell) at a concentration of 50 µg/ml in the medium (endothelial cell medium/RPMI) containing 10mM HEPES. The total volume of coating solution corresponds to 200 µl X 2 (apical and basal side) X Number of inserts. The coating solution also contains 1X antimicrobial/antifungal. The coating solution is kept on ice to slow down the polymerization of collagen in the falcon tube.

3. Cover the surrounding area of the insert in the glass petridish with PBS (containing 1X Anti-microbial/Antifungal). Collagen coating and polymerization on the inserts is done inside the incubator at 37°C for 3 hours. The same procedure for collagen coating is followed for the apical side of the insert. If one is using just the apical side of the insert, the coating solution can be applied only to the apical side of the insert. If cell seeding on the transwell inserts will be performed the next day, then store the collagen coated inserts in the required volume of PBS i.e 500 µl on the apical side and 1.5 ml on basal side.

Day 2: Endothelial cell seeding on bottom side of the transwell insert

4. Proceed to seeding of endothelial cells at a concentration of .1 million cells/ml. The endothelial cells are seeded in endothelial cell medium (supplemented to 25% FBS). Higher concentration of FBS assists in attachment of endothelial cells. Pipette 100 µl of endothelial cell suspension on inverted transwell inserts. The transwell inserts are placed inside the glass petridish surrounded with PBS (1X antimicrobial/antifungal) for humidification. The glass lid of the petridish should not be closed completely to block the 5% CO₂ gas exchange. The glass lid was kept on the petridish with 1-2 mm opening for air exchange by adding a block of certain height. Place carefully the glass petridish with inserts inside the incubator for 2 hours. Avoid shaking the glass petridish too much since it could spill over the endothelial cells on side of the insert). After 2 hours, add 100 µl of endothelial cell medium on inserts (supplemented to 25% FBS). 4 hours after the first round of endothelial cell seeding, check the attachment of endothelial cells by flipping the inserts and putting them inside the 12 well plate. If there is >80% confluency, you can add the endothelial cell medium (500 µL-apical side and 1.5 ml-basal side). If the confluency is still not 80%, try seeding the endothelial cells again for 2 hours.

Notes:

- a. If the inserts are taken out from the refrigerator, warm them inside the incubator at 37 °C for 2 hours. Cells will not stick well on cold plastic surfaces.
- b. Endothelial cells can cluster in a small suspension volume (especially with medium containing 25% FBS), try your best to remove cells from the cluster by using P200 or P20 pipette.

- c. Remaining endothelial cell suspension (after first round of cell seeding) can be kept at room temperature. Endothelial cells will need to be pipetted again from the sedimented cell pellet in the falcon tube.

Day 3: Epithelial cell seeding on apical side of the transwell insert

- 5. Change the endothelial cell medium on both sides of the insert and add 1.5 ml of fresh endothelial cell medium in the bottom of the insert. Seed HTB9 bladder epithelial cells at a density of 1 million cells/ ml in a volume of 500 μ l on the apical side of the insert. The epithelial cells can be left overnight for attachment on the transwell insert.

Notes:

- d. Check the insert for homogenous distribution of epithelial cells. If the cells have higher concentration either in the center and edge of the insert, try to pipette in and out the cell suspension (using P200) to have more uniform distribution of epithelial cells. This problem happens due to the curved geometry of the insert.
- e. Unattached endothelial cells will attach at the bottom of the well plate and start growing in 2D. It is better to change the 12-well plate during the first week of endothelial cell culture on the bottom side of the transwell insert.
- f. While washing the inserts with 500 μ l and 1.0 ml of PBS on the apical and bottom side of the insert, the inserts are transferred to another 12 well plate with aliquoted 1.0 ml PBS in the each well. This process is done to avoid drying of the inserts. Inserts were always washed twice with PBS (prewarmed at 37°C) to remove the waste material and dead cell debris.

Day 4: Removal of unattached epithelial cells post cell seeding

- 6. Wash the apical side of the insert with PBS (1X antimicrobial, antifungal) to remove unattached epithelial cells. The washing step is repeated three times to remove unattached epithelial cells. Allow epithelial cells to achieve 100% confluency within next 1-2 days for all the inserts

Notes:

- g. While washing the apical side of the insert, the insert can be removed from the well plate with a plastic tweezer and kept in the air (slightly tilted to get better perspective on remaining medium inside the insert). Always pipette PBS or medium towards the edge of the insert. Do not go very close to the center of the insert, you can accidentally touch and damage the layer of epithelial cells or worst case, puncture the insert.

Day 5: Attainment of 100% epithelial cell confluency

7. Once the epithelial cells have achieved confluency across all the inserts, remove the epithelial cell medium (RPMI/10% FBS) from the apical side of the insert. Wash twice with 500 µl of pre-warmed PBS and remove the remaining PBS on top of the inserts. The epithelial cells will be cultured on air-liquid interface for the next 5-7 days. At this stage, we add 2 ml of endothelial cell medium in the basal side and place the inserts inside 12 well spacers (CELLnTEC). The CELLnTEC spacers allow larger volumes of media for the cell culture.

Notes:

- h. Change the endothelial cell medium after 4-5 days if the endothelial cell medium appears a bit yellowish. The epithelial cells can be washed to remove dead cells and maintained again on air-liquid interface. Keep on checking the status of stratification of epithelial cells every 3-4 days. The stratified areas should start appearing as small patchy islands. When observed under the optical microscope, light is refracted more from these patchy islands.

Week 3: Generation of islands of stratified epithelium

8. After 7-10 days, epithelial cells reach patchy stratification. Wash both the sides of the insert to remove cell debris. Add 2ml of pre-warmed endothelial cell medium containing (1mM Ca^{2+} , 0.4 µm filter sterilized) into the basal side of the insert and 500 µl of urine on the apical side of the insert (0.4 µm filter sterilized). Both urine and endothelial cell medium were prepared with 1X antimicrobial, antifungal.

Notes:

- i. Change the endothelial cell medium after 4-5 days if the endothelial cell medium appears a bit yellowish. The epithelial cells can be washed to remove dead cells and kept again on

air-liquid interface. Keep on checking the status of stratification of epithelial cells every 3-4 days. The stratified areas should start appearing as small patchy islands. Light is refracted more from these patchy islands

j. We got the initial and best results with experimenter's own pure urine (0.4 μm filter sterilized). Subsequent experiments were performed with pooled urine (Golden West Diagnostics). We diluted the pooled urine: PBS as 1:10 for better stratification results. HTB9 and HBLAK cells did not cope better with pure pooled urine (Golden West Diagnostics).

9. Wash twice with PBS on both apical and basal side of the insert every 4-5 days. Replenish with fresh medium and urine on basal and apical side of the insert respectively.

Notes:

k. Keep on checking for the improvement in stratification of epithelial cells every 3-4 days.

l. Endothelial cell containing 1 mM Ca^{2+} has the tendency to coagulate and form some debris in the medium. Do not get worried by these clusters. However, make sure to check that there is no fungal contamination.

m. Shift the inserts to 12-well plate every alternate wash (in 4-5 days).

Week 5: Generation of larger islands of stratified epithelium

10. The epithelial cells should have reached desired stratification. One day before the infection experiment, both apical and basal sides of the insert are washed thrice with PBS to remove residual antimicrobial/antifungal in the culture. Fresh endothelial cell medium (without antimicrobial / antifungal) and urine (without antimicrobial / antifungal) is supplied to the basal and apical side respectively.

4.10.2 Protocol for seeding of dissociated bladder organoids on transwell inserts

Generation of mouse bladder organoids from mouse bladder uroepithelial cells

The mouse bladder organoids were prepared by selectively isolating luminal cells from the bladder by filling the clamped mouse bladder *ex vivo* with TryPLE as described in a recent study (Mullenders et al., 2019). The procedure for generating the organoids was followed for both ROSA^{MT/MG} (purchased from Jackson Laboratories) and C57Bl/6 mice (purchased from Charles River Laboratories). The luminal uroepithelial cells were isolated from 3 female mice (at an age of four months to isolate most uroepithelial cells) by microinjecting approximately 500 µl TryPLE with a 26G needle and placing the clamped mouse urinary bladder inside a 50ml Falcon tube surrounded by prewarmed 20ml basal medium (Advanced DMEM/F-12 medium). The Falcon tube containing mouse urinary bladder is incubated for 1 hour inside a cell culture incubator at 37°C and 5% CO₂. The mouse urinary bladder is then washed twice with basal medium containing 20% FBS to neutralize the effect of TryPLE. The cell suspension was passed through a 40 µm filter and flow through cells were centrifuged and pelleted at 0.3 rcf for 5 minutes. The isolated uroepithelial cells were resuspended in an appropriate volume of Cultrex® Basement Membrane Extract (BME) and seeded inside as hemispherical domes (with 40-50 µL volume) in 24-well plate. The 24-well plate is inverted to promote 3D growth and BME is allowed to polymerize at 37°C for 30 minutes. The solidified hemispherical domes are supplemented with mouse bladder medium supplemented with 1X antibacterial/antifungal. MBM medium consists of [Advanced DMEM/F-12 (Thermofisher:10565018), 100 ng/ml of FGF10 (Pepro- tech:100-26), 25 ng/ml of FGF7 (Pepro- tech:100-19), 500 nM of A83-01 (Tocris Bioscience: 2939), 2% of B27 (Thermofisher: 17504044) and ROCK inhibitor (Y-27632, 10 µM)]. The uroepithelial cells form tdTomato MBOs (from ROSA^{MT/MG}) or C57Bl/6 MBOs from respective mice strain over next 2-3 weeks. The MBOs were passaged in 5 days or sheared with a fire polished glass pipette. The MBOs were either used for an immediate or cryopreserved in the freezing media (60% FBS, 30% Advanced DMEM/F-12 and 10% DMSO) for later experiments.

Notes:

We have observed and tested that if we harvest uroepithelial cells grown in 2D from the initial isolation from mouse bladder. These harvested uroepithelial cells have the potential to form more and better size-controlled organoids compared to standard passaging the organoids by shearing (using fire-polished glass pipette) the organoids to reduce their size. We harvested 2D cells grown in 1st and 2nd passage (cells cultured in four 24-well plates in each passage) to make enough organoids for all

of our experiments. We were able to harvest ~1 million cells (depends upon how many organoids settle down to start growing in 2D culture) in the first passage. These organoids were cryopreserved (60% FBS, 30% DMEM, 10% DMSO) for experiments at later stage. This approach of cryopreservation also saved us the time and resources for keeping the organoids in culture and continuously shearing them to reduce their size. Long term culture and sequential passaging of the bladder organoids can lead to non-spherical organoids with bud like features. Also Dr. Jasper Mullenders (Mullenders et al., 2019) cautioned us that umbrella cells could be lost after multiple passages. Thus, we used organoids with less than 5 passages for our experiments.

Day 1: Collagen coating on transwell inserts

1. Take out the lid of the 12 well plate with transwell inserts and perform air plasma treatment (Diener electronics Plasma Surface Technology) with Power=6 W, Time= 60 seconds.
2. Post plasma treatment, the plastic surface should be hydrophilic and pipette 100-200 µl of native collagen type1 at a concentration of 100 µg/ml in the medium (DMEM medium) containing 10 mM HEPES.

Notes:

- a. One could try with higher concentration of collagen but collagen sheets (>200-500 µg/ml) create lot of problems and get detached while washing away the unbound collagen.
- b. Other approach could be trying 50% mixture of Collagen (100 µg/ml) and BME.

Day 2: Seeding of sheared bladder organoids

3. Already prepared MTMG organoids were grown in the BME medium 4-5 days before the experiment.

Notes:

- c. Volume of BME depends upon the volume of your organoid pellet.

4. Mouse bladder medium was removed from the wells and BME dome was mechanically broken down with P1000 pipette.
5. Ice-cold DMEM wash medium (without the growth factors) was added to the wells and organoids were collected in a 1% BSA pre-coated falcon tubes.
6. Centrifuge the organoids at .1 rcf for 5 minutes. Remove the supernatant and Resuspend organoids in fresh BME.
7. Stratified organoids were mechanically sheared with fire-polished 2 ml glass pipette. Narrower opening of the pipette will allow better shearing of the organoids.
8. Sheared organoids were resuspended in MBM medium (containing 1X antimicrobial, anti-fungal) and pipetted in 500 μ L volume on the apical side of the 0.4 μ m transwell insert. The basal side of the insert was covered with 1.5 ml MBM medium.

Notes:

- d. Approximately 25-50 of 100-200 μ m sized sheared organoids can be pipetted inside one of the 12 well-insert.
- e. This procedure has been done few times and the number of pipetted organoids depends upon the size of the organoid.
- f. The resuspended sheared organoids will have the tendency to cluster together towards the center and edge of the insert. Make sure to pipette multiple times to ensure the homogeneous distribution of the organoids.
- g. Ideally the same procedure could be applied for human bladder organoids and one could culture settled down human bladder organoids in human urine on the apical side and bladder medium on the basal side.
- h. Sheared organoids take 3-5 days to settle down and unfolded epithelial layers attach to the insert over a period of one week.

9. Exchange the medium on the transwell inserts 3 days after the seeding of the dissociated organoids.

Notes:

- i. The transwell inserts were handled gently to not disturb the settling organoids.
10. Wash the inserts thrice with PBS (without antimicrobial, antifungal) and supplement with fresh MBM medium (without antimicrobial, antifungal). Change the MBM medium on the apical and basal sides of the insert every 3-4 days.
11. The bladder organoids unfolded to form islands of stratified epithelium over 2-3 weeks.

4.11 References

- Apodaca, G. (2004). The Uroepithelium: Not Just a Passive Barrier. *Traffic* 5, 117–128.
- Bennett, R.D., Ysasi, A.B., Belle, J.M., Wagner, W.L., Konerding, M.A., Blainey, P.C., Pyne, S., and Mentzer, S.J. (2014). Laser Microdissection of the Alveolar Duct Enables Single-Cell Genomic Analysis. *Frontiers Oncol* 4, 260.
- Bonakdar, S., Mahmoudi, M., Montazeri, L., Taghipoor, M., Bertsch, A., Shokrgozar, M.A., Sharifi, S., Majidi, M., Mashinchian, O., Sekachaei, M.H., et al. (2016). Cell-Imprinted Substrates Modulate Differentiation, Redifferentiation, and Transdifferentiation. *Acs Appl Mater Inter* 8, 13777–13784.
- Bouhout, S., Chabaud, S., and Bolduc, S. (2019). Collagen hollow structure for bladder tissue engineering. *Mater Sci Eng C* 102, 228–237.
- Carranza-Rosales, P., Carranza-Torres, I.E., Guzmán-Delgado, N.E., Lozano-Garza, G., Villarreal-Treviño, L., Molina-Torres, C., Vargas-Villarreal, J., Vera-Cabrera, L., and Castro-Garza, J. (2017). Modeling tuberculosis pathogenesis through ex vivo lung tissue infection. *Tuberculosis* 107, 126–132.
- Cattan, V., Bernard, G., Rousseau, A., Bouhout, S., Chabaud, S., Auger, F.A., and Bolduc, S. (2011). Mechanical Stimuli-induced Urothelial Differentiation in a Human Tissue-engineered Tubular Genitourinary Graft. *Eur Urol* 60, 1291–1298.
- Chabaud, S., Saba, I., Baratange, C., Boiroux, B., Leclerc, M., Rousseau, A., Bouhout, S., and Bolduc, S. (2017). Urothelial cell expansion and differentiation are improved by exposure to hypoxia. *J Tissue Eng Regen M* 11, 3090–3099.
- Horsley, H., Dharmasena, D., Malone-Lee, J., and Rohn, J.L. (2018). A urine-dependent human urothelial organoid offers a potential alternative to rodent models of infection. *Sci Rep-Uk* 8, 1238.
- Hustler, A., Eardley, I., Hinley, J., Pearson, J., Wezel, F., Radvanyi, F., Baker, S.C., and Southgate, J. (2018). Differential transcription factor expression by human epithelial cells of buccal and urothelial derivation. *Exp Cell Res* 369, 284–294.
- Jost, S.P., Gosling, J.A., and Dixon, J.S. (1989). The morphology of normal human bladder urothelium. *J Anat* 167, 103–115.
- Justice, S.S., Hung, C., Theriot, J.A., Fletcher, D.A., Anderson, G.G., Footer, M.J., and Hultgren, S.J. (2004). Differentiation and developmental pathways of uropathogenic *Escherichia coli* in urinary tract pathogenesis. *Proc National Acad Sci* 101, 1333–1338.
- Kim, H.J., and Ingber, D.E. (2013). Gut-on-a-Chip microenvironment induces human intestinal cells to undergo villus differentiation. *Integr Biol* 5, 1130–1140.

- Larsson, H.M., Gorostidi, F., Hubbell, J.A., Barrandon, Y., and Frey, P. (2014). Clonal, Self-Renewing and Differentiating Human and Porcine Urothelial Cells, a Novel Stem Cell Population. *Plos One* 9, e90006.
- Martinez, J.J., Mulvey, M.A., Schilling, J.D., Pinkner, J.S., and Hultgren, S.J. (2000). Type 1 pilus-mediated bacterial invasion of bladder epithelial cells. *Embo J* 19, 2803–2812.
- Mullenders, J., Jongh, E. de, Brousal, A., Roosen, M., Blom, J.P.A., Begthel, H., Korving, J., Jonges, T., Kranenburg, O., Meijer, R., et al. (2019). Mouse and human urothelial cancer organoids: A tool for bladder cancer research. *Proc National Acad Sci* 116, 201803595.
- Mulvey, M.A., Lopez-Boado, Y.S., Wilson, C.L., Roth, R., Parks, W.C., Heuser, J., and Hultgren, S.J. (1998). Induction and Evasion of Host Defenses by Type 1-Piliated Uropathogenic *Escherichia coli*. *Science* 282, 1494–1497.
- Putrinš, M., Kogermann, K., Lukk, E., Lippus, M., Varik, V., and Tenson, T. (2015). Phenotypic Heterogeneity Enables Uropathogenic *Escherichia coli* To Evade Killing by Antibiotics and Serum Complement. *Infect Immun* 83, 1056–1067.
- Rheinwald, J.G., and Green, H. (1975). Serial cultivation of strains of human epidermal keratinocytes: the formation of keratinizing colonies from single cells. *Cell* 6, 331–343.
- Smith, Y.C., Grande, K.K., Rasmussen, S.B., and O'Brien, A.D. (2006). Novel Three-Dimensional Organoid Model for Evaluation of the Interaction of Uropathogenic *Escherichia coli* with Terminally Differentiated Human Urothelial Cells. *Infect Immun* 74, 750–757.
- Southgate, J., Hutton, K.A., Thomas, D.F., and Trejdosiewicz, L.K. (1994). Normal human urothelial cells in vitro: proliferation and induction of stratification. *Laboratory Investigation J Technical Methods Pathology* 71, 583–594.
- Suzuki, K., Koyanagi-Aoi, M., Uehara, K., Hinata, N., Fujisawa, M., and Aoi, T. (2019). Directed differentiation of human induced pluripotent stem cells into mature stratified bladder urothelium. *Sci Rep-Uk* 9, 10506.
- Tang, L., and Lee, N.Y. (2010). A facile route for irreversible bonding of plastic-PDMS hybrid microdevices at room temperature. *Lab Chip* 10, 1274–1280.
- Vardar, E., Engelhardt, E.-M., Larsson, H.M., Mouloungui, E., Pinnagoda, K., Hubbell, J.A., and Frey, P. (2015). Tubular Compressed Collagen Scaffolds for Ureteral Tissue Engineering in a Flow Bioreactor System. *Tissue Eng Pt A* 21, 2334–2345.
- Varley, C.L., Stahlschmidt, J., Smith, B., Stower, M., and Southgate, J. (2004). Activation of Peroxisome Proliferator-Activated Receptor- γ Reverses Squamous Metaplasia and Induces Transitional Differentiation in Normal Human Urothelial Cells. *Am J Pathology* 164, 1789–1798.
- Višnjić, T., and Kreft, M.E. (2013). Air–liquid and liquid–liquid interfaces influence the formation of the urothelial permeability barrier in vitro. *Vitro Cell Dev Biology - Animal* 49, 196–204.

Wang, Y., Zhao, S., Han, L., Guo, X., Chen, M., Ni, Y., Zhang, Y., Cui, Z., and He, P. (2014). Drug resistance and virulence of uropathogenic *Escherichia coli* from Shanghai, China. *J Antibiotics* 67, 799–805.

Chapter 5. Conclusions and outlook

Urinary tract infections (UTIs) are the second-most common cause of antibiotic prescriptions, and in about one-quarter of all treated cases leads to recurrent infection. Therefore, UTIs have an enormous impact on human health and healthcare costs. Much of our current understanding about UTIs have come from mouse models of UTI, which have highlighted the intracellular lifestyle of this pathogen in the forms of IBCs and QIRs. IBCs and QIRs have been implicated in bacterial persistence and serve to protect bacteria from host immune cells and antibiotic mediated antimicrobial stresses. One of the reasons behind pathogen survival and relapse of infection is attributed to the heterogeneity at both the host as well as the pathogen level. Although the mouse model has provided numerous insights, animal models are inherently not amenable to approaches that allows these heterogeneous interactions to be captured in real-time. Several attempts have been made to develop *in vitro* model systems of UTIs in order to dissect this heterogeneity in host-pathogen interactions. These *in vitro* systems recapitulated either as monolayers or multiple layers of uroepithelium have modelled acute phases of infection including the IBC formation and dispersal. However, these models lack vasculature, the possibility to mimic the processes of bladder filling and voiding experienced by this mechanically active organ as well as the ability to deliver immune cells in a physiologically relevant manner. In the last two decades, two bioengineering approaches have emerged to generate functional and physiological tissues: organoid and organ-chip systems. These developments motivated us to develop bladder organoid and bladder-chip system for studying early stages of UPEC pathogenesis.

Thus, in this doctoral thesis, we have achieved following aims:

- (1) Development and characterization of a bladder organoid model for UPEC pathogenesis, which demonstrated the ability to recapitulate IBC formation and revealed new insights into the role of solitary bacteria in the stratified organoid wall during early infection. The bladder organoid model allowed study of bacterial persistence in response to antibiotics and neutrophil swarms.

- (2) Development and characterization of a bladder-chip model system which recapitulated co-culture of epithelial and endothelial cells under flow-driven urine and nutritional medium interface. Moreover, the system mimicked bladder filling and voiding by application of linear strain. Upon bacterial infection of the bladder epithelium, blood-bladder chemotaxis was achieved with neutrophils, which formed neutrophil swarms and NETs in response to infection. Bladder-chip system has emerged as a novel model system to study IBC persistence in response to antibiotic treatment.
- (3) Further steps towards the recapitulation of the stratified bladder architecture for organ-on-chip type platforms. Islands of stratified uroepithelium can be achieved with co-culture of bladder epithelial and bladder endothelial cells on porous substrates under urine-liquid interface.

We chose to develop bladder organoids from the mouse to take advantage of knock-in reporter lines made in the well-characterized C57BL/6 background, which provided a reliable source of primary uroepithelial cells from a clonal source. The bladder-chip system was developed from human uroepithelial cells to probe the dynamics of IBCs in human cells. Much of the information about the development of IBCs and their persistence *in vivo* is known from mouse models. We wanted to study the development of IBCs *in situ* in human uroepithelial cells. So, we developed a human bladder-chip system to study IBC dynamics and IBC persistence in response to antibiotics. We do understand that the bladder cell line derived from bladder carcinoma might be more susceptible to infection due to structural abnormalities in the cell line, as known in the literature. However, we are in the process of developing a human bladder-chip system using primary uroepithelial cells from healthy individuals available in an anonymized fashion from a reliable commercial supplier. Also, we understand that the sex of the donor, male or female, for pooled urine, blood donors and bladder endothelial cells might elicit different responses to infection. Thus, future studies could be performed with more controlled availability of the resources from one sex.

CFT073, an isolate from a pyelonephritis patient was chosen due to the prior expertise available in the McKinney lab. However, both the mouse bladder organoid and the human bladder-chip system can be easily adapted to study any other clinically relevant UPEC strain. Similar reasoning motivated us to use ampicillin to study bacterial persistence to make comparisons between complex microtissue models with that from monoculture experiments already available in the McKinney lab. Also, ampicillin is known to cause bacterial lysis and loss of bacterial fluorescence. Bacterial lysis was important for us to quantify bacterial killing.

Antibiotic treatment and incubation timings were chosen to mimic the early stages of infection, bacterial killing and some regrowth after drug washout. Earlier experiments with overnight antibiotic incubation did not result in any bacterial regrowth for 4-6 hours. Thus, we chose ampicillin treatment for 3 hours in both the bladder organoid and bladder-chip system. However, now we plan to study bacterial persistence with clinically used drugs such as Fosfomycin, Nitrofurantoin.

Bladder organoids served as a 3D *in vitro* model of the organ but also recapitulated the stratified nature of the uroepithelium. The umbrella cell layer of the different uroepithelium was confirmed by immunofluorescence staining for markers such as UP3a and CK8. The intermediate and basal cell layers were confirmed by staining with antibodies directed against CK13, p63 and CK7. Therefore, bladder organoids recapitulated the stratified architecture of the mouse uroepithelium.

The UPEC infection of these bladder organoids reconstituted bacterial growth both in the lumen and bladder wall as would happen *in situ* in the bladder. Ampicillin treatment allowed us to study bacterial persistence. Compared to the pre-antibiotic phase, bacterial growth in the post-antibiotic phase was observed majorly from solitary bacteria in the organoid wall. Compared to the end of antibiotic treatment, the total bacterial volume was reduced to approximately 10% of the bacterial volume estimated prior to the antibiotic administration. Comparing this kill kinetics with ampicillin mediated killing of UPEC in axenic cultures, suggested that UPEC growing in the organoids were killed at much reduced rates. This reduced bacterial killing could be due to the discrepancy in estimating bacterial killing which was evaluated as proxy of total bacterial volume instead of total bacterial numbers. Also, in a few organoids, bacterial growth continued for the entire duration of antibiotic treatment suggesting a dynamic balance between bacterial division and bacterial killing inside the bladder organoid. Overall, high temporal imaging of multiple organoids allowed us to capture the dynamic heterogeneity of host-pathogen interactions: i.e, differences in bacterial growth, killing and regrowth inside the different bladder organoids.

The host immune response was mimicked by introduction of neutrophils, which revealed directional and coordinated migration of neutrophils towards the lumen of infected organoids. In comparison, neutrophil did not migrate significantly to the bystander uninfected organoids. The migrated neutrophils in the infected organoid aggregated to form neutrophil swarms. Neutrophil swarms displayed remarkably distinct behaviours in clearing infection. Based upon the neutrophil swarm aggregation and dispersal inside the infected organoids, neutrophils swarms were classified as persistent, transient

or dynamic swarms. Neutrophil killing of the bacterial subpopulations was selective. The luminal bacteria were substantially cleared, whereas solitary bacteria survived in intracellular epithelial niche. Bacteria inside IBCs proliferated unrestrainedly despite presence of surrounding persistent neutrophil swarms. Bacteria inside the IBCs were only cleared post IBC shedding, once they became extracellular. Here as well, we observed the heterogeneity in bacterial sterilization within the organoids by the neutrophil swarms. Some organoids were significantly sterilized by the neutrophil swarms, whereas other infected organoids were not. In majority of the cases, we observed solitary bacterial subpopulations in the organoid wall that were protected from neutrophil swarms.

In order to study and localize these solitary bacterial subpopulations in the bladder wall, we resorted to SBEM of infected organoids. Multiple serial stacks (~1000) revealed five distinct microenvironmental niches for the bacteria: luminal, within neutrophils, IBCs, intracellular bacteria and pericellular bacteria. Further investigation of the solitary bacteria within the organoid wall revealed that these bacterial subpopulations retained flagellin expression, which was substantially reduced in IBCs. Overall, the bladder organoid model recapitulated different aspects of the host-pathogen interactions in the early stage of UPEC pathogenesis, as has been previously characterized from patient samples or animal models.

In contrast to the bladder organoid model which lacks the possibility for medium-exchanges and to maintain urine-medium interface as found *in vivo*, the bladder-chip model addresses these limitations with co-culture of bladder epithelial and bladder endothelial cells under their respective media. The bladder-chip model was developed with an established terminally differentiated cell line known to facilitate formation of IBCs. Application of negative pressure controlled via pressure regulator mimicked different stages of bladder filling and voiding cycle. Carrying out UPEC infection under flow, allowed control over infection of epithelial cells, with mean foci of infection less than 1. Using bladder filling and voiding duty cycle, we found that the total bacterial burden inside infected bladder-chips was significantly higher when compared to bladder-chips not stimulated with bladder filling and voiding cycle.

The blood-bladder chemotaxis was mimicked with neutrophil introduction into the endothelial side of the bladder-chip. Compared to the uninfected bladder-chip, neutrophils were observed within ca. 15 minutes on the epithelial side. In infected bladder-chips, neutrophils aggregated and formed neutrophil swarms. However, neutrophils were not able to control the infection and demonstrate swarm disaggregation as observed in the bladder organoid model. This is possibly due to the unrestricted

growth of large numbers of extracellular bacteria and in some instances, exacerbated by the loss of some neutrophils due to flow in the channel. Moreover, geometrically defined array of pores on the PDMS membrane permitted neutrophil diapedesis only at fixed spatial locations in bladder-chip. This way of neutrophil migration was different from neutrophil migration via ECM remodelling of collagen gels in the bladder organoid model. The neutrophils formed NETs which were confirmed via immunostaining for neutrophil myeloperoxidase, neutrophil elastase, and also with SEM.

Extracellular UPEC growth was largely controlled with introduction of ampicillin (~40X MIC) into the bladder-chip. The ampicillin concentration and duration were chosen to mimic the characteristic pharmacokinetic/pharmacodynamic profile of ampicillin concentration in the blood. We chose pulsed exposures to high concentrations of antibiotic, to mimic the periodic boluses of antibiotic taken by patients. Compared to extracellular bacteria that were substantially killed by ampicillin and removed via flow, the intracellular bacteria proliferated with exponential growth to form IBCs. These IBCs that arose initially from few bacteria, exhibited all the characteristic features of IBC dynamics i.e formation, maturation, dispersal and exfoliation. Investigation of multiple IBCs revealed that shedding and exfoliation were not mutually exclusive events.

Mouse models of UTIs have shown that IBCs provide bacteria with a semi-protective niche as an enabler for bacterial persistence. We studied persistence of IBCs by subjecting the bladder-chip to a second round of ampicillin treatment (~40X MIC) treatment for 3 hours. These experiments allowed us to document exponential growth of bacteria in the absence of antibiotic, delayed response to antibiotic, and a lag phase after the antibiotic was removed. Few early-stage IBCs provided a fully protective niche for proliferating bacteria during the entire duration of the ampicillin treatment. Thus, pulsed exposures to high concentrations of antibiotic revealed that IBCs provided bacteria with dynamic niche to persist and evade clearance.

| Features | Bladder organoids | Bladder-chip |
|--|--------------------------|---------------------|
| stratified uroepithelium | +++ | + |
| size invariability | + | +++ |
| vasculature | not done | +++ |
| medium perfusion | + | +++ |
| bladder filling and voiding | + | +++ |
| urine-medium nourishment | not possible | +++ |
| bacterial growth and intracellular lifecycle | ++ | +++ |

| | | |
|--|--------------|----------|
| antibiotic persistence | ++ | +++ |
| solitary bacteria in the uroepithelial wall | +++ | not done |
| co-culture with neutrophils | +++ | +++ |
| neutrophil swarm formation and dispersal | +++ | ++ |
| NETs formation | not detected | +++ |
| | | |
| Techniques/interventions | | |
| multi-position confocal imaging | +++ | +++ |
| molecular readouts (qrt-pcr) | ++ | +++ |
| single IBC tracking | + | +++ |
| non-growing bacteria tracking | +++ | +++ |
| rounds of antibiotic treatment | not done | +++ |
| scanning electron microscopy | +++ | +++ |
| transmission electron microscopy | ++ | +++ |
| serial block face scanning electron microscopy | +++ | not done |

Table 4: Comparative strengths and weaknesses of bladder organoid and bladder chip systems

Despite faithful recapitulation of intracellular UPEC lifestyle in the bladder organoids and bladder-chips, both systems also suffered from some limitations, as highlighted in Table 4. The bladder organoids never reconstituted binucleate cells in the umbrella cell layer. The closed lumen of the organoid also did not facilitate introduction of bacterial culture in urine inside the organoid. Moreover, as the antibiotic was introduced into the collagen surrounding the organoids, the local concentration of the antibiotic inside the bladder lumen needs to be determined experimentally. The slower recovery of UPEC regrowth post-antibiotic washout could also be due to the residual antibiotic in the organoid volume, due to incomplete washout. Also, as the bladder organoids were not surrounded by vasculature, it is plausible that the neutrophil attachment and migration into the organoid was not optimal. Moreover, we did not culture bladder organoids with resident immune cells such as macrophages, mast cells, dendritic cells etc, each of which could have played an important role in UPEC clearance. NETs were also not observed in infected bladder organoids. However, this could be due to the surrounding ECM.

Compared to the bladder organoid model which did not permit bacterial culture in urine, the bladder-chip system allowed distinct perfusion of urine and nutritional medium perfusion on the bladder epithelium and endothelium interface respectively. Antibiotic introduction and removal were also better controlled in bladder-chip system. Apart from these advantages, a major drawback of the bladder-chip was the absence of uniform stratified architecture of the bladder epithelium, which could also be attributed to the umbrella cell type nature of the HTB9 cell line. With other complementary

approaches, including attempts with attempting a feeder layer system, we have demonstrated the ability to achieve islands of stratified uroepithelium. However, this approach was not robust enough for infection studies in the non-uniformly stratified uroepithelium. Thus, we did not proceed with that approach and instead continued with epithelial monolayers. Further intensive efforts in the future either with iPSC approach or further insights about the exact stem cell population in the bladder uroepithelium could help in achieving uniform uroepithelium stratification. The approach of primary uroepithelial cells in microfluidic hydrogels could help in recapitulation of the mature and stratified uroepithelium surrounded by bladder fibroblasts and bladder smooth muscle cells.

Neutrophil's antimicrobial arm of defense manifests in different behaviours: neutrophil swarms and NETs. The bladder-chip recapitulated both types of neutrophil behaviour. By using DNA labelling dyes such as SYTOX, the bladder-chip could be further explored to study the spatiotemporal dynamics of both neutrophil swarm and NETs formation. This could help in understanding whether one type of neutrophil behaviour precedes the other or both occur concurrently as a response to bacterial infections.

The proof of concept for blood-bladder chemotaxis recapitulated only a small proportion of innate immune response to bacterial infection. The bladder-chip did not reconstitute resident immune cell population in the uroepithelium. Further efforts with differentiation of blood derived monocytes and other purified immune cells isolated with miltenyi magnetic isolation beads could help in recapitulating some aspects of the resident immune cell population in the bladder-chip.

Urinary bladder is a highly mechanically active organ that experiences different mechanical stresses. The bladder-chip was subjected to relatively lower linear strain compared to that experienced *in vivo*. This could be improved by culturing epithelial cells on soft and flexible collagen tubes. The uroepithelium experiences shear stress only during the micturition. However, we maintained a continuous flow in the bladder-chip, which also facilitated imaging by getting rid of extracellular bacteria. The continuous perfusion and flow-mediated dilution of the inflammatory chemokines could have influenced the behaviour of neutrophil swarms on the infected epithelium. Moreover, the positive correlation observed between stretching and bacterial burden needs to be further probed. Also, the effect of hydrostatic pressure on bacterial attachment and invasion can be tested by blocking the outlet of the bladder chip and applying pressure with the pressure control system.

The biofilm development within IBCs is mediated through differential regulation of different genes. Using genetic tools to construct fluorescent reporter strains, one can study the heterogeneity in gene expression of these molecular players and how this heterogeneity affects the outcome of the infection process at the biofilm level. While imaging of a tightly packed biofilms even with confocal microscopy is currently challenging, advances in microscopy and image analysis will allow us to capture the heterogeneity and the role of these components in UTI pathogenesis.

IBCs provided bacteria with a semi-protective niche for bacterial persistence. In this study, the experiments have used ampicillin as the candidate antibiotic to study bacterial persistence. However, in the future, it would be very interesting to study bacterial survival in IBCs upon treatment with drugs currently prescribed in the clinic for simple and recurrent UTIs such as Fosfomycin, Nitrofurantoin, Trimethoprim-sulfamethoxazole etc. This could greatly help in understanding the bacterial killing and persistence and aid the design of future treatment regimens. Also, the bladder-chip could be connected downstream to the temporal antibiotic gradient generator such as the devices developed by Dr. Katrin Schneider in the McKinney lab. This approach could allow us to monitor bacterial growth and survival to a more clinically relevant pharmacokinetic/pharmacodynamic profile. These unique capabilities of the bladder-chip to realistically model antibiotic treatment regimens for IBCs can also be leveraged in the future to screen non-antibiotic therapies such as mannositides that can eliminate persistent bacterial populations in IBCs or alter the host-pathogen interaction dynamic in UTIs.

These findings from bladder microtissue models of UTIs will have important ramifications for treatment of not only UTIs but also other bacterial infections that exhibit high levels of recurrence. Thus, we believe that these two bladder microtissue models will be of considerable interest not only to the community of microbiologists and immunologists who research UTIs and bacterial biofilms, but also to the medical doctors who treat bladder morbidities in the clinic. In addition, the development of these two bladder microtissue models either individually or in combination to form bladder organoid-on-chip can serve as a useful tool for bioengineers and researchers studying microbiology, bladder cancers, and immunology.

Publications during this PhD and with collaborations

1. Sharma, K., Thacker, V.V., Dhar, N., Signorino-Gelo, F., Cabrer, M.C., Dubois, A., Mullenders, J., Knott, G., Clevers, H., and McKinney, J.D. (2020). Invasion into the bladder wall generates solitary subpopulations of uropathogenic *Escherichia coli* that are protected from killing by antibiotics and neutrophil swarms in an organoid model. Biorxiv 2020.10.29.358622. (in revision)
2. Sharma, K., Dhar, N., Thacker, V.V., Simonet, T.M., Signorino-Gelo, F., Knott, G., and McKinney, J.D. (2021). Dynamic persistence of intracellular bacterial communities of uropathogenic *Escherichia coli* in a human bladder-chip model of urinary tract infections. Biorxiv 2021.01.03.424836. (under peer review)
3. Thacker, V.V., Dhar, N., Sharma, K., Barrile, R., Karalis, K., and McKinney, J.D. (2020a). A lung-on-chip model of early *M. tuberculosis* infection reveals an essential role for alveolar epithelial cells in controlling bacterial growth. *Elife* 9, e59961.
4. Thacker, V.V., Sharma, K., Dhar, N., Mancini, G.-F., Sordet-Dessimoz, J., and McKinney, J.D. (2020b). Rapid endothelial infection, endothelialitis and vascular damage characterise SARS-CoV-2 infection in a human lung-on-chip model. Biorxiv 2020.08.10.243220. (in revision)
5. Serex, L., Sharma, K., Rizov, V., Bertsch, A., McKinney, J.D., and Renaud, P. (2020). Microfluidic-assisted bioprinting of tissues and organoids at high cell concentrations. *Biofabrication*.

Resume

Kunal Sharma Education



Bio-Micro-Mech Engineer

- 5 years experience of developing technologies and model systems for studying an infectious disease
- Enjoy leading teams, cross collaborations with seniors, peers and student trainees alike
- Displays good analytical, organizational, troubleshooting & presentation skills
- Diversity of engineering skills from mechanical, micro-engineering and bioengineering



- Ph.D** École Polytechnique Fédérale de Lausanne, Switzerland Sept 2015-Present
Doctor of philosophy (Ph.D.) in Bioengineering
- M.Sc** École Polytechnique Fédérale de Lausanne, Switzerland Sep 2012 - Jan 2015
Master of Science (M.Sc) in Mechanical Engineering | Mark: 5.25/6
Relevant Coursework: nanotechnology, biomaterials, microfluidics, biophotonics, numerical methods in biomechanics and heat Transfer, fracture mechanics, applied machine learning, mobile robotics
- B.Tech** National Institute of Technology Kurukshetra, India July 2008 - June 2012
Bachelor of Technology in Mechanical Engineering | Mark : 9.34/10
Relevant Coursework: CAD design and manufacturing, kinematics and dynamics of machines, mechanics of fluids, strength of materials, material science, heat transfer, applied mechanics, operations research, advanced mathematics

Research & Development Experience

PhD thesis

Laboratory of Microbiology and Microtechnology, Global Health Institute, EPFL
Thesis title: Developing organ-on-a-chip and organoids as model systems to study host-pathogen interactions with time-lapse imaging in urinary tract infections

- Developed two cell culture model systems: human bladder-on-a-chip (two-dimensional) and mouse bladder organoids (three-dimensional) for studying an infectious disease. Setup systems compatible for time-lapse imaging, continuous nutritional feeding for living cells and application of mechanical stresses.
- Recapitulated different stages of bladder urination cycle using mechanical stretching and shear stress in human bladder-on-a-chip.
- Characterized systems with techniques: confocal imaging, immunofluorescence, electron microscopy techniques (transmission, scanning and serial block scanning).
- Studied and analysed temporal dynamics of bacterial growth and immune cell migration using Imaris cell imaging software and Matlab.
- Setup collaborations with pioneer research group in the field of organoids and with leading startup in the organ-on-a-chip field.
- Learnt from collaborations with many researchers (scientists, PhD students, students) and core imaging facilities: Biological electron microscopy, Bio Imaging - Optics core facility and Life science workshop.
- Collaborated in a project on microfluidic-assisted 3D bioprinting of tissues and organoids at high cell concentrations.

Master thesis

Laboratory of Microbiology and Microtechnology, Global Health Institute, EPFL
Thesis title: Global responses of mycobacteria to antibiotics

- Applied an array of platforms such as metabolomics, bacterial cytological profiling and scanning electron microscopy to identify mechanism of action signatures of known ten antimycobacterial compounds.
- Numerical modeling (COMSOL Multiphysics) of bacterial trapping and drug concentrations inside microfluidic gradient generators. Cell growth modelling (COMSOL Multiphysics) of cell deformation under different growth patterns in bacterial cells.

Languages

English ● ● ● ● ●

French ● ● ● ● ●

Personal Interests

- Reading books from diverse topics such as entrepreneurship, artificial intelligence, design, creativity, economics, biodesign, psychology and neuroscience.
- Solving puzzles in the domain of physics, mathematics and computer science on brilliant.org.
- Reading articles on management, leadership and economics on Harvard Business Review and Blinkist
- Cooking Indian, Italian and a fusion of various world cuisines
- Playing sports such as hiking, badminton, cricket, swimming snowboarding and PS4 games.

Personal Info



Chemin de chandieu 25,
Lausanne 1006, Switzerland



+ 41 786035643



kunal.sharma@epfl.ch



19 january 1990



kunal123sharma



Swiss B Permit;
Indian Nationality



Linkedin

Semester projects

Topic: Low noise platforms equipped with ultrathin nanopore membranes for base specific sensing

- Worked on developing and optimising cleanroom process flow for MoS₂ nanopore devices on quartz substrates with applications in base specific DNA sequencing. I also did numerical modelling in COMSOL Multiphysics to evaluate force experienced by a DNA strand inside a nanopore and nanocapillary.

Topic: Numerical modelling of Nanofluidic Field Effect Transistors

- Developed COMSOL Multiphysics models to identify influence of difference parameters such as surface charge, external electric field on ionic transport in Nanofluidic Field Effect Transistors.

Awards & Recognition

- Fellowship for attending two weeks course on 'Organotypic and Next Generation Culture Methods' conducted at Cold spring harbor laboratory in Dec 2016.
- Scholarships from national talent search examination and meritorious student examinations conducted at national and state level respectively in India.

Technical Skills

Microscopy and image processing | Confocal time lapse imaging | Matlab | Imaris cell imaging software |

Bioengineering techniques | Organ-on-a-chip technology (2D cell culture) | Organoids (3D cell culture) | Microfluidics | Mechanical stresses | Bioprinting |

Wet lab techniques | Pathogenic bacteria | Human cell culture | Animal experimentation |

Fabrication techniques | Photolithography | Scanning electron microscopy | Focussed ion beam | Wet & dry etching | Microfluidics |

Data, Design and CAD Skills

Programming | Python | Matlab | Imagej |

Numerical Modelling | Imaris | COMSOL multiphysics | ANSYS | SOLIDWORKS |

Software | Adobe illustrator | Latex |

Trainings, Workshops and Courses

- Applied machine learning days (conference and workshop): (Jan 2020, EPFL)
- 14-week business concept training and participated in developing a business project through Innosuisse business concept course (Feb-June 2019, EPFL Innovation Park)
- Organotypic Next Generation Cultural Methods (Dec 2016, USA)
- Practical Holotomographic Microscopy for Live Cell Imaging : Nanolive (Aug 2018, EPFL)
- Developed a prototype of mobile application for on-demand appointment, prescription services for healthcare (Feb 2019, Startup weekend Lausanne)
- Teaching assistant for biomedical optics and global health issues
- Supervised two semester projects, currently supervising a master's thesis project and a semester project.

Internships

- Integration of Pulse Width Flow Modulation with microfluidic platform for doing time-lapse studies of cells exposed to varying concentrations of drugs. Laboratory of Microbiology and Microtechnology, EPFL, Feb-Apr, 2015.
- Integration and design of shock protection features for 3D Silicon structures, CSEM Neuchâtel, Jul-Sept 2013.
- Reliability in JCB Machines, JCB India Limited, Jun-Jul 2010.

Conferences

- K. Sharma et al., "Microtechnologies for studying host-pathogen interactions using uropathogenic Escherichia coli", Engineering Biology for Medicine: Nature Conference, Duke University, USA, 2019.
- K. Sharma et al., "Microtechnologies for studying host-pathogen interactions using uropathogenic Escherichia coli", Molecular advances and novel therapies in UTI, Lund University, Sweden, 2018.
- K. Sharma et al., "Bladder-on-a-chip model for studying host-pathogen interactions in uropathogenic Escherichia coli", Microbial Pathogenesis Host Response Meeting, Cold Spring Harbor Laboratory, USA, 2017.

Publications

- K. Sharma et al., "Effect of distinct conductive and thermodynamic temperatures on the reflection of plane waves in micropolar elastic half-space", UPB Sci Bull Series A-Appl Math Phys, 75 (2), 121-132, 2013.
- K. Sharma et al., "Propagation of plane waves and fundamental solution in thermoviscoelastic medium with voids", Journal of Thermal Stresses, 36(2), 94-111, 2013.
- K. Sharma et al., "Reflection and transmission of waves from imperfect boundary between two heat conducting micropolar thermoelastic solids", Analele Universitatii "Ovidius" Constanta-Seria Matematica, 22(2), 151-176, 2014.
- K. Sharma et al., "Propagation of thermoelastic plane waves at an imperfect boundary of thermal conducting viscous liquid/generalized thermoelastic solid." Afrika Matematika 25 (1), 81-102, 2014 .

Complete list available on Google Scholar: <https://scholar.google.ch/citations?user=ZhCtfVcAAAAJ&hl=en>

The road not taken

By Robert Frost

Two roads diverged in a yellow wood,
And sorry I could not travel both
And be one traveller, long I stood
And looked down one as far as I could
To where it bent in the undergrowth;

Then took the other, as just as fair,
And having perhaps the better claim,
Because it was grassy and wanted wear;
Though as for that the passing there
Had worn them really about the same,

And both that morning equally lay
In leaves no step had trodden black.
Oh, I kept the first for another day!
Yet knowing how way leads on to way,
I doubted if I should ever come back.

I shall be telling this with a sigh
Somewhere ages and ages hence:
Two roads diverged in a wood, and I—
I took the one less travelled by,
And that has made all the difference.